Middle Miocene carbon cycle dynamics: A multi-proxy approach

Marcus Badger

Cardiff University
2010

ProQuest LLC
789 East Eisenhower Parkway
P.O. Box 1346
Ann Arbor, MI 48106-1346

DECLARATION

This work has not previously been accepted in substance for any degree and is not concurrently submitted in candidature for any degree.

Signed ..... Date 17/12/10

STATEMENT 1

This thesis is being submitted in partial fulfilment of the requirements for the degree of PhD

Signed ..... Date 17/12/10

STATEMENT 2

This thesis is the result of my own independent work/investigation, except where otherwise stated. Other sources are acknowledged by explicit references.

Signed ..... Date 17/12/10

STATEMENT 3

I hereby give consent for my thesis, if accepted, to be available for photocopying and for inter-library loan, and for the title and summary to be made available to outside organisations.

Signed ..... Date 17/12/10

STATEMENT 4: PREVIOUSLY APPROVED BAR ON ACCESS

I hereby give consent for my thesis, if accepted, to be available for photocopying and for inter-library loans **after expiry of a bar on access previously approved by the Graduate Development Committee.**

Signed .....Date 17/12/10

For Ellie.

Abstract

The development of permanent, stable ice sheets in Antarctica happened during the middle Miocene, about 14 million years ago (Flower and Kennett, 1995; Zachos et al., 2001). The middle Miocene therefore represents one of the distinct phases of rapid change in the transition from the "greenhouse" of the Cretaceous to the "icehouse" of the present day. Accompanying the middle Miocene growth of the Antarctic Ice Sheet are major perturbations in the global carbon system, represented by some of the largest fluctuations in marine carbonate $\delta^{13}C$ values in the Cenozoic (Flower and Kennett, 1995; Zachos et al., 2001). A broad positive carbon isotope excursion; the "Monterey Excursion" (Vincent and Berger, 1985) begins in the early Miocene (approximately 16.9 Myr ago) and terminates in the middle Miocene ~13.8Myr ago (Holbourn et al., 2007). Within this broad $\delta^{13}C$ excursion, higher frequency fluctuations have been recognised with at least 7 carbon isotope maxima (CM) defined (Woodruff and Savin, 1991).

The Ras il-Pellegrin section, Malta spans the 1.1Myrs following the growth of the ice sheet. The simple tectonic history and clay-rich sediments of the Serravallian Blue Clay Formation has led to exceptional preservation of foraminifera and organic biomarkers.

Stable isotope analysis of bulk carbonate and planktonic foraminifera *Globigerinoides trilobus* at Ras il-Pellegrin show the globally recognised positive carbon isotope excursion CM6 and the final stages of the ice sheet expansion ("E3"; Miller et al. 1993). Combined alkenone unsaturation index ($U^{K'}_{37}$) and *G. trilobus* Mg/Ca ratios were used to reconstruct sea surface temperature. Over CM6 temperatures dropped by ~5°C as the ice sheet expanded, and the temperature contribution to the $\delta^{18}O$ record is ~30%, in agreement with other studies (Billups and Schrag, 2002; Lear et al., 2000; Shevenell et al., 2008). Sea surface temperatures estimated from *G. trilobus* Mg/Ca at this Mediterranean site averaged ~30°C.

Atmospheric pCO_2 decreased as the ice sheet expansion progressed, coinciding with CM6. The magnitude of the decrease is on order ~70 ppm, based on alkenone and boron palaeobarometry. The absolute magnitude of atmospheric pCO_2 is relatively low (~300 ppm) in general agreement with other Neogene studies (Kürschner et al., 2008; Pagani et al., 1999a; Pearson and Palmer, 2000) in a time of relatively high temperatures.

On the basis of ocean carbonate system modelling coupled with the records presented here, the recently suggested "silicate weathering hypothesis" (Shevenell et al., 2008) for CM6 is untenable. The mechanism preferred here is increased organic carbon burial, in agreement with the "Monterey Hypothesis".

Coupled inorganic-organic carbon isotopes spanning the Monterey Excursion (16.9-13.5 Ma) suggest changes in the carbon system consistent with the Monterey Hypothesis. Thermal stratification of the oceans is inferred to have increased during the middle Miocene climate transition.

Acknowledgements

I would like to thank Carrie Lear for her help, support and advice throughout the project, and Rich Pancost for his help and enormous and infectious enthusiasm, which was always welcome, not least when things went wrong. Without Fiona Gill the organic work would never have happened and I warmly thank her for all her assistance, time and patience.

I am grateful to Hemmo Abels who introduced me to the Ras il-Pellegrin section and led the field, to Anja Mourik who assisted in the field and Godwin Debono of the Maltese Oil Exploration Department who organised working permissions.

Many thanks to Trevor Bailey who helped with fieldwork in Italy and Mg/Ca analysis, and to Becca Moremon who assisted with the Italy fieldwork. Thanks also to Ian Bull who supported mass spectrometry work at Bristol, Iain McDonald who performed ICP-OES analysis at Cardiff and Pete Fisher for SEM work. I'd like to thank Melanie Leng, Jo Green and everyone at NIGL for analyses performed there, and to Gavin Foster for producing the boron record at Bristol. For foraminiferal taxonomic assistance and many pleasant chats about research I'd like to thank Paul Pearson.

I would like to thank my office mates: Anna, Helen, Cat and Elaine for making time spent in the office fun and for all the discussions, support and endless cups of tea. Everyone at the OGU also deserves my warmest thanks. Over the last few years the friendship of Christian, Helena, Martin, Sarah, David and Huw have enriched my time at Cardiff. Kate and Rhys have been amazing housemates and all at the Cardiff Branch made life outside work that bit more fulfilling. Finally I'd like to thank my family for everything they've done for me, and Parisa, who probably had a worse time of my write-up than I did.

Abbreviations and Notations Used throughout

Definitions of Isotope Notations

$$\delta^{18}O = \left[\frac{\left({}^{18}O/{}^{16}O\right)_{\text{sample}} - \left({}^{18}O/{}^{16}O\right)_{\text{standard}}}{\left({}^{18}O/{}^{16}O\right)_{\text{standard}}} \right] \cdot 1000$$

$$\delta^{13}C = \left[\frac{\left({}^{13}C/{}^{12}C\right)_{\text{sample}} - \left({}^{13}C/{}^{12}C\right)_{\text{standard}}}{\left({}^{13}C/{}^{12}C\right)_{\text{standard}}} \right] \cdot 1000$$

$$\delta^{11}B = \left[\frac{\left({}^{11}B/{}^{10}B\right)_{\text{sample}}}{\left({}^{11}B/{}^{10}B\right)_{\text{NIST951}}} - 1 \right] \cdot 1000$$

Abbreviations

Ma Million years before present

Myrs Million years

kyrs Thousand years

T Temperature

S Salinity

OM Organic Matter

RIP Ras il-Pellegrin (Malta)

MMCT Middle Miocene climate transition

MMCO Middle Miocene climatic optimum

Contents

1 Introduction

1.1 Cenozoic Temperature, Ice Volume and pCO_2

On a geological timescale, the climate of the Earth is never stable; the boundary conditions which determine the temperature of the Earth's surface (orbital parameters, tectonics) are always varying, albeit slowly. The Earth's climate, therefore, is in a constant state of flux, which is represented in the Cenozoic by long-term quasi-stable periods punctuated by relatively short periods of dramatic and wholesale change (Zachos et al. 2001). It is one of these periods of profound change, the middle Miocene climate transition, which is the focus of this work.

When describing the climate of the Earth, three interlinked parameters are key: temperature, ice volume and atmospheric pCO_2. The early work of Urey (1947), Epstein et al. (1951) and Emiliani (1954) allowed for the development of the oxygen isotope palaeothermometer. Early long-term records of Cenozoic climate change using oxygen isotopes of planktonic and benthic foraminifera record a cooling trend since the Cretaceous (Shackleton and Kennett, 1975). Subsequent records, developed primarily from high resolution archives from the Deep Sea Drilling Project and Ocean Drilling Program, confirmed this but also facilitated our understanding of more rapid or short term Cenozoic climate changes (e.g. Miller and Katz, 1987; Zachos et al., 2001, 2008; Figure 1).

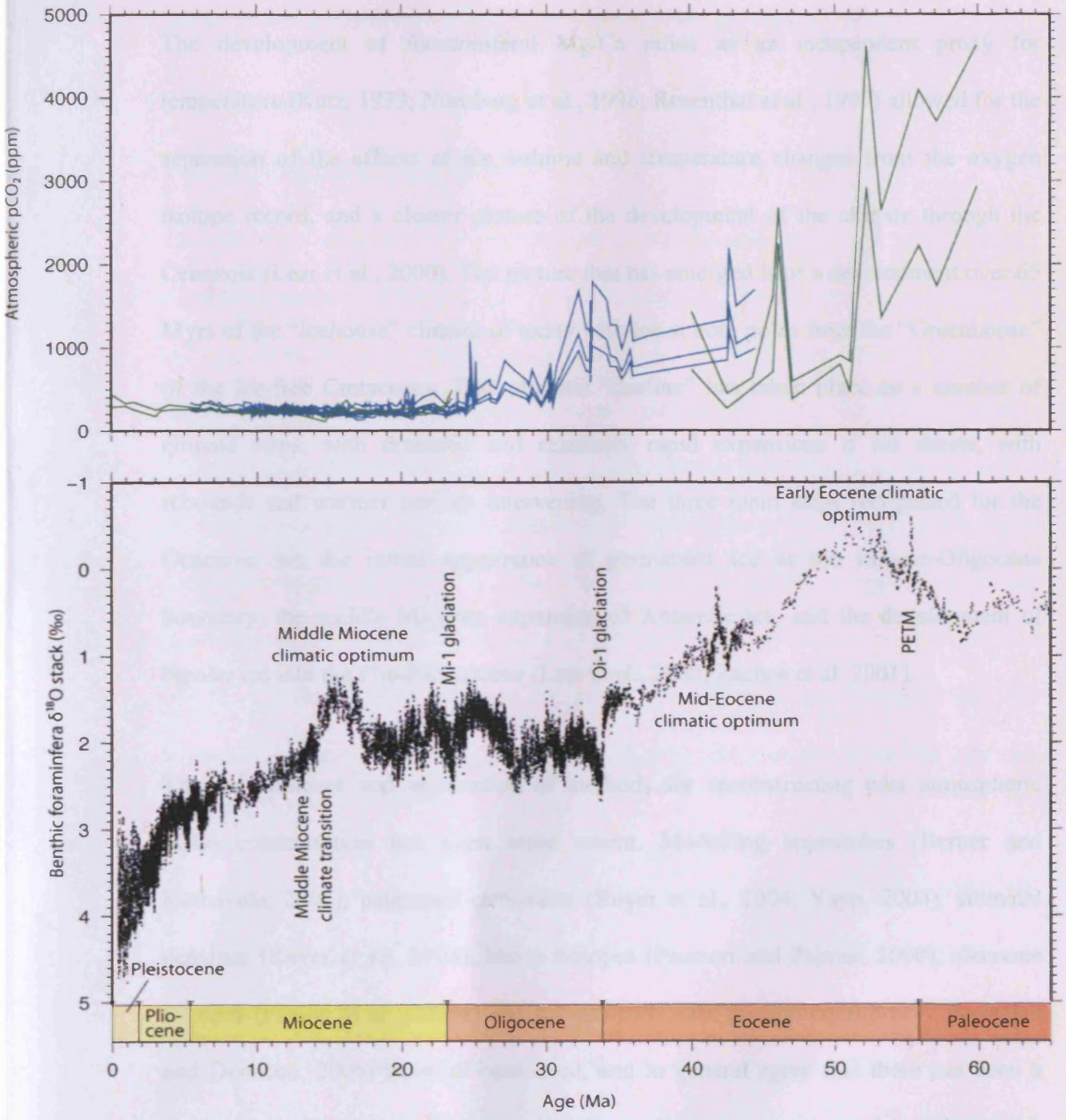

Figure 1 Cenozoic climate and atmospheric CO_2 records. The upper panel shows atmospheric CO_2 reconstructions from alkenone (blue line; (Pagani et al., 2005)) and boron isotopes (green line; Pearson and Palmer, 2000). These are shown as maximum and mimimum estimate envelopes. The lower panel shows a global, stacked benthic foraminiferal oxygen isotope compilation (Zachos et al., 2008). PETM= Paleocene-Eocene thermal maximum. The warmth of the MMCO and the MMCT seem to happen during a period of relatively stable atmospheric CO_2, on the basis of the long-term records shown here.

The development of foraminiferal Mg/Ca ratios as an independent proxy for temperature (Katz, 1973; Nürnberg et al., 1996; Rosenthal et al., 1997) allowed for the separation of the effects of ice volume and temperature changes from the oxygen isotope record, and a clearer picture of the development of the climate through the Cenozoic (Lear et al., 2000). The picture that has emerged is of a development over 65 Myrs of the "Icehouse" climate of today with ice at both poles from the "Greenhouse" of the ice-free Cretaceous. This climatic "decline" has taken place as a number of climate steps, with dramatic and relatively rapid expansions if ice sheets, with rebounds and warmer periods intervening. The three main steps recognised for the Cenozoic are the initial appearance of permanent ice at the Eocene-Oligocene boundary, the middle Miocene expansion of Antarctic ice, and the development of bipolar ice into the Plio-Pleistocene (Lear et al., 2000; Zachos et al. 2001).

The development and application of methods for reconstructing past atmospheric pCO_2 concentration has been more recent. Modelling approaches (Berner and Kothavala, 2001), palaeosol carbonates (Royer et al., 2004; Yapp, 2004), stomatal densities (Royer et al., 2004), boron isotopes (Pearson and Palmer, 2000), alkenone isotopes (Pagani et al., 2005a) and sodium carbonate mineral equilibria (Lowenstein and Demicco, 2006) have all been used, and in general agree that there has been a decline in atmospheric CO_2 over the Cenozoic as temperatures have decreased. Alkenone and boron isotope methods have shown the most promise in terms of the generation of high resolution, continuous records approaching the fidelity of the oxygen isotope records of temperature and ice volume, and although there has been

some concern about the details of each methods (see for example Pagani et al, 2002, 2005b), the two methods record similar patterns over the Cenozoic (Figure 1).

1.2 Miocene Climate

The Miocene is an epoch of climate extremes, from the warmth of the middle Miocene climatic optimum (MMCO), which saw crocodiles in central Europe (Böhme, 2003) and deciduous trees in Alaska (Leopold and Liu, 1994), to the dramatic growth of Antarctic ice at the middle Miocene climate transition (MMCT) which is the focus of this study (Shackleton and Kennett, 1975). The stepwise transition from the warmth of the middle Miocene to the cooler conditions following the growth of permanent ice on Antarctica began around 14.5 Ma, with successive events recognisable in the foraminiferal $\delta^{18}O$ record, known as Mi-3 and Mi-4 in the nomenclature of Miller et al (1993). Although there is evidence of earlier transitory ice in the Miocene (Mi-1, 1a, 1b and 2; Miller et al., 1991), it is not until 14.5 Ma that this transition becomes permanent.

The ultimate cause of the ice growth is unclear. The MMCT took place within the broader setting of cooling through the Cenozoic (Lear et al., 2000; Zachos et al., 2001), and the Mi-3b event (one of the larger steps in the $\delta^{18}O$ record) coincides with a node of low eccentricity and minimum obliquity and precession amplitudes (Abels et al., 2005; Holbourn et al., 2005). Long term records of atmospheric CO_2 do not show any significant decrease in the run up to the MMCT (Pagani et al., 2005a; Pearson and Palmer, 2000), and orbital parameters may have been important in determining the timing of the ice sheet growth, allowing the build-up of a large, stable ice sheet during a period of low summer insolation (Holbourn et al., 2005).

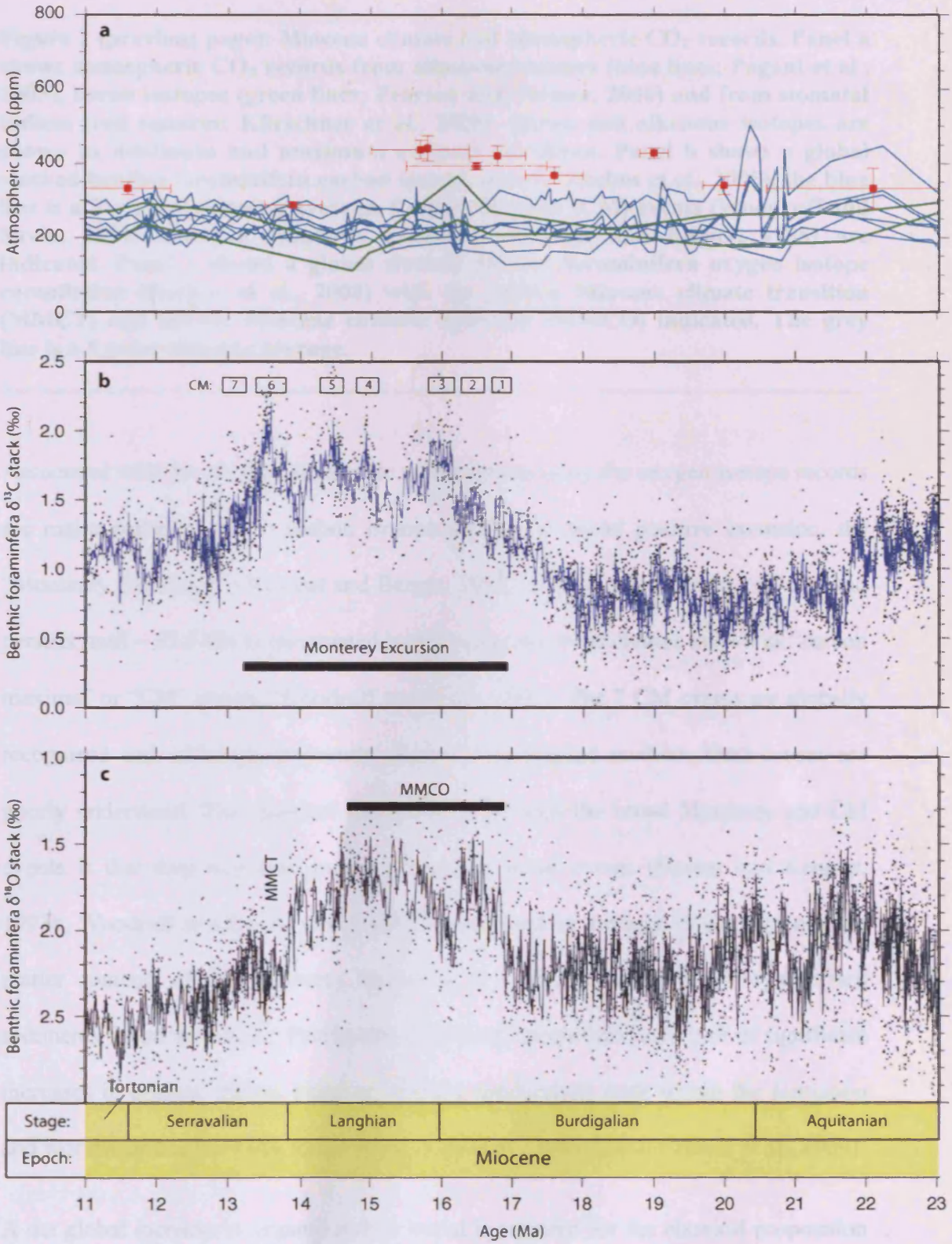
a
Atmospheric pCO_2 (ppm)
800
600
400
200
0
b
CM: 7 6 5 4 3 2 1
Benthic foraminifera $\delta^{13}C$ stack (‰)
2.5
2.0
1.5
1.0
0.5
0.0
Monterey Excursion
c
MMCO
MMCT
Benthic foraminifera $\delta^{18}O$ stack (‰)
1.0
1.5
2.0
2.5
Tortonian
Stage:
Serravalian
Langhian
Burdigalian
Aquitanian
Epoch:
Miocene
11
12
13
14
15
16
17
18
19
20
21
22
23
Age (Ma)

Figure 2 (previous page): Miocene climate and atmospheric CO_2 records. Panel a shows atmospheric CO_2 records from alkenone isotopes (blue lines; Pagani et al., 2005), boron isotopes (green lines; Pearson and Palmer, 2000) and from stomatal indices (red squares; Kürschner et al., 2008). Boron and alkenone isotopes are shown as minimum and maximum estimate envelopes. Panel b shows a global stacked benthic foraminifera carbon isotope record (Zachos et al., 2008), the blue line is a five point running average. Carbon Maxima (CM) events (Woodruff and Savin, 1991) and the Monterey excursion (Vincent and Berger, 1985) are indicated. Panel c shows a global stacked benthic foraminifera oxygen isotope compilation (Zachos et al., 2008) with the middle Miocene climate transition (MMCT) and middle Miocene climatic optimum (MMCO) indicated. The grey line is a 5 point running average.

Associated with the changes in climate as demonstrated by the oxygen isotope records are major perturbations in carbon isotope records. A broad positive excursion, the "Monterey Excursion" (Vincent and Berger, 1985) which begins around 16.9 Ma and persists until ~ 13.5 Ma is punctuated by shorter positive excursions known as "carbon maxima" or "CM" events (Woodruff and Savin, 1991). The 7 CM events are globally recognised and, although frequently used as stratigraphic markers, their causes are poorly understood. The classical interpretation of both the broad Monterey and CM events is that they represent increased organic burial events (Flower and Kennett, 1993b; Woodruff and Savin, 1991), initially proposed on the basis of the high organic matter contents of the Monterey formation in California and similar organic rich sediments found around the Pacific rim. However, unequivocal evidence of significant increases in organic carbon burial or primary productivity both within the formation and worldwide has not been forthcoming (Coe et al., 2008; Diester-Haass et al., 2009).

A net global increase in organic carbon burial is required for the classical proposition of a causal link between the Monterey event in the carbon isotope record and the MMCT in the oxygen isotope record. Under the "Monterey hypothesis", the sequestration of carbon via increased organic carbon burial would lead to a drawdown

of atmospheric CO_2, leading to decreased global temperatures and the ice sheet growth (Vincent and Berger, 1985). Long term reconstructions of atmospheric CO_2 based on alkenone and boron isotopes do not show a significant decrease over the period (Pearson and Palmer 2000; Pagani et al., 2005a), but more recently published work based on stomatal indices do show a decrease over the MMCT (Figure 2; Kürschner et al., 2008), higher resolution records of the atmospheric CO_2 are needed to resolve the discrepancy.

More recently, an alternative interpretation for the CM events, and specifically the largest excursion, CM6, has been suggested (Shevenell et al., 2008). The position of CM6 immediately following the increase in the oxygen isotope increase has led to suggestions that it may be related to a negative feedback related to the ice sheet growth. Under this scenario, the blanketing of a large area of silicate basement by the expansion of ice cover could lead to a slowdown in silicate weathering and decrease the weathering sink for atmospheric CO_2; this would cause atmospheric CO_2 concentrations to increase, and by increasing photosynthetic carbon isotope fractionation by marine phytoplankton, drive a positive carbon isotope excursion (Lear et al., 2004; Pagani et al., 1999a; Shevenell et al., 2008).

As these two hypotheses would have opposite effects on atmospheric CO_2 (organic carbon burial driving pCO_2 down, a reduction in silicate weathering driving pCO_2 up), a high resolution reconstruction of atmospheric CO_2 over CM6 could resolve which is most likely, and this one of the key aims of this work.

1.3 Palaeoclimate Proxies

1.3.1 Inorganic Proxies

Stable oxygen and carbon isotopes in carbonates can provide significant information about the state of the climate and carbon systems. There is a fractionation between the oxygen isotopic composition of the seawater in which an organism is calcifying, and the calcite it produces. The degree of fractionation is dependant on the temperature of the water in which the organism is living, and vital effects that vary slightly from species to species. In order to use this fractionation to determine the temperature at the time of calcification, the oxygen isotopic composition of the water in which calcification takes place ($\delta^{18}O_{sw}$) needs to be known. $\delta^{18}O_{sw}$ varies depending on the local salinity (the balance between evaporation and precipitation at the site) and, via Rayleigh fractionation that locks the light isotope in ice, the prevailing ice volume at the time. In an ice-free world, such as likely prevailed in the greenhouse climate of the Cretaceous, $\delta^{18}O$ can be used directly as a palaeothermometer. However, as permanent ice has been present for much of the Cenozoic, a second proxy is required to deconvolve the ice volume and temperature signals from oxygen isotopes. Foraminifera Mg/Ca fulfils this role. The uptake of Mg into the calcite lattice during calcification is temperature dependent, and so this can be used as an independent proxy for temperature, which allows the ice volume signal from oxygen isotopes to be estimated (Lear et al., 2000).

The interpretation of carbonate carbon isotopes is more complicated. Carbon isotopes, like oxygen isotopes, are fractionated by organisms during calcification. However the complexity of the global carbon cycle means that the carbon isotopic composition of the carbon pool from which this fractionation takes place ($\delta^{13}C_{DIC}$) is controlled by a

large number of factors. These include factors that are linked to the climate system, such as weathering, CO_2 emissions from volcanism and metamorphism, deposition of carbonate and organic carbon, and terrestrial biomass changes. Within the oceans the carbon pool varies spatially as the light isotope (^{12}C) is preferentially taken up in surface water by primary production, and the amount of light carbon which is removed varies with the productivity of the surface ocean, surface water CO_2 concentration ($[CO_{2(aq)}]$) and surface temperature. Determining what is causing changes in the $\delta^{13}C$ which is ultimately preserved in marine organic carbonates is therefore complex, but nevertheless $\delta^{13}C$ can tell us about when major perturbations of the carbon system are happening (such as the "CM" events and Monterey excursion in the Miocene) and by combining a number of proxies which relate to the carbon system, the cause of such perturbations may be determined.

Boron exists in the oceans in two aqueous species, boric acid ($B(OH)_3$) and borate ($B(OH)_4^-$). Only the charged species (borate) is incorporated into foraminiferal calcium carbonate, and the strong isotopic fractionation in the boron between boric acid and borate is pH dependent (Hemming and Hanson 1992; Kakihana et al. 1997) . The boron isotopic composition of boron in foraminifera is pH dependent, and if one other parameter in the ocean carbonate system can be constrained, $[CO_{2(aq)}]$ can be determined. Foraminiferal B/Ca can be used to determine carbonate ion concentration, and so a coupled record of foraminiferal $\delta^{11}B$ and B/Ca can be used to calculate $[CO_{2(aq)}]$, and from this atmospheric carbon dioxide concentration can be calculated (Foster, 2008).

1.3.2 Organic Proxies

Organic carbon is preserved in sediments, and the carbon isotope composition of the preserved organic matter (OM) can provide information about the carbon system. Similar to the $\delta^{13}C$ of carbonate material, the complexity of the carbon system means that direct interpretation of OM carbon isotopes is difficult. Further complicating this is that the $\delta^{13}C$ measured from bulk OM preserved at a site comes from a large number of different sources, each with its own $\delta^{13}C$ and fractionating processes. Nevertheless, bulk OM $\delta^{13}C$ can provide a second proxy for changes occurring in the carbon cycle, and when combined with carbonate $\delta^{13}C$ can provide insight into the nature of the changes.

Due to the ambiguity of the source of the bulk organic matter much work has been done on biomarkers. Biomarkers are "molecular fossils"; specific molecules which relate exclusively to a single marine species or group. By narrowing down the source of the organic carbon being analysed the $\delta^{13}C$ of the carbon can be more useful. During photosynthesis there is isotopic fractionation of carbon, and the degree of fractionation is controlled by $[CO_{2(aq)}]$ (Hollander and McKenzie, 1991). By combining carbonate and biomarker $\delta^{13}C$ aqueous CO_2 can be calculated, and from that atmospheric CO_2 can be calculated (Jasper and Hayes, 1990; Jasper et al., 1994)

Biomarkers can also be used to trace changing sources of organic material to a site, the distribution of *n*-alkanes varies between terrestrial and marine organisms, and can be used to determine whether the relative contributions from the terrestrial and marine realm change. Alkenone (long chain biomarkers specific to a restricted group of algae) distribution can also be used to estimate temperatures. The relative proportions of di-

and tri-unsaturated alkenones produced is dependent on the temperature of the water at time of synthesis (Brassell et al., 1986; Müller et al., 1998).

1.4 Thesis Outline

The aim of this thesis is to use a multi-proxy approach to answer questions of middle Miocene climate change. The exceptional preservation of the Ras il-Pellegrin section in Malta has allowed for both organic and inorganic proxies to be used in the same samples. The multi-proxy approach allows questions of the veracity of assumptions of individual proxy records to be answered by using multiple independent methods to reconstruct the same climate parameter (boron and alkenone reconstructions of atmospheric CO_2, Mg/Ca and alkenone unsaturation reconstructions of temperature (Chapter 5)). The aim of this thesis is to determine the climate conditions following the growth of the major ice sheet at the MMCT, and to explore the likely causes of the significant perturbations in the carbon system through the middle Miocene, as evident in the "CM" and Monterey events identified in the carbonate $\delta^{13}C$ records.

The thesis begins with an explanation of the method used (Chapter 2) and introduction to the Ras il-Pellegrin (Chapter 3) and Moria (Chapter 4) sections. In Chapter 5, I use a multi-proxy approach to reconstruct the variations in temperature and atmospheric CO_2 following the MMCT ice growth. In Chapter 6 the results are coupled with a carbon system model to identify likely causes for the perturbations identified.

2 Methods

2.1 Carbonate Analysis

2.1.1 Sample Preparation

Sediment samples were split into sub-samples for bulk, foraminiferal and biomarker analyses. Bulk samples were dried at 40°C overnight in an oven before being ground to a fine powder by hand. Samples for foraminiferal analysis were disaggregated in de-ionised water (15 $M\Omega cm^{-1}$) in a vertical plane spinner for 3-5 hours as needed and washed over a 63 μm mesh using de-ionised water (15 $M\Omega cm^{-1}$). The <63 μm fraction (fine fraction) was collected in plastic bags, allowed to settle out and supernatant water siphoned off, these fractions were combined and dried over a period of weeks in an oven at 40°C and weighed. Coarse fractions (>63 μm) were dried at 40°C and weighed to calculate coarse per cent. *Globigerinoides trilobus*, the most abundant planktonic foraminifer throughout the section, was picked from the 250 – 355 μm fraction for trace metal and stable isotope analysis.

2.1.2 Sample Cleaning

For stable isotope analysis, 8-10 glassy specimens of *G. trilobus* were cracked open to reveal interiors of chambers and obvious contaminant phases (pyrite and any infill) removed under the microscope. Samples were cleaned by addition of 3% H_2O_2 for 30 minutes to oxidise remnant organic material. A drop of methanol was added, before they were ultrasonicated for a few seconds, to aid drying.

For foraminiferal trace metal analysis samples were cleaned using a stepwise method adapted from Boyle and Keigwin (1985), detailed in Barker et al. (2003). This utilises

visual inspection to remove contaminant phases before and after the clay removal step; clay removal by ultrasonic suspension and rinses with de-ionised water (18.2 $M\Omega cm^{-1}$) and methanol, an oxidative step (H_2O_2 alkali buffered with 0.1M NaOH) to remove organic material and a final weak acid leach (0.001M HNO_3) to remove adsorbed contaminants. The reductive step of Boyle and Keigwin (1985) was omitted due to concerns over dissolution effects on Mg/Ca ratios (Barker et al. 2003; Rosenthal et al. 2004; Yu et al. 2007). Trace metal cleaning was performed under clean laboratory conditions, and all labware acid cleaned before use. Final sample dissolution was performed immediately before analysis to prevent leaching from sample tubes. Samples were dissolved in 120 µl 0.065M HNO_3, centrifuged and the top 100 µl transferred to clean tubes to remove non-carbonate fractions. The remaining 20 µl was centrifuged again and 10 µl taken to be analysed for Ca concentration.

For boron isotope and B/Ca analysis, 100 glassy specimens of *G. trilobus* were picked (~2 mg calcium carbonate). Cleaning and analysis were performed by G. Foster at the University of Bristol, cleaning procedures for boron analysis are detailed in Foster, (2008) and Ni et al., (2007). Initial sample cleaning was identical to that used for trace metal analysis, followed by a further overnight bleaching in sodium hypochlorite (NaClO; 5% Cl). Samples were dissolved in 100 – 300 µl of Teflon distilled 0.5 M HNO_3 in acid cleaned Teflon beakers. An aliquot of the solution was taken at this stage for trace metal analysis (to determine B/Ca ratio and to assess efficiency of cleaning). Prior to boron isotope analysis the Ca matrix must be removed. This was performed using Amberlite IRA 743 boron specific resin. Samples were dissolved in 0.5 M HNO_3 and buffered to pH 5 using 2 M Na acetate 0.5 M acetic acid buffer. Samples were loaded on 25 µl columns and the matrix removed with repeated rinses of deionised water (18 $M\Omega\ cm^{-1}$). Boron was washed off the resin using 0.5 M HNO_3.

Fine fraction (<63μm) carbonate samples were cleaned using reductive (hydroxyl ammonium chloride) and ion exchange (1M ammonia) steps, similar to Delaney and Linn (1993).

Coccolith fractions for analysis by analytical scanning electron microscopy were separated from sieved fine fractions (<63μm) by settling in methanol following the procedure of Stoll and Schrag (2000).

2.1.3 Sample Analysis

Bulk and *G. trilobus* stable isotope analyses were performed on a ThermoFinnigan MAT252 mass spectrometer with online sample dissolution using an automated Kiel II carbonate device at the School of Earth and Ocean Sciences, Cardiff University. Long term uncertainties based on repeat analysis of NBS-19 are ±0.08‰ and ±0.05‰ for $\delta^{18}O$ and $\delta^{13}C$ respectively (2σ). Fine fraction stable isotope analyses were performed on a VG Optima duel inlet gas source mass spectrometer at the NERC Isotope Geosciences Laboratory, Keyworth. Sample dissolution was performed offline. Samples were placed in reaction tubes within a reaction chamber to which 4 ml of anhydrous phosphoric acid was added (samples and acid were initially isolated from one another within the reaction chambers). Reaction chambers were then evacuated to better that 1.0^{-4} mb, removing atmospheric CO_2 and moisture. Reaction chambers were then equilibrated in a water bath to 25.2 °C before acid and samples were combined within the chambers and allowed to go to completion for at least 16 hrs. Resultant CO_2 was cleaned cryogenically on a high-pressure manifold by way of an acetone trap, and collected in dry sample chambers using liquid nitrogen. Isotope values are reported as per mille on the Vienna Pedee belemnite (VPDB) scale using an in-run internal laboratory standard (KCM) with known composition with respect to NBS-19. Internal

precision was monitored using two further in-run laboratory standards (MCS-18 and CCS-3). Values were corrected for small levels of ^{17}O using Craig's correction (Craig, 1957) and to the solid carbonate value using a fractionation factor of 1.01025 (Sharma and Clayton, 1965). Analytical errors are typically better than ±0.3‰ for $\delta^{18}O$ and ±0.1‰ for $\delta^{13}C$ (2σ).

Trace metal analyses (excluding fine fraction Sr/Ca and foraminiferal B/Ca) were performed on a ThermoFinnigan ELEMENT-XR high resolution inductively coupled plasma mass spectrometer (ICP-MS) at the School of Earth and Ocean Sciences, Cardiff University. To avoid matrix effects due to variable Ca concentration upon analysis, samples were run with standards of matched Ca concentration. To determine the Ca concentration aliquots of samples were diluted using 0.5M HNO_3 and run in batches of 4 bracketed by 0.5 M Ca standards and Ca concentration of the samples calculated. To determine trace metal ratios sample specific standards of known trace metal composition were diluted to the Ca concentration of the samples and run immediately following the sample. Samples were run in batches of 2 sample-standard pairs, bracketed by a consistency standard and blank, and were run in order of increasing Ca concentration to minimise cross-contamination. Mean analytical precision of the consistency standards was 0.7% relative standard deviation (r.s.d., n=12). Uptake time was ~47s and one minute washes were performed after each sample analysis.

Boron isotope and B/Ca analyses were carried out by G. Foster at the University of Bristol. B/Ca analyses were carried out on a ThermoFinnigan ELEMENT 2 ICP-MS (Ni et al., 2007). The long-term reproducibility of the in house consistency standards for B/Ca is ± 2% (2σ) and the accuracy is better than 5% (Foster, 2008; Ni et al.,

2007). Boron isotope analyses were carried out on a ThermoFinnigan NEPTUNE multi-collector ICP-MS following the methodology of Foster (2008). The analytical precision of the boron isotope analyses is ± 0.22‰ (2σ) based on long-term reproducibility of full procedural replicates of an in house coral standard.

Fine fraction (<63 μm) carbonate samples analyses were carried out on a JY Horiba Ultima 2 inductively coupled plasma optical emission spectrometer at the School of Earth and Ocean Sciences, Cardiff University, long term precision is 4-10% (r.s.d.). Sr/Ca ratios were corrected for changing Sr/Ca of seawater using the long-term record of Lear et al. (2003).

A single coccolith sample (MT31/10.50) was analysed by analytical electron microscopy using wavelength dispersive spectrometry (WDS) on a Cambridge Instruments (LEO) S360 fitted with an INCA WAVE (WDX). Samples were splutter coated with carbon prior to analysis and optimisation was performed at the start of the analytical session using an in-house cobalt standard. Precision, based on repeat measurements was poor (±0.9 mmol/mol; 2σ). Accuracy was assessed by analysis of a cultured coccolith sample of for which Sr/Ca had been measured by inductively coupled plasma mass spectrometry (ICP-MS), and the ICP-MS measurement was within the error of the WDS analysis (P. Halloran pers. comm., 2006).

2.2 Biomarker Analysis

2.2.1 Reagents and Glassware

To prevent contamination high purity HPLC grade reagents (supplied by Rathburn Chemical Ltd., Walkerburn, Scotland) were used throughout sample preparation, all glassware was heated to 450 °C for a minimum of 3 hours and PTFE bottles were solvent rinsed before use.

2.2.2 Biomarker extraction

Extraction was performed in randomised batches of 7 samples with a procedural blank in each batch. 5 g samples were gently washed with methanol to remove surface handling and environmental contamination and ground using a mortar and pestle. Powdered samples were saponified at 70°C for 2 hours (ultrasonicated for 5 minutes at the beginning, midpoint, and end) using methanoic 0.1M potassium hydroxide (5% H_2O) and ultrasonically extracted with methanol and dichloromethane (DCM):methanol 3:1 azeotrope (v:v).

Table 1 Biomarker extraction batches

Batch Number	1	2	3	4	5	6
Start Date	6/3/07	15/3/07	2/4/07	11/4/07	8/5/07	28/4/07
Samples	MT1	MT28	MT2	MT29	MT14	MT1[1]
	MT6	MT25	MT5	MT26	MT9	MT2
	MT10	MT20	MT13	MT24	MT98	MT3
	MT12	MT11	MT16	MT27	MT53	MT14
	MT15	MT8	MT17	MT21	MT66	BLANK_
	MT23	MT4	MT22	MT18	MT124	28/4/08
	MT30	MT3	MT19	MT7	MT32	
	BLANK_ 6/3/07	BLANK_ 15/3/07	BLANK_ 11/4/07	BLANK_ 11/4/07	BLANK_ 8/5/07	

Combined extracts were reduced by rotary evaporation and remaining solvent evaporated under a stream of nitrogen with gentle heating (~40°C). Neutral fractions were isolated from the total extract using a liquid-liquid procedure in *n*-hexane:DCM 9:1 from double-distilled, DCM extracted water. Remnant total extract was acidified using 5M HCl and acid fractions isolated using DCM. Fractions were reduced by rotary evaporation under vacuum and evaporated to dryness at 30°C under a flow of nitrogen. Neutral fractions were re-dissolved in *n*-hexane and silica gel column

[1] Double (repeat) extracted to increase alkenone yield and combined before liquid-liquid separation

chromatography was used to divide samples into four further fractions (Kawamura and Gagosian, 1987), loaded in *n*-hexane and eluted in *n*-hexane (4 ml, Fraction 1), *n*-hexane:DCM (2:1 v:v; 2 ml, F2), DCM (5 ml, F3) and DCM:methanol (95:5 v:v; 5 ml, F4) alkenones were eluted in F3, *n*-alkanes eluted in F1. Columns were custom built from 150 mm Pasteur pipettes and packed with 40 mm of DCM and methanol extracted silica gel on top of phosphoric acid and DCM extracted glass wool plugs, capillary length was 60 mm. All fractions were evaporated to dryness under a flow of nitrogen with gentle heating (~40°C) and stored below 0°C until analysis.

2.2.3 Biomarker Quantification

Alkenone (F3) quantifications were performed on a Carlo Erba Instruments HRGC5300 gas chromatograph fitted with a flame ionisation detector at the Organic Geochemistry Unit, University of Bristol. The GC was fitted with a Chrompack fused silica capillary column (50 m × 0.32 mm internal diameter) coated with a CP Sil-5CB stationary phase (dimethylpolysiloxane equivalent, 0.12 μm film thickness). H_2 was used as the mobile phase (carrier gas). Samples were dissolved in ethyl acetate and 1 μl injected on-column at 70°C (samples were typically dissolved in 50 μl solvent but this varied with sample concentration), and the oven programmed to increase in temperature to 200°C at 20°Cmin^{-1} then to 305°C at 6°Cmin^{-1}, remaining isothermal at 305°C for 25 minutes. As the tetra-unsaturated alkenone ($C_{37:4}$) is not present, alkenone unsaturation indices were calculated using equation **(1)** (Prahl and Wakeham, 1987).

$$U_{37}^{K'} = \frac{[C_{37:2}]}{[C_{37:2} + C_{37:3}]} \qquad (1)$$

Alkane analyses were performed on the same instrument but with a different temperature program: samples were injected at 70°C and the oven programmed to increase in temperature to 130°C at 20°Cmin^{-1} then to 300°C at 4°Cmin^{-1}, remaining isothermal at 300°C for 25 minutes. The odd-over-even predominance (Scalan and Smith, 1970) ratios were calculated using equation **(2)**.

$$OEP = \frac{c_{n-2} + 6c_n + c_{n+2}}{4c_{n-1} + 4c_{n+1}} \qquad (2)$$

c = carbon number
n = C_{31}

2.2.4 Alkenone Carbon Isotopic Determinations

Alkenone carbon isotope analyses were performed on a Finnigan MAT Delta S isotope ratio monitoring mass spectrometer at the Organic Geochemistry Unit, University of Bristol. This was coupled to a Varian 3400 gas chromatograph via a modified Finnigan Type I combustion interface with copped oxide and platinum catalyst (0.1 mm diameter) maintained at 850°C within an alumina reactor (0.5 mm internal diameter). An internal standard of n-heptatriacontane was added to samples (2 μg per sample) before injection and a fatty acid methyl ester mixture was run periodically to monitor instrument performance. Samples were dissolved in ethyl acetate and injected at 70°C using an on column injector and the oven programmed to increase from an initial temperature of 70°C to 200°C at 20°Cmin^{-1} then to 300°C at 6°Cmin^{-1} and remain isothermal for 25 minutes. Water was removed using a Nafion membrane and the GC was fitted with a silica capillary column (50 m × 0.32 mm internal diameter) with a ZB1 stationary phase (dimethylpolysiloxane equivalent, 0.12 μm film

thickness). The GC carrier gas was He. Samples were calibrated against reference CO_2 of known isotopic composition introduced directly into the ion source at the start and end of each run. Sample concentrations and injection volumes were optimised to maximise signal strength, and no evidence of a concentration effect on isotopic ratio was seen for the co-injected standard (Figure 3).

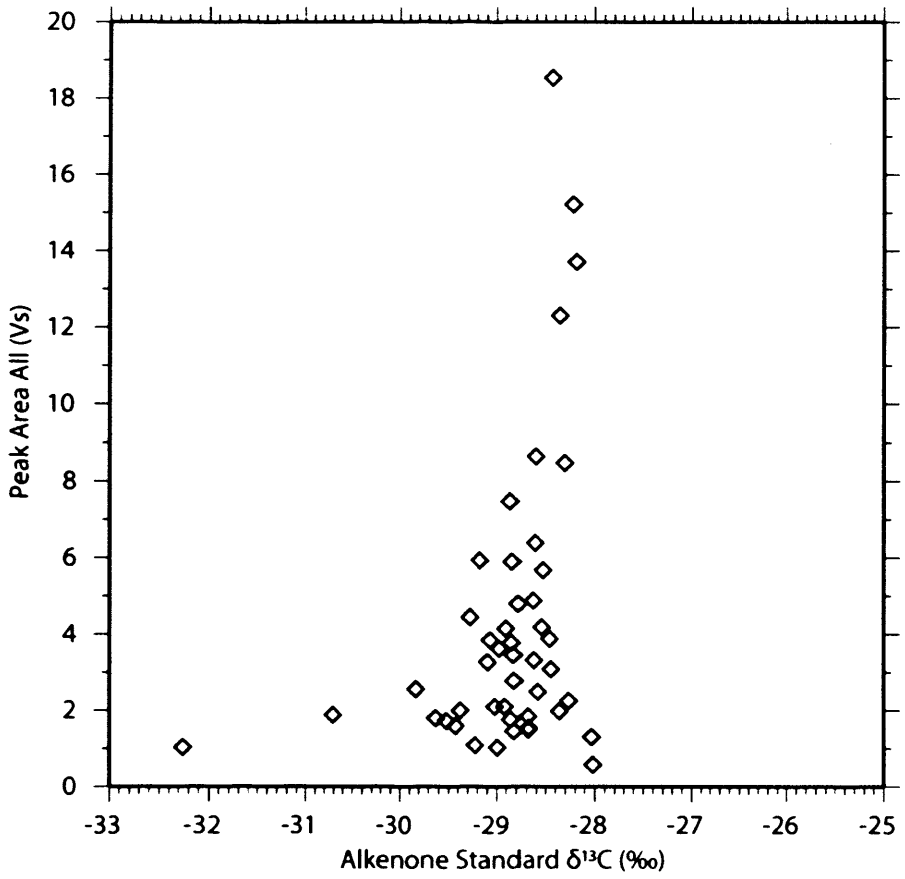

Figure 3: Carbon isotope ratio of co-injected *n*-alkane standard vs. peak response (area) for all isotopes.

Isotopic values were normalised by comparison to a gas standard of known isotopic value bracketing sample analyses, and are reported in delta notation ($\delta^{13}C$) with respect to the Vienna Pee Dee belemnite (VPDB).

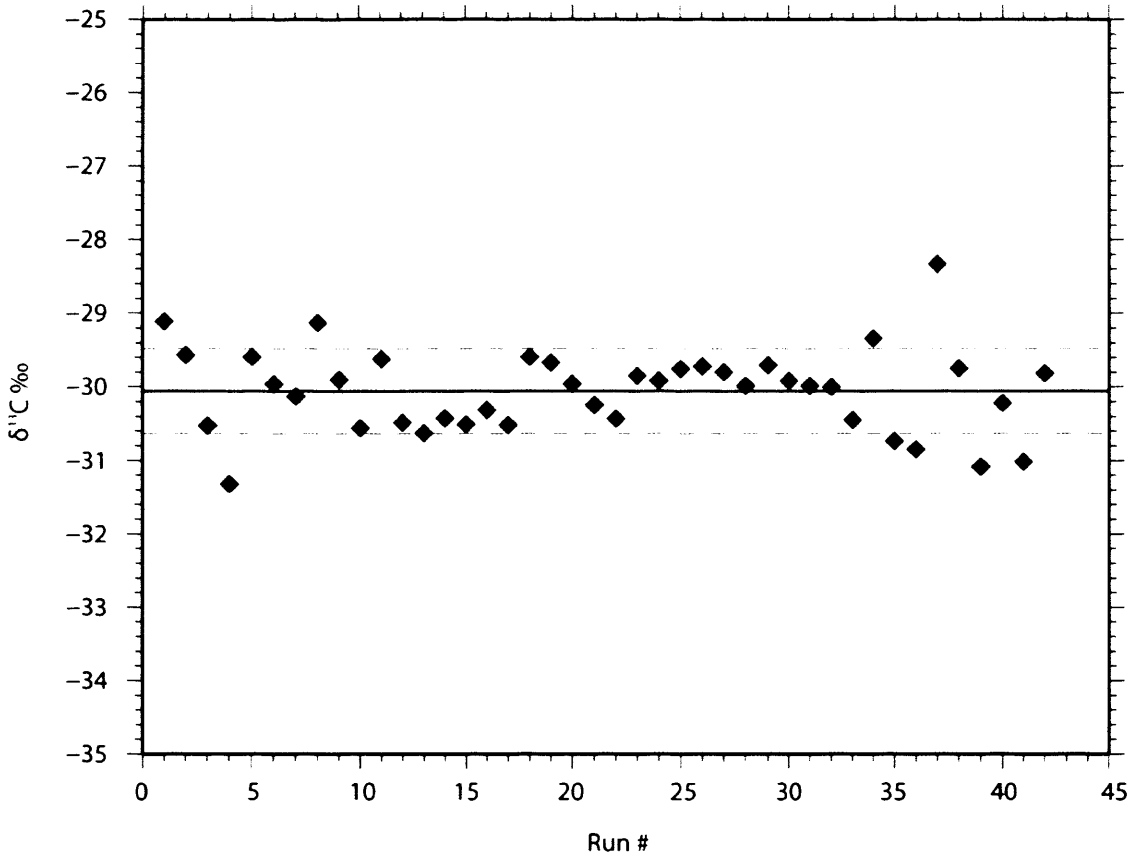

Figure 4: Repeat analysis of the co-injected *n*-alkane standard shows instrument stability over the length of the run. Mean $\delta^{13}C$ was -30.05 (solid line) and 1σ=±0.574 (dashed lines).

The long-term stability and precision of the GC-C-IRMS based on repeat runs of an in house standard mix is ±0.3‰. The stability of the instrument over the 2 weeks (30/5/08 – 15/6/08) of data collection was monitored using the co-injected n-alkane standard (Figure 4). Instrument drift was corrected by oxidising the combustion reactor as needed, and external precision monitored by periodic injection of an in-house fatter acid methyl ester mix (FAMES). The accuracy of the alkenone measurements was ±0.3‰ based on repeat measurements.

2.2.5 Bulk Organic Matter preparation and analysis

Carbonate was removed from ~1.5 g of sediment using 3 treatments with <1M HCl, which removes >99.8% of the carbonate. Samples were then rinsed with DCM-

extracted water and dried at 40°C. These were then ground, and samples weighed to give 1-2 mg carbon loaded into tin capsules.

Bulk organic isotope analysis were carried out using a Carlo Erba NA 1500 nitrogen/carbon analyser connected to a VG Optima isotope ratio monitoring mass spectrometer via a VG triple trap at the NERC Isotope Geosciences Laboratory, Keyworth. Values were corrected for small levels of ^{17}O using Craig's correction (Craig, 1957) and were converted to the VPDB scale by reference to an internal laboratory standard (BROC1) calibrated against NBS-19. Internal precision was monitored by repeat measurements of BROC1 and was ±0.2‰ (2σ).

3 The Ras il-Pellegrin Section, Malta

The Ras il-Pellegrin section is a coastal exposure of the middle Miocene Blue Clay Formation on the island of Malta in the central Mediterranean sea. The section was chosen as it is clay rich and so preservation of foraminifera is exceptional. The aim of this chapter is to demonstrate that the proxy records generated from the site represent a global, rather than local signal.

3.1 Sampling Site

The Ras il-Pellegrin section is a 46 m (vertical) coastal exposure to the north of Fomm Ir-Rih Bay, Malta at 55°4.93'N 14° 20.06'E (Figure 5) and it is the Global Boundary Stratotype Section and Point (GSSP) for the base of the Serravallian stage (at the base of the Blue Clay Formation; Hilgen et al. 2009). The Blue Clay Formation has been studied in the Maltese archipelago at a number of other locations (Jacobs et al., 1996; John et al., 2003), however the Ras il-Pellegrin section was chosen due to its thickness and apparent completeness (other sites show some evidence of slumping or dissolution events). Weathering rates here are high – the ~1 m deep sampling trenches dug by Abels et al. (2005) in 2002 were barely visible by 2005. The surface is loose and friable, however ~0.5 m into the cliff there is a clear transition into harder material and a colour change from grey to darker blue-grey. Sampling took place from the 7th to the 11th November 2005. Sampling trenches of ~0.75 m deep were dug, and samples taken at 0.35 m (vertical) intervals. 33 samples taken over the lower 12 m (the location of the CM6 excursion (Abels et al., 2005)) were wrapped in aluminium foil to prevent handling contamination in preparation for biomarker analysis, and a total of 130 samples were taken over 6 sub-sections, aligned using the clear banded strata (Figure

5). The top 3.85 m (samples MT119A-130) were sampled at a sub-section further to the north (35°55.09'N 14°20.02'E) to avoid any minor movements and more intense weathering at the top of the section. The base of the sampled section lies in the "transitional bed" of Abels et al. (2005), approximately 0.5 m below their 0 m mark.

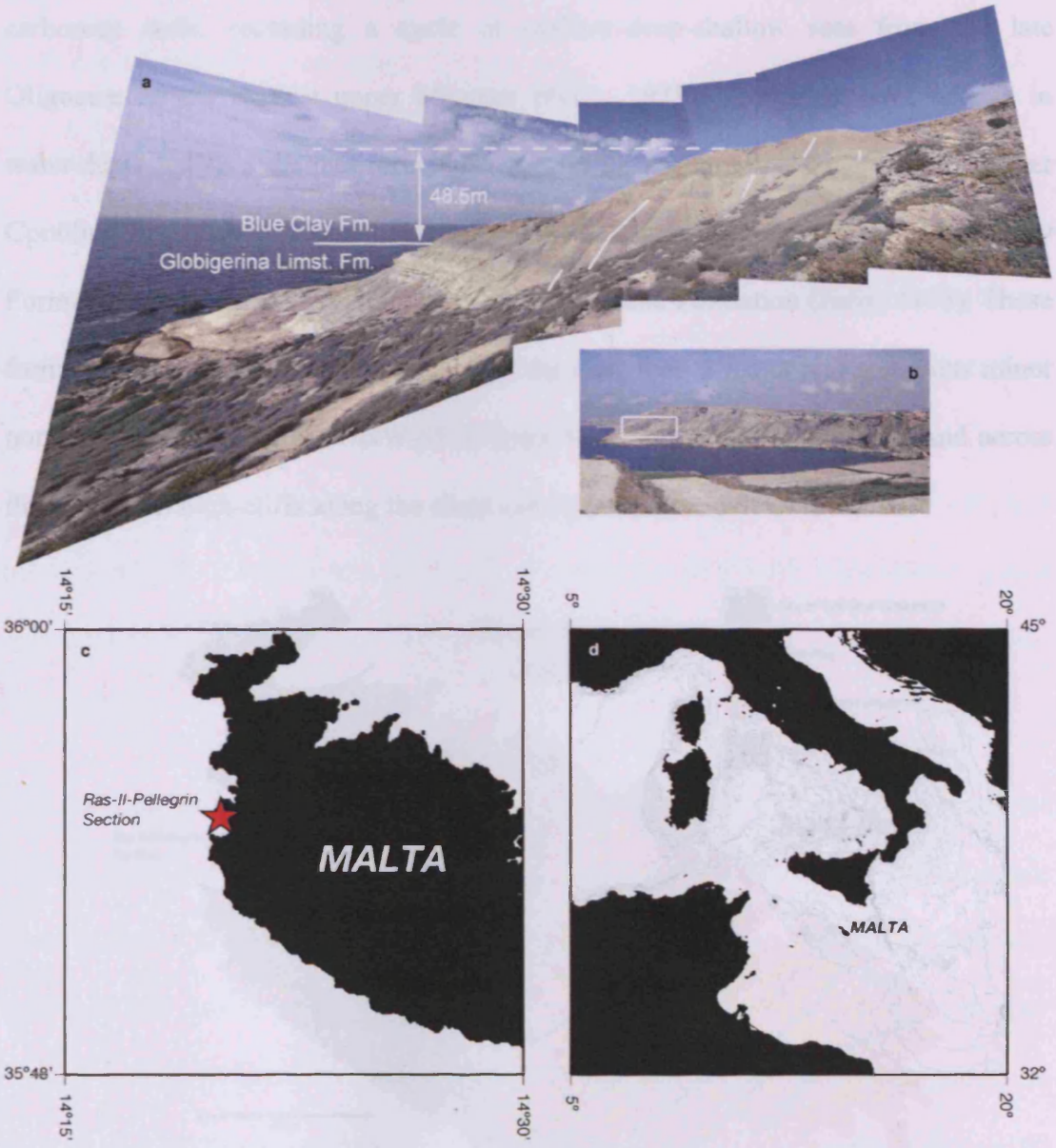

Figure 5: Sampling site at (a) The Ras il-Pellegrin section, with positions of sampling trenches (sub-sections) shown in white on (b) the north-eastern side of the Fomm Ir-Rih Bay (55°4.93'N 14° 20.06'E), located on the island of Malta (c) in the central Mediterranean (d).

3.1.1 Geological Setting

The islands of Malta and Gozo lie in the central Mediterranean and as part of the Ragusa platform were effectively attached to the African continent in the Oligocene-Miocene (Dart et al., 1993). As such these islands formed the edge of the Tunisian carbonate shelf, recording a cycle of shallow-deep-shallow seas from the late Oligocene to the earliest upper Miocene (Felix, 1973). The progressive change in water depth led to 5 distinct formations within the stratigraphic sequence; the Lower Coralline Limestone Formation, Globigerina Limestone Formation, Blue Clay Formation, Greensand Formation and Upper Coralline Formation (Felix, 1973). These formations are flat lying or dip slightly to the east, with 5 major and numerous minor normal faults trending E-W/NW-SE (Figure 6). Good exposure can be found across the islands, in high cliffs along the coast and inland on the side of low hills.

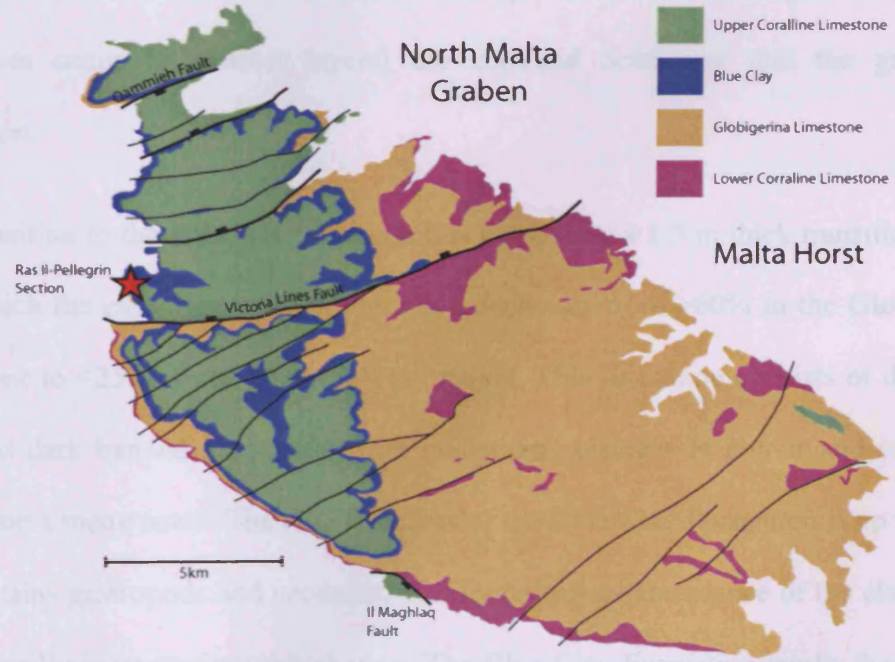

Figure 6 Geological sketch map of Malta, adapted from Jacobs et al. (1996). For simplicity the Greensand Formation is treated as the lowermost member of the Upper Corraline Formation (after Felix (1973)).

The base of the exposed Maltese sequence is the Lower Coralline Limestone Formation reaching a maximum thickness of 140 m. It is a massive shallow water limestone, principally made up of skeletal remains of various marine organisms including calcareous algae, foraminifera, corals, bryozoans, brachiopods, serpulids, molluscs and echinoderms. This lowermost formation is Oligocene in age, and represents the shallow ramp phase of deposition.

Above the Lower Coralline Formation lies the Globigerina Limestone Formation, which was deposited from the Chattian to the late middle Miocene. The limestone here represents water depths of 40-150 m (Felix, 1973) and consists of 3 members (lower, middle and upper) separated by two phosphatic beds, the lower of which is a hardground with molluscs, phosphatic pebble clasts and shark teeth (which can by found throughout the Globigerina Formation), the upper phosphate bed is more of a pebble bed. The limestone is a biomicrite with sparse macrofossils of pectenids (which sometimes occur in distinct layers) the echinoid *Schizaster* and the gastropod *Epitonium*.

The transition to the Blue Clay Formation is marked by a 1.5 m thick transitional bed over which the carbonate content gradually decreases from >60% in the Globigerina Limestone to <25% in the Blue Clay Formation. This formation consists of distinctly light and dark banded clay-marls, with gradational changes in colour and carbonate content on a metre scale. The total thickness of the Blue Clay Formation is up to 65 m, and contains gastropods and pectinids. The foraminiferal abundance of the clay varies and generally increases towards the top. The Blue Clay Formation marks the greatest water depths in the sequence, with estimates from benthic foraminifera varying from 150-200 m at the base of the formation, decreasing to 100 m at the top (Jacobs et al.,

1996; Pedley et al., 1976) whereas ostracod analysis and multivariable analysis of benthic foraminifera suggested depths of 500 – 700 m (Bellanca et al., 2002; Bonaduce and Barra, 2002). A gradual increase in glauconite is reported towards the top of the Blue Clay Formation where it is uncomformably overlain by the Greensand Formation. The boundary between the Greensand and the Blue Clay Formations is a slight angular unconformity and significant hiatus, varying in length across the archipelago.

The Greensand Formation is a clayey to calcereous glauconitic poorly cemented limestone, up to 12 m thick, although as the upper and lower boundaries are marked by clay rich layers not seen at all locations the true thickness of the formation may be greater. Large echinoids, as well as the fauna present in the Blue Clay Formation are abundant, and the appearance of the benthic foraminifera *Heterostegina* in this formation indicates a return to waters shallower than 70 m (Jacobs et al., 1996).

Further shallowing is marked by the transition to the Upper Coralline Formation, which, with a maximum preserved thickness of 27 m is the uppermost unit in the Maltese sequence. Palaeo-water depths are less than 50 m representing a back reef environment (Jacobs et al., 1996).

3.1.2 Tectonic History

The Maltese archipelago lies in the 600 km Pantelleria/Strait of Sicily rift system in the foreland of the Apennine-Maghebien thrust and fold belt (Dart et al., 1993). The islands are divided by three major normal faults, forming the North Gozo Graben, the Gozo Horst, the North Malta Graben and the Malta Horst. Three broad models for the basin wide structural evolution have been proposed: (1) That the basin is part of a

large pull-apart strutcture within and E-W/NW-SE trending dextral wrench (Jongsma et al., 1985); (2) That it lies in a pull-apart associated with differential rates of underthrusting beneath the Apennine-Maghebian thrust in the Sicily wrench zone (Grasso and Reuther, 1988); (3) Compression in the Appenine-Maghrebian thrust belt led to N-S trending foreland extension in which the Maltese system formed a back-arc basin. Of these three, field mapping by Dart et al. (1993) found evidence which supports (3) and discounts both (1) and (2).

Rifting was active during the deposition of all the Neogene sequences except the Lower Coralline Formation and Lower Globigerina Limestone member which are pre-rift. Significant thickness variation is therefore found throughout the archipelago. Of the onshore exposure, the Blue Clay is thickest (30-82 m) on the North Malta Horst, and thicker still (up to ~96 m) in the offshore Pantelleria Rift. The sequence thins significantly across southern Gozo (10-60 m) and on the Malta Horst. The middle limestone member also thins significantly to the south on Gozo, and is absent in the south east of the island.

The sedimentary sequence can be divided into 4 tectono-stratigraphic sequences across the islands; Pre-rift, early syn-rift, late syn-rift and post rift. These are synchronous, demonstrating the coeval nature of both the ENE-WSW and NW-SE trending fault sets which are present. The pre-rift phase is dated as >21 Ma and encompasses the Lower Coralline Formation and lower Globigerina Limestone member, the early syn-rift phase from 21-6 Ma includes the Middle and Upper Globigerina Limestone members, Blue Clay Formation, Greensand and depositional sequences 1 and 2 of the Upper Coralline Formation. The final third depositional sequence of the Upper Coralline Formation falls within the Late syn-rift phase, with the late/early syn rift

boundary at ~5 Ma. Offshore Plio-Quaternary sequences within the Pantelleria Rift also form part of the late-syn rift phase and were deposited during the re-flooding of the Mediterranean. Rifting was complete by ~1.5 Ma, with post-rift hemi-pelagic and turbiditic sediments deposited in the Pantelleria rift from the late Quaternary to present with sedimentation rates of 0.20-0.25 $mKyr^{-1}$.

The onset of rifting is marked by neptunian dykes cross-cutting the lowermost hardground capping the Lower Globigerina Limestone (Dart et al., 1993). Neptunian dykes are also found throughout syn-rift phases, growing up to 3 m thick in the Globigerina Limestone. Syn-rift sediments are marked by thickness variations across faults, with minimal fault related bathymetric relief.

The main faults lie in ENE-WSW and NE-SE trends, the maximum displacement on which is 195 m, found on the Victoria Lines Fault (VLF). Some faults, including the VLF, show hanging wall deformation including minor synclines, roll-over anticlines and footwall tilting (up to 20°). Fault blocks are full grabens and horsts, bounded by planar faults of opposite polarity. The tilt of fault blocks is generally less than 10°.

Extension of the basin is in NW-SE and NE-SW directions, which show coeval evolution and homogenous fault kinematics throughout. The broad direction of extension in the larger basin area is N-S and is up to 40% over the full evolution of the basin (Dart et al., 1993).

3.1.3 Previous Palaeonvironmental Work

Work in earnest on the geology of the Maltese archipelago began in the 1970s with detailed stratigraphic investigation and identification of the Blue Clay Formation within an Oligo-Miocene framework (Felix, 1973; Pedley, 1975; Pedley et al., 1976).

Release of commercially acquired seismic lines and exploration well data was integrated with detailed onshore structural mapping to place the Blue Clay Formation in a regional structural setting (Dart et al., 1993; see section 3.1.2 above).

Ostracod analysis at RIP suggested that the Blue Clay Formation represented a drop in oxygenation levels from the Globigerina Limestone Formation below, with a further drop in oxygenation within the top 20 m of the section (Bonaduce and Barra, 2002). The estimated paleo-water depth for the Blue Clay was also increased by this study to a maximum of 500-700 m (Bonaduce and Barra, 2002). An integrated oceanographic investigation of the section using multivariate analysis of benthic foraminifera assemblages, stable oxygen and carbon isotopes and barium concentration confirmed an upper bathyal environment for the Blue Clay Formation with a depth estimation of 500 – 600 m (Bellanca et al., 2002). Foraminiferal assemblage analysis also confirmed the poor oxygenation interpretation, although not extreme anoxia (Bellanca et al., 2002). Ba and benthic carbon isotope records suggest periods of enhanced surface water productivity at the base and top of the section, possibly linked to upwelling or enhanced continental runoff (Bellanca et al., 2002). Negative correlation between the $CaCO_3$ % and oxygen isotope records in the Blue Clay Formation has been linked to variations in rates of continentally derived material linked to rainfall increasing during cooler periods (John et al., 2003).

Clay mineral analysis was performed for the Blue Clay Formation (at the Xatt-L'Ahmar section to the north of RIP on the island of Gozo) by John et al. (2003). The assemblage of clay minerals is dominated by kaolinite throughout the Blue Clay Formation (~60%) with minor contributions from illite (~15%) chlorite (~10%), smectite (~10%), and palygorskite (~5%). This is a significant departure from the

assemblage found in the Globigerina Formation below, where smectite dominates, with higher contributions from palygorskite and illite and limited kaolinite and chlorite present.

Detrital kaolinite is indicative of a continental weathering regime dominated by a warm and humid environment, and is generally formed in well drained conditions under high precipitation where bedrock degradation is accelerated, typical of present day tropical soils (Robert and Chamley, 1991). Detrital smectite is indicative of a warm climate where seasonal variations between humid and dry seasons dominate (Chamley, 1989). The shift from an assemblage dominated by smectite to one where kaolinite dominates is indicative of a shift in climate regime from warm arid to warm humid, and the coincidence of this shift with the transition from the Globigerina Limestone Formation to the Blue Clay Formation suggests this was linked to the wider global climate changes associated with the expansion of the Antarctic ice sheet. This shift in clay assemblage is not limited to the Miocene sediments in Malta, but found throughout the Mediterranean basin, suggesting that this shift was a major regional change in weathering regime (Visser, 1991).

Dating of the Maltese successions with strontium isotopes and bulk sediment and foraminiferal stable oxygen and carbon isotope analysis identified the Monterey event, CM events 3, 6 and 7 and the Antarctic cooling as recorded in the Maltese sediments (Jacobs et al., 1996). The astronomical tuning of the age model for the Ras il-Pellegrin section to the $La90_{1,1}$ using a record of $CaCO_3$% and *Globigeriniodes sp.* improved the age model for the Blue Clay Formation (Jacobs et al., 1996; Laskar et al., 1993). This age model was improved further by an integrated stratigraphy (magnetostratigraphy, biostratigraphy and astronomical tuning of Ca/K to the ATNTS2004 (Lourens et al.,

2004) and CK95 (Cande and Kent, 1995) timescales; (Abels et al., 2005)) for the Ras il-Pellegrin section to which the age model of this study is tied, and which is detailed further below (section 3.2.1). The work of Abels et al. (2005) also recognised the coincidence of the step in the oxygen isotope record ("Mi-3" from the nomenclature of Miller et al (1991) or "E3" using the nomenclature of Flower and Kennett (1993)) at Ras il-Pellegrin with minima in eccentricity and obliquity.

The formation boundary between the Globigerina and Blue Clay Formations has been proposed (Abels et al., 2005) and ratified by the International Commission of Stratigraphy as the Global Boundary Stratotype Section and Point (GSSP) for the boundary between the Langhian and Serravallian stages (Hilgen et al., 2009).

3.2 Lithostratigraphy

3.2.1 Age Model (for this study)

The age model for Ras il-Pellegrin is based on the astronomically tuned intergrated stratigraphy of Abels et al. (2005). In order to develop the age model for this work the bulk carbon isotope curve was tuned to the bulk carbon isotope curve of Abels et al. (2005), which is a higher resolution record (average sample spacing was 9 cm) from the same section. The tuning was achieved by graphical correlation of 7 prominent peaks in the carbon isotope curves using Analyseries 2.0.3 (Paillard et al. 1996), and one physical tie point in the field (the zero point of the Abels et al. (2005) record lies at 0.5m on the scale presented here). Tie points are shown in Table 2 and Figure 7.

Table 2: Tie points based on carbon isotope stratigraphy used to construct the age model for this work.

Height in Section (m)	Age (Ma)
0.35	13.860
3.50	13.789
7.70	13.642
17.50	13.408
24.50	13.245
34.30	13.034
44.50	12.762

The starting point for the age model of Abels et al. (2005) was a detailed magneto- and calcareous plankton biostratigraphy, which provides first order age control for the astronomical tuning. Fully independent orbital tuning is not possible as the cyclicity at RIP does not provide enough characteristic detail to provide a unique solution. The calcareous plankton biostratigaphy allowed for 4 astronomically dated tie points to be imported from the astronomically dated Tremiti section in the central Mediterranean (Figure 8; Hilgen et al. 2003; Abels et al. 2005). These bioevents, combined with the position of chondrite trace fossils at the RIP and Tremiti sections allow the phase relationship between cycles seen at RIP and precession to be understood (Abels et al. 2005). 44 small scale cycles were recognised in the field, and in Ca% and Ca/K ratio records and were tuned to precession (Abels et al., 2005).

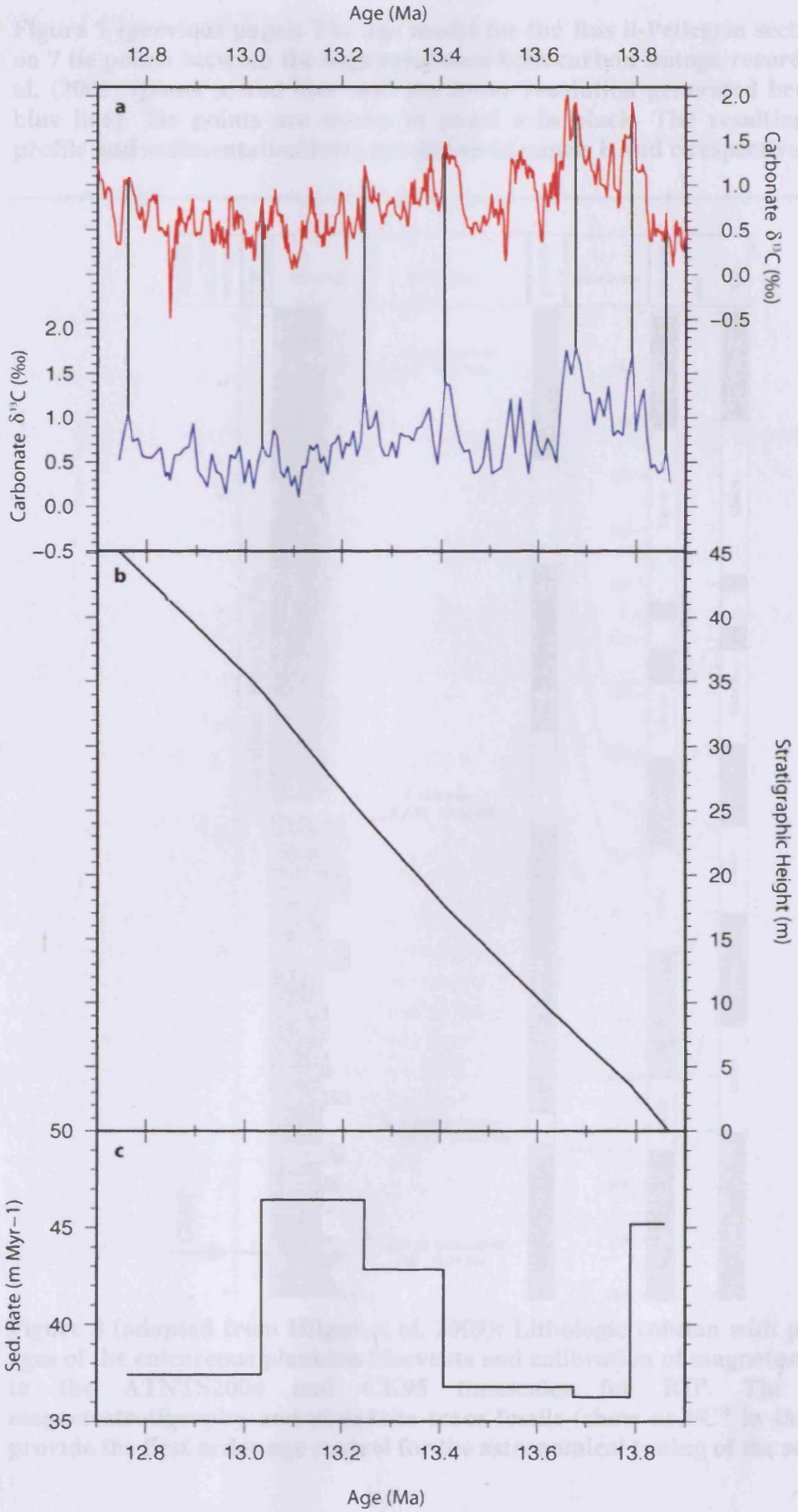
Age (Ma)
12.8
13.0
13.2
13.4
13.6
13.8
a
Carbonate δ13C (‰)
2.0
1.5
1.0
0.5
0.0
−0.5
Carbonate δ13C (‰)
b
Stratigraphic Height (m)
45
40
35
30
25
20
15
10
5
0
c
Sed. Rate (m Myr−1)
50
45
40
35
Age (Ma)

Figure 7 (previous page): The age model for the Ras il-Pellegrin section is based on 7 tie points between the high resolution bulk carbon isotope record of Abels et al. (2005) (panel a; red line) and the lower resolution generated here (panel a; blue line). Tie points are shown in panel a in black. The resulting age-depth profile and sedimentation rates are shown in panels b and c respectively.

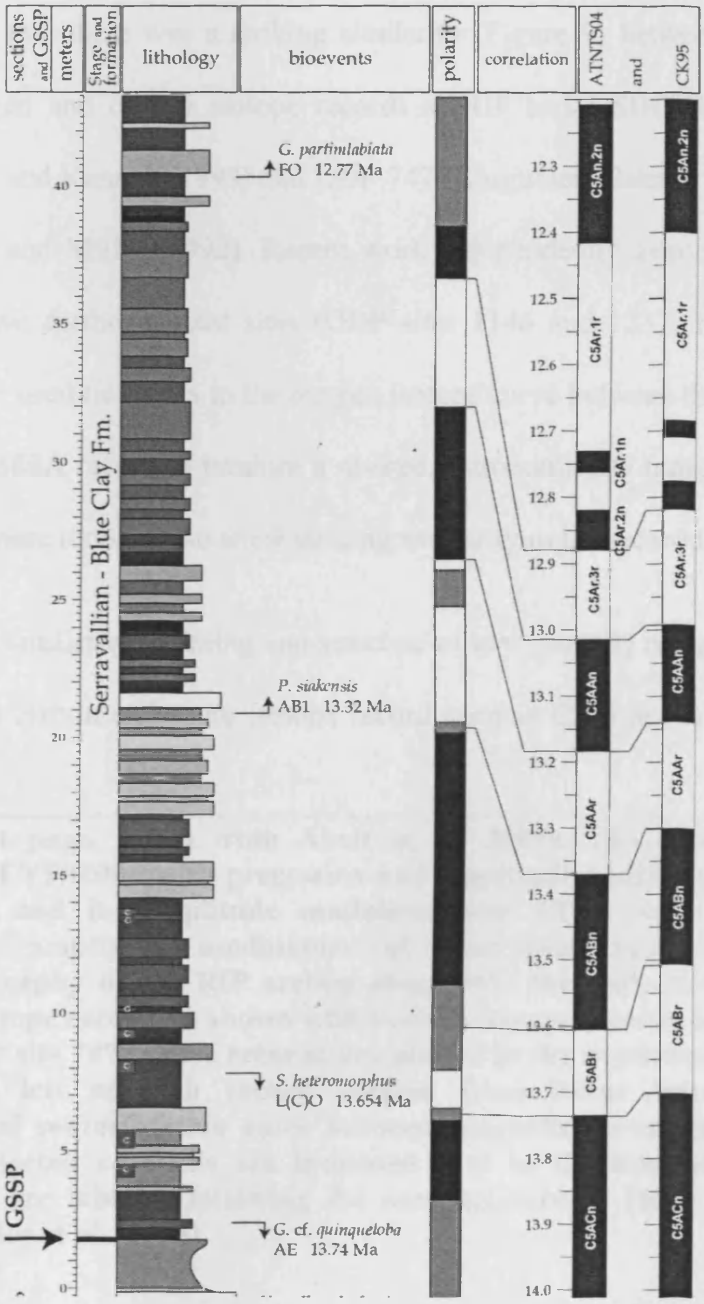

Figure 8 (adapted from Hilgen et al. 2009): Lithologic column with position and ages of the calcareous plankton bioevents and calibration of magnetostratigraphy to the ATNTS2004 and CK95 timescales for RIP. The bioevents, magnetostratigraphy and chondrite trace fossils (show as "C" in the lithology) provide the first order age control for the astronomical tuning of the section.

Stable isotope records for the middle Miocene are characterised by a series of globally recognised events in both the carbonate oxygen and carbon isotope records (Woodruff and Savin, 1991). To ascertain whether local or global controls dominate the isotope records at RIP they can be compared to geographically distant sites. Abels et al. (2005) showed that there was a striking similarity (Figure 9) between events in the carbonate oxygen and carbon isotope records at RIP and DSDP 588A (southwest Pacific; Flower and Kennett, 1993) and ODP 747 (Kerguelen Plateau, southern Indian Ocean; Wright and Miller, 1992). Recent work independently astronomically tuned records from two further distant sites (ODP sites 1146 and 1237; Holbourn et al., 2005, 2007) and used tie points in the oxygen isotope curve between these two records and the DSDP 588A record to produce a revised, astronomically tuned age model for DSDP 588A. These records also show striking similarity to the record from RIP (

Figure 10). The similarity in timing and structure of key, globally recognised events in the oxygen and carbon carbonate isotope record such as CM6 in the carbon isotope

---

Figure 9 (next page, taken from Abels et al. 2005): The magnetic polarity timescale of ATNTS2004 with precession and amplitude modulator eccentricity, and obliquity and its amplitude modulator and EOA target curve which combines the amplitude modulators of precession and obliquity. The magnetostratigraphy of the RIP section along with the bulk carbonate oxygen and carbon isotope records is shown with benthic isotope records from DSDP site 588A and ODP site 747. These records are plotted in the depth domain, with age scales on the left of each record derived from linear interpolation and extrapolation of sedimentation rates between magnetic reversals. ATNTS2004 ages of the selected reversals are indicated next to the magentostratigraphy. Isotope events are labelled following the nomenclature of Flower and Kennett (1993) and Miller et al. (1996).

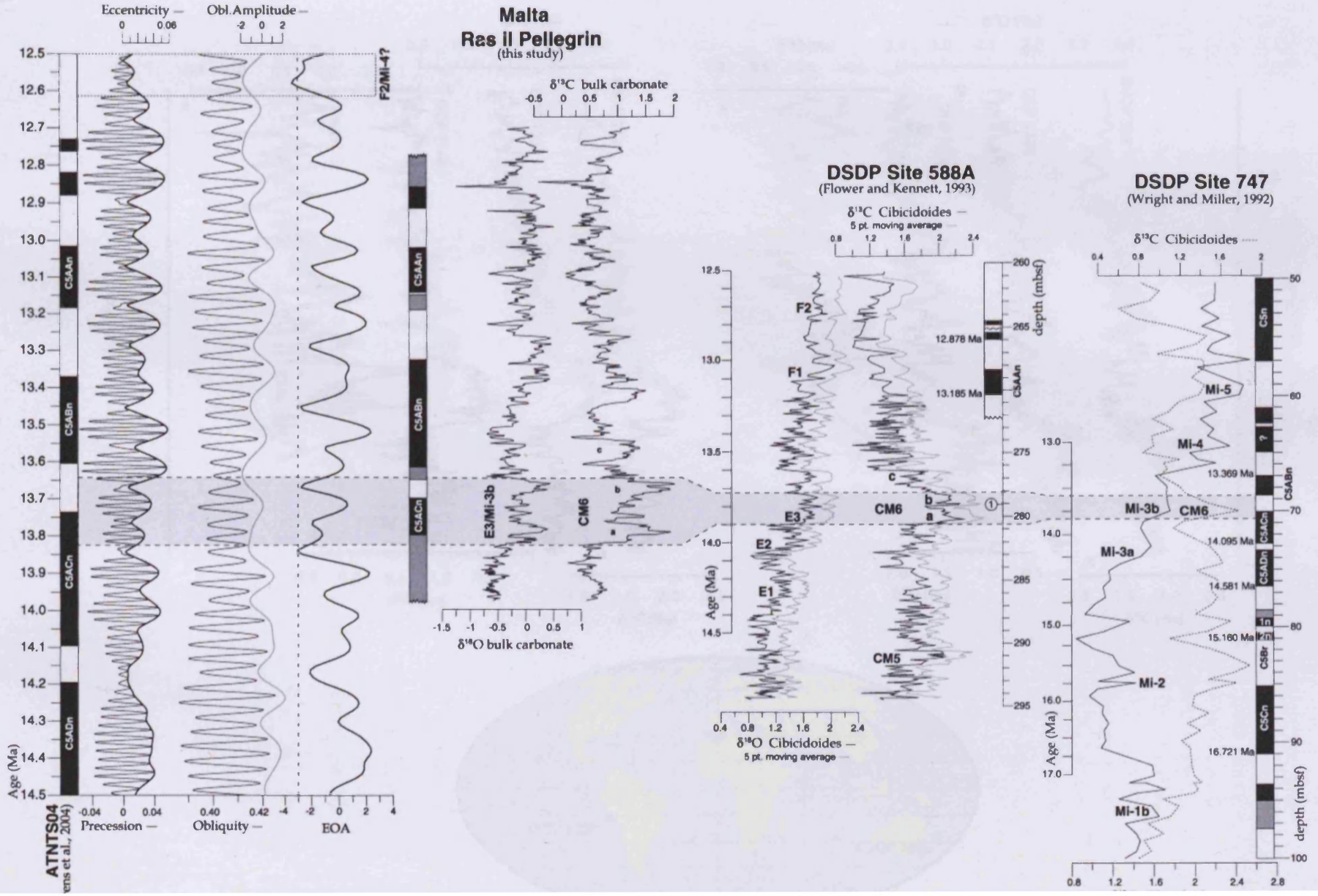
Eccentricity
Obl. Amplitude
F2/MI-4?
ATNTS04
(Laskar et al., 2004)
Precession
Obliquity
EOA
Age (Ma)
C5AAn
C5ABn
C5ACn
C5ADn
Malta
Ras il Pellegrin
(this study)
δ13C bulk carbonate
δ18O bulk carbonate
E3/MI-3b
CM6
DSDP Site 588A
(Flower and Kennett, 1993)
δ13C Cibicidoides
5 pt. moving average
δ18O Cibicidoides
F2
F1
E3
E2
E1
CM6
CM5
12.878 Ma
13.185 Ma
depth (mbsf)
DSDP Site 747
(Wright and Miller, 1992)
MI-5
MI-4
MI-3b
MI-3a
MI-2
MI-1b
13.369 Ma
14.095 Ma
14.581 Ma
15.160 Ma
16.721 Ma
C5n
C5Br
C5Cn

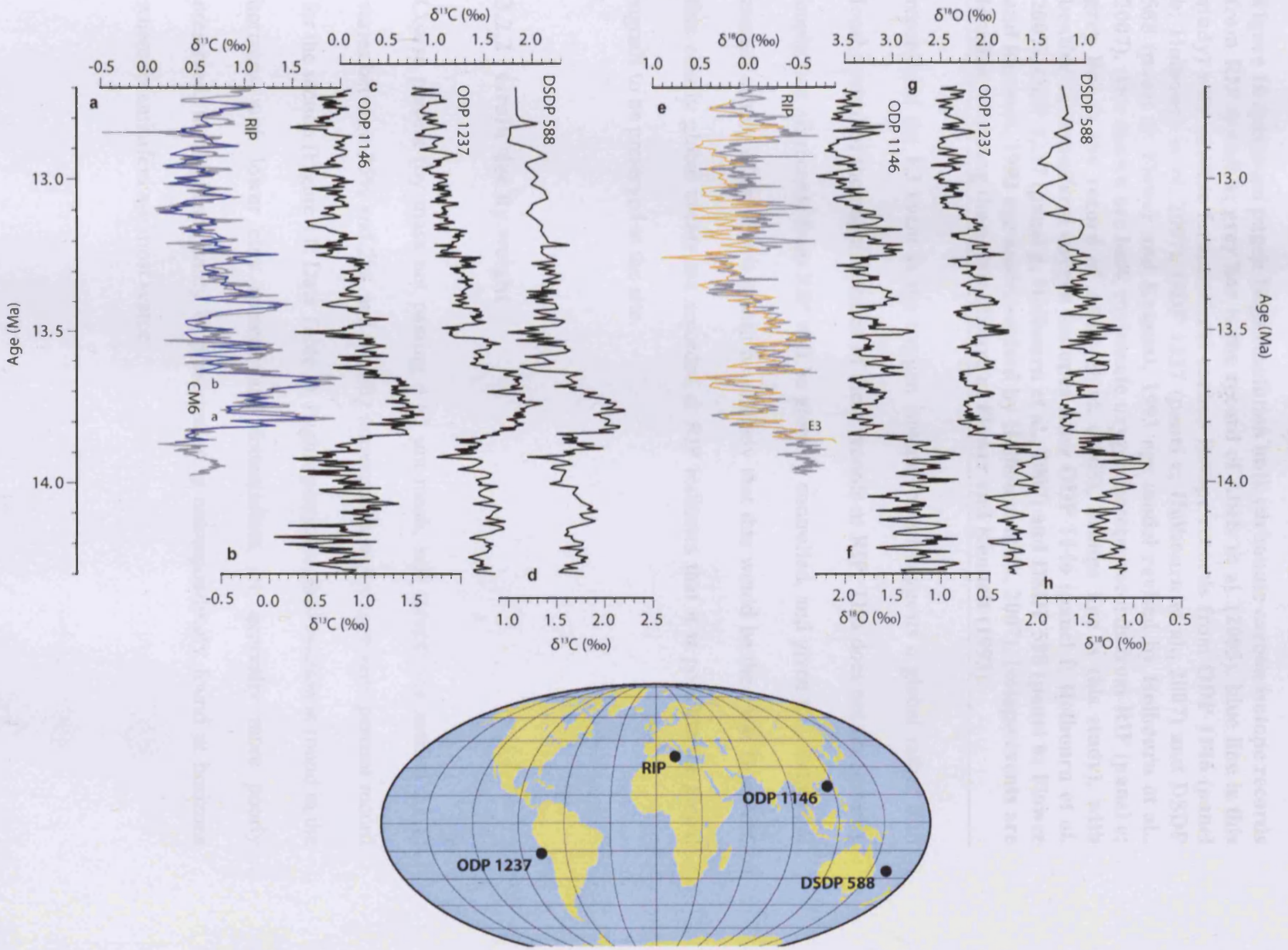
δ13C (‰)
δ18O (‰)
Age (Ma)
RIP
ODP 1146
ODP 1237
DSDP 588
CM6
E3
a
b
c
d
e
f
g
h

Figure 10 (previous page): High resolution bulk carbonate carbon isotope records from RIP (panel a; grey line is the record of Abels et al. (2005), blue line is this study) with benthic foraminiferal carbon isotope records from ODP 1146 (panel b; Holbourn et al. 2007), ODP 1237 (panel c; Holbourn et al., 2007) and DSDP 588 (panel d; Flower and Kennett, 1993 age model revised by Holbourn et al., 2007). Also shown are bulk carbonate oxygen isotope records from RIP (panel e; grey line is the record of Abels et al. (2005), orange line is this study), with benthic foraminiferal oxygen isotopes from ODP 1146 (panel f; Holbourn et al. 2007), ODP 1237 (panel g; Holbourn et al., 2007) and DSDP 588 (panel h; Flower and Kennett, 1993 age model revised by Holbourn et al., 2007). Isotope events are labelled following the nomenclature of Flower and Kennett (1993).

record and the E3 event in the oxygen isotope record suggests a global rather than local control of the major features of these records at RIP. This does not neccersarily imply that all records from RIP will be globally controlled, and given the continental margin setting of the site it would be unlikely that this would be the case. However, that clearly global events are recorded at RIP indicates that it is possible for global signals to be preserved at the site.

3.2.2 Grain size by weight

Coarse percent (by mass not passing a 63 μm mesh, wet sieved, see section 2.1.1) varies between 35% and 2%, and broadly corresponds to the carbonate percent record for the section (Figure 11; Data Table 1). Higher percent coarse fraction is found in the horizons with lower clay content, and foraminifera are generally more poorly preserved, the highest quality of preservation is correspondingly found at horizons where foraminifera are most scarce.

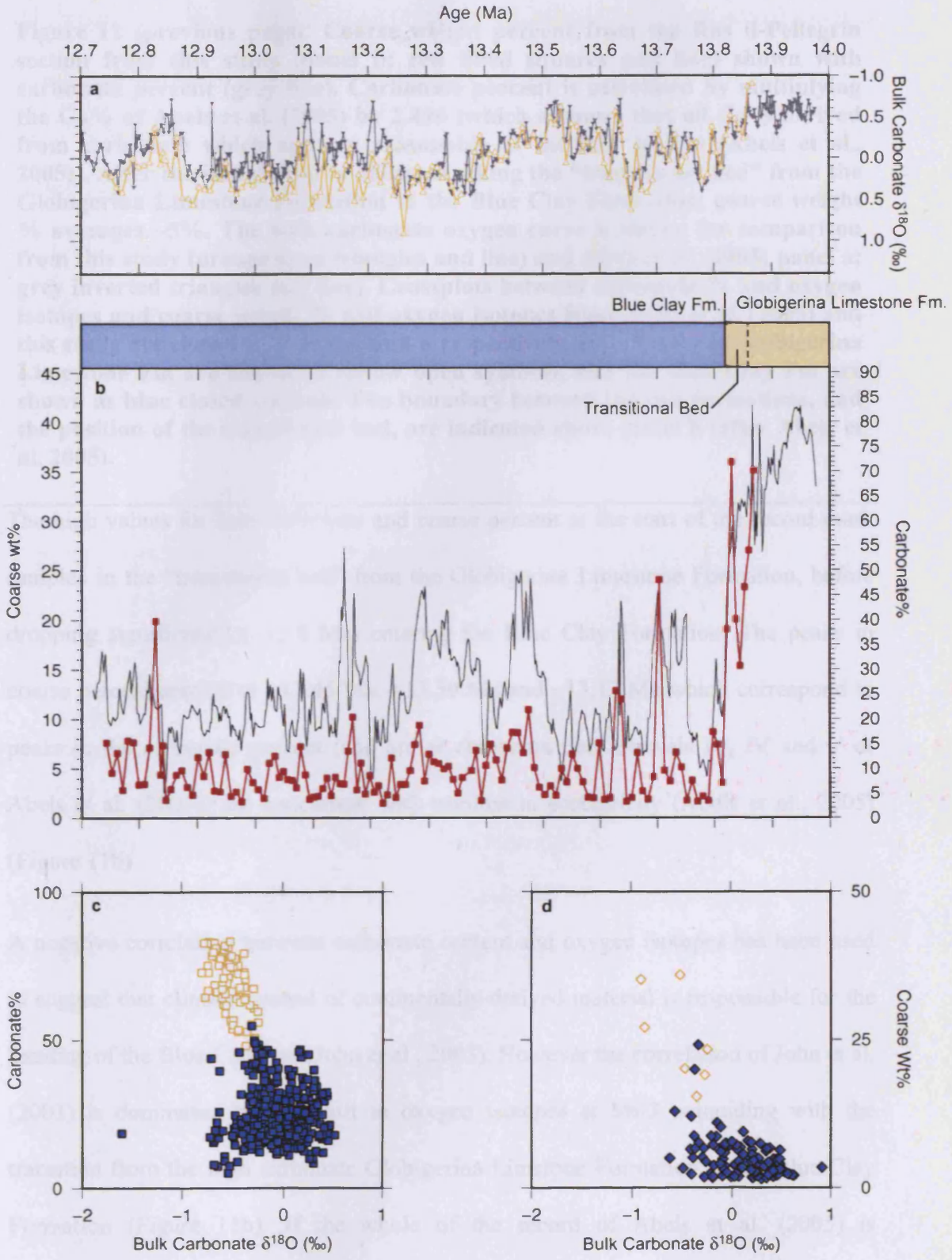
Age (Ma)
12.7 12.8 12.9 13.0 13.1 13.2 13.3 13.4 13.5 13.6 13.7 13.8 13.9 14.0
a
−1.0 −0.5 0.0 0.5 1.0
Bulk Carbonate δ18O (‰)
Blue Clay Fm.
Globigerina Limestone Fm.
b
Transitional Bed
Coarse wt%
Carbonate%
c
d
Carbonate%
Coarse Wt%
Bulk Carbonate δ18O (‰)
Bulk Carbonate δ18O (‰)

Figure 11 (previous page): Coarse weight percent from the Ras il-Pellegrin section from this study (panel b; red filled squares and line) shown with carbonate percent (grey line). Carbonate percent is calculated by multiplying the Ca% of Abels et al. (2005) by 2.496 (which assumes that all Ca is derived from carbonate which appears reasonable at the RIP section (Abels et al., 2005)). After the initial drop in values marking the "transitional bed" from the Globigerina Limestone Formation to the Blue Clay Formation, coarse weight % averages ~5%. The bulk carbonate oxygen curve is shown for comparison from this study (orange open triangles and line) and Abels et al. (2005; panel a; grey inverted triangles and line). Crossplots between carbonate % and oxygen isotopes and coarse weight % and oxygen isotopes from Abels et al. (2005) and this study are shown in panels c and d respectively. Data from the Globigerina Limestone Fm are shown as yellow open symbols, and the Blue Clay Fm are shown as blue closed symbols. The boundary between the two formations, and the position of the transitional bed, are indicated above panel b (after Abels et al. 2005).

The high values for both carbonate and coarse percent at the start of the record mark samples in the "transitional bed" from the Globigerina Limestone Formation, before dropping significantly (~13.8 Ma) entering the Blue Clay Formation. The peaks in coarse percent centred at ~13.45 Ma, ~13.30 Ma and ~13.17 Ma which correspond to peaks in the carbonate percent (and are at carbonate rich intervals III, IV and V of Abels et al. (2005)) are concurrent with minima in eccentricity (Abels et al., 2005) (Figure 11b)

A negative correlation between carbonate content and oxygen isotopes has been used to suggest that climate control of continentally derived material is responsible for the banding of the Blue Clay Fm (John et al., 2003). However the correlation of John et al. (2003) is dominated by the shift in oxygen isotopes at Mi-3 coinciding with the transition from the high carbonate Globigerina Limstone Formation to the Blue Clay Formation (Figure 11b). If the whole of the record of Abels et al. (2005) is considerered (which includes the transition from the Globigerina Limestone Fm to the Blue Clay Fm) then there is significant correlation between carbonate percent and oxygen isotopes (Figure 11c; $r=-0.52$, $n=496$, $p<0.05$). However there is no significant

correlation between the bulk oxygen isotopes and carbonate content within to Blue Clay Fm itself at RIP (Figure 11c; blue filled squares; r=0.03, n=496, p>0.05). Therefore although there may be a connection between the isotope shift at Mi-3 and the transition from the Globigerina Fm to the Blue Clay Fm, a connection between climate shifts as evident in the $\delta^{18}O$ record and carbonate percent for the smaller changes within the Blue Clay Fm is not evident.

For coarse percent there is significant correlation with oxygen isotopes throughout the the record (Figure 11d; r=-0.43, n=130, p<0.05) whether the transitional bed is included or not, suggesting that there may be climate may be controlling the variations in this parameter in the Blue Clay Fm at RIP.

3.3 Organic Analysis

3.3.1 Total Organic Carbon

Total organic carbon (TOC) weight percent was measured at full resolution over CM6 and at half resolution for the remainder of the record (section 2.2.4). Organic carbon is present throughout the Ras il-Pellegrin section, with a mean content of 0.25 wt%, ranging between a minimum of 0.11% and a maximum of 0.57% (Figure 12; Data Table 2). TOC increases at the base (oldest part) of the section from low values in the carbonate rich transitional bed to higher levels at the start of the Blue Clay Formation. TOC decreases again to a minimum value of 0.11% at 13.64 Ma before gradually increasing until 12.9 Ma when levels again drop to similar to those present in the transitional bed. Apart from the low TOC in the carbonate rich transitional bed from the Globigerina Limestone to the Blue Clay, there is no overall correlation between carbonate % and TOC (r=-0.11, n=79, p>0.05). TOC increases at the start of CM6 (at

the base of the section) which would be consistent with hypotheses which suggest greater organic matter burial could be responsible for CM6, however the levels of organic matter over CM6 are not significantly higher than any other point later in the record, and the increase does happen over a change in lithology (from the limestone to the clay). The TOC record does not therefore suggest significantly increased organic matter burial at this site over CM6.

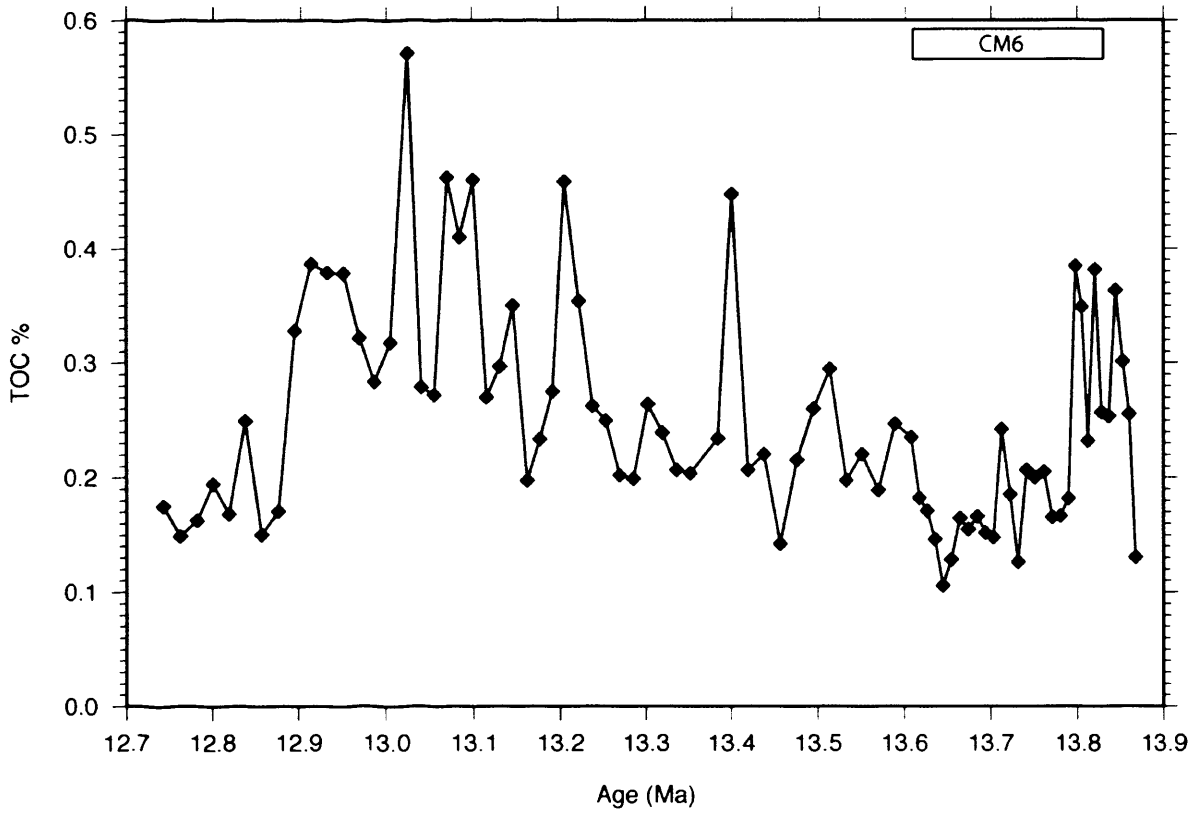

Figure 12: Total Organic Carbon % from Ras il-Pellegrin section. The initial increase in TOC coincides with the transition from the Globigerina Limestone Formation to the Blue Clay Formation, the position of CM6 is indicated.

3.3.2 Organic Matter Provenance: C/N Ratio

Identifying the source of organic matter reaching Ras il-Pellegrin is essential if correct interpretations of the bulk organic carbon isotope record are to be reached. The ratio of organic carbon to organic nitrogen (C/N ratio) in sediments has been used in various

settings to estimate the proportion of terrestrial and marine sourced organic matter reaching a deposition site (Lazerte, 1983; Matson and Brinson, 1990; Prahl et al., 1994; Schubert and Calvert, 2001; Tan and Strain, 1979) and was measured for samples from RIP (section 2.2.4). Although variable, terrestrial plants have much higher proportions of carbon to nitrogen compared to marine organisms, leading to a much greater C/N ratio for terrigenous organic matter (Hedges et al., 1986; Hedges et al., 1997). The C/N ratio for organic matter at RIP is variable (Figure 13; Data Table 3) ranging from a maximum of 7.8 to a minimum of 1.7. A steady decline in C/N from a high point early in the record to the lowest value at 13.65 Ma is followed by a more gradual increase over the following 800 Kyrs before dropping back to lower levels at the end of the record.

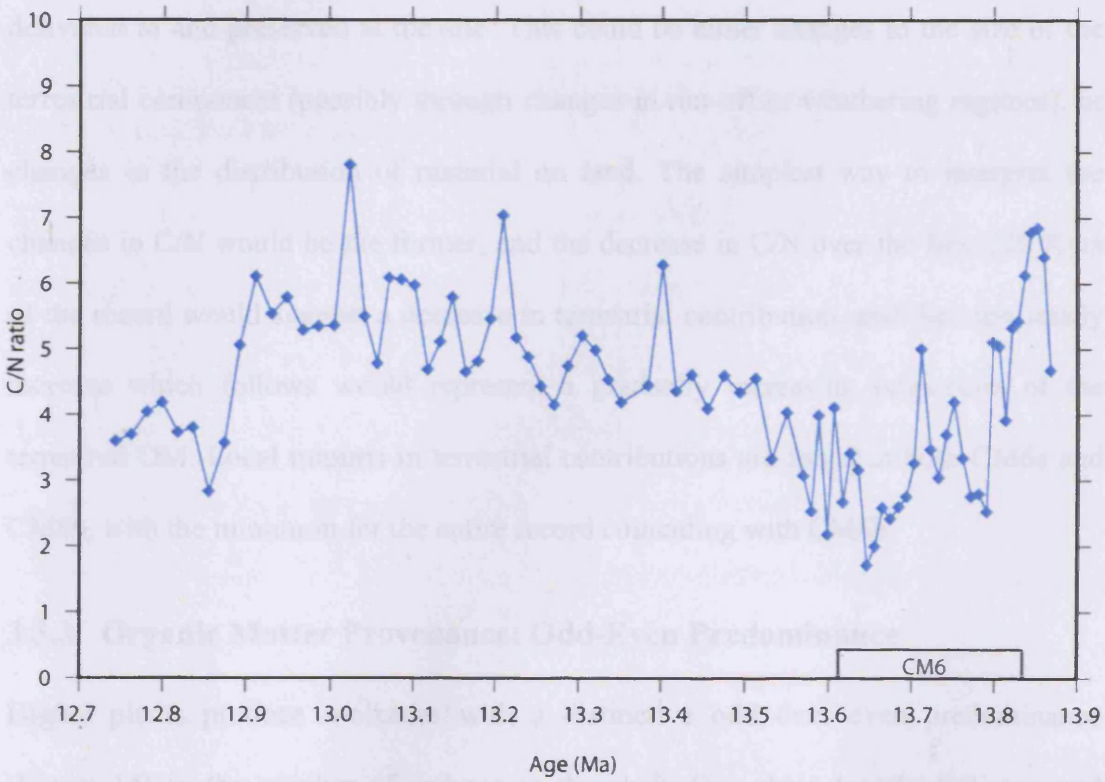

Figure 13: Carbon to nitrogen ratio for organic matter from the Ras il-Pellegrin section. Traditionally this is interpreted as higher C/N ratio suggesting a greater contribution of terrestrial organic matter.

Estimates of absolute levels of terrigenous organic matter (OM) from C/N ratios are complicated by variations in the source of terrestrial organic material (plant, soil etc.) to the site and by degradation of the organic matter in transit (see discussion in Weigers et al. (2009)). However a C/N ratio of < 10 such as that found at RIP is typical of a distribution dominated by marine organic matter but with some contribution from terrestrial sources. This sort of distribution would be typical of a marine setting on the continental margin, which is consistent with the sedimentological evidence of the palaeoenvironmental setting of RIP (Tan and Strain, 1979; Weigers et al., 2009).

Although the variations in C/N must be considered with some caution, they are quite sizable and would suggest that there are changes in the distribution of organic matter delivered to and preserved at the site. This could be either changes in the size of the terrestrial component (possibly through changes in run-off or weathering regimes), or changes in the distribution of material on land. The simplest way to interpret the changes in C/N would be the former, and the decrease in C/N over the first 220 Kyrs of the record would suggest a decrease in terrestrial contribution, and then the steady increase which follows would represent a gradually increasing proportion of the terrestrial OM. Local minima in terrestrial contributions are found at both CM6a and CM6b, with the minimum for the entire record coinciding with CM6b.

3.3.3 Organic Matter Provenance: Odd-Even Predominance

Higher plants produce *n*-alkanes with a distinctive odd over even predominance (Figure 14) in the number of carbons in the chain (i.e. chain length; Eglinton and Hamilton, (1967)). Marine organisms do not share this feature, and so the degree of odd-even predominance (OEP) in the *n*-alkanes found at a marine site can be used as a

tracer for changing contribution of terrestrial plant derived organic matter (Scalan and Smith, 1970). Samples were analysed for *n*-alkanes from selected horizons from RIP (section 2.2.3; equation (2); Data Table 5)

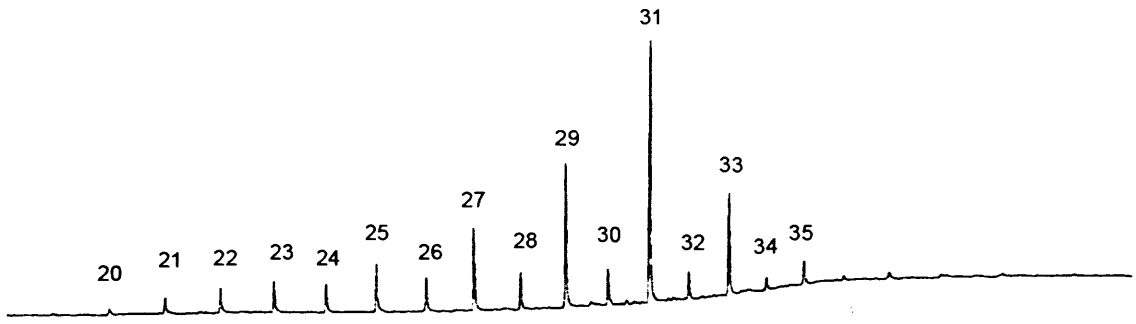

Figure 14: A typical extract from a gas chromatogram trace of an aliphatic hydrocarbon fraction from Ras il-Pellegrin, showing odd over even predominance in the *n*-alkanes.

The OEP evidence from *n*-alkanes at RIP (Figure 15) shows that there is a definite odd-even predominance in the organic matter found at the site. This suggests two things. Firstly that material derived from higher plants is preserved at the site. Although there is evidence that this contribution varies with time, there does not seem to be variation which changes systematically in concert with any of the other proxy evidence which could be influenced by changing terrigenous OM such as C/N ratio or organic $\delta^{13}C$ (although it is interesting that the two lowest values co-incide with the peaks of CM6a and b). Secondly, the preservation of an odd over even predominance suggests that the OM at the site is thermally immature (Scalan and Smith, 1970), and has not been degraded by diagenetic processes, further increasing confidence in the excellent preservation of material at RIP.

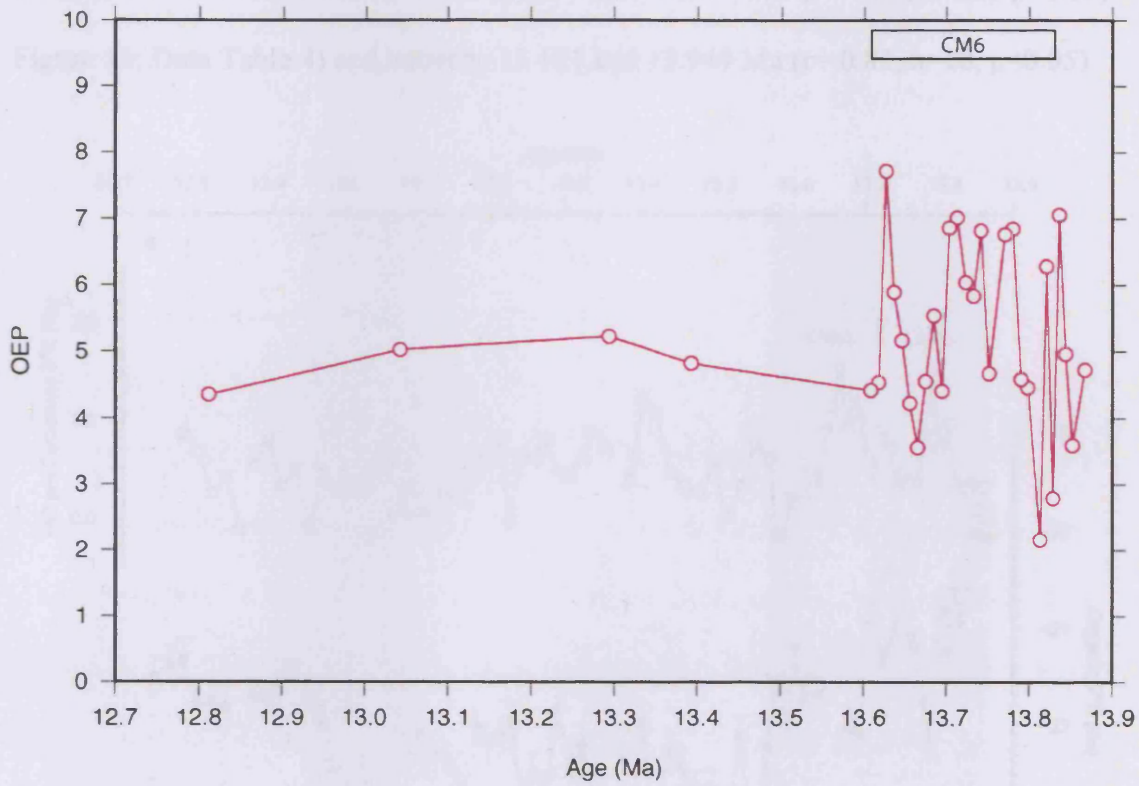

Figure 15: *n*-alkane Odd-Even predominance for Ras il-Pellegrin. Although variable, the OEP record shows no trends which would suggest that the organic carbon isotope record for RIP is driven by a changing contribution of terrestrial organic material.

3.3.4 Bulk Organic Carbon Isotopes

Samples were analysed for bulk organic carbon isotopes at full resolution across CM6 (~9 Kyrs), and at half resolution for the remainder of the section (see section 2.2.4; Data Table 4). The bulk organic $\delta^{13}C$ record from the Ras il-Pellegrin section ranges from a maximum value of -20.0‰ towards the start of the record at 13.85 Ma and drops to a minimum of -23.3‰ at 13.57 Ma. Following this initial decrease there is a gradual increase until the end of the record at 12.75 Ma. Within this long term pattern are fluctuations of ~1‰ on a timescale on the order of 10s of Kyrs. These smaller scale fluctuations in bulk organic $\delta^{13}C$ are negatively correlated with fine fraction

carbonate $\delta^{13}C$ over CM6 between 13.867 and 13.570 Ma (r=-0.49, n=32, p<0.05; Figure 16; Data Table 4) and between 13.101 and 12.949 Ma (r=-0.83, n=10, p<0.05).

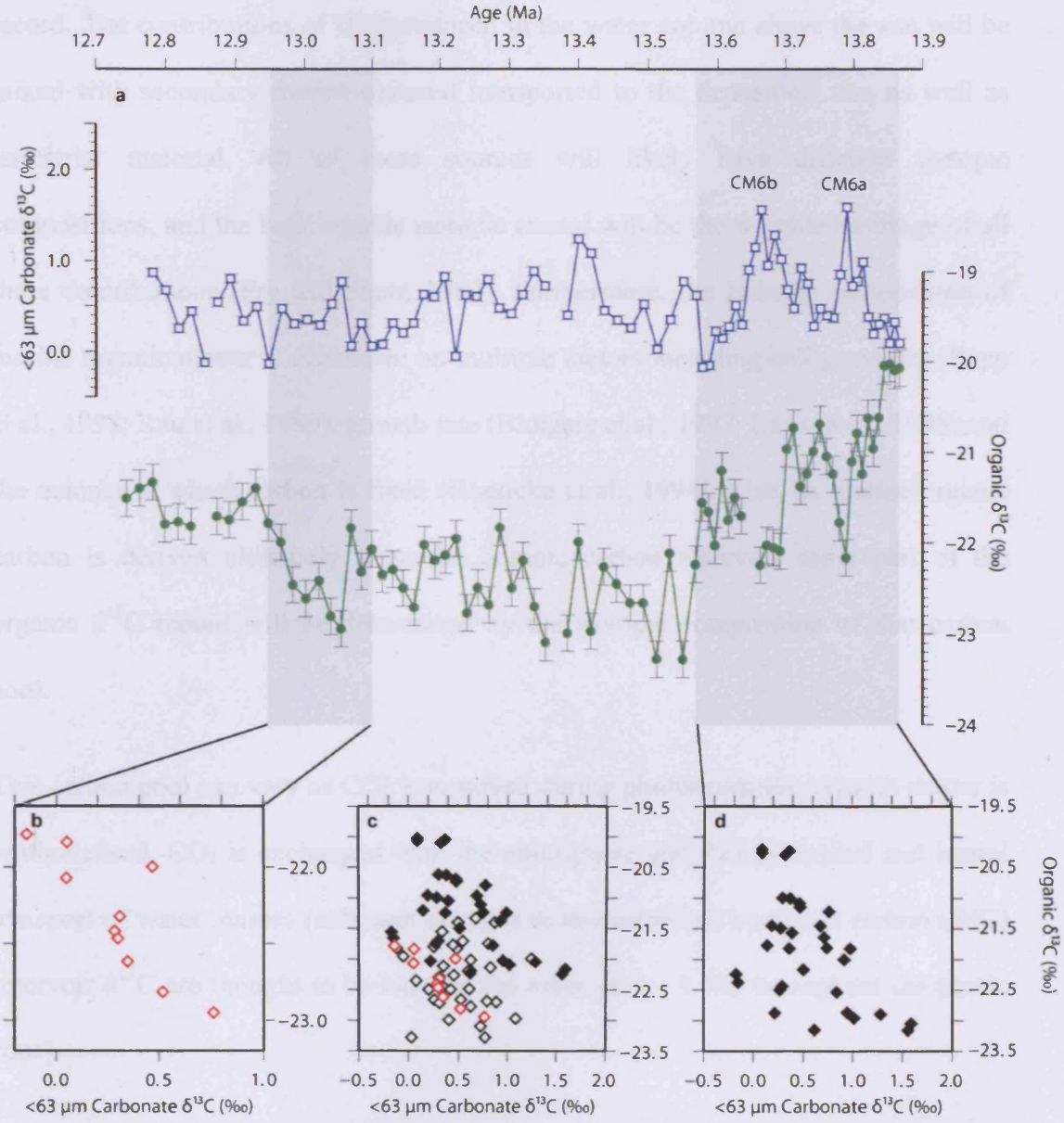

Figure 16: Fine fraction (<63 µm) carbonate $\delta^{13}C$ (blue open squares and line) and organic matter $\delta^{13}C$ (green filled circles and line) from the Ras il-Pellegrin section. Considered as a whole, there is no correlation between these two records (panel d, all points; r=-0.17, n=75, p>0.15), however there are two periods with negative correlation, one spanning CM6 between 13.867 and 13.570 Ma (panel d and filled diamonds in panel c; r=-0.49, n-32, p<0.05, shown as the grey shading in to the right of panel a) and a second between 13.101 and 12.949 Ma (panel b and red open diamonds in panel c; r=-0.83, n=10, p<0.05; shown as the grey shading to the left of panel a).

The interpretation of bulk organic carbon isotope records is complicated by variations in the source organism for the organic matter which is preserved in the sedimentary record. The contributions of OM produced in the water column above the site will be mixed with secondary marine material transported to the deposition site, as well as terrestrial material. All of these sources will likely have different isotopic compositions, and the bulk organic isotopic record will be the weighted average of all these contributions (Fry and Sherr, 1984). Furthermore, the isotopic composition of marine organic matter is dependant on multiple factors including cell geometry (Popp et al., 1998; Rau et al., 1989), growth rate (Bidigare et al., 1997; Laws et al., 1995) and the manner in which carbon is fixed (Goericke et al., 1994). Also, as marine organic carbon is derived ultimately from the oceanic carbon reservoir some part of the organic $\delta^{13}C$ record will be determined by the isotopic composition of that carbon pool.

This carbon pool can vary as CO_2 is removed during photosynthesis, organic matter is remineralised, CO_2 is exchanged with the atmosphere and during vertical and lateral transport of water masses (although changes in this dissolved inorganic carbon (DIC) reservoir $\delta^{13}C$ are thought to be only on the order of 1 – 1.5‰ throughout the photic zone).

As noted above, interpretation of a bulk organic isotope record is complicated by the multiple possible causes of variations in the isotopic composition of the bulk organic matter. Possible interpretations are:

(1) That the organic matter preserved represents material from a single photosynthetic species of marine organism which is living in near

surface waters. Under these circumstances the variations may represent changes in the isotopic fractionation imparted by marine organisms during photosynthesis (ε_p) which could be related to atmospheric CO_2 (Hollander and McKenzie, 1991) or variations in growth rate or cell size (Laws et al., 1997; Laws et al., 1995).

(2) Changes in the distribution of organic material to the site; although still from a primarily marine source (and the $\delta^{13}C$ values are what you would expect from a predominantly marine source), variations in transport of material to the site from throughout the basin could affect the isotopic composition of what is preserved at the site. Similarly changing populations of species present in the water column above the site could affect the isotopic composition of the bulk organic material preserved.

(3) Changes in the proportion or distribution of terrestrial derived organic matter are responsible for the variations in $\delta^{13}C$, even if the material is predominantly marine. Further complicating this possibility is the fact that there are two end-member possibilities for the terrestrial organic matter reaching the site. This could have higher $\delta^{13}C$ (C_4 plants are around -10 – -16‰) or lower $\delta^{13}C$ (C_3 plants are around -25 – -30‰) than the marine organic matter being deposited (typically -20 to -28‰; Fogel and Cifuentes, 1993; Kuypers et al., 1999). Further information would still be needed to determine whether increases in bulk organic $\delta^{13}C$ represent increased or decreased terrestrial input, or possibly changing distribution of plant type on land draining to the site.

(4) Changes in ocean thermal stratification could lead to variations in organic matter isotopes. The organic matter sampled by the bulk organic $\delta^{13}C$ presented here is sourced from the whole water column, and contains contributions from phytoplankton, zooplankton and bacteria. In a more thermally stratified ocean, greater temperature gradients could lead to variations in $[CO_{2(aq)}]$ with depth. In a more stratified ocean, colder, more CO_2 rich waters deeper in the photic zone would lead to organic matter production with lower $\delta^{13}C$. As this would change the isotopic balance of carbon being removed from the DIC reservoir this could conceivably alter carbonate $\delta^{13}C$ as well.

Of the above models, (1) is not supported by the alkenone and boron based isotopic reconstructions of CO_2 discussed in Chapter 5; this suggests that the organic matter may not be predominantly from photosynthetic organisms.

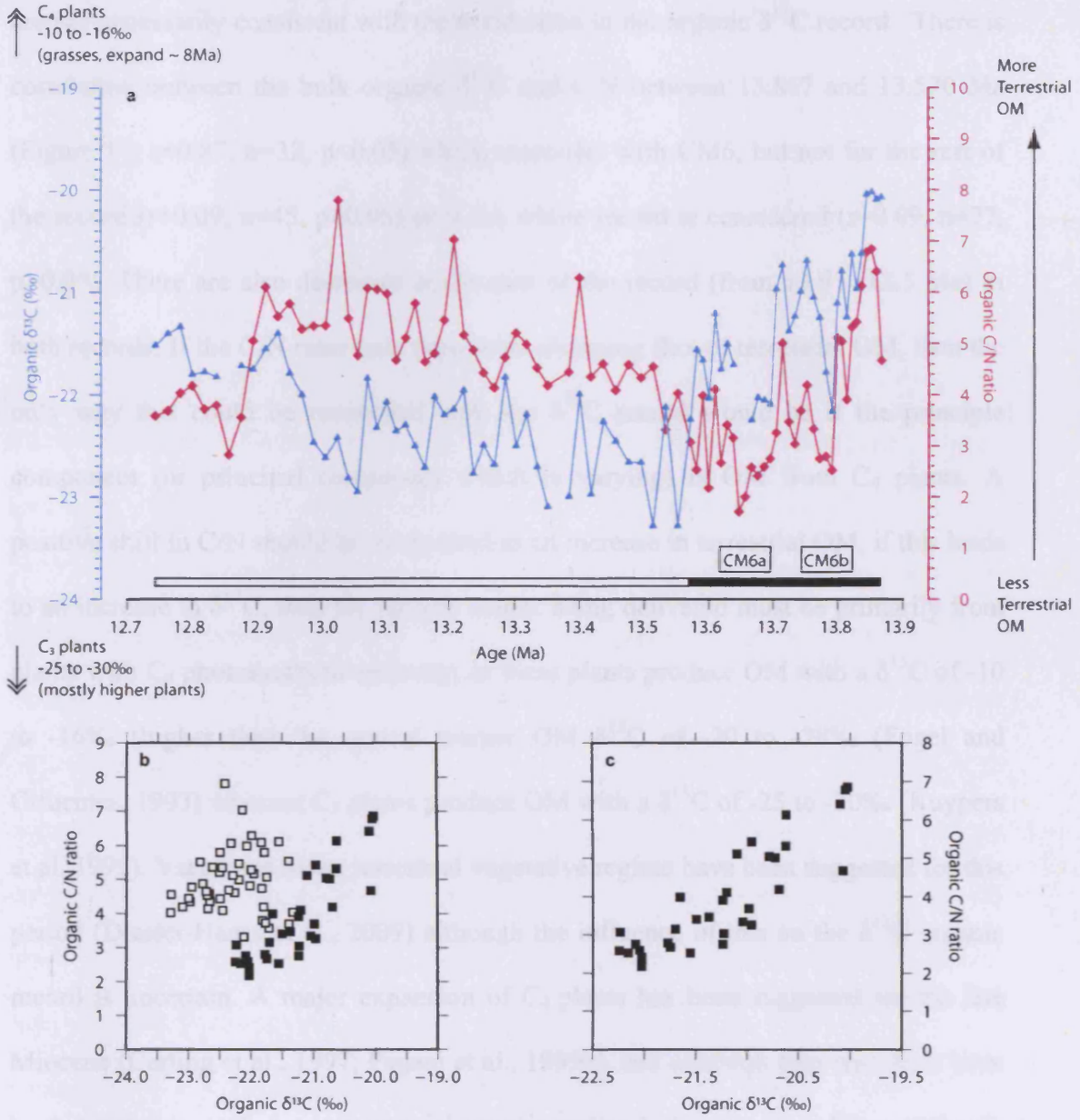

Figure 17: Bulk organic carbon isotopes (panel a; blue triangles and line) and organic C/N ratio (panel a; pink diamonds and line) from the Ras il-Pellegrin section. The temporal positions of CM6 a and b are indicated. Crossplots for the whole record (panel b; all symbols) and for between 13.867-13.570 Ma (panel c and filled squares in panel b) show that there is correlation between the two parameters over CM6 ($r=0.87$, $n=32$, $p<0.05$) but not for the entire record ($r=0.09$, $n=77$, $p>0.05$). The location of the open vs. filled symbols in panel b is indicated by the filled and open bar at the bottom of panel a.

The influence of changing the terrestrial OM contribution (option 3) is supported by the C/N ratios presented in section 3.3.2, although the direction of the C/N variations

are not necessarily consistent with the trends seen in the organic $\delta^{13}C$ record. There is correlation between the bulk organic $\delta^{13}C$ and C/N between 13.867 and 13.570 Ma (Figure 17; $r=0.87$, $n=32$, $p<0.05$) which coincides with CM6, but not for the rest of the record ($r=0.09$, $n=45$, $p>0.05$) or if the whole record is considered ($r=0.09$, $n=77$, $p>0.05$). There are also decreases at the start of the record (from 13.9 – 13.5 Ma) in both records. If the C/N ratio truly represents changing flux of terrestrial OM, then the only way this could be reconciled with the $\delta^{13}C$ record would be if the principle component (or principal component which is varying) is OM from C_4 plants. A positive shift in C/N should be interpreted as an increase in terrestrial OM, if this leads to an increase in $\delta^{13}C$, then the organic matter being delivered must be primarily from plants with C_4 photosynthetic pathway, as these plants produce OM with a $\delta^{13}C$ of -10 to -16‰ (higher than the typical marine OM $\delta^{13}C$ of -20 to -28‰ (Fogel and Cifuentes, 1993) whereas C_3 plants produce OM with a $\delta^{13}C$ of -25 to -30‰ (Kuypers et al. 1999). Variations in the terrestrial vegetative regime have been suggested for this period (Diester-Haass et al., 2009) although the influence of this on the $\delta^{13}C$ organic record is uncertain. A major expansion of C_4 plants has been suggested for the late Miocene (Cerling et al., 1997; Pagani et al., 1999b), and although they may only have been a minor contributor to terrestrial organic matter before then, evidence of the C_4 photosynthetic pathway stretches back to the Cretaceous (Kuypers et al., 1999). The large difference in the carbon isotopic composition of C_3 and C_4 plants means that even a small change in the proportion of plants utilising each pathway could cause a shift in the $\delta^{13}C_{org}$ record if terrestrial oganic matter made a significant contribution to organic matter buried at the site. The C_4 photosynthetic pathway is favoured in lower atmospheric CO_2 concentrations as plants using this pathway are capable of internally concentrating CO_2 before fixation (Hatch, 1987). The balance between C_3 and C_4

plants is therefore influenced by the prevailing atmospheric CO_2 (Pearcy and Ehleringer, 1983). A reduction in CO_2 at the expansion of the EAIS would potentially be a driver of a shift towards more C_4 plants, however as OM produced via this pathway has a higher $\delta^{13}C$, this would not explain the reduction in organic $\delta^{13}C$ shown in the record.

The pronounced thermocline present in todays ocean first developed during the Miocene (plausibly related to the growth of an Antarctic ice sheet and related formation of cold deep waters transported from the southern ocean) (Savin et al., 1975). There is some support for the onset of thermal stratification at the time of the middle Miocene growth of an Antarctic ice sheet from molecular organic carbon isotope analysis, which also supports the formation of organic material with different carbon isotopic composition at different water depths (Schoell et al., 1994). The periods of negative correlation between the organic and carbonate carbon isotope records may therefore represent changing intensity in stratification (option (4)), with times of greater stratification recorded as negative shifts in the organic $\delta^{13}C$ record (and matched by positive shifts in the carbonate record) as the difference between surface and lower photic zone temperature increases. Such an increase in stratification would lead to lower temperatures at the base of the photic zone, and corresponding higher $[CO_{2(aq)}]$ and lower OM $\delta^{13}C$. The change in carbonate $\delta^{13}C$ could, in turn, be caused by the removal of more highly ^{13}C depleted organic matter from the DIC pool.

The above discussion highlights the uncertainty surrounding the use of bulk organic carbon isotopes, where multiple possible sources of variation are possible. Much of the difficulty is due to uncertainty surrounding the source of the material being analysed, and it is for this reason that compound specific carbon isotope analysis of biomarkers

from a restricted group of organisms is used to elucidate changes in atmospheric CO_2 (see Chapter 5). On the basis of the bulk organic carbon isotope record, and given the lack of conclusive evidence for changing terrestrial input varying with the isotope record, it is option (4); changing thermal stratification, which is the preferred option here.

4 Moria Section, Italy

The Moria section in central Italy has undergone significantly more tectonic disturbance that the Ras il-Pellegrin section, and therefore the preservation of foraminifera is significantly poorer, and does not allow for the same number of proxies to be utilised as is the case at RIP. Nevertheless, the excellent exposure of the Burdigalian and Langhian material at Moria affords an opportunity to develop a high-resolution coupled organic-inorganic isotope record of the start of the Monterey excursion.

4.1 Sampling Site

The Moria section lies in the foothills of the northern Apennine mountains in the Marche region of Italy, as a 100 m thick exposure beside the mountain road between the villages of Palcano and Moria (43° 30.23' N 12° 35.65' E; Figure 18).

Exposed within the Moria section is the top 20 m of the Bisciaro Formation and the contact between this and the Schlier Formation, covering the uppermost Burdigalian stage and the transition to the Langhian (Deino et al., 1997), steeply dipping to the northwest. The section contains 3 volcaniclastic ash layers allowing direct radiometric dating and is a candidate section for the Global Stratotype Section and Point for the base of the Langhian (Subcommision for Stratigraphic Information, 2009). The Lower marly member of the Schlier Formation consists of dark, friable marls, which make way to interbedded marls and siliceous marly limestones in the Siliceous Calcareous member.

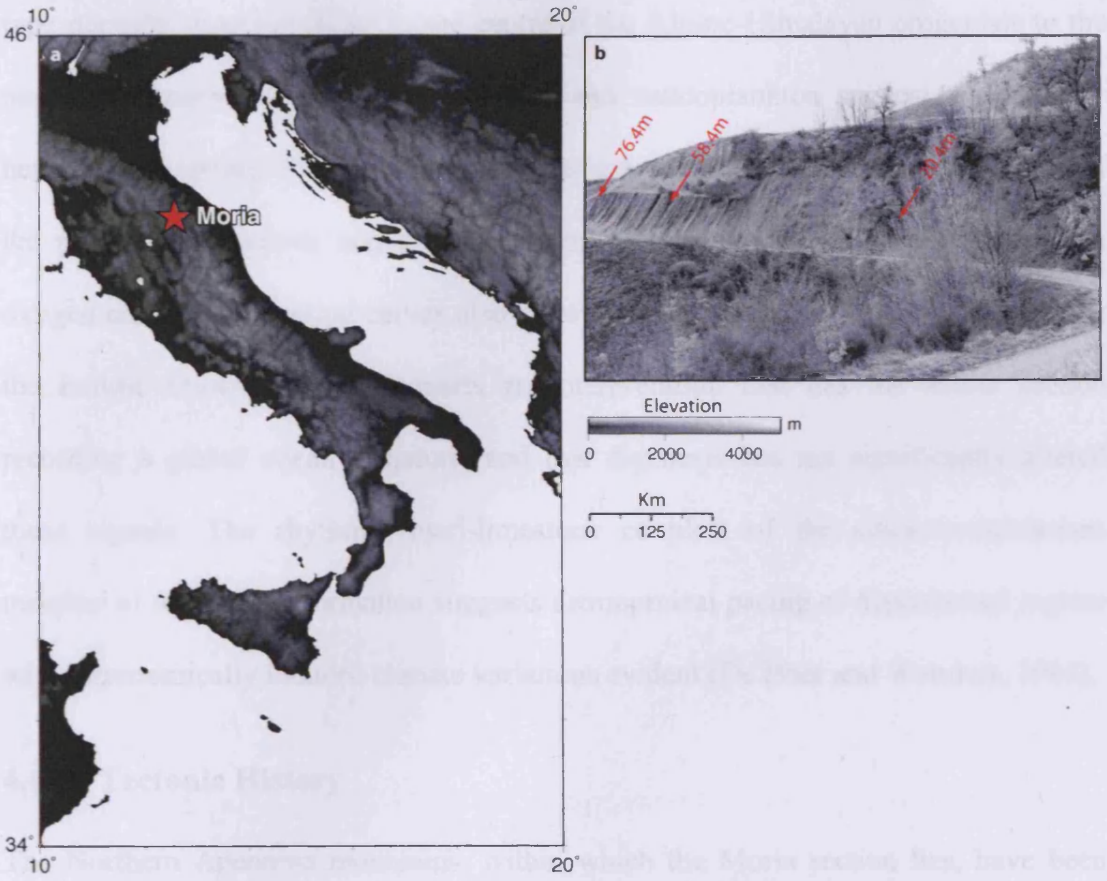

Figure 18: The Moria section, showing a; the location of the Moria section (indicated by red star) in the Apennine mountains of central Italy and b; view of the section (looking north) showing the location of the three dated ash layers (arrowed).

Sampling of the Schlier Formation took place on the 13th September 2006, with a sampling resolution of 1m between 20 m and 45 m (the Lower marly member of the Schlier Formation), increasing to 0.25 m resolution between 45 m and 81 m (the Siliceous-calcareous member of the Schlier Formation and lowermost part of the Upper marly member) except where vegetation cover made 0.25 m sample spacing impossible (between 49 m and 52 m).

4.1.1 Geological Setting

The marls of the Moria section represents a hemi-pelagic open sea setting, rare amongst Tethyan basin deposits of this time in that it lacks the flysch and mollasse

type deposits common closer to the centre of the Alpine-Himalayan orogenisis to the north. The marls, planktonic foraminifera and nannoplankton suggest a pelagic or hemi-pelagic setting and Sr isotopes suggest some connection between the waters of the proto-Mediterranean and the open ocean (Deino et al., 1997). Low-resolution oxygen and carbon isotope curves also show features similar to the global curves for the middle Miocene. This supports an interpretation that has the Moria section recording a global ocean signature, and that digenesis has not significantly altered these signals. The rhythmic marl-limestone couplets of the siliceous-calcareous member of the Schlier formation suggests astronomical pacing of depositional regime with astronomically induced climate variations evident (De Boer and Wonders, 1984).

4.1.2 Tectonic History

The Northern Apennine mountains, within which the Moria section lies, have been exposed to major tectonic disturbance during the Alpine orogeny, evident from the steep dip of the Moria sediments and the present day elevation of ~600 m (Vrielynck et al., 1997). Underlying the Apennine range the crust has been thickened by thrusting, with extensional and transtensive processes in the upper 15 km, whilst compressional processes are active at depth. The thickening of the Northern Apennine crust took place as the lithospheric base of the northern Tyrrhenian Sea and Tuscany to the west of the Apennines was thrusted and then sank beneath the Apennine ridge. The Moria section lies within the Marnosa-Arenacea foredeep basin, the second of three major foreland basins which developed as a tectonic nappe pile and peripheral bulge which migrated progressively towards the Adriatic foreland during the Neogene (Pialli and Alvarez, 1997). The hemipelagic sediments of the Schlier Formation overlie pre-flysch sediments and are overlain by distal and then proximal turbidites of Serravallian age as the deformation front progressed towards the site (Deino et al., 1997; Pialli and

Alvarez, 1997). The main stage deformation of the basin took place in the late Tortonian – early Messinian, although synsedimentary tectonics are evident during the Langhian-Serravallian, with late stage Tortonian thrusting refolding parts of the area (Pialli and Alvarez, 1997). Miocene – Pliocene activity in adjacent nappe system translated the stress regime in the Apennine system to extensional, and although the exact age of initiation of extensional tectonics in the Apennines in uncertain it was likely initiated in the late Tortonian (Pialli and Alvarez, 1997).

4.2 Lithostratigraphy

4.2.1 Isotope Stratigraphy

The bulk carbonate stable isotope record generated for the Moria section allows correlation of the proto-Mediterranean record to the global ocean record, by way of clearly identifiable isotope events (Figure 19; Data Table 6).

Although there are limited clear oxygen isotope events in the period that the Moria event spans (like the E3/Mi-3 event at Ras il-Pellegrin), there are three "Carbon Maxima" (CM) events within the timespan of the Moria section (Deino et al., 1997; Woodruff and Savin, 1991). These are CM1, CM2 and CM3, and are recognisable in the Moria carbonate carbon isotope record (Figure 19). Also present is the start of the more gradual increase in $\delta^{13}C$ that marks the start of the "Monterey excursion" (Vincent and Berger, 1985).

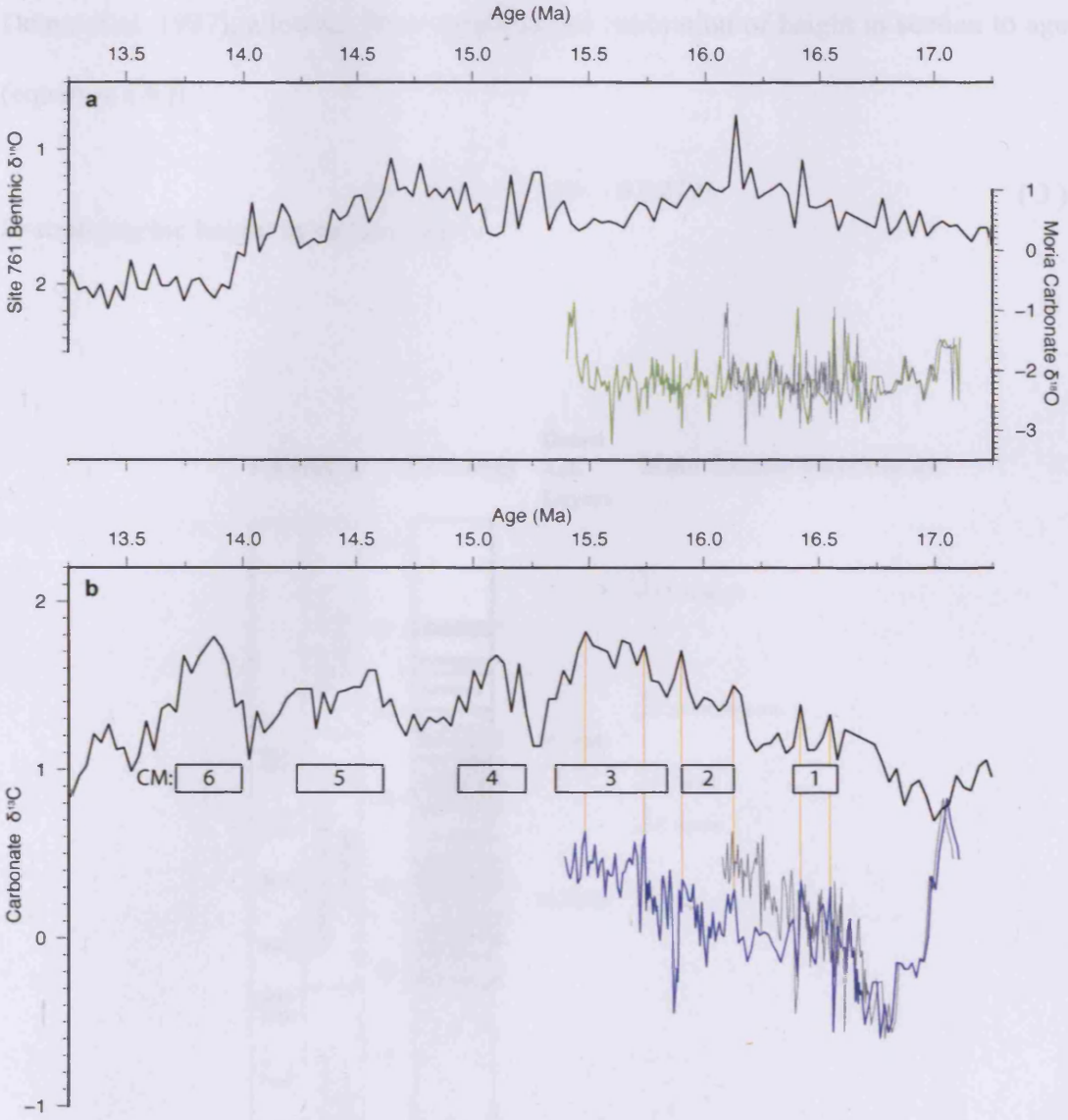

Figure 19: Stable oxygen (green line, panel a) and carbon (blue line, panel b) bulk carbonate isotope analyses from Moria, shown with a representative low resolution ocean record from ODP site 761 (Holbourn et al., 2004). Carbon maximum (CM) events are shown, following the definitions of Holbourn et al. (2004) and Woodruff and Savin (1991). Orange vertical lines in panel b show tie points between the two records used to construct the age model, and thin grey lines in both panels show alternative age models constructed using only foraminifera datums.

4.2.2 Age Model

An initial age model was developed for the Moria section based on the timing of the 3 well-dated ash layers which are distributed through the section (Figure 20; Table 3;

Deino et al. 1997), allowing for a simple linear calibration of height in section to age (equation (3)).

$$Age\ (Ma) = 17.703 - 0.0279h \qquad (3)$$

h=stratigraphic height in section (m)

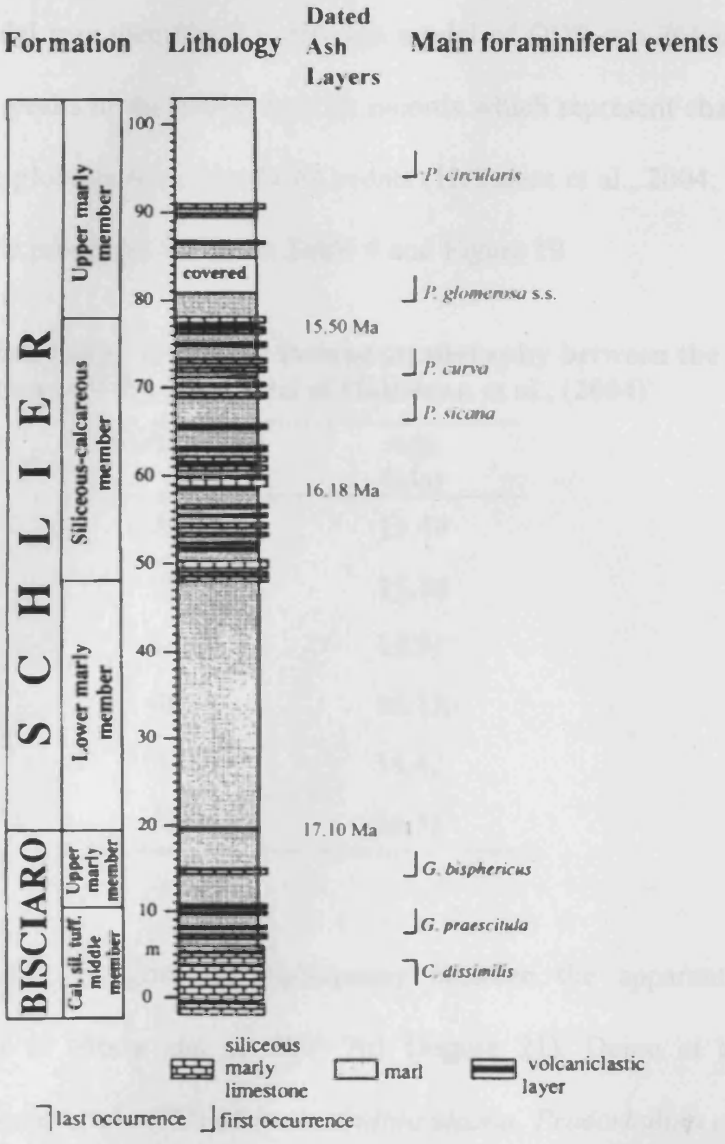

Figure 20: Stratigraphy of the Moria section, showing formation boundaries, metres height scale, lithology, position of dated as layers and main foraminiferal events. Adapted from Deino et al., (1997).

Table 3: Stratigraphic position and Age of dated ash layers (Deino et al., 1997)

Horizon (m)	Age (Ma; with 2σ uncertainties)
76.5	15.50 (±0.16)
58.4	16.18 (±0.16)
20.4	17.1 (±0.20)

This initial age model was then tuned to the age model of ODP site 761 using 6 tie points at prominent peaks in the carbon isotope records which represent characteristic peaks which are the globally recognised CM events (Holbourn et al., 2004; Woodruff and Savin, 1991). Tie points are shown in Table 4 and Figure 19.

Table 4: Tie points based on carbon isotope stratigraphy between the Moria section and the age model of Holbourn et al., (2004)

Horizon (m)	Age (Ma)
79.00	15.49
73.00	15.74
64.75	15.91
58.75	16.13
54.75	16.42
52.75	16.55

This approach reveals a significant discrepancy between the apparent ages of foraminifera datums at Moria and at ODP 761 (Figure 21). Deino et al. (1997) recognise the first occurrences (FO) of *Praeorbulina sicana, Praeorbulina curva,* and *Praeorbulina glomerosa* sensu stricto at 66.2 m, 71.69 m and 94.00 m respectively in the Schlier Formation (Figure 20 and Figure 21). The ages for these bioevents based on the integrated ash layer and carbon isotope stratigraphy presented here vary by 520

kyrs, 530 kyrs and 650 kyrs respectively from their apparent ages at Site 761. As the two age models have been tied using carbon isotope stratigraphy this suggests significant diachrony between the appearances of these species at the two sites. Diachrony of similar magnitude has been recognised for other bioevents in the Miocene (Shackleton et al. 1999).

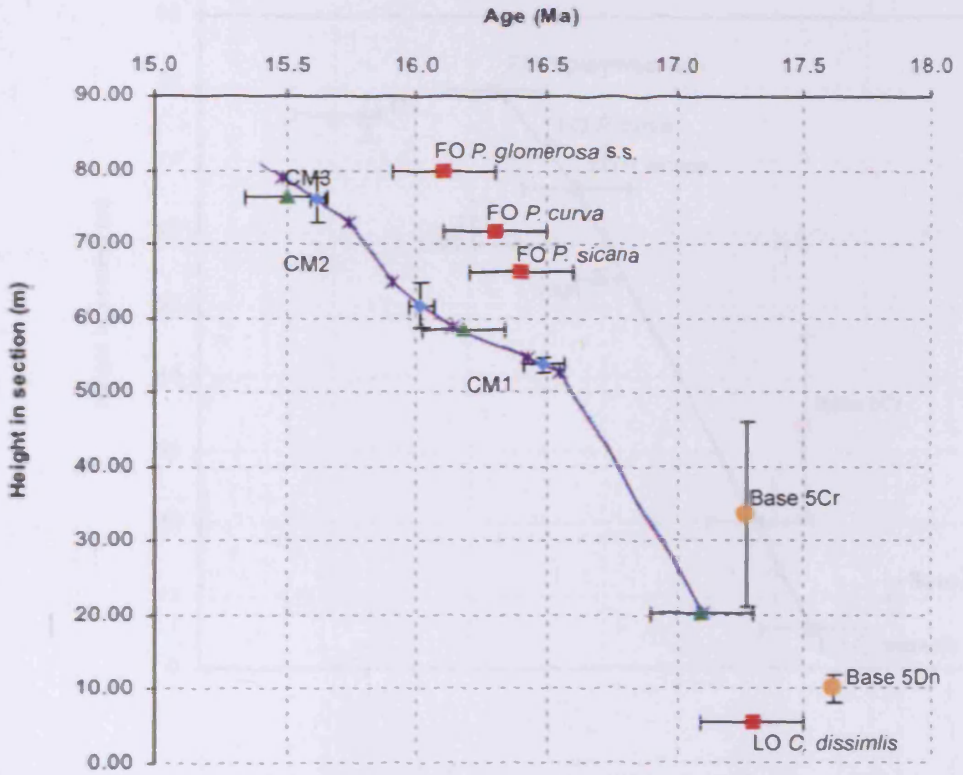

Figure 21: Height vs. age plot for the datum events at Moria. Foraminiferal datums (red filled squares and 2σ uncertainties) are shown with ages of Berggren et al. (1995a,b) with stratigraphic heights from Deino et al (1995). Revised magnetic reversals (orange filled circles) are shown with ages of Cande and Kent (1995). Ages of and definitions of CM events (blue filled circles) follow Woodruff and Savin, (1991), Flower and Kennett (1993) and Holbourn et al., (2004), with heights taken shown as the midpoints of the events at Moria (this work), age uncertainties follow the definitions of Holbourn et al. (2004). Dated ash layers (green filled triangles) are from Deino et al. (1997) with 2σ uncertainties. The purple line is the preferred age model for the Moria section (see text) with tie points shown as purple crosses.

An alternative age model was constructed based purely on the foraminiferal datums (Figure 22), which results in a carbon isotope curve which departs significantly from the ODP 761 carbon isotope curve (grey line in panel b; Figure 19) and on this basis the age model shown in Figure 21 is preferred.

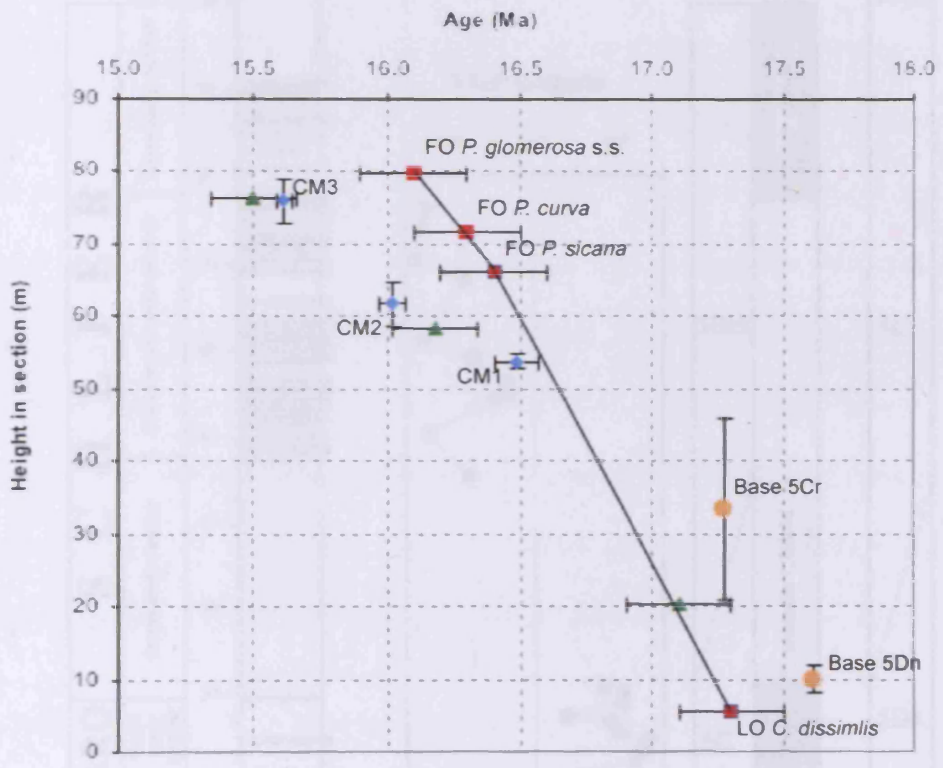

Figure 22: Alternative age model (black line) for the Moria section based on only the planktonic foraminiferal datums (after Berger et al. 1995). Symbols and colours are as in Figure 21.

Deino et al. (1997) recognise one clear magnetic reversal at 10 m, and infer a second between 21 and 46 m (Figure 23), and tentatively assign these to the bases of chrons 5Cn and 5Br.2r respectively. However Deino et al. (1997) note that this interpretation results in significant discrepancy between the dated ash layers at the Moria section and the geomagnetic timescale of Cande and Kent (1992). On the basis of the age model presented here, and given the possible uncertainty of timings of the biostratigraphy (which guided Deino et al. (1997) in their identification of the chrons) it seems is

plausible that these reversals are in fact the bases of chrons 5Cr and 5Dn, and that the reversed interval at the base of the section is 5Dr.1r (Figure 23).

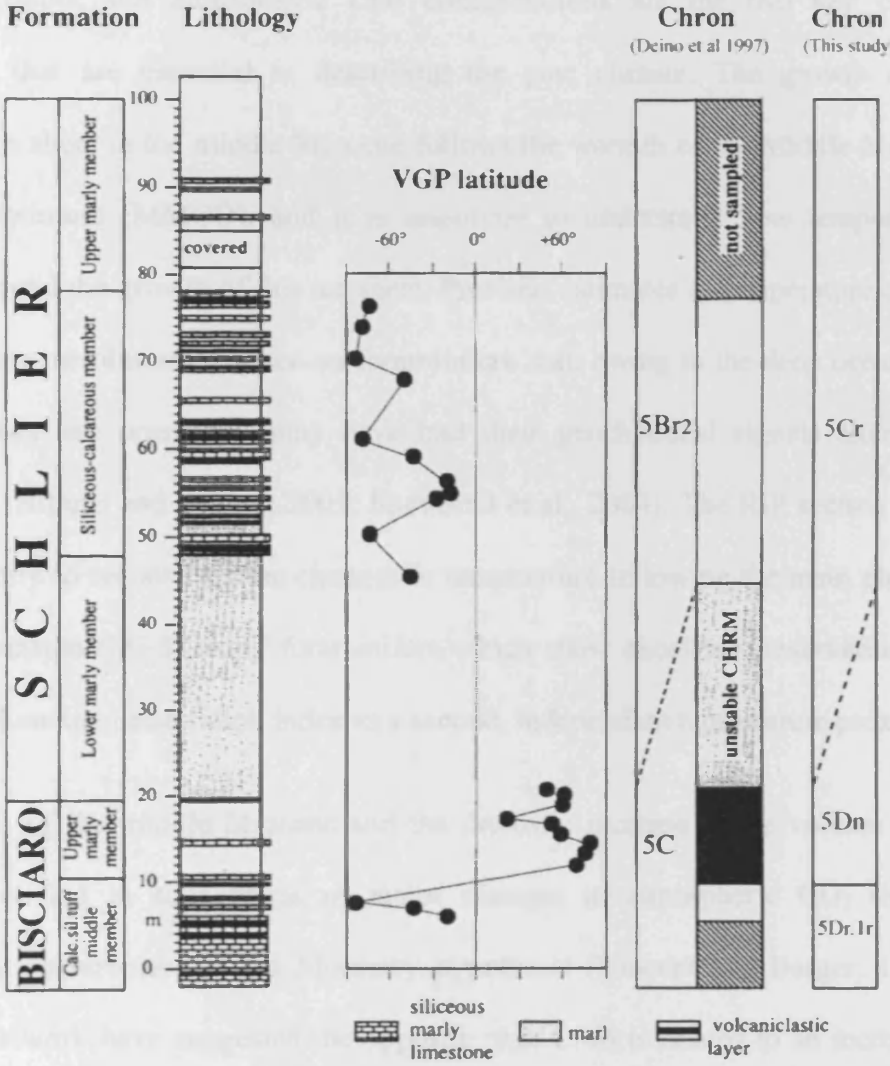

Figure 23: Magnetostratigraphy of the Moria section (adapted from Deino et al. 1997), showing lithostratigraphic column, virtual geomagnetic pole (VGP) latitude and interpretation of magnetic reversals from Deino et al. (1997) and this study.

5 Middle Miocene Temperature and Atmospheric pCO_2

Past temperature and atmospheric CO_2 concentrations are the two key climate parameters that are essential in describing the past climate. The growth of the Antarctic ice sheet in the middle Miocene follows the warmth of the Middle Miocene Climatic Optimum (MMCO), and it is important to understand how temperatures changed around the growth of this ice sheet. Previous estimates of temperature change have been low resolution or based on foraminifera that, owing to the deep ocean sites at which they are preserved, may have had their geochemical signals altered by dissolution (Billups and Schrag, 2003; Shevenell et al., 2004). The RIP section offers an opportunity to reconstruct the changes in temperature following the main phase of the ice expansion (Mi-3) using foraminifera which show excellent preservation, and using the alkenone unsaturation index as a second, independent temperature proxy.

The warmth of the middle Miocene and the dramatic increase in ice volume at the MMCT have led to suggestions of major changes in atmospheric CO_2 (it is a fundamental requirement of the Monterey hypothesis (Vincent and Berger, 1985)). More recent work have suggested the opposite; that CM6 is related to an increase in atmospheric CO_2 resulting from a negative feedback due to ice sheet blanketing of silicate basement (see section 1.2; Lear et al., 2004; Pagani et al., 1999a; Shevenell et al., 2008). To resolve these two hypotheses, it is essential to have an accurate knowledge of how atmospheric CO_2 evolved over CM6, and through a combination of alkenone and boron palaeobarometers, the RIP section offers an opportunity to determine this behaviour.

5.1 Palaeotemperature Proxies

5.1.1 Alkenone Unsaturation Index

Alkenones are "molecular fossils' – organic molecules produced by organisms and preserved in marine sediments. Alkenones are long chained (37-39 carbon atoms) unsaturated methyl and ethyl ketones (Figure 24) produced within the mixed layer by a restricted group of photosynthetic haptophyte algae (Conte et al., 1994). In the modern ocean alkenone production is dominated by the coccolithophores *Emiliania huxleyi*, and alkenones have been isolated in Eocene (Marlowe et al., 1984) and Cretaceous sediments (Brassell et al., 2004; Farrimond et al., 1986), which demonstrates both their extensive fossil records and their resistance to diagenetic degradation.

Long-chain di-, tri- and tetraunsaturated C_{37} methyl ketones (alkenones)

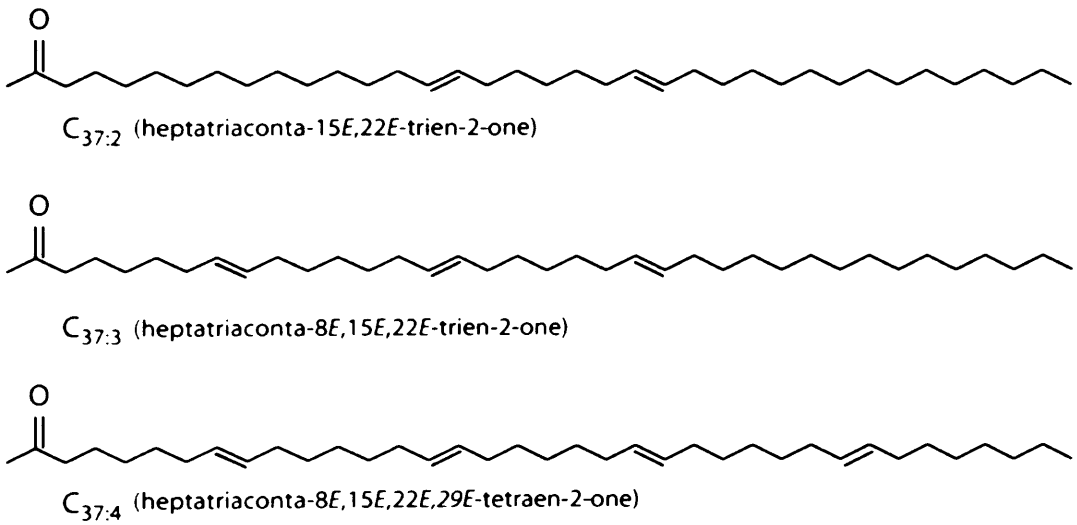

Figure 24: C_{37} Alkenones in di-, tri- and tetra-unsaturated form.

Temperature reconstruction based on alkenones are based on the capability of the Prymensiphyceae class of marine algae to synthesis alkenones of varying degrees of

unsaturation dependant upon the prevailing sea temperature at the time of growth (Brassell et al., 1986; Marlowe, 1984; Prahl and Wakeham, 1987). The development and temperature calibration of first the U_{37}^{K} index (equation (4); Brassell et al., 1986) and later the $U_{37}^{K'}$ index (equation (5) Brassell, 1993; Prahl and Wakeham, 1987) for situations where the tetra-unsaturated alkenone ($C_{37:4}$) is not present has led to a robust proxy for sea surface temperature (Brassell, 1993).

$$U_{37}^{K} = \frac{C_{37:2} - C_{37:4}}{C_{37:2} + C_{37:3} + C_{37:4}} \quad (4)$$

$$U_{37}^{K'} = \frac{C_{37:2}}{C_{37:2} + C_{37:3}} \quad (5)$$

The $U_{37}^{K'}$ proxy can reconstruct temperatures ranging from 0 to 29°C (Müller et al., 1998), at temperatures higher than 29°C only the di-unsaturated alkenone remains and the $U_{37}^{K'}$ index reaches 1. The temperature calibration used here is based on a global core top calibration to annual mean sea surface temperature (equation (6); (Müller et al., 1998) and is widely used in palaeotemperature estimation.

$$U_{37}^{K'} = 0.033T + 0.044 \quad (6)$$

The analytical uncertainty based on 4 full procedural replicates ±1.5°C, which is similar to the uncertainty found by others (Müller et al., 1998).

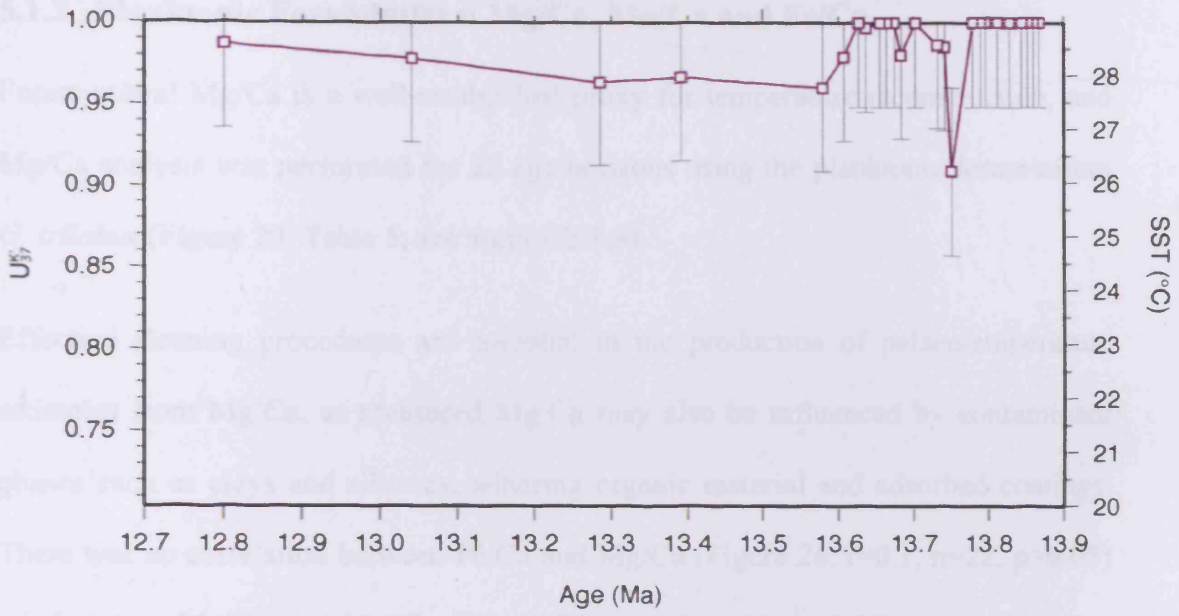

Figure 25: Alkenone unsaturation index results from RIP and resulting temperature reconstruction using calibration of Müller et al. (1998). Note that as at temperatures exceeding 28.9°C $U^{K'}_{37}$ is 1, so points which lie on the upper limit of the plot (with $U^{K'}_{37}$=1) should be read as 28.9°C *or higher.*

The nine samples from the base of the section at 13.86 Ma to 13.77 Ma have a $U^{K'}_{37}$ of 1, with only the di-unsaturated alkenone ($C_{37:2}$) present, which translates to a sea surface temperature of 28.9°C or higher (Figure 25). Between 13.74 Ma and and 13.66 Ma temperatures range between the lowest recorded temperature of 26.2°C at 13.74 Ma and 28.9°C, where only the $C_{37:2}$ is present. Within this period there are also horizons where the tri-unsaturated alkenone is present but only at very low concentrations, suggesting temperatures close to the 28.9°C maximum. From 13.61 Ma to the end of the section at 12.81 Ma the $C_{37:3}$ alkenone is present, with temperatures ranging from 27.8 – 28.6°C.

5.1.2 Planktonic Foraminiferal Mg/Ca, Mn/Ca and Fe/Ca

Foraminiferal Mg/Ca is a well-established proxy for temperature reconstruction, and Mg/Ca analysis was performed for 22 age horizons using the planktonic foraminifera *G. trilobus* (Figure 29; Table 5; see section 2.1.3).

Effective cleaning procedures are essential in the production of palaeotemperature estimates from Mg/Ca, as measured Mg/Ca may also be influenced by contaminant phases such as clays and silicates, adhering organic material and adsorbed coatings. There was no correlation between Fe/Ca and Mg/Ca (Figure 26; $r=0.1$, $n=22$, $p>0.05$) nor between Mn/Ca and Mg/Ca (Figure 26; $r=-0.3$, $n=22$, $p>0.05$), suggesting that cleaning had effectively removed sources of contaminant Mg. Although Fe/Ca and Mn/Ca are relatively high, the absence of correlation between these elemental ratios and Mg/Ca, suggests that they are not influencing the measured Mg/Ca.

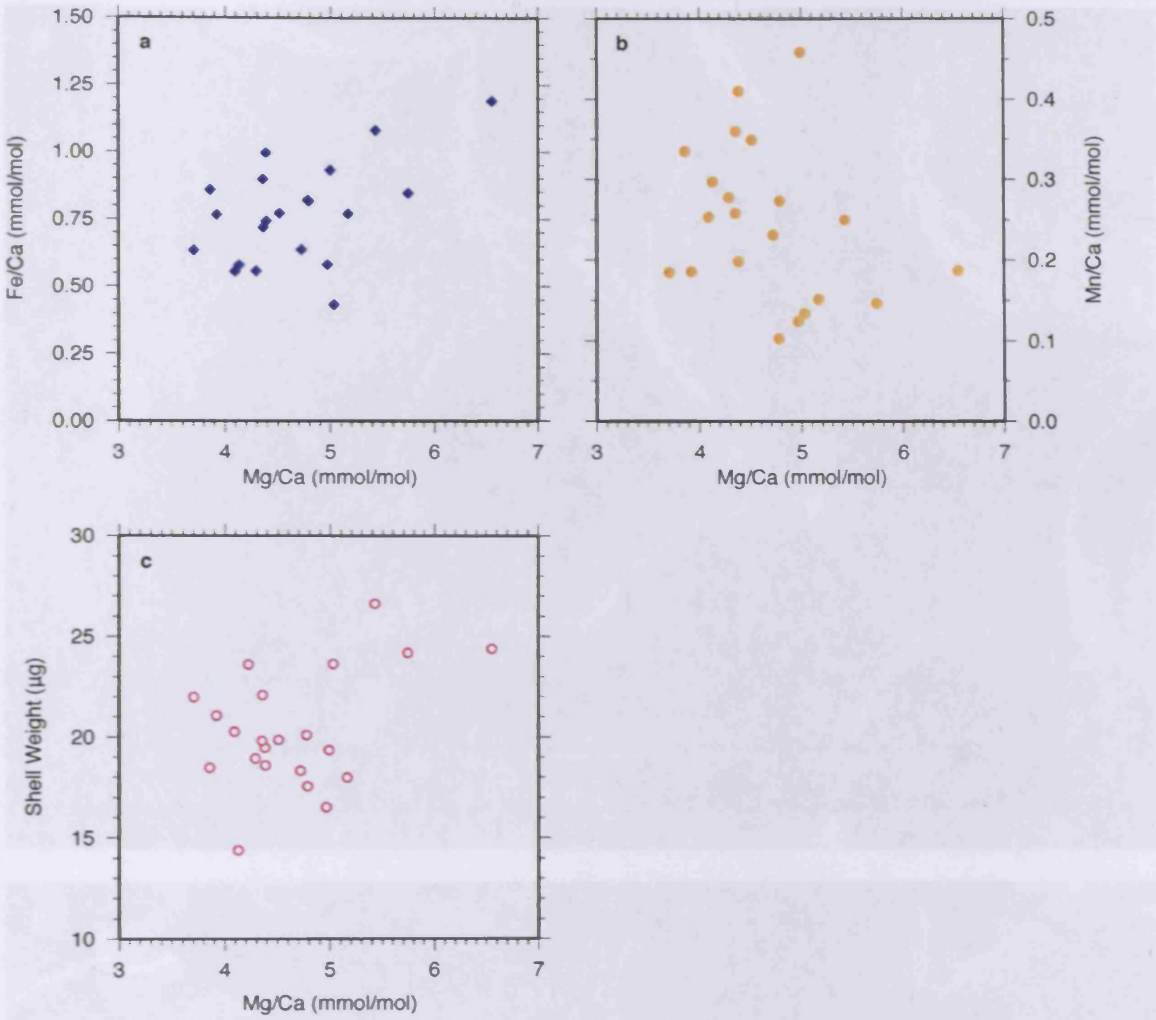

Figure 26: Fe/Ca (panel a; blue diamonds), Mn/Ca (panel b; orange circles) and shell weight (panel c; pink open circles) plotted versus Mg/Ca in *G. trilobus*.

Recrystallisation is unlikely at Ras il-Pellegrin, as the maximum estimate of palaeo-depth is only 700 m (Bellanca et al., 2002), well above the CCD, and post depositional recrystallisation is less likely in clay rich lithologies such as the Blue Clay. SEM micrographs (Figure 27) show no evidence of recrystalisation. However there is variability in shell weight at RIP and a weak correlation exists between shell weight and Mg/Ca (Figure 26; r=0.41, n=22, p=0.057) suggesting that some minor dissolution may be influencing Mg/Ca measurements, and this is corrected for within the Mg/Ca SST calibration (equation (7)).

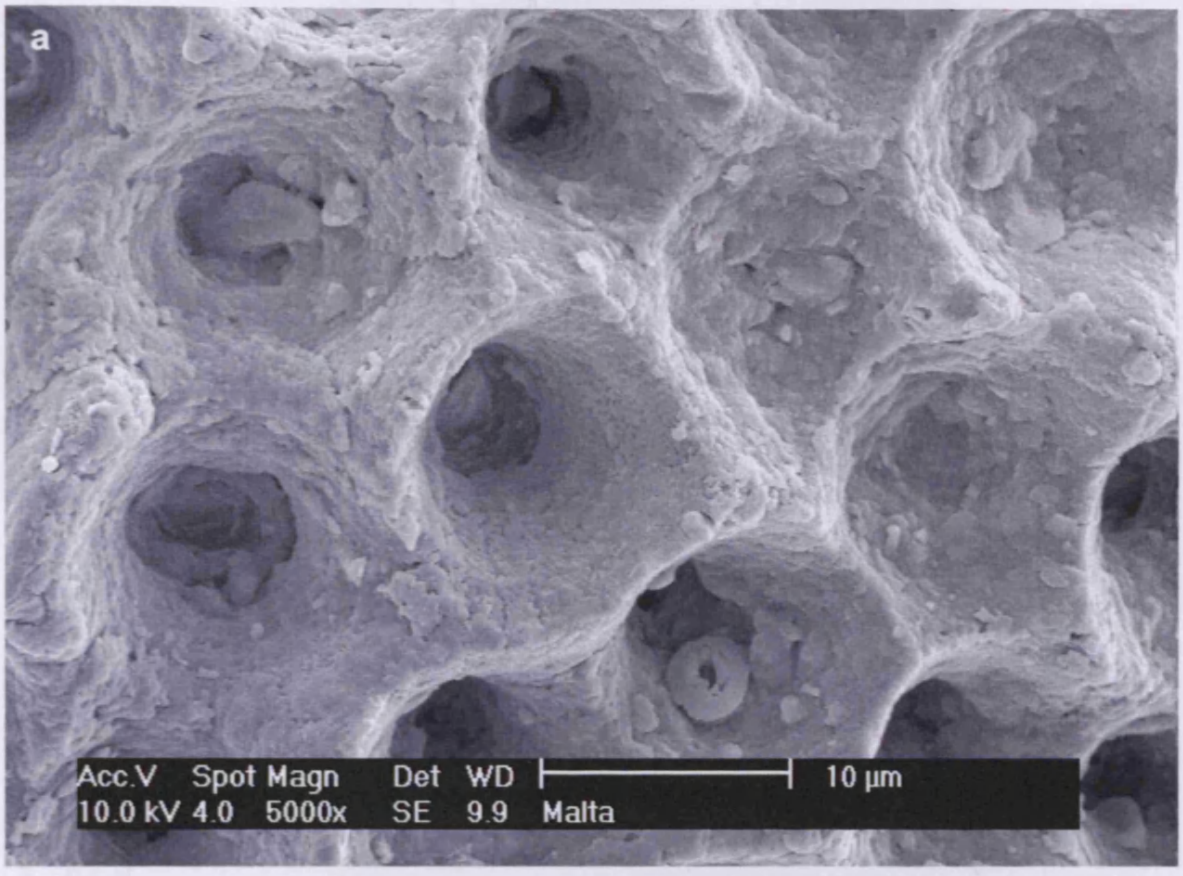
a
Acc.V Spot Magn Det WD 10 µm
10.0 kV 4.0 5000x SE 9.9 Malta

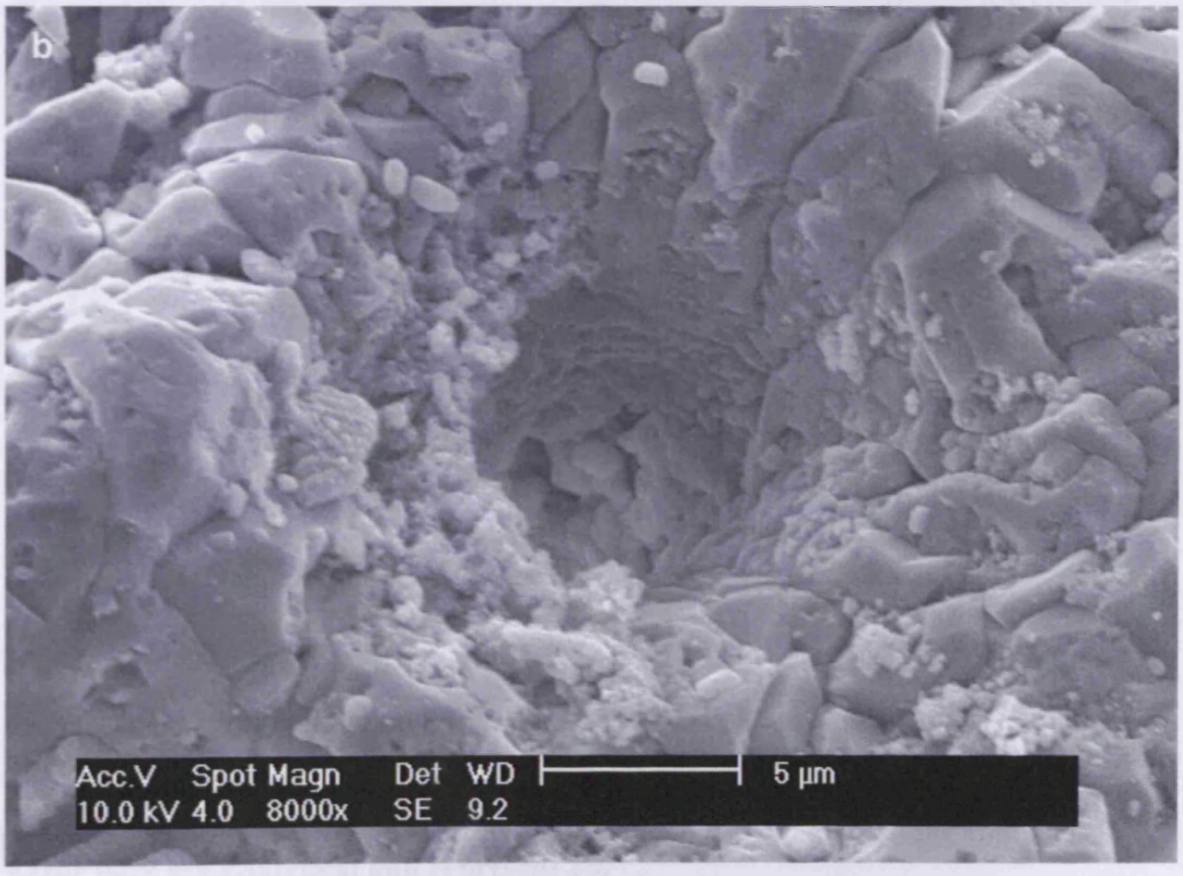
b
Acc.V Spot Magn Det WD 5 µm
10.0 kV 4.0 8000x SE 9.2

Figure 27 (previous page): SEM micrograph of a typical *G. trilobus* from RIP (panel a), with image of the same species of similar age from a deepwater site which has been close to or below the lysocline since the Miocene for comparison (panel b; DSDP 92-598*-4H-6,1-5; Rea and Leinen (1984); Ravizza et al. in prep.)

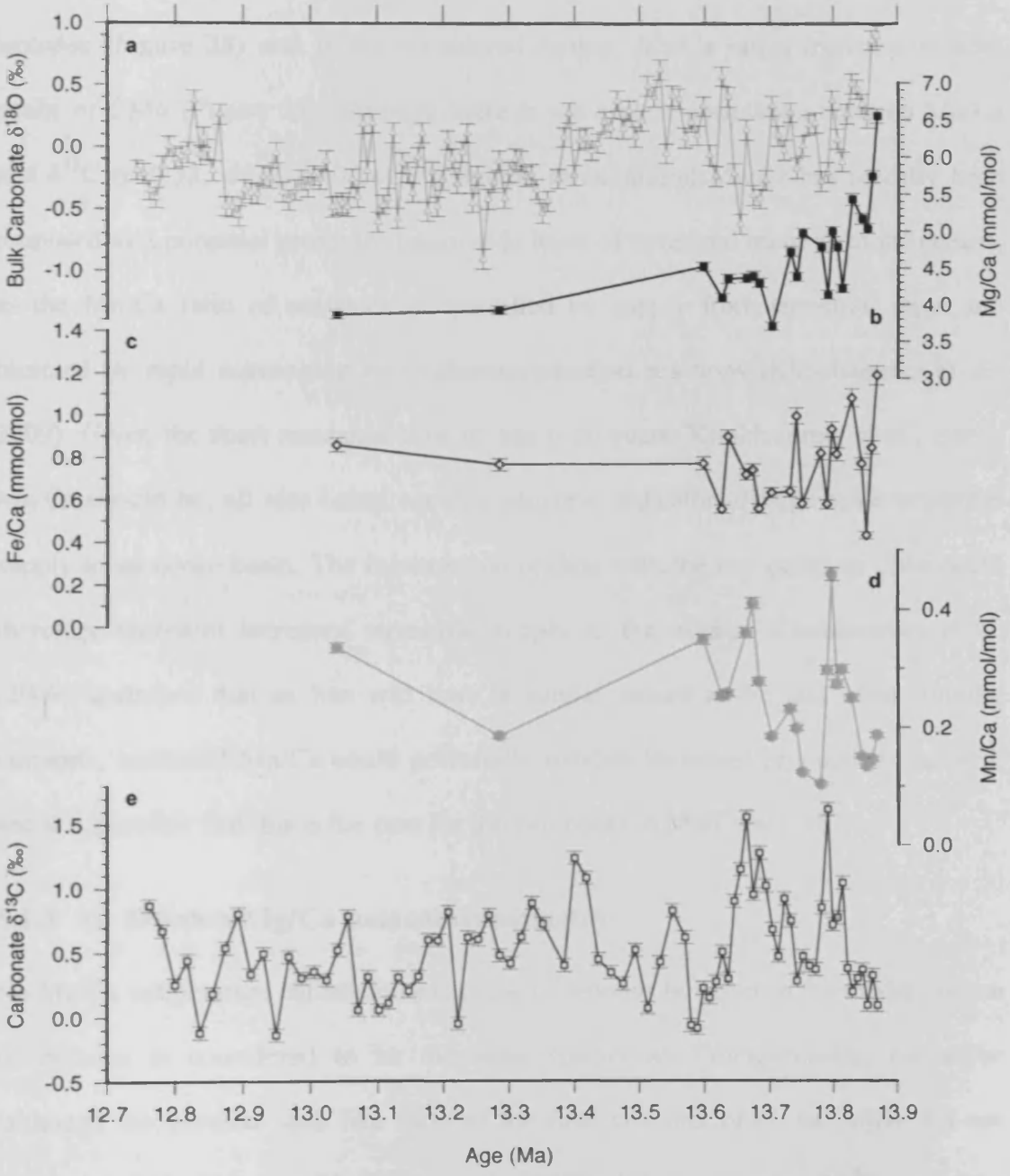

Figure 28: Trace metal records from *G. trilobus*. Shown are Mg/Ca (panel b; black filled squares), Fe/Ca (panel c; blue open triangles) and Mn/Ca (panel d; orange filled circles) shown with bulk carbonate $\delta^{18}O$ (panel a; orange open diamonds) and bulk carbonate $\delta^{13}C$ (panel e; blue open squares) for comparison. Error bars are analytical and represent 2σ.

G. trilobus Mg/Ca declines at the same time as the increase in carbonate $\delta^{18}O$ from ~13.9 to ~13.7 Ma (Figure 28), representing a cooling of sea surface temperatures as the ice sheet expanded (see section 5.1.3 below). Fe/Ca ratios show no clear trends over the period, and does not show a similar structure to either oxygen or carbon isotopes (Figure 28) and is not considered further. Mn/Ca ratios increases at both peaks of CM6 (Figure 28), although there is not a clear correlation between Mn/Ca and $\delta^{13}C$ ($r=0.32$, $n=22$, $p>0.14$). Planktonic foraminiferal Mn/Ca has recently been proposed as a potential proxy for basin-wide input of terrestrial material to the oceans, as the Mn/Ca ratio of seawater is controlled by supply from terrestrial input and removal by rapid scavenging by oxidation-reduction reactions (Klinkhammer et al., 2009). Given the short residence time of Mn (~50 years; Klinkhammer et al., 2009), Mn/Ca should be, all else being equal, a sensitive indicator of large scale terrestrial supply to an ocean basin. The increases coinciding with the two peaks of CM6 could therefore represent increased terrestrial supply to the oceans. Klinkhammer et al. (2009) speculate that as Mn will have a similar source as Fe and other limiting nutrients, increased Mn/Ca could potentially indicate increased productivity as well, and it is possible that this is the case for the two peaks in Mn/Ca at CM6.

5.1.3 *G. Trilobus* Mg/Ca palaeothermometry

No Mg/Ca temperature calibration exists for *G. trilobus* however in the modern ocean *G. trilobus* is considered to be the same species as *Globigerinoides sacculifer* (although the peculiar sack like form of the final chamber of *G. sacculifer* did not develop until the Pliocene (Hemleben et al., 1989)). It is a calibration for *G. sacculifer* that is used here (Rosenthal and Lohmann, 2002). A value of 4.2 is used for Miocene seawater Mg/Ca (Mg/Ca_{sw}; Wilkinson and Algeo, 1989) to correct for the effect of a changing seawater ratio over time. In order to correct for the effects of dissolution a

term is included in the calibration based on dissolution related variations of Mg/Ca in *G. sacculifer* (Rosenthal and Lohmann, 2002), this removes the weak correlation seen between Mg/Ca and shell weight ($r=0.19$, $n=22$, $p>0.05$).

Foraminiferal shell weight has been proposed as a proxy for atmospheric CO_2, on the basis of culture and core-top studies (Bijma et al., 1999; Barker and Elderfield, 2002; Bijma et al. 2002). If applied to the foraminiferal weight data presented here (Figure 29; Table 5) then it would suggest a decrease in $[CO_3^{2-}]$ and an increase in atmospheric CO_2 from 13.87 to 13.78 Ma as shell weights declined and the SST record shows a cooling, and then a slight decrease in CO_2 from 13.78 to 13.63 Ma. However more recently it has been suggested that $[CO_3^{2-}]$ may not be the primary control on foraminiferal weight (Beer et al. 2010). Furthermore the proxy relies on surface water processes being the dominant control of foraminiferal weights, the control preferred here is minor post-depositional dissolution, and as such it is used to correct for dissolution effects in the Mg/Ca SST calibration.

The pre-exponential term is adjusted slightly to cross calibrate with the ketone unsaturation index ($U^{K'}_{37}$) presented below (Figure 29; Table 5) to account for Miocene-Recent changes to *G. trilobus* vital effects. This is achieved by altering the pre-exponential term so that the mean calculated SST from Mg/Ca matches the mean SST calculated from $U^{K'}_{37}$ for the two younger points in the $U^{K'}_{37}$ record where both Mg/Ca and alkenone data is available (at 13.286 and 13.041 Ma), and where $U^{K'}_{37}$ is well below 1. It is possible that the ketone unsaturation index based temperatures relate to a slightly different part of the water column, but as one of the key uses for the temperature record produced here is to correct for temperature dependent effects in alkenone fractionation, it is more appropriate here to use temperatures which more

closely relates to the temperatures at which the alkenones are being synthesised. The cross calibration does not affect the sensitivity of the changes in Mg/Ca to temperature, and so conclusions based on the relative change in temperature recorded by the Mg/Ca record are not affected. The full calibration is shown in equation (7).

$$Mg/Ca = \left[\frac{Mg/Ca_{(t)}}{Mg/Ca_{(0)}}\right] \cdot (0.0032wt + 0.27) \cdot e^{0.095T} \qquad (7)$$

$Mg/Ca_{(t)}$ = Miocene seawater concentration = 4.2 (Wilkinson and Algeo, 1989)
$Mg/Ca_{(0)}$ = Modern ocean seawater concentration = 5.2
wt = Shell weight (μg)

Table 5: Ketone unsaturation index SST, Mg/Ca ratios, Mg/Ca SST and mean foraminifera weight for *G. trilobus* from RIP.

Height in section (m)	Age (Ma)	$U^{K'}_{37}$	$U^{K'}_{37}$ SST (Muller et al. 1998)	Mg/Ca ratio (mmol/mol)	Mg/Ca SST (°C)	Mean foram. weight (μg)
0.00	13.867	1	29.0*	6.56	33.1	24.4
0.35	13.860	1	29.0*	5.74	31.7	24.2
0.70	13.852	1	29.0*	5.03	30.4	23.6
1.05	13.844	1	29.0*	5.17	31.2	18.0
1.75	13.829	1	29.0*	5.43	30.9	26.6
2.45	13.813	1	29.0*	4.22	28.5	23.6
2.80	13.805			4.79	30.5	17.6
3.15	13.798	1	29.0*	5.00	30.7	19.4
3.50	13.780	1	29.0*	4.13	29.2	14.4
3.85	13.780	1	29.0*	4.78	30.2	20.1
4.90	13.751	0.909	26.2	4.97	31.0	16.5
5.25	13.742	0.985	28.5	4.38	29.3	19.5
5.60	13.732	0.987	28.6	4.72	30.2	18.4
6.65	13.703	1	29.0*	3.71	27.3	22.0
7.35	13.684	0.981	28.4	4.29	29.2	19.0
7.70	13.674	1	29.0*	4.39	29.4	18.6
8.05	13.665	1	29.0*	4.36	29.0	22.1
9.10	13.636	1	29.0*	4.36	29.2	19.8
9.45	13.627	1	29.0*	4.09	28.5	20.3
10.15	13.607	0.979	28.3			
10.50	13.598			4.52	29.6	19.9
22.75	13.286	0.964	27.9	3.92	28.0	21.1
33.95	13.041	0.978	28.3	3.86	28.1	18.5
43.05	12.800	0.987	28.6			

*At temperatures greater than 29°C only the di-unsaturated alkenone remains, and so these temperatures should be considered minimum estimates.

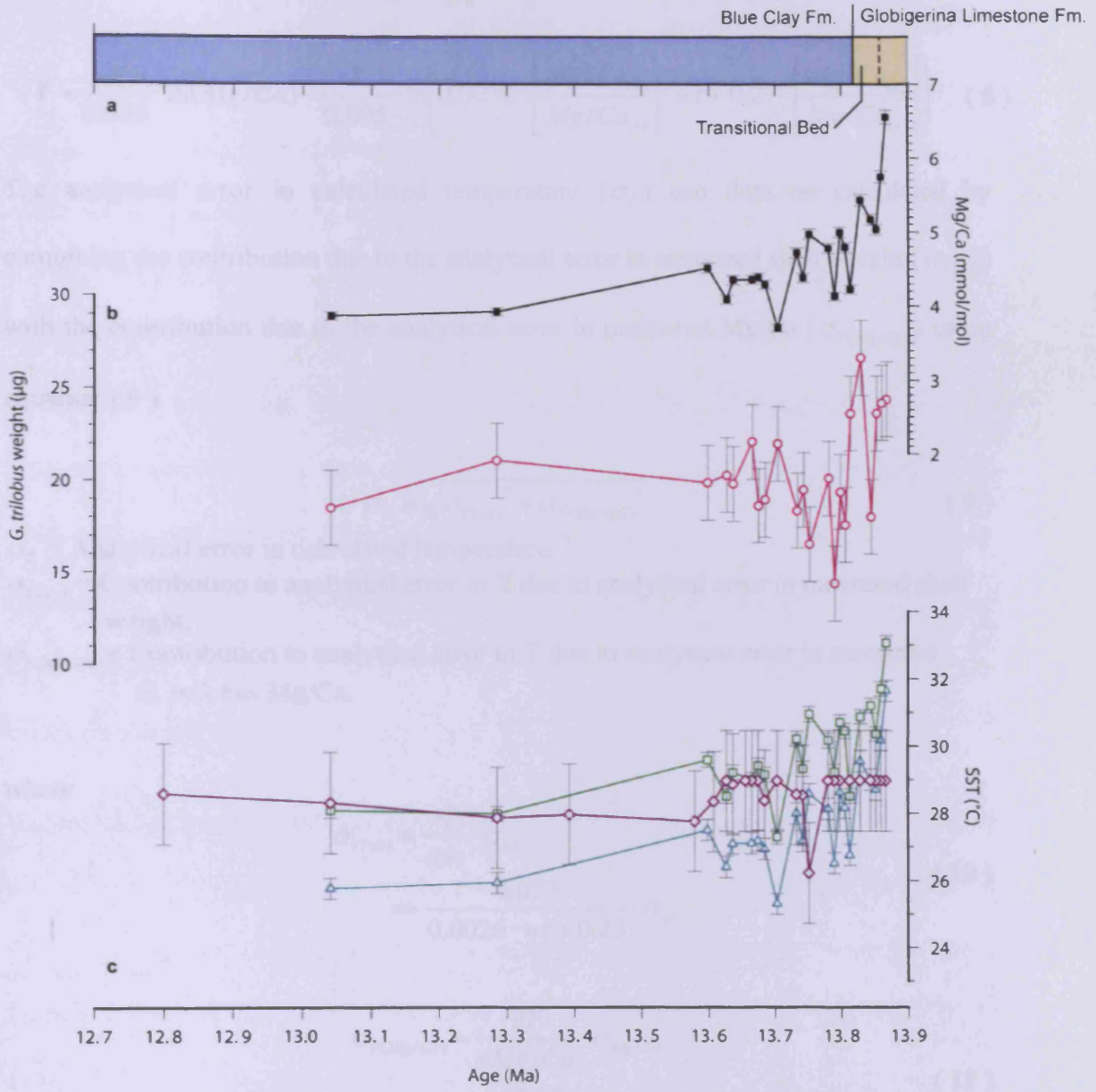

Figure 29: *G. trilobus* Mg/Ca ratio (panel a; black filled squares) and mean shell weight (panel b; open pink circles). Panel c shows the sea surface temperature reconstructions based on $U^{K'}_{37}$ (purple open diamonds) and the Mg/Ca calibration from this work (green open triangles; equation (7)) and the multi-species calibration of Anand et al. (2003). Error bars represent analytical errors and are 2σ.

Analytical errors (based on repeat measurement of consistency standards) for Mg/Ca and foraminiferal weight are shown in Figure 29 and are propagated through to analytical error in T using equations (8) to (11). Equation (7) is first rearranged to the form of equation (8)

$$T = \frac{1}{0.095} \cdot \ln(Mg/Ca) - \frac{1}{0.095} \cdot \ln\left(0.0032 \cdot \left[\frac{Mg/Ca_{(0)}}{Mg/Ca_{(t)}}\right] \cdot wt + 0.27 \cdot \left[\frac{Mg/Ca_{(0)}}{Mg/Ca_{(t)}}\right]\right) \quad (8)$$

The analytical error in calculated temperature (σ_T) can then be calculated by combining the contribution due to the analytical error in measured shell weight ($\sigma_{T(wt)}$) with the contribution due to the analytical error in measured Mg/Ca ($\sigma_{T(Mg/Ca)}$) using equation (9)

$$\sigma_T = \sqrt{\sigma_{T(wt)}^2 + \sigma_{T(Mg/Ca)}^2} \quad (9)$$

σ_T = Analytical error in calculated temperature
$\sigma_{T(wt)}$ = Contribution to analytical error in T due to analytical error in measured shell weight.
$\sigma_{T(Mg/Ca)}$= Contribution to analytical error in T due to analytical error in measured *G. trilobus* Mg/Ca.

where

$$\sigma_{T(wt)} = \frac{\partial T}{\partial wt} \cdot \sigma_{wt} \Rightarrow \frac{0.027}{0.0026 \cdot wt + 0.23} \cdot \sigma_{wt} \quad (10)$$

$$\sigma_{T(Mg/Ca)} = \frac{\partial T}{\partial Mg/Ca} \cdot \sigma_{Mg/Ca} \Rightarrow \frac{10.53}{Mg/Ca} \cdot \sigma_{Mg/Ca} \quad (11)$$

σ_{wt}= Analytical error in measured shell weight
$\sigma_{Mg/Ca}$=Analytical error in measured *G. trilobus* Mg/Ca

This results in an analytical uncertainty in Mg/Ca SST of ~0.2°C (2σ). It is important to note that this only represents the analytical uncertainty, and does not account for uncertainty relating to the calibration, nor arising due to the value chosen for Miocene Mg/Ca_{sw}. Uncertainty from scatter in Mg/Ca calibrations are reported to be equivalent to ±1.1 – 1.4°C (Dekens et al., 2002; Anand et al., 2003), and although models of

Mg/Ca_{sw} agree that this parameter was lower in the Miocene than the present, the exact value is model dependent and varies from 3.5 – 4.2 mmol/mol (Wilkinson and Algeo, 1989; Stanley and Hardie, 1998). This range in Mg/Ca_{sw} is equivalent to a ~2°C range in absolute temperature and given the long residence time of Ca and Mg (13 and 1 Myrs respectively; Broecker and Peng, 1982) Mg/Ca_{sw} is not expected to change significantly over the period which RIP covers (1.1 Myrs). Therefore the uncertainty surrounding Mg/Ca_{sw} only effects the absolute temperature, not the relative change over the period covered. This uncertainty is, in effect, removed by the cross-calibration between Mg/Ca and $U_{37}^{K'}$ described above, as $U_{37}^{K'}$ is unaffected by changes in Mg/Ca_{sw}. However the $U_{37}^{K'}$ reconstruction has an uncertainty of approximately ±1.5°C, but again, this only affects the absolute temperature, not the dramatic change in temperature seen here.

Reconstructed temperatures are high (Figure 30 and Table 5), ranging from 27.3°C to a maximum of 33.1°C (compared to a modern day mean zonal average for 35°N of ~20°C; Locarnini et al., 2006) in agreement with temperature estimates from elsewhere suggest that the Miocene ocean was significantly warmer than today (Lear et al., 2000; Shevenell et al., 2004).

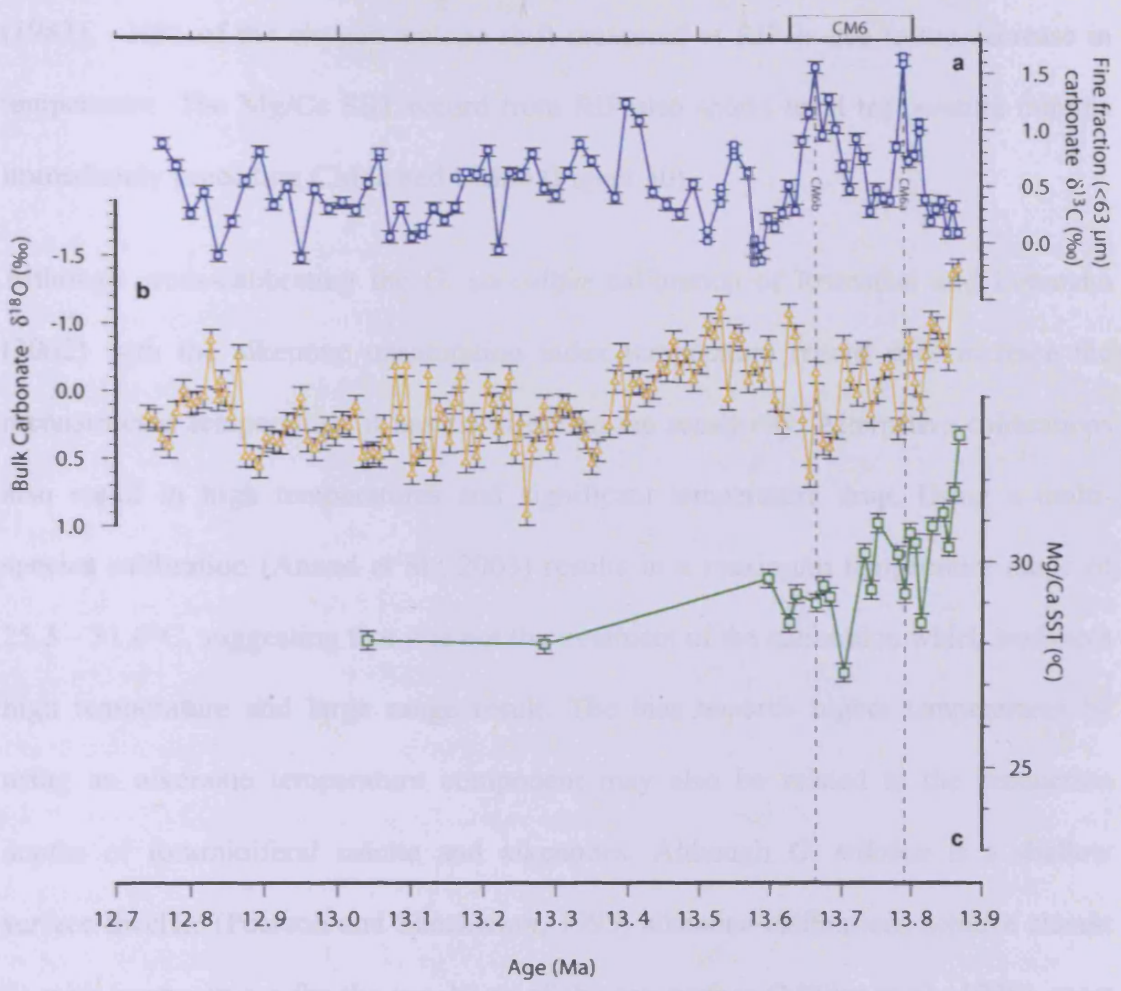

Figure 30: Sea surface temperature reconstruction from Mg/Ca ratios in the planktonic foraminifera *G. trilobus* (c; green open squares and line), shown with bulk carbonate oxygen isotopes (b; yellow open triangles and line) and fine fraction carbonate carbon isotopes (a; blue open squares and line). The reconstruction shows a dramatic drop in sea surface temperature as the ice sheet expansion progressed. The position of CM6 is indicated, with the individual peaks of CM6 a and b shown by the dashed lines.

The Mg/Ca SST record also shows a significant drop in temperature during and following the ice sheet expansion at Mi-3/E3, (a drop of around 5°C). Large drops in sea surface temperature have also been recorded at this time at other sites, including a 7°C (point to point) drop in sea surface temperatures in the southwest Pacific and 2-3°C of bottom water temperature decrease (Shevenell et al., 2004; Shevenell et al., 2008). The dramatic drop in temperature also matches a similar steep increase in oxygen isotopes. Using the oxygen isotope temperature sensitivity of Erez and Luz

(1983), ~30% of the oxygen isotope shift measured at RIP is due to the decrease in temperature. The Mg/Ca SST record from RIP also shows local temperature minima immediately preceding CM6a and CM6b (Figure 30).

Although cross-calibrating the *G. sacculifer* calibration of Rosenthal and Lohmann (2002) with the alkenone unsaturation index temperature record does increase the reconstructed temperature, it has no effect on the sensitivity. Alternative calibrations also result in high temperatures and significant temperature drop. Using a multi-species calibration (Anand et al., 2003) results in a maximum temperature range of 25.3 – 31.6°C, suggesting that it is not the treatment of the calibration which leads to a high temperature and large range result. The bias towards higher temperatures by using an alkenone temperature component may also be related to the production depths of foraminiferal calcite and alkenones. Although *G. trilobus* is a shallow surface dweller (Pearson and Shackleton, 1995) alkenone calibrations achieve closest fit with temperatures for the top 10 m of the sea surface (Müller et al., 1998), most likely shallower than the habitat of *G. trilobus*. Similarly, although sediment studies show best fit with mean annual temperature, it is possible that the alkenones preserved at RIP could be dominated by a more seasonal signal biased towards warmer temperatures, as has been observed at some sites (Conte et al., 2006). In general this bias is not a drawback of using this calibration in this study, as one of the principle uses of the temperature record here is to control temperature effects within the calculation of pCO_2 from alkenones (see 5.2 below) and so a near surface and alkenone production temperature is what is required. However, this does mean that the temperature record presented here may not be directly comparable with other foraminiferal Mg/Ca SST estimates.

5.2 pCO_2 proxies: Alkenone Palaeobarometry

5.2.1 Introduction

The degree of carbon isotopic fractionation that takes place during photosynthesis (ε_p) is controlled by the concentration of dissolved CO_2, and it is this effect that is the basis of the alkenone palaeobarometer (Freeman and Hayes, 1992; Jasper and Hayes, 1990; Jasper et al., 1994). Culture experiments have demonstrated that the aqueous CO_2 concentration ($[CO_{2(aq)}]$) is a control on the carbon isotopic composition of the di-unsaturated alkenone with 37 carbon atoms ($C_{37:2}$) that is produced ($\delta^{13}C_{37:2}$) (Bidigare et al., 1997; Laws et al., 1995; Popp et al., 1998; Riebesell et al., 2000a). The proxy has been used to reconstruct atmospheric CO_2 over the Pleistocene (Andersen et al., 1999; Jasper and Hayes, 1990; Jasper et al., 1994) and Neogene (Henderiks and Pagani, 2007; Pagani et al., 1999a; Pagani et al., 1999b; Pagani et al., 2005a), and critical appraisals of the proxy have suggested that it is a robust indicator of atmospheric CO_2 so long as variations from secondary controls (e.g. growth rate, cell size) are minor (Pagani, 2002; Pagani et al., 2002).

Although produced by both coccolith and non-coccolith bearing haptophytes, alkenone production appears to be restricted to the family Noelaerhabdaceae (Marlowe et al., 1990; Volkman, 2000). This restriction to a small group of organisms reduces the likely effects of interspecific offsets, and also reduces the opportunity for ecological changes to significantly affect the isotopic composition of the alkenones preserved in the fossil record.

The basis of the barometer is to first reconstruct ε_p and then use an empirical relationship between ε_p and $[CO_{2(aq)}]$ to estimate $[CO_{2(aq)}]$ before calculating atmospheric pCO_2. In order to calculate ε_p the first step is to adjust the analysed

alkenone result for the fractionation between the alkenone molecules and haptophyte biomass ($\varepsilon_{alkenone}$; equation (12); Bidigare et al., 1997; Popp et al., 1998).

$$\varepsilon_{alkenone} = \left[\frac{\delta^{13}C_{37:2} + 1000}{\delta^{13}C_{org} + 1000} - 1\right] \cdot 10^3 \qquad (12)$$

$\delta^{13}C_{37:2}$ = Carbon isotopic composition of di-unsaturated C_{37} alkenone
$\delta^{13}C_{org}$ = Carbon isotopic composition of haptophyte biomass

Assuming an ε value of 4.2 (Bidigare et al., 1997; Popp et al., 1998), the haptophyte biomass composition can then be calculated using equation (13) (Pagani et al 1999a).

$$\delta^{13}C_{org} = \frac{\delta^{13}C_{37:2} + 1000}{0.9958} - 1000 \qquad (13)$$

In order to calculate the fractionation between the haptophyte biomass and $[CO_{2(aq)}]$, the carbon isotopic composition of the aqueous carbon dioxide ($\delta^{13}C_{CO2(aq)}$) needs to be known. This is calculated by determining the $\delta^{13}C$ of carbonate from planktonic foraminifera and then using an empirical relationship for the fractionation between calcite and CO_2 (Romanek et al., 1992) .

$$\varepsilon_{calcite-CO_2(g)} = 11.98 - 0.12T \qquad (14)$$

T = Temperature in degrees Celsius (derived from planktonic foraminiferal Mg/Cal see section 5.1.1)

From equation (14) the carbon isotopic value of gaseous carbon dioxide can be calculated using equation (15).

$$\delta^{13}C_{CO_2(g)} = \frac{\delta^{13}C_{carbonate} + 1000}{\varepsilon_{calcite-CO_2(g)} / 1000 + 1} - 1000 \qquad (15)$$

Using the empirical relationship of (Mook et al., 1974; equation (16)) from this the carbon isotopic composition of aqueous carbon dioxide can be calculated (equation (17)).

$$\varepsilon_{CO_2(aq)-CO_2(g)} = \frac{-373}{T+273.15} + 0.19 \qquad (16)$$

$$\delta^{13}C_{CO_2(aq)} = \left[\frac{\varepsilon_{CO_2(aq)-CO_2(g)}}{1000} + 1\right] \cdot \left[\delta^{13}C_{CO_2(g)} + 1000\right] - 1000 \qquad (17)$$

Finally from this ε_p can be calculated (equation (18)).

$$\varepsilon_p = \left[\frac{\delta^{13}C_{CO_2(aq)} + 1000}{\delta^{13}C_{org} + 1000} - 1\right] \cdot 10^3 \qquad (18)$$

this calculated ε_p value, and assuming a value of 25 for the isotopic fractionation imparted during carbon fixation (ε_f) the concentration of carbon dioxide can be calculated (Bidigaire et al., 1997; Laws et al., 1997).

$$[CO_{2(aq)}] = \frac{b}{\varepsilon_f - \varepsilon_p} \qquad (19)$$

b = the summation of all physiological factors (see text for discussion and definition)

The empirically derived "b" relates to the summation of all physiological factors that can further affect the isotopic composition of the alkenones. For reconstructions of ancient atmospheric carbon dioxide b is generally estimated by relating it to the concentration of nutrients in the water column (Pagani et al., 1999a; Pagani et al., 1999b; Pagani et al., 2005a), and for convenience an empirical relationship between b and the dissolved concentration of phosphate ($[PO_4^{3-}]$) is used (Pagani et al., 2005a). Here a modern day Mediterranean value for $[PO_4^{3-}]$ (Garcia et al., 2006) is assumed.

$$b = 118.52 \cdot [PO_4^{3-}] + 84.07 \qquad (20)$$

Equilibrium between the atmosphere and surface ocean is assumed. Using a temperature dependent relationship (equation (21)) for Henry's constant and the solubility constants listed in Table 6 (Weiss, 1970; Weiss, 1974), atmospheric CO_2 can be calculated (equation (22)).

$$\ln K_H = A_1 + A_2(100/T) + A_3 \ln(T/100) + S[B_1 + B_2(T/1000 + B_3(T/100)^2] \quad (21)$$

K_H = Henry's constant
T = Temperature in Kelvin
S =Salinity

Table 6 Solubility Constants (mol.L^{-1}; Weiss, 1970; Weiss, 1974)

A_1	-58.0931
A_2	90.5069
A_3	22.2940
B_1	0.027766
B_2	-0.025888
B_3	0.0050578

$$pCO_2 = \frac{[CO_{2(aq)}]}{K_H} \quad (22)$$

5.2.2 Assumptions and uncertainty modelling

In order to calculate the carbon isotopic composition of dissolved carbon dioxide as shown above, carbonate carbon isotope measurements are used. Previous pCO_2 reconstructions (Henderiks and Pagani, 2007, 2008; Pagani et al., 1999a; Pagani et al., 1999b; Pagani et al., 2005a) have used foraminiferal calcite to perform this role, but inherent in this are two potential problems. Firstly, as few individuals go into each analysis, the inter-test variability means that the signal to noise ratio for foraminiferal

analysis is greater than for bulk or fine fraction carbonate analysis, which samples a large number of individuals and has contributions from coccolith and other carbonate debris. This effect can be seen in the much smoother records produced and replicated in shape by the fine fraction and bulk carbonate isotope records compared to the foraminiferal records. The approach here therefore is to take the fine fraction $\delta^{13}C$ record, and estimate the foraminiferal isotopic composition by simply adding the mean offset between the fine fraction and foraminiferal calcite records over CM6 (Pagani et al., 2005a). Secondly, in deriving the value of $\delta^{13}C_{CO2(g)}$ an empirical relationship is used (equation (14)) which is based upon experiments performed on abiotic calcite (Romanek et al., 1992). This may introduce error into the calculation if foraminiferal calcite fractionation differs from abiotic calcite. The effect of this is likely to be fairly minor, and will only affect the validity of absolute estimates, not any trends that are recognised. Continued use of this relationship (equation (14)) also means that the data produced here are directly comparable with previously published longer term and lower resolution records of Miocene pCO_2 (Pagani et al., 1999a).

The alkenone palaeobarometry proxy outlined above assumes that $[CO_{2(aq)}]$ is the only factor controlling alkenone $\delta^{13}C$. However other factors have also been shown to exert a controlling influence. Culture experiments have demonstrated that further factors are important to the eventual $\delta^{13}C$ of the alkenones produced; growth rate (Bidigare et al., 1997; Laws et al., 1997; Laws et al., 1995) cell size and cell carbon content relative to surface area (Burkhardt et al., 1999; Popp et al., 1998) and light intensity (Cassar et al., 2006; Rost et al., 2002). These factors combined are included in the factor "b" (equation (19)) which is determined through culture experiments

Attempts have been made recently to estimate the effects of changing cell size on CO_2 records generated using the alkenone palaeobarometer (Henderiks and Pagani, 2007, 2008). These records have demonstrated that changes in cell size likely do occur, and that they can occur quite rapidly (over less than 1 Myrs). However, the magnitude of the changes in cell sizes did not have a significant effect on the CO_2 records studied by Henderiks and Pagani (2007) and the corrected records they produced were generally within the error of the original CO_2 reconstructions. These records show that although there may be cases where rapid and dramatic changes in cell size (such as a major evolutionary event) could be responsible for changes in the alkenone $\delta^{13}C$ record rather than changes in CO_2, generally speaking the required adjustment to pCO_2 records is small (Henderiks and Pagani, 2007). Furthermore, Popp et al. (1998) demonstrate that the relationship with between $\delta^{13}C_{37:2}$ and cell geometry is controlled by the cell volume to surface area ratio. Modern haptophyte producing coccolithophores have close to perfect spherical cell geometry, and so changes in the cell diameter would have a small effect on the volume to surface area ratio. The large variation in ε_p seen in cell geometry culture experiments have been performed using diatoms, and the shapes of these organisms mean that variation in cell diameter changes the volume to surface area ratio more dramatically than is the case for coccolithophores (Laws et al., 1997)

5.2.3 Growth rate estimation using Sr/Ca ratios in calcite

Growth rate reconstructions have been attempted using coccolithophores Sr/Ca ratios (Rickaby et al., 2002; Stoll et al., 2002a; Stoll et al., 2001; Stoll and Schrag, 2000; Stoll et al., 2002b). Sr/Ca ratios can be used with a record of seawater Sr/Ca to estimate the Sr distribution coefficient (D_{Sr}) that has been used to reconstruct growth rates (Billups et al., 2004). There is no correlation between growth rate as recorded by

D_{Sr} and the ε_p record generated from alkenone $\delta^{13}C$ (r=0.08, n=20, p>0.05, Figure 31) at RIP.

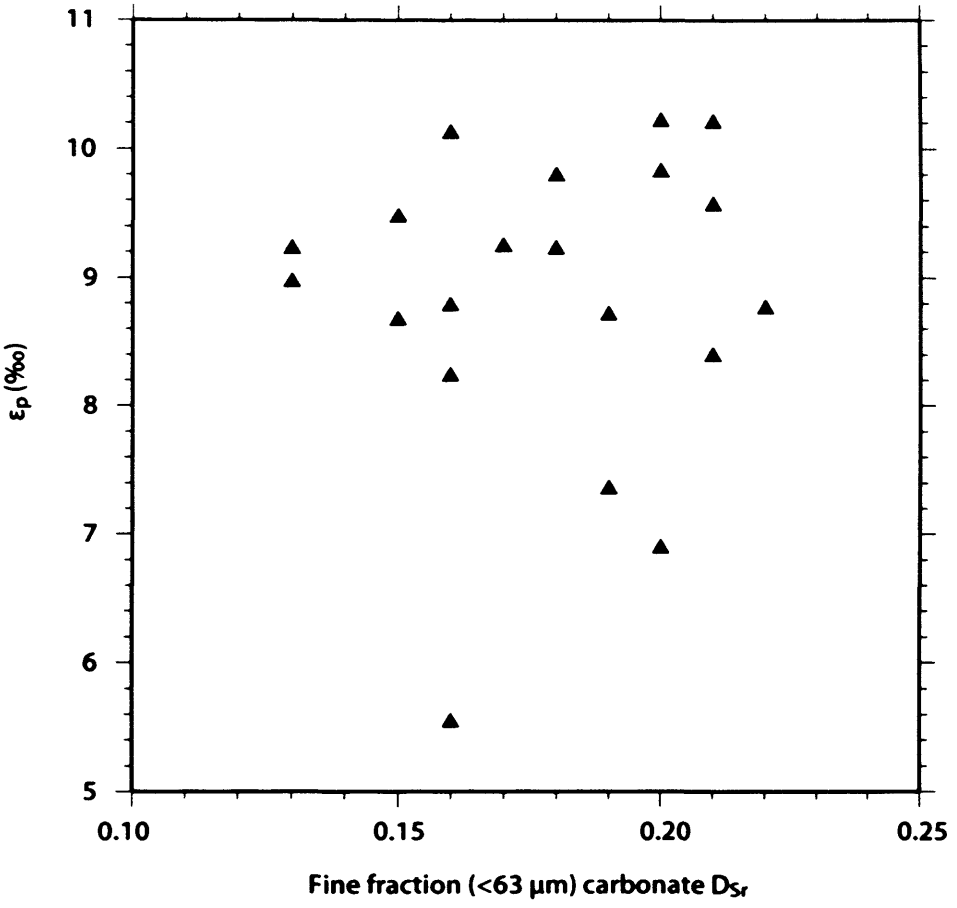

Figure 31: No correlation is observed between D_{Sr} (a potential indicator of growth rate) and ε_p as reconstructed from alkenone $\delta^{13}C$.

This suggests that either D_{Sr} is not indicating growth rates, or that growth rates are not a significant influence on ε_p. It is possible that growth rate was not an important factor for carbon fractionation in organic matter production in the species producing alkenones in the middle Miocene, as it has been found that not all algal species show a correlation between growth rates and ε_p (Burkhardt et al., 1999).

5.2.4 Uncertainty Modelling

Uncertainty in the CO_2 calculation detailed above was modelled using the Monte Carlo method (e.g. Anderson (1976)). The Monte Carlo method has advantages over

classical propagation or regression analysis in that the nature of uncertainties of the different input parameters can be treated differently. For example for input parameters, which are not measured but have been estimated (for example the phosphate concentration and salinity, both of which are effectively educated guesses based upon modern day parameters in the Mediterranean near to RIP; Garcia et al., 2006; Locarnini et al., 2006) a probability distribution function (PDF) which take this into account can be selected. For these two parameters square functions were chosen, which gives equal likelihood for any value within the given range. For the remaining parameters where values are based upon analysis, a normal PDF was used, with standard deviations derived from analytical uncertainty. An 11% uncertainty in the slope and intersect of the regression of equation (20) was included in the model and represents a 95% confidence interval about the correlation (Pagani et al., 1999a).

The output of the Monte Carlo calculation is an array of data representing an approximation of the probability density function of the CO_2 calculation given the input variables. As variables for each run within the Monte Carlo calculation are randomly selected (on the basis of the PDF of each variable) the approximation of the PDF of the CO_2 calculation approaches the true PDF as a greater number of runs are included.

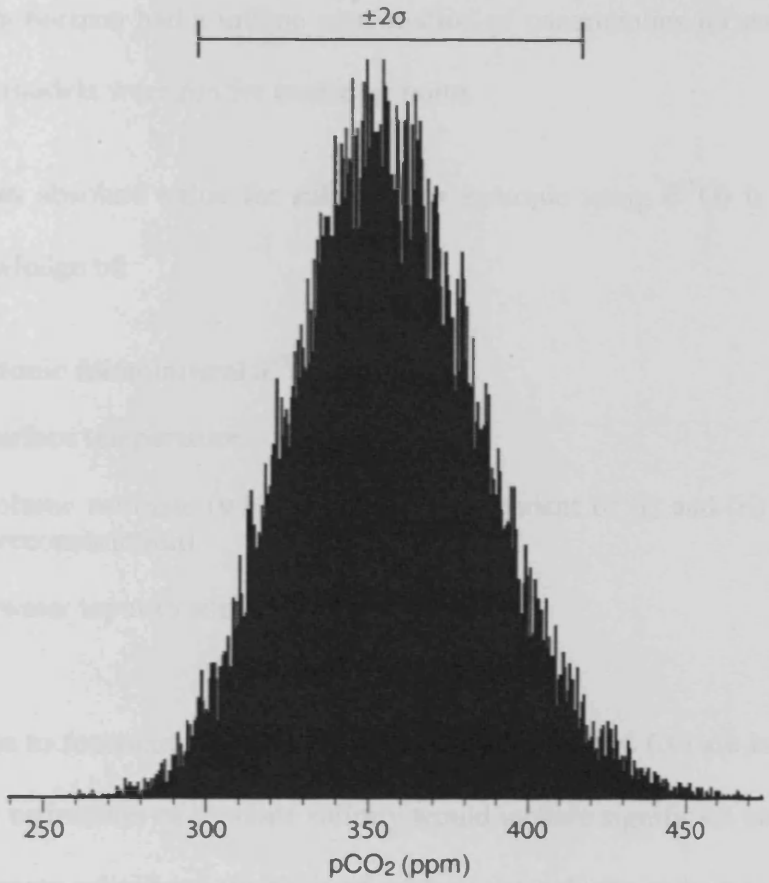

Figure 32: A typical output histogram of a Monte Carlo model of uncertainty within the calculation of pCO_2. Mean CO_2 is 357 ppm, with a 2σ value of 60 ppm from a model with n=25,000 and a bin size of 0.5 ppm.

With modern computer hardware each run takes a fraction of a second to calculate using appropriate software (MATLAB was used throughout the Monte Carlo modelling) and so a large number of runs can easily be included. The degree to which the approximation fits the true PDF can be estimated on the basis of the shape of the spread of the data array (which can be estimated by the shape of a histogram), the closeness of the mean value of the data array to the calculated value of CO_2 using actual parameters, and the "stability" of the mean and standard deviation upon repeated application of the Monte Carlo model. A model with 25,000 runs was found to be a good balance between stability of the standard deviation and computational

time. As each horizon had a unique combination of uncertainties for each parameter, Monte Carlo models were run for each data point.

Calculating an absolute value for salinity (for example using $\delta^{18}O$) is difficult, and requires knowledge of:

i. Planktonic foraminiferal $\delta^{18}O$.
ii. Sea surface temperature.
iii. Ice volume estimate (which must be independent of (i) and (ii) e.g. from sea level reconstruction).
iv. Freshwater input to site.

Although data to reconstruct (i) and (ii) is available, (iii) and (iv) are lacking, and so therefore any estimation of absolute salinity would include significant uncertainty. We therefore estimate salinity on the basis of modern day salinity at the site. It is possible however to quantitatively estimate *variability* in salinity during the period of interest, and use this to inform the uncertainty modelling. It is possible to estimate salinity variations using the oxygen isotope composition of seawater ($\delta^{18}O_{sw}$). $\delta^{18}O_{sw}$ can be estimated if an independent reconstruction of seawater temperature is available (Erez and Boaz, 1983; equation (23)) .

$$SST = 17.0 - 4.52 \cdot (\delta^{18}O_{cc} - \delta^{18}O_{sw}) + 0.03 \cdot (\delta^{18}O_{cc} - \delta^{18}O_{sw})^2 \qquad (23)$$

$\delta^{18}O_{cc}$ =planktonic foraminiferal oxygen isotopic composition
SST = Sea surface temperature

Using the SST reconstruction from foraminiferal Mg/Ca and $\delta^{18}O_{cc}$ from *G. trilobus* it is therefore possible to estimate $\delta^{18}O_{sw}$ (Figure 33, Data Table 7).

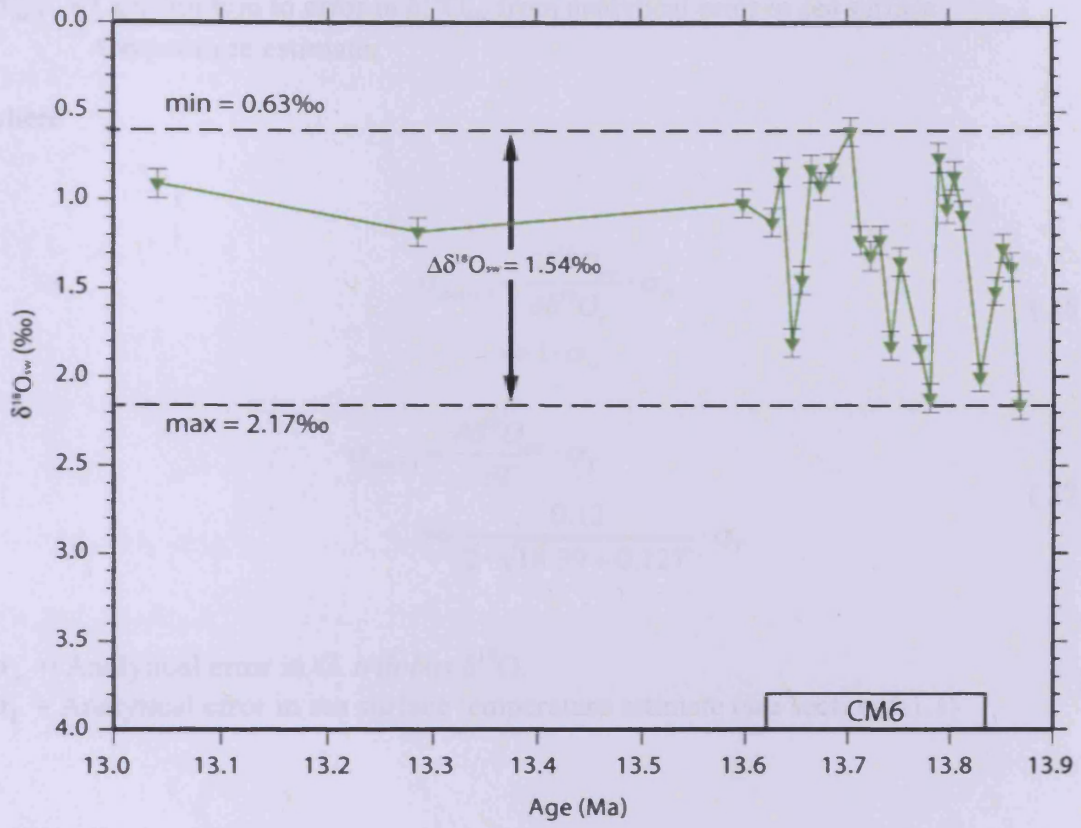

Figure 33: Reconstruction of $\delta^{18}O_{sw}$ from *G. trilobus* $\delta^{18}O$ and Mg/Ca SST reconstructions.

To calculate the analytical error in $\delta^{18}O_{sw}$ equation (23) must first be rearranged into the form of equation (24).

$$\delta^{18}O_{sw} = \delta^{18}O_{cc} - \left(\frac{4.52 \pm \sqrt{4.52^2 - 0.12 \cdot (17 - T)}}{0.06} \right) \qquad (24)$$

The analytical error is then calculated by considering the contribution of error due to the analytical error in T (see section 5.1.1) and the contribution of error due to analytical error in $\delta^{18}O_{cc}$ using equations (25) to (27).

$$\sigma_{sw} = \sqrt{\sigma_{sw(cc)}^{\ 2} + \sigma_{sw(T)}^{\ 2}} \qquad (25)$$

σ_{sw} = Analytical error in $\delta^{18}O_{sw}$.
$\sigma_{sw(cc)}$ = Contribution to error in $\delta^{18}O_{sw}$ from analytical error in *G. trilobus* $\delta^{18}O$.

$\sigma_{sw(T)}$ = Contribution to error in $\delta^{18}O_{sw}$ from analytical error in sea surface temperature estimate.

where

$$\sigma_{sw(cc)} = \frac{\partial \delta^{18}O_{sw}}{\partial \delta^{18}O_{cc}} \cdot \sigma_{cc} \Rightarrow 1 \cdot \sigma_{cc} \quad (26)$$

$$\sigma_{sw(T)} = \frac{\partial \delta^{18}O_{sw}}{\partial T} \cdot \sigma_T \Rightarrow \frac{0.12}{2 \cdot \sqrt{18.39 + 0.12T}} \cdot \sigma_T \quad (27)$$

σ_{cc} = Analytical error in *G. trilobus* $\delta^{18}O$.
σ_T = Analytical error in sea surface temperature estimate (see section 5.1.1)

This gives a maximum variability of $\delta^{18}O_{sw}$ of 1.54 ±0.08‰ (2σ). Seawater salinity can be estimated using equation (28) (Duplessy et al., 1991; Maslin et al., 1995) .

$$S = S_m + S_v + 1.735\delta_w^* \quad (28)$$

S = Salinity (‰)
S_m = Present mean ocean salinity
S_v = Mean ocean changes due to changing ice volume
δ_w^* = $\delta^{18}O_{sw}$ anomaly

So using the sensitivity from equation (28) it can be calculated that the maximum possible variability in surface water salinity is ±1.3‰. This is a maximum estimate as in reality most of this variability is likely due to changing ice volume. This treatment of $\delta^{18}O$ assumes that the sensitivity of $\delta^{18}O_{sw}$ to salinity has remained constant over time, which may not be a valid assumption (Rohling and Bigg, 1998; Schmidt, 1999). However given that the use here is to estimate a maximum change in salinity, and that much of the variability in $\delta^{18}O_{sw}$ will be due to ice volume rather than salinity, it

seems a useful exercise to apply such a relationship to gain some insight into maximum variability in salinity in this way.

5.2.5 Results

The alkenone isotopes show a slight positive trend over CM6 from 13.85 – 13.61 Ma, before a return to more negative values at 12.8 Ma (based on a single horizon) (Figure 34, Data Table 8). The positive carbonate $\delta^{13}C$ excursion recognised as CM6 in the carbonate records is not matched by a similar excursion in the alkenone record, and the twin peaks CM6a and CM6b are not evident either. The accuracy of alkenone isotope data means caution should be taken when interpreting finer scale variations in the record, however in closer detail it appears that the positive peaks of CM6a and CM6b in the carbonate record are mirrored by slight negative shifts in the alkenone records. The magnitude of variation in alkenone $\delta^{13}C$ is greater than that shown in the carbonate isotope record over the same period, which is similar to other records of alkenone and carbonate $\delta^{13}C$ (e.g. Pagani et al., 1999a) – even though CM6 is one of the largest short term fluctuations in carbonate $\delta^{13}C$ of the Cenozoic. The ε_p record produced from these records will therefore be dominated by the alkenone results (as has been seen in other ε_p records generated from alkenone $\delta^{13}C$ (Jasper and Hayes, 1990; Jasper et al., 1994; Pagani et al., 1999a)). The mean value of the alkenone $\delta^{13}C$ (-21.1‰) is similar to the values recorded in the longer-term records for this point in the Miocene from ODP Sites 608 and 730 (north Atlantic and Arabian sea respectively), and slightly lower than those seen at Site 588 (south-west Pacific; Pagani et al., 1999a). Using the procedure detailed in section 5.2.1, these data are converted into ε_p, shown in Figure 35 (Data Table 8).

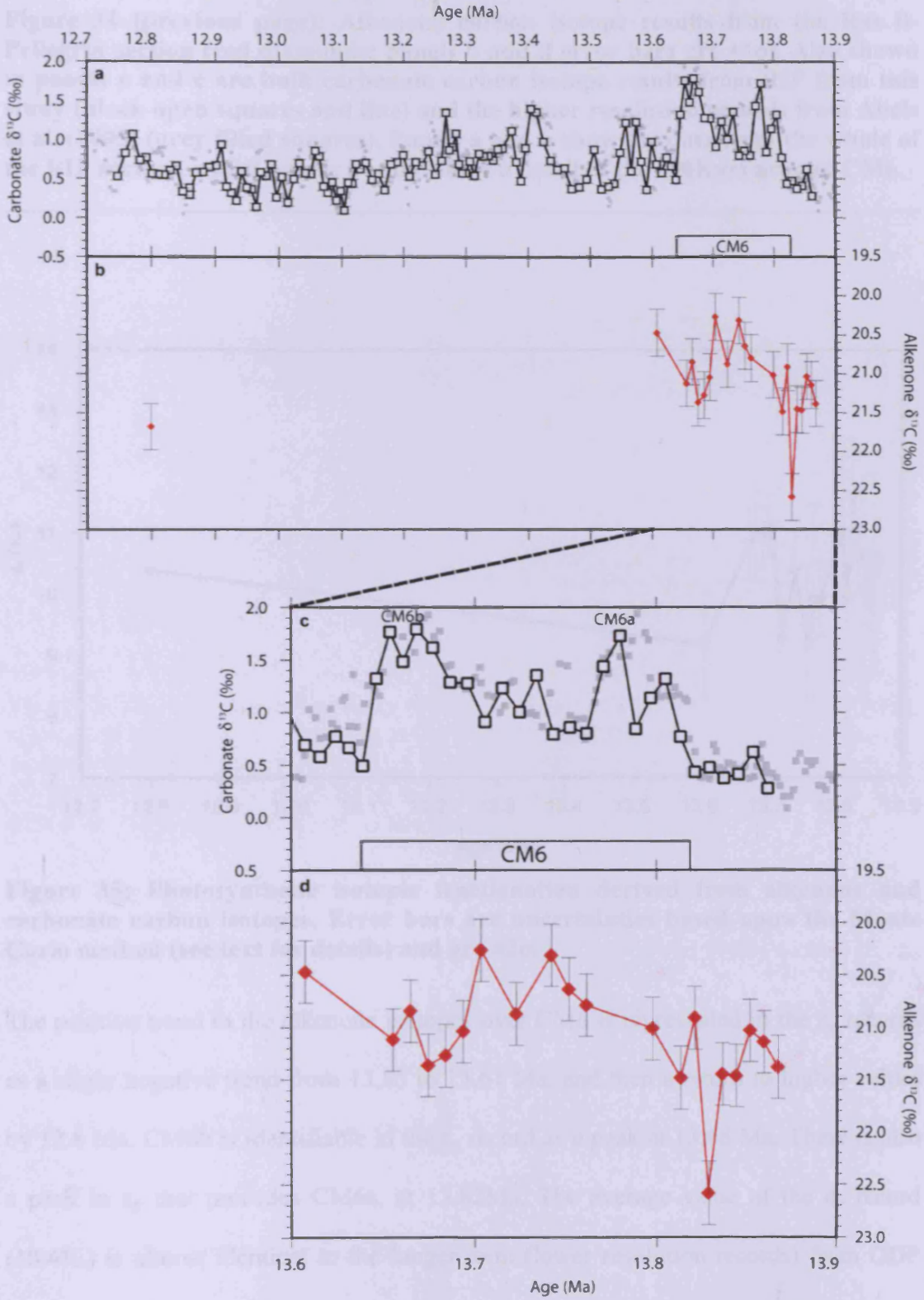

Figure 34 (previous page): Alkenone carbon isotope results from the Ras il-Pellegrin section (red diamonds; panels b and d error bars are ±1σ). Also shown in panels a and c are bulk carbonate carbon isotope results from RIP from this study (black open squares and line) and the higher resolution records from Abels et al. (2005) (grey filled squares). Panels a and b show the data from the whole of the RIP section, whilst panels c and d show a detail of the 300Kyrs around CM6.

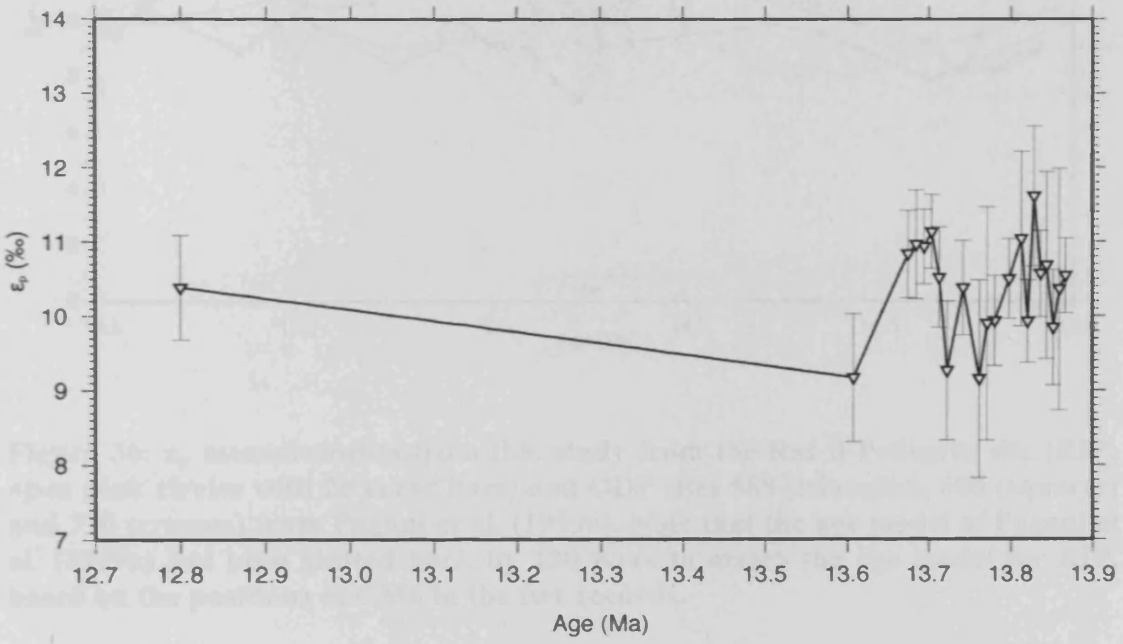

Figure 35: Photosynthetic isotopic fractionation derived from alkenone and carbonate carbon isotopes. Error bars are uncertainties based upon the Monte Carlo method (see text for details) and are ±2σ.

The positive trend in the alkenone isotopes over CM6 is represented in the ε_p records as a slight negative trend from 13.85 to 13.61 Ma, and then a return to higher values by 12.8 Ma. CM6b is identifiable in the ε_p record as a peak at 13.68 Ma. There is also a peak in ε_p that precedes CM6a, at 13.82Ma. The average value of the ε_p record (10.4‰) is almost identical to the longer term (lower resolution records) from ODP sites 608, 730 and 588; (Pagani et al., 1999a)) which were determined from oligotrophic regions. This similarity increases the confidence that growth rate effects were minimal at the RIP section, and that the reconstructed pCO_2 represents a global

atmospheric, rather than local ($[CO_{2(aq)}]$ out of equilibrium with the atmosphere) signal.

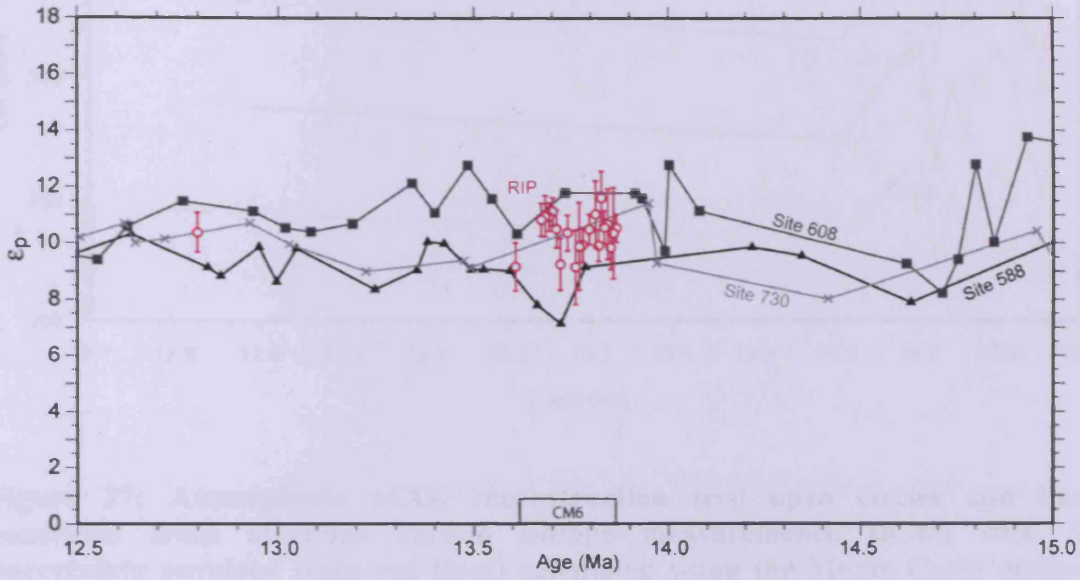

Figure 36: ε_p measurements from this study from the Ras il-Pellegrin site (RIP; open pink circles with 2σ error bars) and ODP sites 588 (triangles), 608 (squares) and 730 (crosses) from Pagani et al. (1999a). Note that the age model of Pagani et al. (1999a) has been shifted back by 130 Kyrs to match the age model for RIP, based on the positions of CM6 in the two records.

The CO_2 reconstruction shows fairly low levels of CO_2, with an average value of 302 ppm over the 1.1 Myrs represented by the RIP section (Figure 37, Data Table 8). This is higher than the previously published estimate for this period in the Miocene (Pagani et al., 1999a). The CO_2 record shows a slight (but significant) decrease in atmospheric CO_2 over the period of CM6, dropping from 328 ppm at 13.82 Ma to 275 ppm at 13.6 Ma, with a single analysis at 12.8 Ma showing similarly low levels.

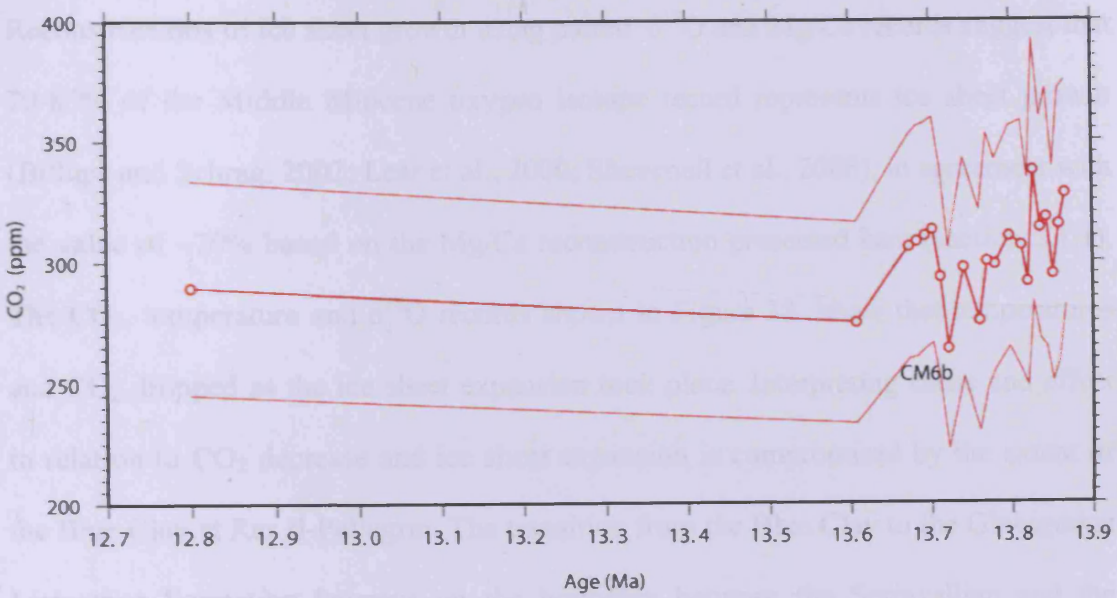

Figure 37: Atmospheric pCO_2 reconstruction (red open circles and line) generated from alkenone carbon isotope measurements, shown with 2σ uncertainty envelope (thin red lines) calculated using the Monte Carlo method (see section 5.2.4 for details).

The uncertainties discussed above mean that interpreting the finer scale variations in the CO_2 records should be done with caution. The 10 – 20 ppm variations are within the uncertainty of the reconstruction, however there is a possible peak in CO_2 following CM6b.

5.2.6 Discussion

The alkenone based CO_2 reconstruction is best interpreted in the full context of the multi-proxy records generated from the Ras Il-Pellegrin section. A compilation figure of climate proxy records is shown in Figure 38. The figure shows that both the decrease in temperature as recorded by the Mg/Ca proxy and the decrease in atmospheric CO_2 as shown by the alkenone proxy happen concurrent with the oxygen isotope increase, recorded at both RIP and globally, which represents the combination of ice sheet expansion and temperature drop.

Reconstructions of ice sheet growth using paired $\delta^{18}O$ and Mg/Ca records suggest that 70-85% of the Middle Miocene oxygen isotope record represents ice sheet growth (Billups and Schrag, 2002; Lear et al., 2000; Shevenell et al., 2008), in agreement with the value of ~70% based on the Mg/Ca reconstruction presented here (section 5.1.1). The CO_2, temperature and $\delta^{18}O$ records shown in Figure 38 show that temperatures and CO_2 dropped as the ice sheet expansion took place. Interpreting cause and effect in relation to CO_2 decrease and ice sheet expansion is compromised by the extent of the Blue Clay at Ras il-Pellegrin. The transition from the Blue Clay to the Globigerina Limestone Formation happens on the boundary between the Serravallian and the Langhian and the ice sheet expansion (E3/Mi-3) coincides with the boundary. The record from the Blue Clay at RIP is therefore limited to the period immediately following the ice sheet growth, and indeed the sea level and temperature variations were most likely important in determining the transition from the Globigerina Limestone to the Blue Clay. The Globigerina Limestone Formation is not as suitable for alkenone and other proxy records. The lowermost (oldest) samples from the RIP records presented here are from the transitional bed into the Globigerina Limestone Formation where the carbonate content increases significantly.

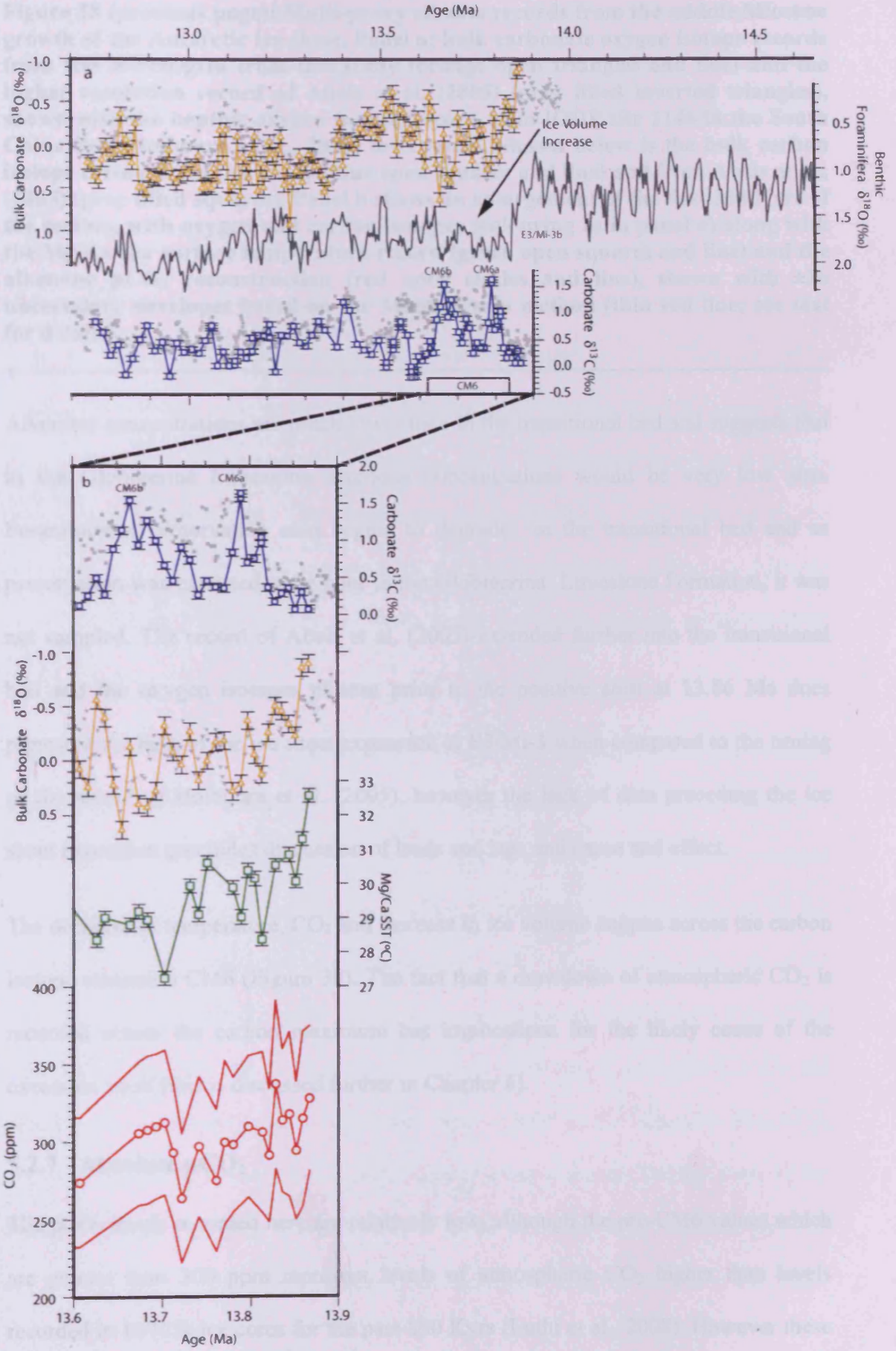
Age (Ma)
13.0
13.5
14.0
14.5
a
Bulk Carbonate δ18O (‰)
-1.0
-0.5
0.0
0.5
1.0
Ice Volume Increase
E3/Mi-3b
Benthic Foraminifera δ18O (‰)
0.5
1.0
1.5
2.0
CM6b
CM6a
CM6
Carbonate δ13C (‰)
1.5
1.0
0.5
0.0
-0.5
b
CM6b
CM6a
Carbonate δ13C (‰)
2.0
1.5
1.0
0.5
0.0
Bulk Carbonate δ18O (‰)
-1.0
-0.5
0.0
0.5
Mg/Ca SST (°C)
33
32
31
30
29
28
27
CO2 (ppm)
400
350
300
250
200
13.6
13.7
13.8
13.9
Age (Ma)

Figure 38 (previous page): Multi-proxy climate records from the middle Miocene growth of the Antarctic Ice sheet. Panel a; bulk carbonate oxygen isotope records from Ras il-Pellegrin from this study (orange open triangles and line) and the higher resolution record of Abels et al. (2005) (grey filled inverted triangles), shown with the benthic oxygen isotope record from IODP site 1146 in the South China Sea (Holbourn et al., 2005) for context. Shown below is the bulk carbon isotope record from this study (blue open squares and line) and from Abels et al., (2005) (grey filled squares). Panel b shows an enlargement of the first 300 Kyrs of the section, with oxygen and carbon isotopes (colouring as in panel a) along with the Mg/Ca sea surface temperature record (green open squares and line) and the alkenone pCO_2 reconstruction (red open circles and line), shown with $\pm 2\sigma$ uncertainty envelopes based on the Monte Carlo method (thin red line; see text for details).

Alkenone concentrations are much lower than in the transitional bed and suggests that in the Globigerina Limestone alkenone concentrations would be very low also. Foraminiferal preservation also begins to degrade in the transitional bed and as preservation was expected to be poor in the Globigerina Limestone Formation, it was not sampled. The record of Abels et al. (2005) extended further into the transitional bed and the oxygen isotopes plateau prior to the positive shift at 13.86 Ma does represent the bulk of the ice sheet expansion at E3/Mi-3 when compared to the timing of the record of Holbourn et al. (2005), however the lack of data preceding the ice sheet expansion precludes discussion of leads and lags and cause and effect.

The decrease in temperature, CO_2 and increase in ice volume happen across the carbon isotope excursion CM6 (Figure 38). The fact that a drawdown of atmospheric CO_2 is recorded across the carbon maximum has implications for the likely cause of the excursion itself (this is discussed further in Chapter 6).

5.2.7 Absolute pCO_2

The pCO_2 levels recorded here are relatively low, although the pre-CM6 values which are greater than 300 ppm represent levels of atmospheric CO_2 higher than levels recorded in EPICA ice cores for the past 800 Kyrs (Luthi et al., 2008). However these

values are close to the threshold required for sustained bipolar glaciation (DeConto et al., 2008) although the onset of northern hemisphere glaciation is not thought to be widespread before 11 Ma (Holbourn et al., 2005; Lea et al., 2000; Miller et al., 1991; Zachos et al., 2001).

Although low, the pCO_2 record presented here is not as low as that of Pagani et al. (1999a) (Figure 39). This record is also based on alkenones, from multiple sites, and as is discussed above, the ε_p record generated by Pagani et al. (1999a) is nearly identical in average value to the record presented here (Figure 36). The likely reason for the offset between the two pCO_2 records is due to the different temperature models used in each reconstruction. The temperature record is used to reconstruct the air-sea equilibrium, and using higher temperatures as reconstructed here results in a different air-sea equilibria which in turn results in higher absolute estimates of atmospheric pCO_2.

Pagani et al. (1999a) use a foraminiferal $\delta^{18}O$ approach to reconstruct the sea surface temperatures for their calculations. Post-depositional preservation effects at the type of deep-sea carbonate rich sites such as those used by Pagani et al. (1999a) can produce artificially cool temperature estimates if using foraminiferal oxygen isotopes for sea surface temperature reconstruction (Pearson et al., 2001). The clay-rich lithology at the Blue Clay of the Ras il-Pellegrin section has resulted in excellent preservation of the foraminifera used for our sea surface temperature reconstruction, suggesting that the temperature estimates presented here are more likely to be accurate. The pCO_2 estimates presented here are also very similar to other estimates for this point in the Miocene (Figure 39) from two independent proxy methods; boron isotopes (Pearson and Palmer, 2000) and stomatal indices from fossilised leaves (Kürschner et al., 2008).

The use of foraminiferal $\delta^{13}C$ to reconstruct $\delta^{13}C_{CO2(aq)}$ assumes that the foraminiferal calcite $\delta^{13}C$ is produced in equilibrium with seawater. However, the effect of algal symbionts in a species such as *G. trilobus* used here potentially results in calcite enriched in ^{13}C by up to 1.5‰ (Spero and Lea, 1993). To put this into context, a disequilibrium offset of +1.5‰ in $\delta^{13}C_{carbonate}$ would result in an overestimate in reconstructed atmospheric CO_2 by about 10% (e.g. within the uncertainty envelope shown in Figure 37). As the number of symbionts increases with test size, the size of any potential offset $\delta^{13}C$ also varies with test size (Spero and Lea, 1993), which could potentially affect the reconstructed trends in atmospheric CO_2 as well as the absolute levels. However the approach used here to determine $\delta^{13}C_{CO2(aq)}$ uses fine fraction carbonate $\delta^{13}C$ to reconstruct the trends in $\delta^{13}C$ over time, which should remove the potential for a foraminiferal size effect to influence reconstructed $\delta^{13}C_{CO2(aq)}$.

Similarly, diagenetic alteration can effect the preservation of original $\delta^{13}C$ in planktonic foraminiferal calcite (Pearson et al. 2001). This was part of the motivation of using the RIP section, as preservation effects are thought to be far less likely in the type of shallow water depth, clay rich sediments found at RIP (Pearson et al. 2001), and as expected the foraminiferal shells show exceptional preservation and diagenetic alteration of the $\delta^{13}C$ signal is not expected to have occurred.

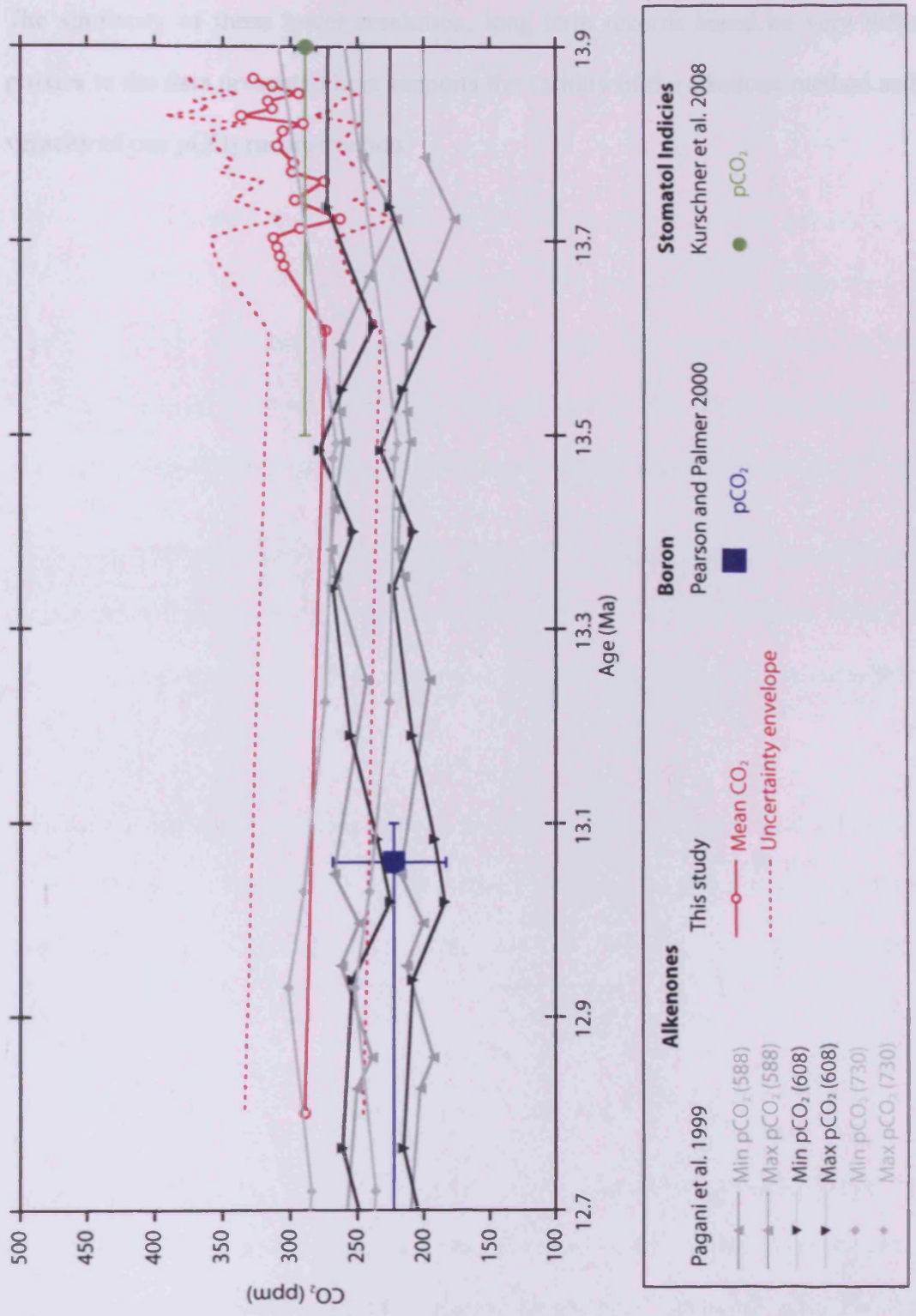

Figure 39: Atmospheric carbon dioxide reconstructions over the time period covered by the Ras il-Pellegrin section. The alkenone reconstruction of this study is shown along with published studies based on alkenone isotopes (Pagani et al., 1999a), boron isotopes (Pearson and Palmer, 2000) and the stomatal indices of fossilised leaves (Kürschner et al., 2008).

The similarity of these lower resolution, long term records based on very different proxies to the data presented here supports the validity of the alkenone method and the veracity of our pCO_2 reconstruction.

5.3 pCO_2 proxies: Coupled boron isotope and B/Ca ratios

5.3.1 Introduction

The ocean carbonate system can be described by six co-varying parameters; pH, $[CO_{2(aq)}]$, $[HCO_3^-]$, $[CO_3^{2-}]$, Total Alkalinity (TA) and Dissolved Inorganic Carbon (DIC). To fully constrain the system, two of these six parameters must be known, allowing $[CO_{2(aq)}]$ to be calculated, and through Henry's law (assuming surface water-atmosphere equilibrium) atmospheric pCO_2 can be calculated (see equation (22)).

The boron isotopic composition ($\delta^{11}B$) and boron to calcium ratio (B/Ca) of planktonic foraminifera allow reconstruction of pH and $[CO_3^{2-}]$ respectively (Foster, 2008) which allows full reconstruction of all carbonate system parameters, and so calculation of $[CO_{2(aq)}]$ and atmospheric pCO_2.

Boron exists in the ocean principally as two aqueous species; boric acid ($B(OH)_3$) and borate ($B(OH)_4^-$). The relative concentrations of boric acid and borate vary under the dissociation equilibrium shown in equation (29) which is strongly controlled by oceanic pH.

$$B(OH)_3 + H_2O \leftrightharpoons B(OH)_4^- + H^+ \qquad (29)$$

on has two isotopes, ^{11}B and ^{10}B with natural abundances of 19.9% and 80.1% respectively. Boron isotope variations are expressed in the standard delta notation (see equation (30)) relative to the National Institute of Standards and Technology Standard Reference Material 951 (NIST951).

$$\delta^{11}B = \left[\frac{{}^{11}B/{}^{10}B_{sample}}{{}^{11}B/{}^{10}B_{NIST\,951}} - 1 \right] \cdot 1000 \qquad (30)$$

There is a strong isotopic fractionation between the species of -19.5‰ which is largely independent of temperature and boron concentration (Kakihana et al., 1977; Klochko et al., 2006) and therefore the isotopic composition of the two species in seawater is pH controlled (see Figure 40)).

Only the charged borate species is incorporated into the calcite of foraminifera with HBO_3^{2-} substituting for CO_3^{2-} (equation (31); (Hemming and Hanson, 1992))

$$CaCO_3 + B(OH)_4^- \leftrightharpoons Ca(HBO_3) + HCO_3^- + H_2O \qquad (31)$$

If the boron isotopic composition of foraminifera can be accurately determined, then past pH can be reconstructed using equation (32).

$$pH = pK_b^* - \log\left[-\frac{\delta^{11}B_{sw} - \delta^{11}B_{foram}}{\delta^{11}B_{sw} - (1.0272 \cdot \delta^{11}B_{foram}) - 27.2} \right] \qquad (32)$$

pK_b^* = log of the stochiometric dissociation constant for boric acid/borate equilibria

Boron isotopes from foraminifera have been used to reconstruct pH and, through estimation of a second carbonate system parameter such as carbonate ion concentration or alkalinity, atmospheric pCO_2 in the Pleistocene (Sanyal et al., 1997; Sanyal et al., 1995) and over the Cenozoic (Palmer et al., 1998; Pearson and Palmer, 1999; 2000).

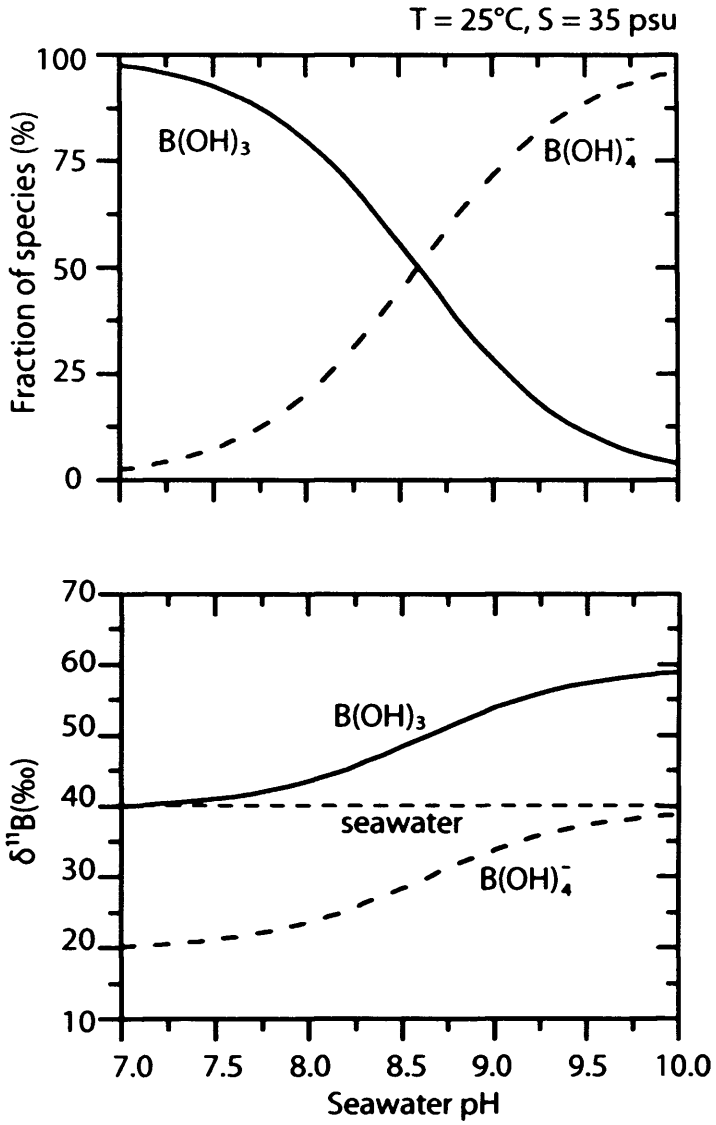

Figure 40: Boron speciation (top panel) and isotopic fractionation (bottom panel) as a function of seawater pH (adapted from Yu et al. (2007))

Under the equilibrium substitution conditions for boron into calcite expressed in equation (31) the distribution coefficient for the equilibrium can be expressed as in equation (33).

$$K_D = \frac{[B/Ca]_{foram}}{[B(OH)_4^-/HCO_3^-]_{seawater}} \quad (33)$$

Inspection of this relationship reveals that the B/Ca ratio in foraminifera is dependant on the ratio of borate to bicarbonate in seawater, which is itself pH dependant. By using the pH information gained from boron isotopes (equation (32)) the carbonate system can be fully constrained. The $[CO_3^{2-}]$ is estimated from the measured B/Ca ratio of *G. trilobus* using a relationship between $[CO_3^{2-}]$ and K_D based on core top data for *G. sacculifer* (Foster, 2008), and corrected for an offset (11.6 μmol mol^{-1}) between the two species observed in core tops (Foster, 2008). The boron concentration of seawater was assumed to be the same as today (416 μmol Kg^{-1}) and there was assumed to be no offset between the $\delta^{11}B$ of *G. trilobus* and the $\delta^{11}B$ of borate in seawater. These two assumptions may have an effect on a reconstruction of absolute pCO_2, but no significant effect on the magnitude of change, and due to our treatment of $\delta^{11}B_{sw}$ (see below) these assumptions do not affect our conclusions.

A complicating factor is the need for an accurate knowledge of the boron isotopic composition of Miocene seawater ($\delta^{11}B_{sw}$) in order to calculate pH from $\delta^{11}B$ (equation (32)). Attempts have been made to estimate past $\delta^{11}B_{sw}$ through modelling approaches (Lemarchand et al., 2000, 2002; Simon et al., 2006) and through the reconstruction of $\delta^{11}B$ depth profiles (Palmer et al., 1998; Pearson and Palmer, 1999; 2000) and there is general agreement that $\delta^{11}B_{sw}$ was lower in the past, but there is little consensus as to the magnitude of change and the likely value during the Miocene. The approach taken here is to use the boron palaeobarometer principally as a tool for the reconstruction of *relative* change, rather than attempt to estimate absolute pCO_2 values. To this end, the oldest point of the boron record is tuned to the oldest point of the alkenone record (they lie on the same horizon, at 0.00m; 13.86 Ma) so the pCO_2(boron)=pCO_2(alkenone), using $\delta^{11}B_{sw}$ as the free variable. $\delta^{11}B_{sw}$ is then assumed to have remained constant over the period of the remaining record. Fixing the

seawater value is valid, given the long residence time of boron in the oceans, which is in excess of 10 Myrs (estimates vary between 14 Myrs (Lemarchand et al., 2000) and 20 Myrs (Spivack and Edmond, 1987; Taylor and McLennan, 1985)).

Table 7: Estimates of Serravallian seawater $\delta^{11}B$

Source	Serravallian $\delta^{11}B_{sw}$ (‰)
Pearson and Palmer (2000)	37.7
Lemarchand et al. (2002)	37.5 – 39.5
Simon et al. (2006)	32.5 – 37.5
This study	35.6

The value of $\delta^{11}B_{sw}$ that this method yields is 35.6 ‰, which is within the range deemed reasonable on the basis of modelling studies (32 - 40‰; Table 7; Lemarchand et al., 2002; Simon et al., 2006) and close to the value estimated by Pearson and Palmer (2000) based on reconstructed water column profiles. The value of $\delta^{11}B_{sw}$ does affect the maximum change in pCO_2 measured by foraminiferal calcite $\delta^{11}B$. Figure 41 shows the influence of changing $\delta^{11}B_{sw}$ on the maximum change in pCO_2 estimated in the reconstruction presented below, and suggests that the effect of unknown $\delta^{11}B_{sw}$ is an uncertainty of ±25 ppm pCO_2.

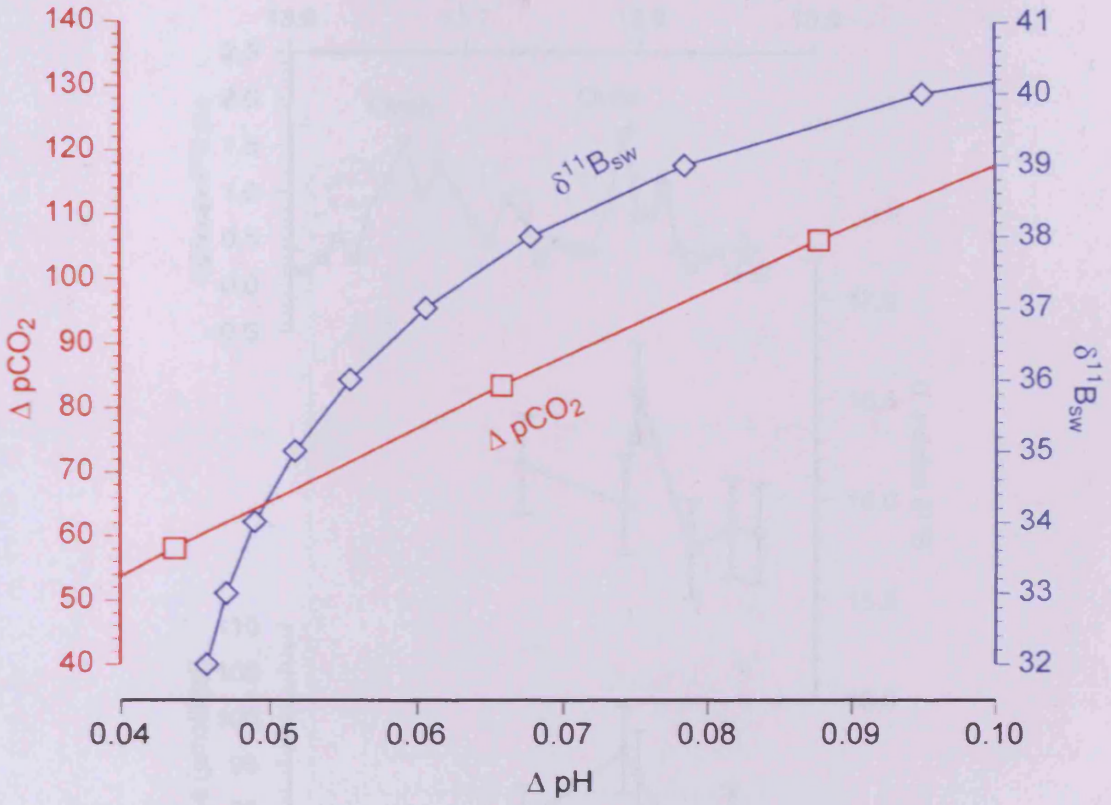

Figure 41: The influence of changing the $\delta^{11}B$ of seawater (blue diamonds and line) on the magnitude of maximum pH and pCO_2 change (red squares and line) suggested by the maximum change in *G. trilobus* $\delta^{11}B$ (from 16.53‰ to 15.83‰) over a range of seawater $\delta^{11}B$ deemed reasonable from modelling studies (32 – 40 ‰; Lemarchand et al., 2002; Simon et al., 2006). pCO_2 was calculated at a constant $[CO_3^{2-}]$ concentration of 300 µmol kg^{-1}.

5.3.2 Results

The boron record, which covers the period of CM6a, shows an increase in $\delta^{11}B$ from 15.8‰ at the start of the record, to 16.2‰ by 13.72 Ma (Figure 42). The peak value of 16.53‰ at 13.79 Ma occurs one sample (~9 Kyrs) before the peak of CM6a in the carbonate carbon isotope record. The B/Ca record also shows an increase over CM6a, starting at 79.5 µmol mol^{-1} and increasing to 88.2 µmol mol^{-1} by 13.72 Ma, with a maximum value of 96.5 µmol mol^{-1} at 13.78 Ma, coinciding with the peak value of $\delta^{13}C$ of CM6a in the carbonate carbon isotope record.

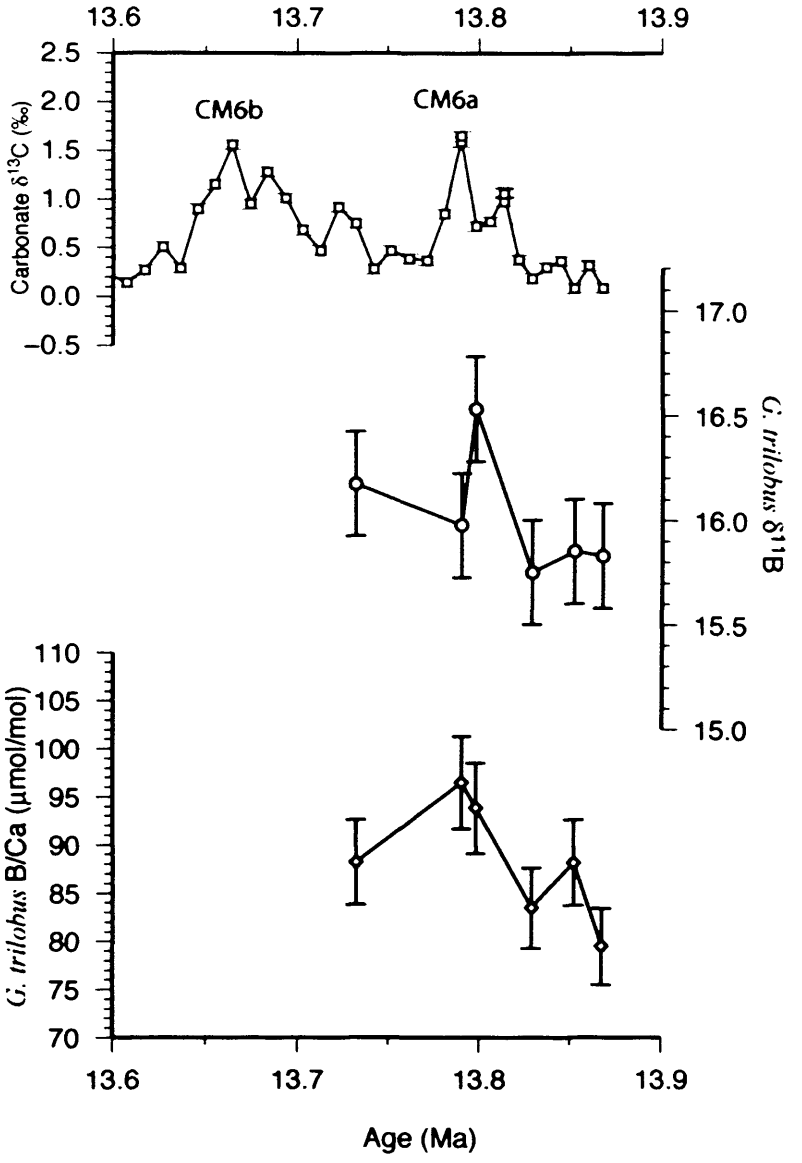

Figure 42: Bulk carbonate carbon isotope record for context showing data from this study (top; blue open squares and line) and data from Abels et al. (2005) (grey filled squares), boron isotope (middle; open circles and line) and B/Ca (bottom; open diamonds and line) results from measurements of *G. trilobus*. Error bars are ±2σ analytical uncertainties.

The boron pCO_2 reconstruction (Figure 43, Data Table 9) shows a decline in CO_2 of ~60 ppm over ~140 Kyrs, from 328 ppm (which is the value tuned to the alkenone record) to 270 ppm, and reaches a minimum value of 250 ppm at 13.79 Ma (Δ=~80 ppm). The minimum point is immediately before the peak of CM6a, and the atmospheric CO_2 at this point is ~260 ppm (Δ=~70 ppm).

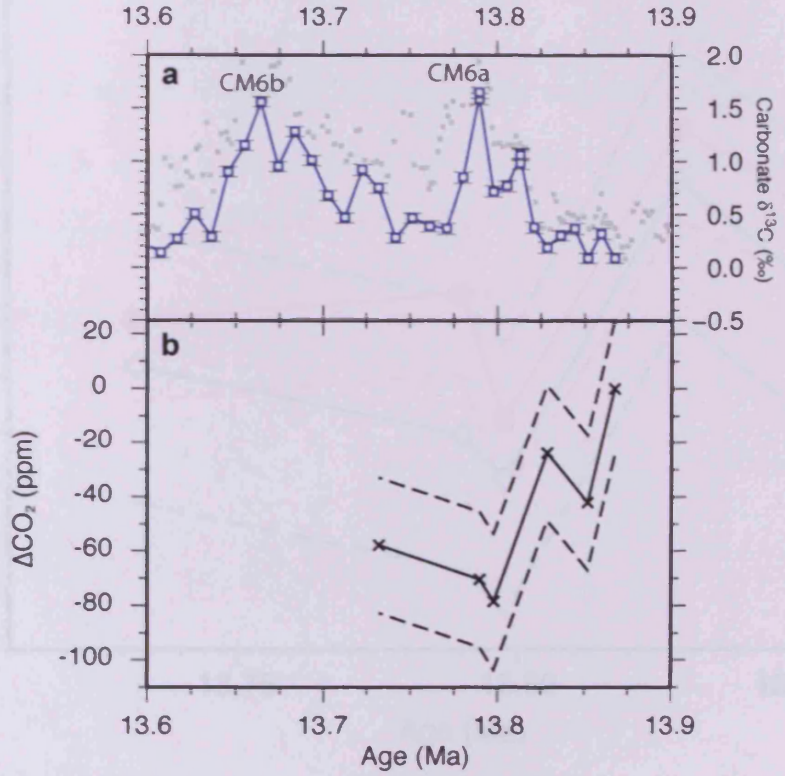

Figure 43: Boron based atmospheric CO_2 reconstruction (panel b; black crosses and line) shown with 2σ analytical error. Panel a; bulk carbonate carbon isotope record for context showing data from this study (blue open squares and line) and data from Abels et al. (2005) (grey filled squares).

The reconstructed CO_2 is driven principally by the increase in $\delta^{11}B$ and not by the measured B/Ca. In fact the B/Ca increase and the changes in $[CO_3^{2-}]$ that is reconstructed from it only plays a minor role in the CO_2 reconstruction, as can be seen from Figure 44. Similarly the decrease in temperature which recorded from Mg/Ca at RIP, although included in the calculation of pCO_2 from boron, plays a minor role in comparison to $\delta^{11}B$, and the pCO_2 drop reconstructed from boron is fairly insensitive to the temperature change.

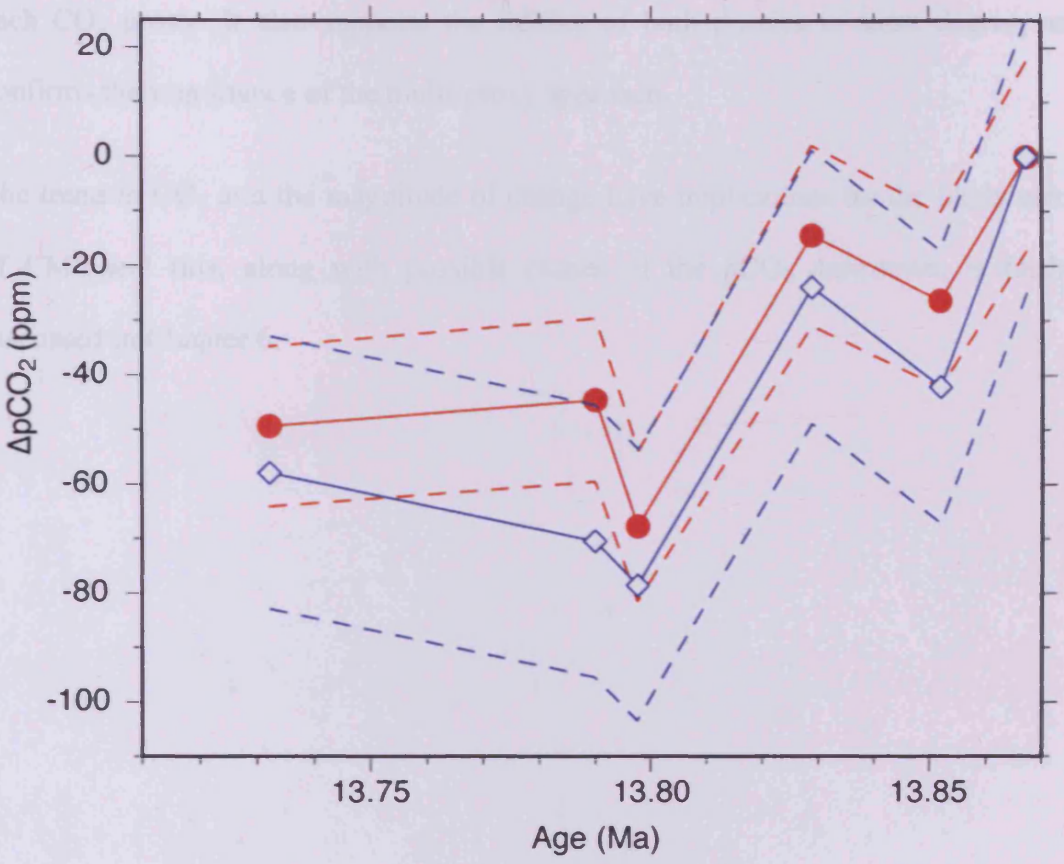

Figure 44: Boron based pCO_2 estimates with $[CO_3^{2-}]$ determined by B/Ca measurements (blue open diamonds and line) with analytical uncertainty (blue dashed lines) and by assuming total alkalinity (TA) remains constant (red filled circles) ±5% TA (red dashed lines).

5.3.3 Discussion

Seen in the context of the other proxy data (Figure 45) the boron CO_2 reconstruction shows general agreement. Although recording a larger and more rapid drop in CO_2 than the alkenone record, the boron record is largely within error of the alkenone record. It is also important to note the direction of the trend of the boron record; both the boron and the alkenone record show declining CO_2 following/concurrent with the growth of the ice sheet. The two proxies are independent recorders of the CO_2 trend, and that both record a decrease of similar magnitude lends confidence to the conclusion, given the number of assumptions and parameters which are included in

each CO_2 proxy. It also supports the fidelity of both proxies to some degree, and confirms the importance of the multi-proxy approach.

The trend in CO_2 and the magnitude of change have implications for the likely cause of CM6 and this, along with possible causes of the pCO_2 drawdown, is further discussed in Chapter 6.

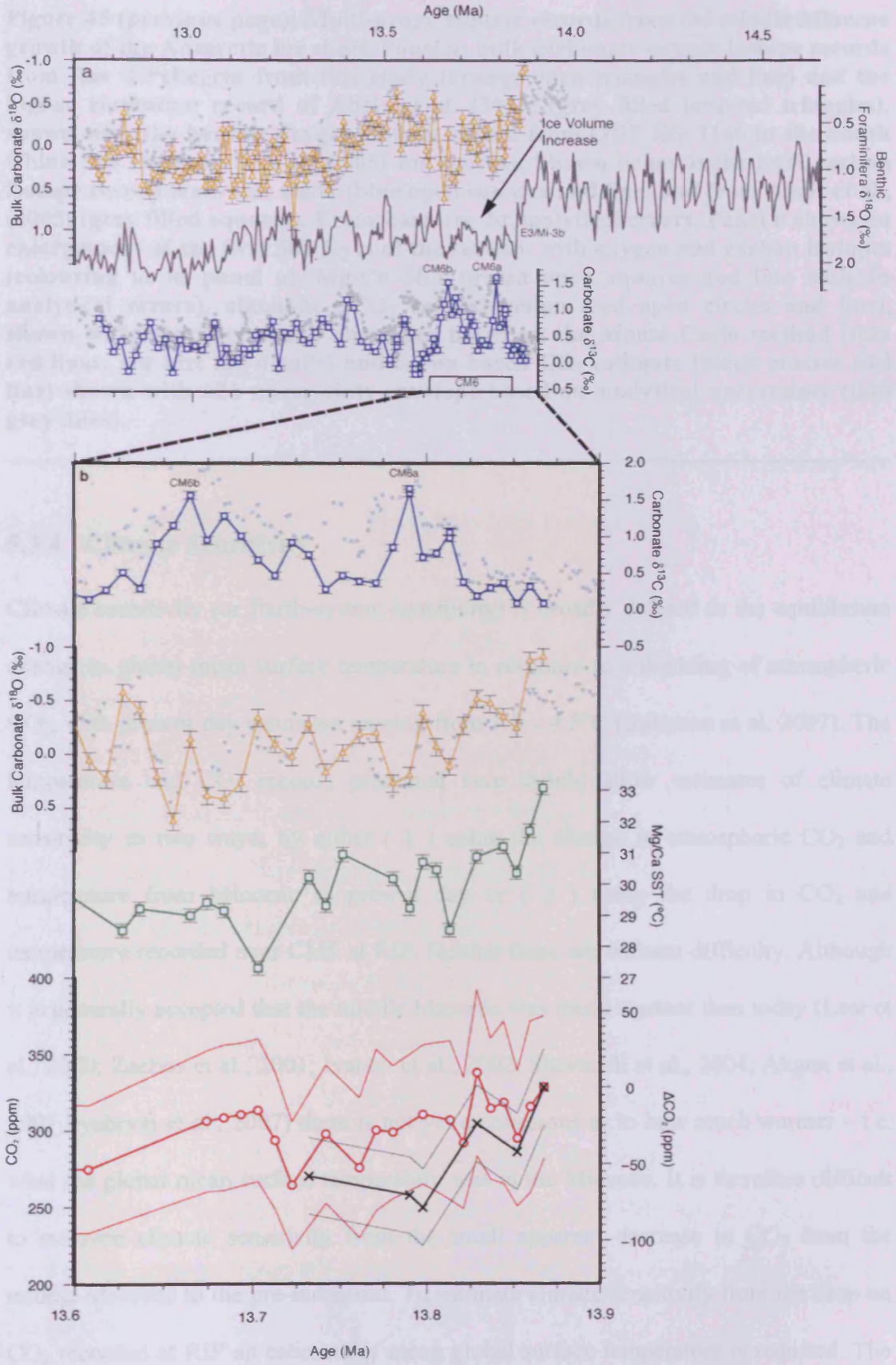
Age (Ma)
13.0
13.5
14.0
14.5
a
Bulk Carbonate δ18O (‰)
-1.0
-0.5
0.0
0.5
1.0
Ice Volume Increase
E3/Mi-3b
Benthic Foraminifera δ18O (‰)
0.5
1.0
1.5
2.0
CM5b
CM6a
Carbonate δ13C (‰)
1.5
1.0
0.5
0.0
-0.5
CM6
b
CM5b
CM6a
Carbonate δ13C (‰)
2.0
1.5
1.0
0.5
0.0
-0.5
Bulk Carbonate δ18O (‰)
-1.0
-0.5
0.0
0.5
Mg/Ca SST (°C)
33
32
31
30
29
28
27
CO2 (ppm)
400
350
300
250
200
ΔCO2 (ppm)
50
0
-50
-100
13.6
13.7
13.8
13.9
Age (Ma)

Figure 45 (previous page): Multi-proxy climate records from the middle Miocene growth of the Antarctic Ice sheet. Panel a; bulk carbonate oxygen isotope records from Ras il-Pellegrin from this study (orange open triangles and line) and the higher resolution record of Abels et al. (2005) (grey filled inverted triangles), shown with the benthic oxygen isotope record from ODP site 1146 in the South China Sea (Holbourn et al., 2005) for context. Shown below is the bulk carbon isotope record from this study (blue open squares and line) and from Abels et al., (2005) (grey filled squares). Error bars are 2σ analytical errors. Panel b shows an enlargement of the first 300 Kyrs of the section, with oxygen and carbon isotopes (colouring as in panel a), Mg/Ca SST (green open squares and line with 2σ analytical errors), alkenone pCO_2 reconstruction (red open circles and line), shown with ±2σ uncertainty envelopes based on the Monte Carlo method (thin red lines; see text for details) and boron based CO_2 estimate (black crosses and line) shown with ±2σ uncertainty envelope based on analytical uncertainty (thin grey lines).

5.3.4 Climate Sensitivity

Climate sensitivity (or Earth-system sensitivity) is broadly defined as the equilibrium change in global mean surface temperature in response to a doubling of atmospheric CO_2, with present day estimates ranging from 1.5 – 4.5°C (Solomon et al. 2007). The temperature and CO_2 records presented here should allow estimates of climate sensitivity in two ways; by either (1) using the change in atmospheric CO_2 and temperature from Miocene to present day or (2) using the drop in CO_2 and temperature recorded over CM6 at RIP. Neither these are without difficulty. Although it is generally accepted that the middle Miocene was much warmer than today (Lear et al., 2000; Zachos et al., 2001; Ivanov et al., 2002; Shevenell et al., 2004; Akgun et al., 2007 Syabryaj et al., 2007) there is not yet a consensus as to how much warmer – i.e. what the global mean surface temperature was in the Miocene. It is therefore difficult to estimate climate sensitivity from the small apparent decrease in CO_2 from the middle Miocene to the pre-industrial. To estimate climate sensitivity from the drop on CO_2 recorded at RIP an estimate of mean global surface temperature is required. The SST temperature record presented here is unlikely to represent a good estimate of

mean global surface temperature, and would imply a very large climate sensitivity. From the ~60 ppm decrease in CO_2 recorded by the alkenone record from RIP over CM6 the change in radiative forcing can be estimated using equation **(34)** (Myhre et al., 1998).

$$\Delta F_{CO2} = 5.35 \cdot \ln\left(\frac{C}{C_0}\right) \qquad (34)$$

ΔF_{CO2} = Change in radiative forcing due to CO_2
C = CO_2 after perturbation
C_0 = Unperturbed CO_2

This results in a radiative forcing change of ~1.1 Wm^{-2}. The climate sensitivity can then be estimated using equation **(35)** (Chylek and Lohman, 2008).

$$\lambda = \frac{\Delta T}{\Delta F_{CO2}} \qquad (35)$$

λ = Climate sensitivity
ΔT = Change in temperature

If the change in temperature from the SST reconstruction from RIP over CM6 is used (~5°C), this implies a climate sensitivity of ~4.6 K/Wm^{-2}, which would mean a 17.2°C change in temperature for a doubling of atmospheric CO_2. This is much higher than the estimated climate sensitivity for the present day (1.5 – 4.5°C; Solomon et al. 2007) or recent estimates of climate sensitivity from the Pliocene (7.1-9.6°C; Pagani et al. 2010). The boron isotope based CO_2 record from RIP suggests a similar decrease in atmospheric CO_2,, but over a shorter period of time and a smaller decrease in temperature (~3°C) if this record is used climate sensitivity is estimated at ~2.8 K/Wm^{-2} or a 10.3°C temperature change per doubling of CO_2, which is again much higher than estimates from the present day, but close to the higher end of estimates from the Pliocene.

These estimates assume that CO_2 is the only factor controlling the change in radiative forcing (ΔF), whereas in truth large contributions will come from other factors, including other greenhouse gasses such as methane, surface albedo, and aerosols which are likely to have changed, and the estimation of which are outside the scope of this work. Surface albedo is likely to be a significant influence given the large ice sheet growth. These influences, combined with the uncertainty about the true global mean surface temperature changes at the time, mean that the climate sensitivities presented here are likely to be overestimates.

5.4 Conclusions

The proxy based reconstructions presented here show decreasing CO_2 and temperature following the middle Miocene growth of a major ice sheet, and co-incident with one of the largest carbonate carbon isotope excursions in the Cenozoic. The decrease in CO_2 is estimated at approximately 60 ppm, and the drop in temperature is estimated at approximately 5°C. The absolute level of CO_2 is seemingly very low (~300 ppm; roughly equivalent to pre-industrial levels) given the much higher absolute temperatures for the Miocene recorded in this and other studies. This may suggest that parameters other than CO_2 are important in controlling the global temperatures in the Miocene, the smaller polar ice caps would result in lower global albedo than during the Pleistocene, and there have been suggestions that levels of water vapour in the atmosphere may have been important in controlling the Miocene warmth (Lyle et al., 2008).

None of the proxy records presented here show a cause for the decrease in CO_2, although the position of the CO_2 drop directly following the growth of the ice sheet

may suggest that a positive feedback is involved, and the presence of CM6 suggests that there are major changes happening in the carbon cycle. The use of carbon system models, coupled with the proxy records presented here, may shed light on the possible cause of the CO_2 drop, and CM6, and this approach is attempted in Chapter 6.

6 Miocene Carbon Cycle Dynamics

6.1 Carbon Maximum 6

6.1.1 Introduction

As a tool, computational modelling allows for testing of hypotheses relating to complex systems, in which interactions between system parameters mean that often unexpected and counterintuitive outcomes result. Choosing the complexity of the model for a specific problem is an important part of the process, models of limited complexity may fail to account for all interactions, whereas an over complex model requires both greater computation expenditure and more assumptions to be made, which can mean that, although seemingly more robust, results can deviate significantly from real-world situations.

The use of computational models allows for hypotheses to be tested against data, and this is the approach used here. Comparing the magnitude and direction of change in parameters can give greater confidence of causative mechanisms, especially given that different causative mechanisms can generate similar perturbations in certain parameters such as carbonate $\delta^{13}C$ (Kump and Arthur, 1999). The first model used here was developed specifically to improve the interpretation of carbonate $\delta^{13}C$ records which have often been interpreted without enough emphasis on the inherent ambiguity of the proxy (Kump and Arthur, 1999). The aim of this chapter is to test various causative mechanisms for CM6 against data. The models used in this chapter are both fairly simple, single box ocean models, and as such cannot encompass all possible scenarios. However, since atmospheric CO_2 and carbonate $\delta^{13}C$ appear to be representative of global changes over CM6 at least it is plausible that it is a global scale driver which forces the changes, and as such simplifying to single box model can

be useful. The simplicity of the model also allows for rapid runs which are not computationally intensive, and so multiple scenarios can be easily tested. Due to the simplicity of the models the aim of this chapter is not and cannot be to determine the definite cause of CM6, but it should be possible to rule out as implausible certain scenarios.

CM6 (nomenclature of Woodruff and Savin (1991)) is the largest individual "carbon maximum" in the broader Monterey Excursion, immediately following the major ice sheet expansion event of the middle Miocene ("E3"; (Flower and Kennett, 1993a) or "Mi-3"; (Miller et al., 1991)). The size of the excursion, rapidity and relation to the ice growth make CM6 of interest. The possibility that the excursion represents an important feedback related to the ice sheet growth makes understanding what it represents for global carbon cycle dynamics of particular interest.

Three hypotheses for the cause of CM6 will be examined in this chapter, along with two subsidiary mechanisms which could be of some importance. The hypotheses which have been suggested for CM6 are the "Burial Hypothesis" (Flower and Kennett, 1993b; Vincent and Berger, 1985); "Silicate Weathering Hypothesis" (Lear et al., 2004; Pagani et al., 1999a; Shevenell et al., 2008) and "Methane Hypothesis" (Berger, 2007). Also investigated here are the influences of changing global temperatures and volcanic carbon flux on the carbon isotope record.

6.1.2 Burial Hypothesis

The Burial hypothesis draws on the most common interpretation of carbonate carbon isotope records which states that variations in $\delta^{13}C_{carb}$ are the result of changes in the organic matter burial rate, usually due to changes in primary productivity or bottom water conditions which favour organic matter preservation and burial (e.g. anoxia). In

the Miocene this is a main component of the "Monterey hypothesis" which states that increased burial of organic matter on shelf areas around the Pacific led to the drawdown of atmospheric CO_2 and resulted in global cooling, ice sheet growth, and the "Monterey excursion' in the carbon isotope record from 17.5 – 13.5Ma (Vincent and Berger, 1985). CM6 is part of the Monterey excursion, and its timing after the ice sheet growth at Mi-3 could reflect a positive feedback. Such a feedback could involve ice sheet growth and cooling encouraging even greater organic matter burial. Cooling and ice sheet growth would have led to increased meridional thermal gradients, which could have in turn led to increased ocean circulation vigour, higher wind speeds and greater nutrient upwelling. This, in turn could increase biological productivity further, leading to greater organic matter burial and therefore even greater CO_2 drawdown (Flower and Kennett, 1993b; Vincent and Berger, 1985). The Monterey hypothesis was based primarily on evidence from the stable oxygen and carbon isotope records. Apart from one recent exception (Kürschner et al., 2008), long term records of CO_2 have failed to record a substantial drop in atmospheric CO_2 over the Monterey excursion (Pagani et al., 1999a; Pearson and Palmer, 2000). However the resolution and precision of these records are not great enough to recognise individual CO_2 drawdown events associated with "CM" events. Neither the degree of CO_2 drawdown associated with positive isotope excursions of this size, nor the sensitivity of the climate system to CO_2 drawdown during the Miocene are well known. Whether the expected CO_2 drawdown under the burial hypothesis would be large enough to detect with available proxies is therefore not known. By modelling a burial scenario the size of CO_2 drawdown expected from the 1.6‰ magnitude of CM6 can be estimated, and compared with both the uncertainty envelopes of published proxy records, and

compared to the higher resolution proxy records presented here, which are concentrated over of timeframe of CM6.

6.1.3 Silicate Weathering Hypothesis

Weathering of silicate rocks is a net sink for atmospheric CO_2, which is drawn down as a result of the weathering reaction. Over long timescales this sink acts as an important balance to the input of CO_2 from volcanism and carbonate deposition (e.g.. Berner et al., 1983). Any rapid changes in either the input from volcanism or the extent and intensity of silicate weathering will lead to a temporary imbalance in this equilibrium, and therefore has the potential to change pCO_2 and climate. One mechanism for changing the drawdown of CO_2 due to weathering would be to change the exposure area of silicate basement (Bluth and Kump, 1991) another would be by uplifting and exposing silicate material during mountain building (Raymo and Ruddiman, 1992).

A decrease in silicate weathering also has the ability to affect the carbon cycle, and to be potentially recognised through the carbon isotope record in marine carbonates. Any mechanism which increases pCO_2 in the atmosphere, and through equilibrium with the oceans, $[CO_{2(aq)}]$ has the potential to change the photosynthetic fractionation of carbon isotopes in marine organisms (ε_p). With increased $[CO_{2(aq)}]$, ε_p would also increase, leading to the burial and removal from the ocean carbon reservoir of organic matter with lower $\delta^{13}C$ values. This process would leave the ocean carbon reservoir relatively enriched in ^{13}C and therefore any carbonate produced and deposited would also become ^{13}C enriched, leading to a positive $\delta^{13}C$ shift over time.

This process has been suggested for various times in the geologic past. For example this mechanism is proposed as a negative feedback during the Late Ordovician

glaciation (Kump et al., 1999). At this time it is suggested that the expansion of an ice sheet blanketed continental terrains of silicate basement, leading to reduced CO_2 drawdown, pCO_2 increase, and ultimately to the end of the glaciation.

The silicate weathering feedback mechanism is also proposed for the glaciations during the earliest Oligocene and Miocene (Oi-1 and Mi-1 using the nomenclature of Miller et al. (1991)). For these glaciations deep and intermediate ocean temperature records show warming immediately following ice sheet expansion (Lear et al., 2004). The rising temperatures are seen as evidence of increased greenhouse warming due to higher pCO_2 caused by a similar ice-sheet expansion negative feedback. This suggestion is supported by the positive carbonate carbon isotope excursion is also recorded following both these glaciation events (Lear et al., 2004; Paul et al., 2000).

The silicate weathering feedback mechanism may also be at work during the middle Miocene. It has been suggested as a possible causative mechanism for the carbon isotope excursion CM6 (Shevenell et al., 2008), again on the basis of rising temperatures following the expansion of an ice sheet. The carbon isotope excursion at CM6 shares this temporal relation to the expansion of an ice sheet with Oi-1 and Mi-1, and so it may be reasonable to expect a similar causal mechanism (if the causal mechanism is in fact related to the ice sheet expansion and is not coincidental). However, none of these records show direct and unequivocal evidence for silicate weathering to be the ultimate driver of the changes observed in the carbonate carbon isotope record. As has been stated above, many factors combine to ultimately determine the $\delta^{13}C$ value of the carbonate which makes it into the geological record.

More direct evidence for changing CO_2 following an ice sheet growth are available following the EAIS expansion from published alkenone based reconstructions (Pagani

et al., 1999a). Pagani et al. (1999a) suggest that a 60ppm rise in atmospheric CO_2 from 14 to 10Ma is due to the silicate weathering mechanism, and although this apparent CO_2 rise is concurrent with a rise in temperature, the major positive $\delta^{13}C$ rise of the middle Miocene has abated by this point, and the $\delta^{13}C$ record is fairly flat.

The above examples show that although the silicate weathering hypothesis has been proposed for several stages in the Cenozoic, the evidence for it is not wholly convincing, and so care needs to be taken when applying it to CM6. The approach here is to investigate using models how large a change in silicate weathering would be required to drive the observed increase in the carbonate $\delta^{13}C$ values recorded at CM6, and what are the implications for other climate system parameters such as atmospheric CO_2 and organic matter $\delta^{13}C$.

6.1.4 Methane

The role methane plays in the global carbon cycle, and its influence on carbon isotopes, is an area of active research, with much focus concentrated on the likelihood, effects and recognition of rapid release events of methane from clathrates (such as its possible influence at the PETM (e.g. Dickens et al., 1995). The influence of smaller scale and less dramatic methane cycling have not been overly focused on, but due to the extreme $\delta^{13}C$ signature of methane released from clatharate sources (~ -60‰) the possibility of methane influencing the $\delta^{13}C_{carb}$ record should not be ignored. The stability field for the formation of methane clatharates in ocean basins is delicate, and rapid changes in ocean temperature and depth could quickly change the extent of ocean floor available for their formation from methane produced in the sediment pile (e.g. Reagan and Moridis, 2008). As such, temperature and sea level variations could have a profound effect on the amount of methane released from the sea floor. If

temperatures were to drop, the area of seafloor within the stability field for the formation of methane ice could expand rapidly, reducing from the ocean-atmosphere system a source of carbon, and through oxidation of the methane, CO_2. The reduction of the input of methane to the carbon system would also have an effect on the $\delta^{13}C$ of the ocean reservoir, by reducing a source of carbon with a very negative $\delta^{13}C$. This could then in turn cause an increase in $\delta^{13}C_{carb}$.

6.1.5 Temperature

Global ocean temperature change could also have a more direct influence on $\delta^{13}C_{carb.}$ At lower ocean temperatures, both isotopic fractionations between CO_2 in water in the gaseous and aqueous phases ($\varepsilon_{CO2(g)\text{-}CO2(aq)}$), and between aqueous CO_2 and carbonate ($\varepsilon_{CO2(aq)\text{-}Carb}$) will be greater (Hayes et al., 1999; Mook et al., 1974; Romanek et al., 1992). Also affected by temperature is the capacity of the oceans to uptake CO_2 (i.e. the Henry's law constant, K_H (Weiss, 1974)), so at lower temperatures, all with atmospheric CO_2 held constant, ε_p will be greater. The combined effect of this is that as temperature decreases $\delta^{13}C_{carb}$ will increase. As there are changes in ocean temperatures over CM6, as recorded both at our site and at sites spread globally, it is important to quantify the size of the temperature effect on the $\delta^{13}C_{carb}$ when trying to interpret CM6.

6.1.6 Volcanic and Metamorphic CO_2 Flux

The global input of CO_2 from volcanoes is an important boundary condition to the carbon system, and the effect of this parameter changing should also be considered. As the carbon isotopic signature of the incoming carbon from volcanism is comparable to that derived from riverine flux, changes in the $\delta^{13}C$ of carbonate and organic carbon

deposited would be due to the effect of changing ε_p as atmospheric CO_2 changes. The direction and magnitude of changes in the carbon isotope signature of carbonate leaving the system can be tested, and is briefly considered at the end of this chapter.

6.1.7 Model Description: KA1

Model KA1 is adapted from Kump and Arthur (1999) and is a one box model of the ocean/atmosphere system with each carbon flux carrying an appropriate $\delta^{13}C$ signature. The workings of the model can be described by two principle equations describing the movement of carbon through the carbon cycle (equation (36)) and the $\delta^{13}C$ of the carbonate and organic carbon being buried (equation (37)).

$$\frac{dM_o}{dt} = F_{w,org} + F_{volc} - F_{b,org} - F_{w,sil} \qquad (36)$$

M_0 = The amount of inorganic carbon in the ocean and atmosphere.
$F_{w,org}$ = Input flux from weathering of organic matter.
F_{volc} = Input flux from volcanic activity
$F_{b,org}$ = Output flux of buried organic matter.
$F_{w,sil}$ = Output flux from weathering of silicate rocks

$$\frac{d\delta_{carb}}{dt} = \frac{F_w^{'}(\delta_w^{'} - \delta_{carb}) - F_{b,org}\Delta_B}{M_o} \qquad (37)$$

δ_{carb} = Isotopic composition of carbonate sediments.
$F_w^{'}$ = Combined volcanic and weathering flux.
$\delta_w^{'}$ = Average carbon isotopic composition of riverine flux into the ocean.
Δ_B = Isotopic difference between organic matter and deposited carbonate (expressed as a negative).

The model assumes that the atmosphere is fully equilibrated with the ocean, and that the ocean is saturated with respect to CO_2, on the timescales under investigation here (thousands to tens of thousands of years) this is most likely reasonable (Broecker and Peng, 1987). Atmospheric pCO_2 is then calculated by scaling it to the change in the amount of inorganic carbon in the ocean/atmosphere with time (equation (38)).

$$pCO_2(t) = \left(\frac{M_0(t)}{M_0(0)}\right)^2 pCO_2(0) \qquad (38)$$

One potentially problematic assumption inherent with this treatment of pCO_2 is that there are no large changes in temperature.

The effect of changing photosynthetic isotopic fractionation is dealt with using equation (39), which assumes equilibration according to Henry's law at a fixed temperature of 25 °C and constant $[PO_4]$ of 0.25 μmol kg^{-1}.

$$\Delta_B = \left(\frac{(159.5[PO_4]) + 38.39}{0.034 pCO_2}\right) - 33 \qquad (39)$$

model includes a simple negative feedback on in increases in pCO_2, relying on changing the silicate-carbonate weathering balance as pCO_2 changes to attempt to return CO_2 to steady state values after perturbation of the carbon cycle has been removed (i.e. Berner et al. (1983)).

$$F_{w,sil} = F^0_{w,sil} \cdot \frac{pCO_2(t)}{pCO_2(0)} \qquad (40)$$

Kump and Arthur (1999) applied this feedback (equation (40)) for some of their model runs, however as silicate weathering has been proposed as key in understanding CM6 (see below) and is an area of interest in the models run here, the feedback is active in all model runs.

Initial conditions for model runs are shown in Table 8. All model runs were allowed to equilibrate for 1000 time steps (1 Myrs) before being perturbed, and runs were typically 2000 time steps long. Simulations were compiled and run using MATLAB Simulink using solver ode45 (Dormand-Prince).

Variable	Initial Condition
F_w	5×10^{15} mol C kyr^{-1}
$F_{w,org}$	10×10^{15} mol C kyr^{-1}
$F_{w,sil}$	6×10^{15} mol C kyr^{-1}
F_{volc}	6×10^{15} mol C kyr^{-1}
$F_{b,org}$	10×10^{15} mol C kyr^{-1}
$M_0(0)$	3.8×10^{18} mol C kyr^{-1}
$[PO_4^{-3}]$	0.25 μmol Kg^{-1}
δ_w	-5‰
$pCO_2(0)$	328 ppm

Table 8 Model KA1 initial conditions.

6.1.8 Model Description: LS3

Model LS3 is adapted from Louis-Schmid et al., (2007) and is a mass-balance model similar to KA1. However LS3 includes more complexity, including treatments of sea surface temperature and the ability to add emissions from methane clathrates. The model is based on two differential equations, describing the change in dissolved inorganic carbon (DIC) in the system (equation (41)) and the change in $\delta^{13}C$ of the DIC with time (equation (42)).

$$\frac{dDIC}{dt} = F_{volc} + F_{w,carb} + F_{w,org} + F_{meth} - F_{d,carb} - F_{d,org} \qquad (41)$$

F_{volc} = Input flux from volcanic outgassing
$F_{w,carb}$ = Input flux from weathering of carbonate rocks
$F_{w,org}$ = Input flux from weathering of organic matter
F_{meth} = Input flux from methane hydrate dissociation
$F_{d,carb}$ = Output flux from deposition of carbonate sediments
$F_{d,org}$ = Output flux from deposition of organic matter

$$\frac{d}{dt}(\delta_{DIC}(t).DIC(t)) = \delta_{volc}.F_{volc} + \delta_{w.carb}.F_{w.carb} + \delta_{w.org}.F_{w.org} + \delta_{meth}.F_{meth} - \delta_{d.carb}(t).F_{d.carb} - \delta_{d.org}(t).F_{d.org} \quad (42)$$

δ_{DIC} = Carbon isotopic composition of DIC reservoir
δ_{volc} = Carbon isotopic composition of volcanic input
$\delta_{w.carb}$ = Carbon isotopic composition of weathered carbonate
$\delta_{w.org}$ = Carbon isotopic composition of weathered organic matter
δ_{meth} = Carbon isotopic composition of methane input
$\delta_{d.carb}$ = Carbon isotopic composition of deposited carbonate
$\delta_{d.org}$ = Carbon isotopic composition of deposited organic matter

The effect of changing photosynthetic isotopic fractionation is handled in a similar way to KA1, however rather than assuming fixed Henry's constant calculated using stationary temperature and phosphate concentration, both are treated as variables and Henry's constant calculated using equation (21) with A and B constants in Table 6 (Weiss, 1970; Weiss, 1974).

$$\ln K_H = A_1 + A_2(100/T) + A_3 \ln(T/100) + S[B_1 + B_2(T/1000 + B_3(T/100)^2] \quad (43)$$

K_H = Henry's constant
T = Temperature in Kelvin
S =Salinity

This treatment of K_H is a slight departure from the model presented in Louis-Schmid et al. (2007), which uses a routine from Zeebe and Wolf-Gladrow (2001), but results in model data which are more closely comparable to the results of our CO_2 reconstructions as it is the same treatment used in the proxy reconstructions in Chapter 5.

Table 9 Solubility Constants ($mol.L^{-1}$)

A_1	-58.0931
A_2	90.5069
A_3	22.2940
B_1	0.027766
B_2	-0.025888
B_3	0.0050578

A weathering feedback is included within the model, using a similar concept to KA1 but a slightly different application (equation (44)). Model derived atmospheric CO_2 drives changes in the intensity of weathering ($f_{weathering}$) which is then applied to the initial programmed weathering fluxes ($F_{w,carb}$ and $F_{w,org}$) to give a time varying weathering flux. In order to balance the time varying weathering fluxes the carbonate burial rate ($F_{d,carb}$) is also modified from initial conditions by multiplying through by $f_{weathering}$ on the basis that increased delivery of Ca ions to the ocean derived from more intense weathering would encourage carbonate burial (and vice versa).

$$f_{weathering} = \left[\frac{pCO_2(t)}{pCO_2(steady\ \ state)}\right]^{0.5} \qquad (44)$$

Organic matter deposition ($F_{d,org}$) is also modified by $f_{weathering}$ via the phosphate term (equation (45)), on the basis that increased delivery of nutrients to the ocean would increase primary productivity.

$$F_{d,org} = \frac{F_{d,org}(0)\cdot[PO_4^{-3}](t)\cdot f_{weathering}}{[PO_4^{-3}](steady\ \ state)} \qquad (45)$$

Further definitions of variables and initial conditions are shown in Table 10. Models were allowed to equilibrate for 1000 time steps (1 Myrs) before being perturbed, and runs were typically 2000 time steps long (in total). Simulations were compiled and run using MATLAB Simulink using solver ode45 (Dormand-Prince).

Parameter	Initial Conditions
δ_{volc}	-5‰
$\delta_{w.carb}$	2.9‰
$\delta_{w.org}$	-22‰
δ_{meth}	-60‰
T(steady state)	31°C
$[PO_4^{-3}]$	0.5 μmol Kg^{-1}
pCO_2(steady state)	328 ppm
DIC(steady state)	3.8×10^{18} mol C Kyr^{-1}
$F_{w.carb}(0)$	3.4×10^{16} mol C Kyr^{-1}
$F_{d.carb}(0)$	4.0×10^{16} mol C Kyr^{-1}
$F_{w.org}(0)$	1.0×10^{16} mol C Kyr^{-1}
$F_{d.org}(0)$	1.0×10^{16} mol C Kyr^{-1}
$F_{volc}(0)$	6.0×10^{16} mol C Kyr^{-1}
$F_{meth}(0)$	0 (conditions for methane runs defined below)
$\delta_{d.carb}(t)$	$= \delta_{DIC}(t) + 1.2$
$\Delta_{d.org}$	$= \varepsilon_p + \Delta_{carb} + 1.5$
Δ_{carb}	$= 11.98 - 0.12T$

Table 10 Model LS3 initial conditions.

6.1.9 Model Results

6.1.9.1 Experiment 1: Silicate Weathering Crash

Kump and Arthur (1999) model a scenario whereby silicate weathering is reduced by 50% for 500 Kyrs which results in only a modest rise in carbonate $\delta^{13}C$. Here, using KA1 (which is an adaptation of the model used by Kump and Arthur (1999) with Miocene starting pCO_2) the model is driven by a 50% reduction which continues for 2 Myrs, and the results are shown in Figure 46. As expected, the reduction in silicate weathering flux drives a steady increase in atmospheric CO_2 (upper panel, Figure 46).

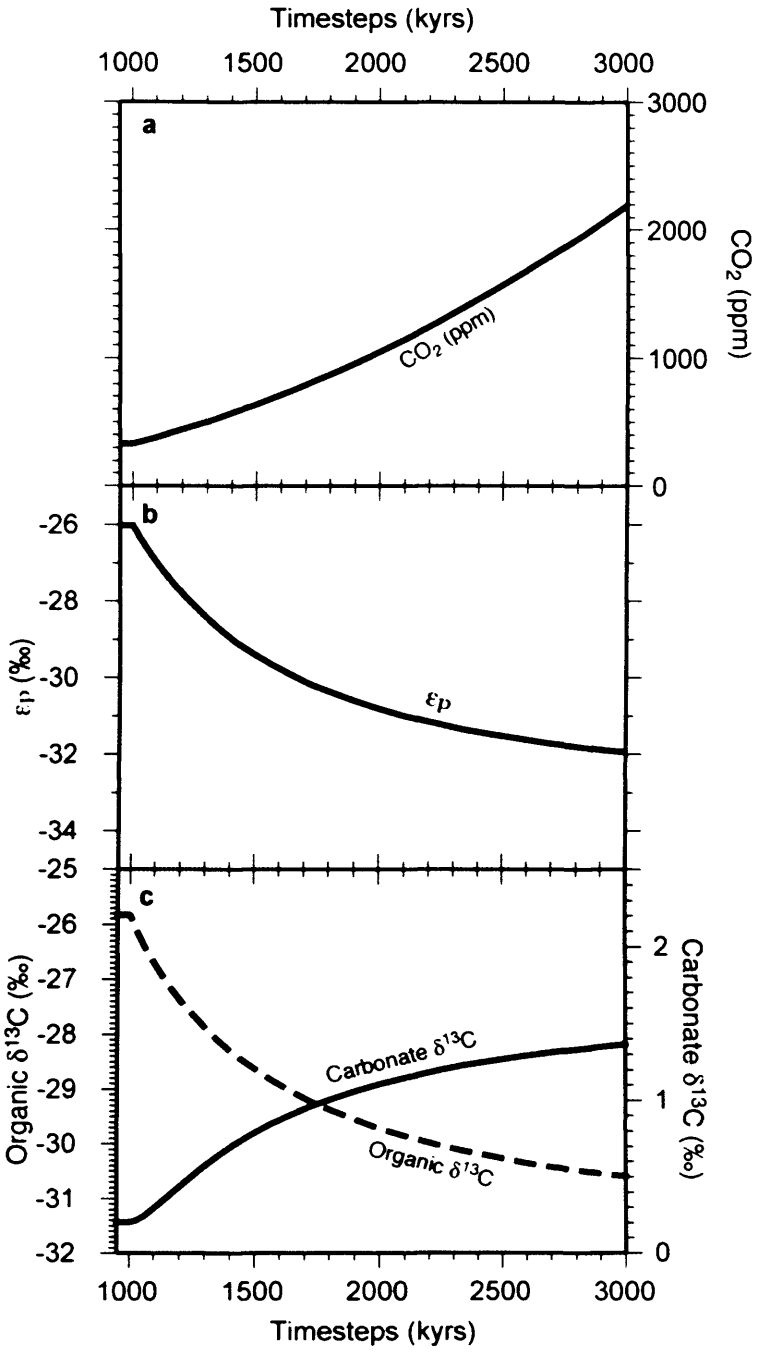

Figure 46. The response of model KA1 to a 50% reduction in silicate weathering ($F_{w.sil}$) which persists for 2 Myrs. Panel a; modelled atmospheric CO_2 (solid line). Panel b; modelled ε_p (solid line). Panel c; modelled carbonate $\delta^{13}C$ (solid line) and organic matter $\delta^{13}C$ (dashed line).

This increase in atmospheric CO_2 in turn affects ε_p and drives a decrease in organic $\delta^{13}C$ and an increase in carbonate $\delta^{13}C$. The effect is gradual, as although the reduction in weathering flux occurs instantaneously at timestep 1000 it takes time for CO_2 to build up and affect the $\delta^{13}C$ of the buried material. After 500 Kyrs (almost double the

time span of CM6) pCO_2 has almost doubled (636ppm at 1492 time steps[2]) whilst carbonate $\delta^{13}C$ has increased only 0.58‰, from a steady state value of 0.2‰, to 0.78‰ (at 1492 time steps). Over the full run of 2 Myrs of reduced weathering, CO_2 reached 2280 ppm, whilst carbonate $\delta^{13}C$ increased to 1.37‰ (at 3062 time steps).

6.1.9.2 Experiment 2: Organic Matter Burial Fluxes

Initial model runs (i.e. green line, Figure 47) suggested that organic matter burial could explain both the carbonate isotope record and the CO_2 proxy reconstructions presented in Chapter 5. Therefore a suite of model runs were undertaken to attempt to fit different aspects of the multi-proxy data records. The runs are summarised in Table 11 and presented in Figure 47.

Table 11: Details of organic burial experiment model runs, see text and Figure 47. One timestep is equivalent to 1 kyr.

Colour in Figure 47	% increase in organic matter burial flux (Fb_org)	First Pulse		Second Pulse		Minimum CO_2 (ppm)	Maximum carbonate $\delta^{13}C$ (‰)
		Start time (Time steps)	End Time (Time steps)	Start Time (Time steps)	End Time (Time steps)		
Green	19	1000	1247	-	-	273	0.93
Dark Blue	65	1030	1071	1150	1191	259	1.68
Red	50	1000	1071	1122	1191	242	1,71
Light Blue	50	1000	1071	-	-	275	1.67
Yellow	25	1000	1140	-	-	281	1.14
Pink	70	1000	1071	-	-	255	2.24

[2]The dynamic timestepping interval of the ode solver results in uneven datapoint spacing, which is designed to capture the important details of curves without oversampling in order to reduce processing needs. Data from model runs is therefore reported at timesteps for which there is outputted data, rather than interpolating between datapoints

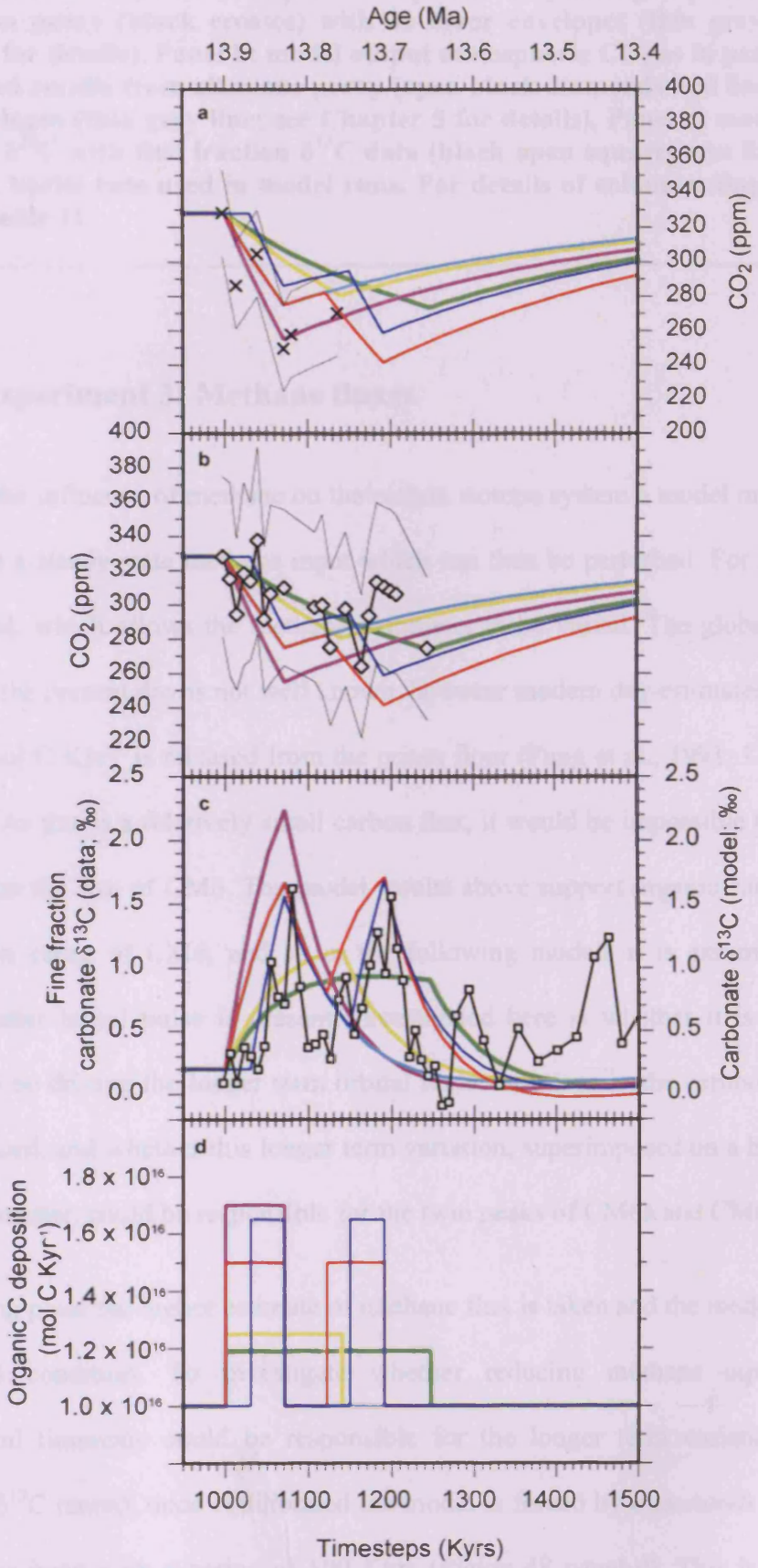
Age (Ma)
13.9
13.8
13.7
13.6
13.5
13.4
a
b
c
d
CO_2 (ppm)
Fine fraction carbonate $\delta^{13}C$ (data; ‰)
Carbonate $\delta^{13}C$ (model; ‰)
Organic C deposition (mol C Kyr^{-1})
1.8 x 10^{16}
1.6 x 10^{16}
1.4 x 10^{16}
1.2 x 10^{16}
1.0 x 10^{16}
1000
1100
1200
1300
1400
1500
Timesteps (Kyrs)

Figure 47 (previous page): Results of organic matter burial experiment from model KA1. Panel a; model output atmospheric CO_2 with proxy based results from boron proxy (black crosses) with 2σ error envelopes (thin grey line; see Chapter 5 for details). Panel b; model output atmospheric CO_2 as in panel a, with proxy based results from alkenone proxy (open black diamonds and line) with 2σ error envelopes (thin grey line; see Chapter 5 for details). Panel c; model output carbonate $\delta^{13}C$ with fine fraction $\delta^{13}C$ data (black open squares and line). Panel d; organic burial rate used in model runs. For details of colour coding of model runs see Table 11.

6.1.9.3 Experiment 3: Methane fluxes

To model the influence of methane on the carbon isotope system a model must first be set up with a steady state methane input which can then be perturbed. For this model LS3 is used, which allows the methane parameter to be varied. The global methane budget for the present day is not well known, however modern day estimates suggest 3 - 6×10^{14} mol C Kyr^{-1} is released from the ocean floor (Fung et al., 1991; Lelieveld et al., 1998). As this is a relatively small carbon flux, it would be impossible to generate an excursion the size of CM6. The model results above support organic carbon burial as the main cause of CM6, and so in the following models it is assumed that an organic matter burial pulse is present. Investigated here is whether it is viable for methane to be driving the longer term orbital scale variations in the carbonate carbon isotope record, and whether this longer term variation, superimposed on a burial pulse of organic matter, could be responsible for the twin peaks of CM6a and CM6b.

As a starting point the higher estimate of methane flux is taken and the model run with this initial condition. To investigate whether reducing methane input on an astronomical timescale could be responsible for the longer term variations in the carbonate $\delta^{13}C$ record, once equilibrated the model is forced by a sawtooth halving of the methane input with a period of 100 Kyrs (Figure 48 panel d). This is combined

with a pulsed increase in organic carbon burial similar to experiment 2 above. The results are shown in Figure 48.

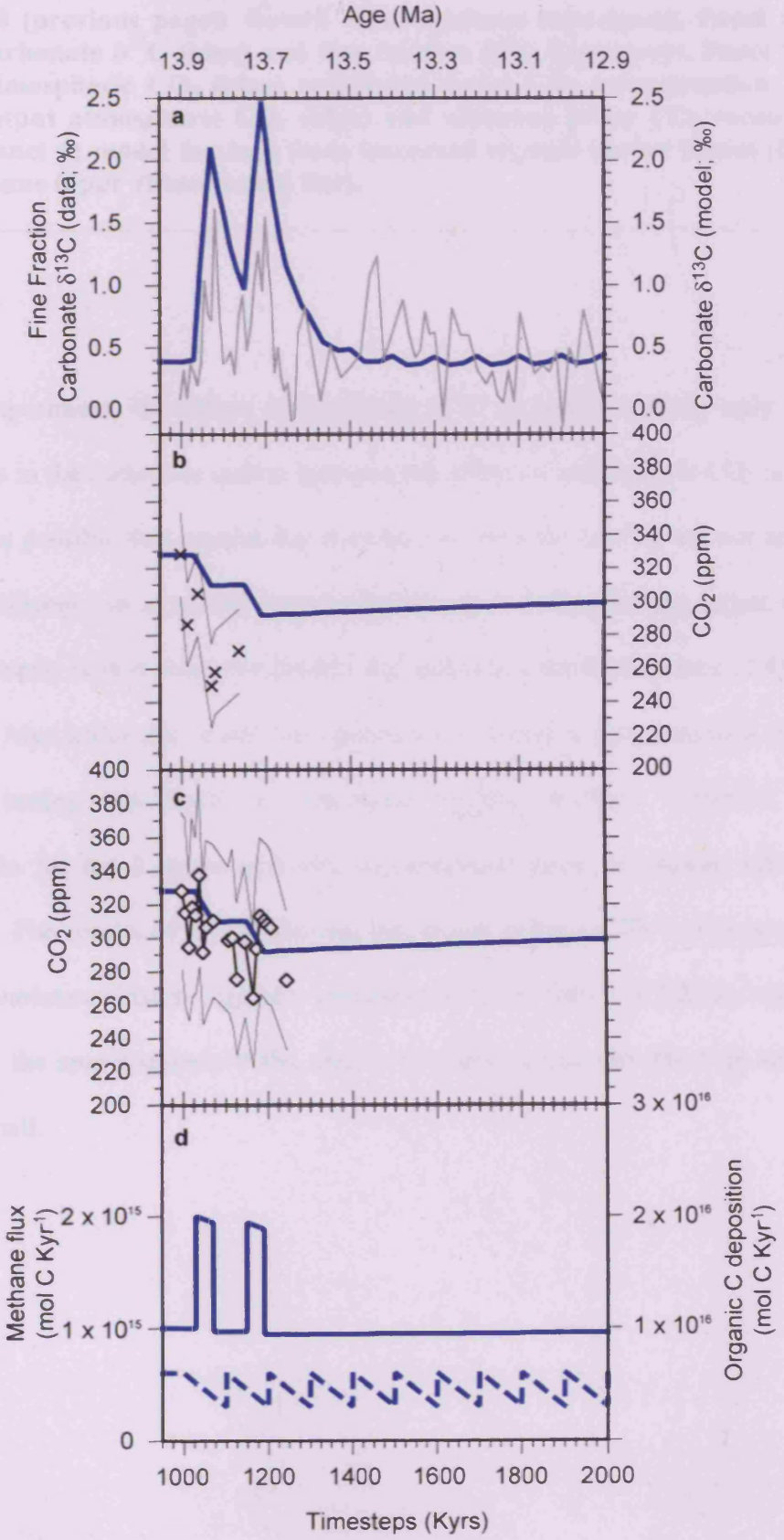
Age (Ma)
13.9
13.7
13.5
13.3
13.1
12.9
a
Fine Fraction Carbonate δ13C (data; ‰)
Carbonate δ13C (model; ‰)
2.5
2.0
1.5
1.0
0.5
0.0
b
c
CO2 (ppm)
400
380
360
340
320
300
280
260
240
220
200
d
Methane flux (mol C Kyr-1)
2 x 10^15
1 x 10^15
0
3 x 10^16
2 x 10^16
1 x 10^16
Organic C deposition (mol C Kyr-1)
1000
1200
1400
1600
1800
2000
Timesteps (Kyrs)

Figure 48 (previous page): Results from methane experiment. Panel a; model output carbonate $\delta^{13}C$ (blue) and fine fraction $\delta^{13}C$ data (grey). Panel b; model output atmospheric CO_2 (blue) and boron proxy CO_2 reconstruction. Panel c; model output atmospheric CO_2 (blue) and alkenone proxy CO_2 reconstruction (grey). Panel d; model forcings from increased organic matter burial (blue line) and methane input (blue dashed line).

In this experiment, the effect on carbonate $\delta^{13}C$ is minor, causing only a 0.06‰ oscillation in the carbonate carbon isotopes, the effect on atmospheric CO_2 is also very small. It is possible that present day estimates of methane cycling are not appropriate for the Miocene, so a second model was run with a significantly larger degree of methane input, with 4 times the present day methane contribution used (2.4×10^{15} mol C Kyr^{-1}). Also under this model the organic matter burial is increased by a single 25% increase lasting 200 Kyrs, to investigate whether methane variations may be responsible for the 2 peaks of CM6, superimposed upon an organic matter burial increase. The results of this model run are shown in Figure 49. In this scenario, the methane variations lead to a greater carbonate $\delta^{13}C$ oscillation of 0.25‰, which is still less than the approximately 0.8‰ seen in the data. Again, the effect on atmospheric CO_2 is small.

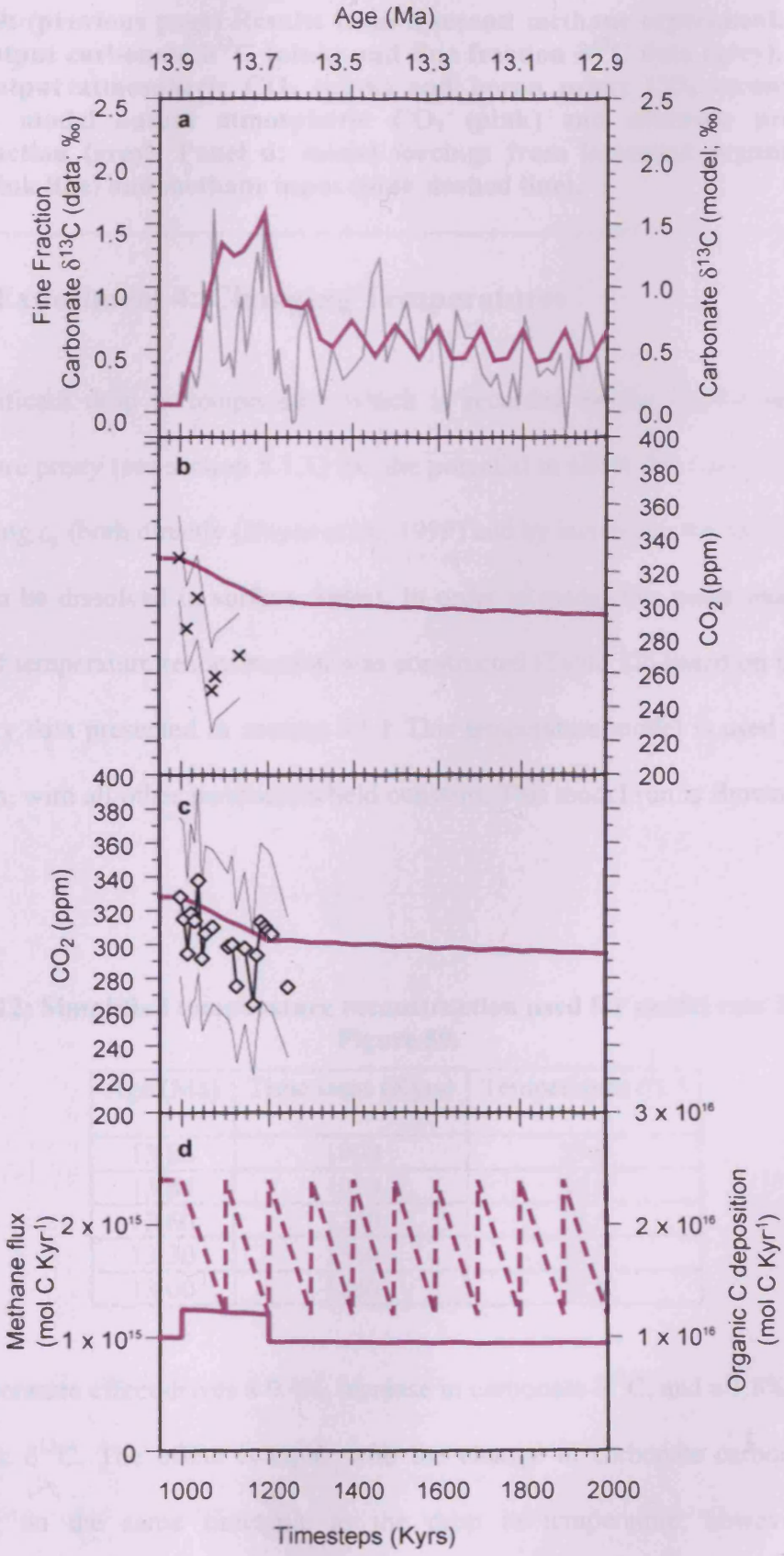
Age (Ma)
13.9
13.7
13.5
13.3
13.1
12.9
a
Fine Fraction Carbonate δ13C (data; ‰)
Carbonate δ13C (model; ‰)
2.5
2.0
1.5
1.0
0.5
0.0
b
c
CO2 (ppm)
400
380
360
340
320
300
280
260
240
220
200
d
Methane flux (mol C Kyr-1)
2 x 10^15
1 x 10^15
0
3 x 10^16
2 x 10^16
1 x 10^16
Organic C deposition (mol C Kyr-1)
1000
1200
1400
1600
1800
2000
Timesteps (Kyrs)

Figure 49: (previous page) Results from a second methane experiment. Panel a; model output carbonate $\delta^{13}C$ (pink) and fine fraction $\delta^{13}C$ data (grey). Panel b; model output atmospheric CO_2 (pink) and boron proxy CO_2 reconstruction. Panel c; model output atmospheric CO_2 (pink) and alkenone proxy CO_2 reconstruction (grey). Panel d; model forcings from increased organic matter burial (pink line) and methane input (pink dashed line).

6.1.9.4 Experiment 4: Changing Temperatures

The significant drop in temperature which is recorded by the Mg/Ca sea surface temperature proxy (see section 5.1.1) has the potential to affect the carbonate isotopes by changing ε_p (both directly (Hayes et al., 1999) and by increasing the amount of CO_2 which can be dissolved in surface water). In order to model this using model LS3 a simplified temperature reconstruction was constructed (Table 12) based on the Mg/Ca SST proxy data presented in section 5.1.1 This temperature model is used to drive a model run, with all other parameters held constant. This model run is shown in Figure 50.

Table 12: Simplified temperature reconstruction used for model run. See also Figure 50.

Age (Ma)	Time steps (Kyrs)	Temperature (°C)
13.86	1000	33.0
13.84	1020	30.0
13.60	1260	28.5
13.30	1560	28.0
13.00	1860	28.0

The temperature effect drives a 0.4‰ increase in carbonate $\delta^{13}C$, and a 1.8‰ decrease in organic $\delta^{13}C$. The effect is rapid, with the change in carbonate carbon isotopes occurring on the same timescale as the drop in temperature, however as the

temperature change is unidirectional, so is the isotope effect, driving an increase which reaches a new steady state, rather than causing an excursion which recovers.

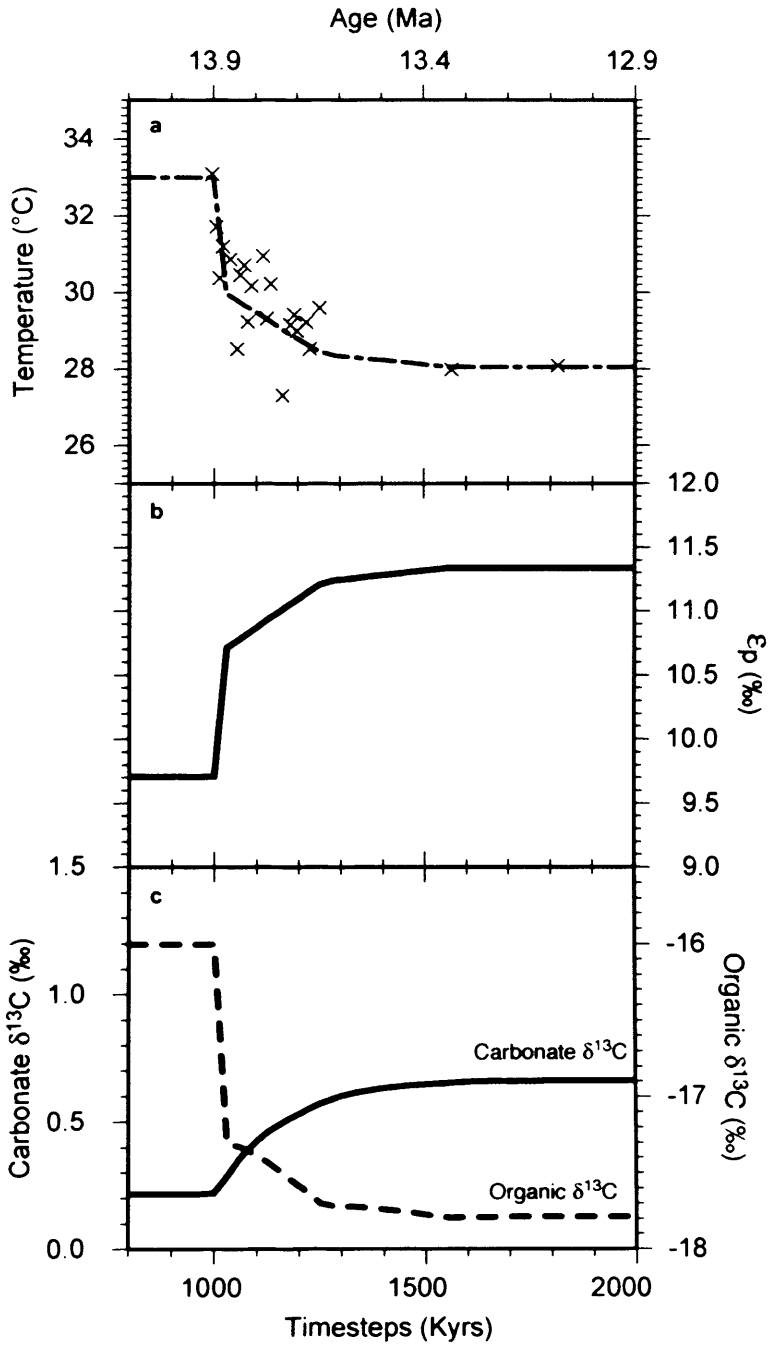

Figure 50: Results from modelling carbon isotope changes driven by the temperature variation reconstructed using Mg/Ca proxy. Panel a; temperature profile used to drive model (dashed line) and observed Mg/Ca SST (crosses). Panel b; the effect of temperature changes on ε_p. Panel c; the effect of temperature changes on carbonate $\delta^{13}C$ (solid line) and organic $\delta^{13}C$ (dashed line).

6.1.9.5 Experiment 5: Volcanic input variations

In the final experiment the effects of varying volcanic inputs on the carbonate carbon isotope system are investigated. The effect of volcanic input changing is two-fold. Firstly it varies the atmospheric concentration of atmospheric CO_2 directly, which can then influence ε_p and the isotopic composition of the material being buried, which in turn affects the composition of the ocean carbon reservoir (as has been shown for silicate weathering, above). Secondly, it has a direct influence on the isotopic composition of the ocean reservoir, as the isotopic composition of the carbon output due to volcanism is -5‰, different to the 0‰ input from weathering runoff (Kump and Arthur 1999). The approach in this experiment is to try and drive the changes in carbonate $\delta^{13}C$ and CO_2 which is shown in the data record from RIP. The first model run involved a 50% increase in volcanism which lasted for 250 Kyrs. The results are shown in Figure 51. The modelled CO_2 increases to over 400 ppm rapidly, but the carbonate isotope record shows an initial decrease as the effect of the more negative volcanic carbon is felt, and then increases as the effects of higher CO_2 overcomes the more negative isotopic inputs. An increase in volcanism can, therefore, drive a positive carbonate $\delta^{13}C$ isotope excursion, but the effect is moderate (only a 0.2‰ with a 50% increase for 250 Kyrs) and is led by a negative excursion. Even with a 1000% increase in volcanic CO_2 lasting for 250 Kyrs the ability to create a large positive carbon isotope excursion is confined to a 0.6‰ excursion, as shown in Figure 52, and again is preceded by a large negative isotope excursion.

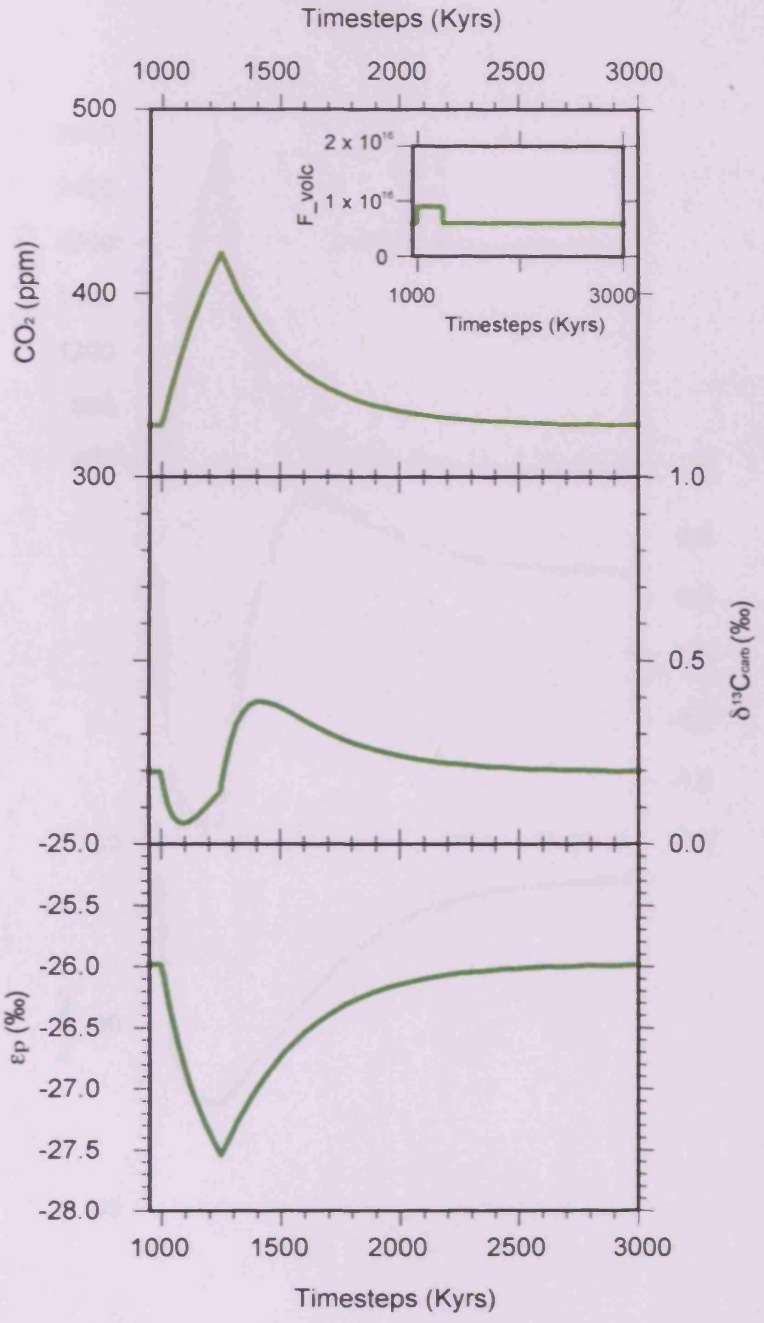

Figure 51: Results from model KA1 showing an increase in volcanism of 50% over 250 Kyrs. Upper panel; Modelled atmospheric CO_2, with volcanic input parameter shown inset, units of F_vol are mol C Kyr^{-1}. Middle panel; modelled carbonate $\delta^{13}C$ output. Lower panel; modelled ε_p.

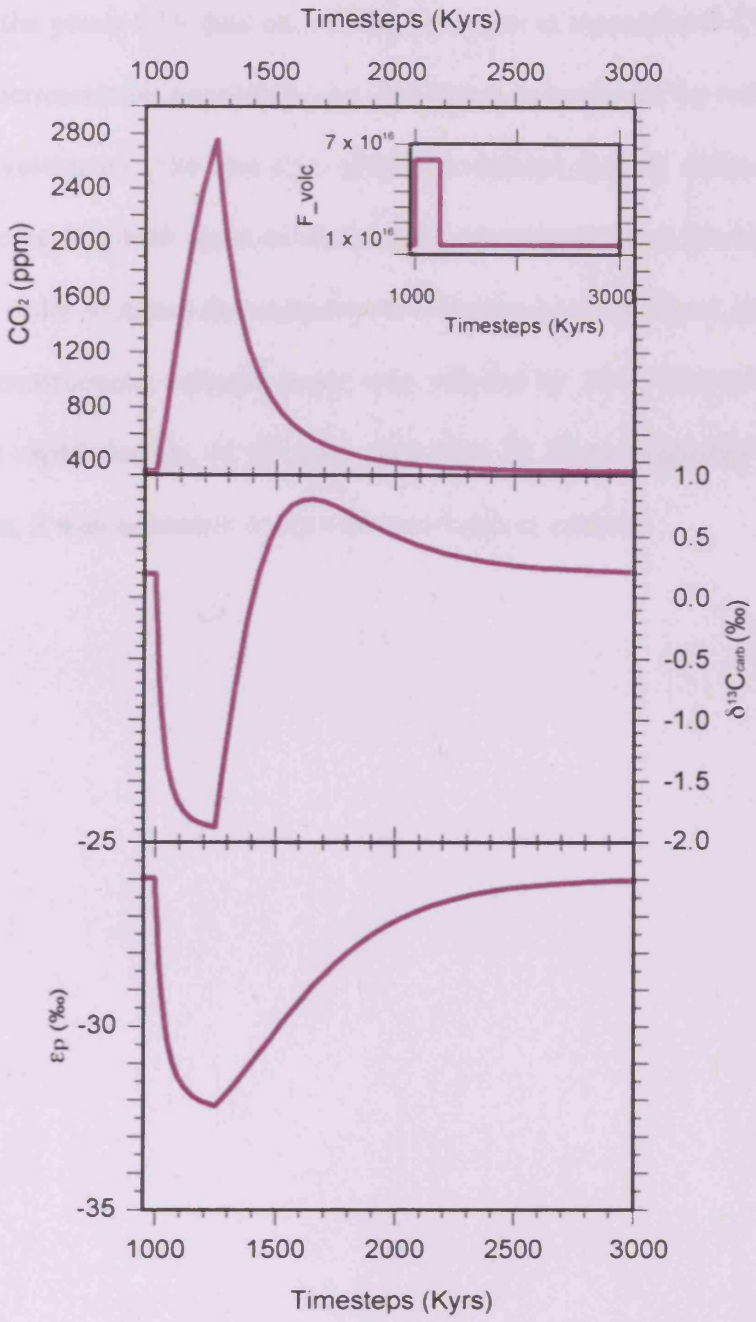

Figure 52: The results of an order of magnitude increase in volcanic input (inset, upper panel; F_vol in mol C Kyr^{-1}), as modelled by KA1. The large two-stage carbon isotope effect is shown in the middle panel, with the effects of the increased CO_2 on isotopic fractionation in the lower panel.

In Chapter 5 the proxy CO_2 data recorded a reduction in atmospheric CO_2 over CM6. In a final experiment the possibility that this decrease is driven by reduced volcanic activity in investigated. The two CO_2 proxies indicated slightly different degrees of CO_2 reduction, and so both these reconstructions are targeted, and the results shown in Figure 53. In order to match the reduction to 270 ppm over 250 Kyrs, as shown by the alkenone reconstruction, volcanic input was reduced by 25%. However, in order to approach the rapid decline of 63 ppm over just 71 Kyrs suggested by the boron reconstruction, it was necessary to shutdown volcanism entirely.

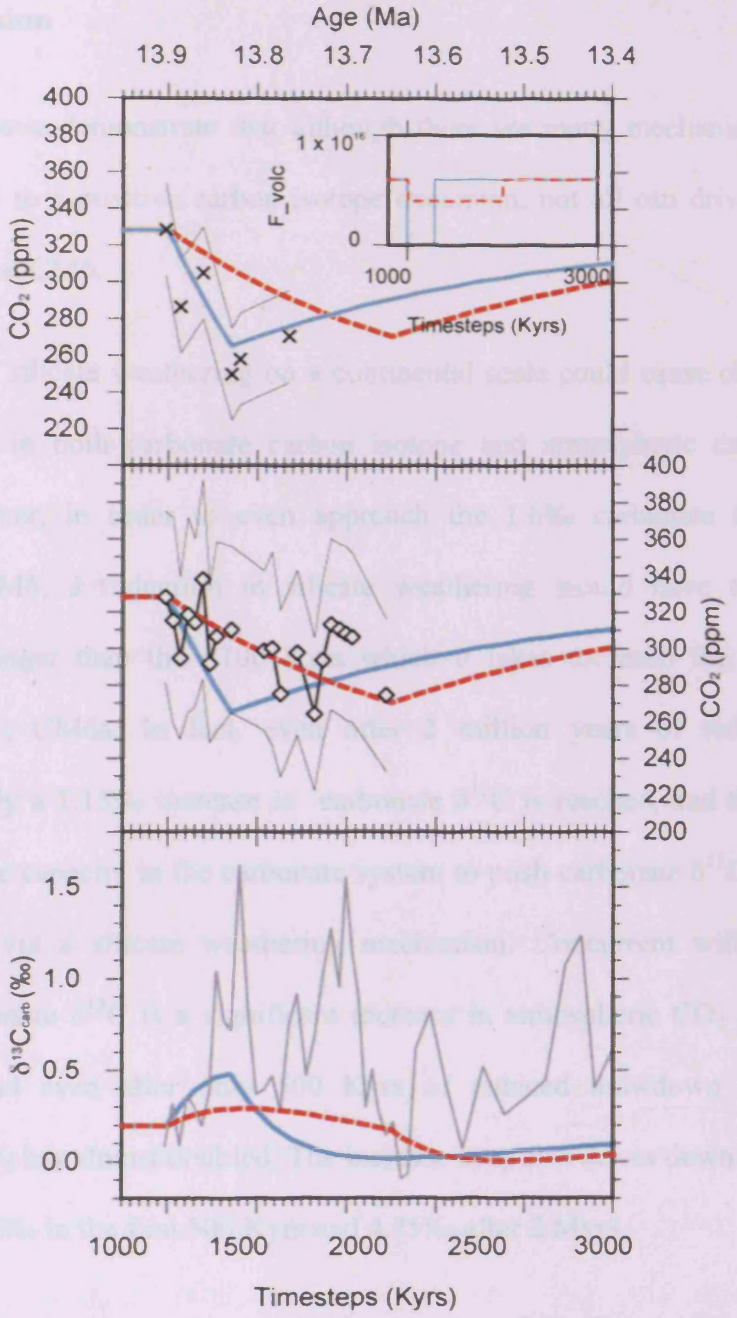

Figure 53: Modelling the proxy data CO_2 reconstructions from Chapter 6, as if all the recorded CO_2 reduction is driven by volcanism. The blue model was the attempt to model the boron reconstruction (shown as black crosses in the top panel) and the red dashed line is the attempt to reconstruct the alkenone CO_2 data (shown in the middle panel by the black open diamonds).

6.1.10 Discussion

The models above demonstrate that although there are many mechanisms available which can lead to a positive carbon isotope excursion, not all can drive the type of excursion seen at CM6.

A shutdown of silicate weathering on a continental scale could cause changes which could be seen in both carbonate carbon isotope and atmospheric carbon dioxide records. However, in order to even approach the 1.6‰ carbonate $\delta^{13}C$ increase recorded at CM6, a reduction in silicate weathering would have to persist for significantly longer than the <100 Kyrs which it takes to reach the first peak in carbonate $\delta^{13}C$; CM6a. In fact, even after 2 million years of reduced silicate weathering, only a 1.15‰ increase in carbonate $\delta^{13}C$ is reached, and there does not appear to be the capacity in the carbonate system to push carbonate $\delta^{13}C$ to the 1.6‰ seen at CM6 via a silicate weathering mechanism. Concurrent with the rise in modelled carbonate $\delta^{13}C$ is a significant increase in atmospheric CO_2 (upper panel; Figure 46), and even after only 500 Kyrs of reduced drawdown from silicate weathering, CO_2 has almost doubled. The increase in ε_p also drives down organic $\delta^{13}C$, which drops 2.8‰ in the first 500 Kyrs and 4.75‰ after 2 Myrs.

None of these results are consistent with the data from RIP. The modelled rise in CO_2 is dramatic, and although it is true that the uncertainty envelopes for the alkenone and boron datasets presented in Chapter 5 are quite large, a doubling of CO_2 in 500 Kyrs should certainly be measurable by these methods. Instead the data show a decline in atmospheric CO_2 in both records. Even if it could be accepted that our CO_2 proxy results were unreliable – such a dramatic rise in atmospheric CO_2 would certainly lead to an increased greenhouse effect and a rise in temperatures, and again the temperature

proxy data presented in Chapter 5 show a decline rather than rise in temperature. The rapid rise in carbonate $\delta^{13}C$ values seen over CM6 are at odds with the more gradual rise which would be observed if silicate weathering were the driver.

On the basis of these model results, it seems that a silicate weathering reduction is untenable as a driver of the changes seen over CM6.

The success of the organic burial experiments to match both the carbonate carbon isotope and atmospheric carbon dioxide records suggest that organic carbon burial may be the main driver of CM6. The suite of models produced have varying degrees of success in matching each of the three records. The models which match most closely the carbonate carbon isotope record (which has the highest degree of analytical accuracy and the fewest underlying uncertainties), are within the uncertainties of the CO_2 records. The consistency between the model and two independent carbon system proxies is strong evidence that organic matter burial could drive the observed changes. The models which most closely match the data are those which are driven by twin pulses of organic matter burial, which may not be surprising given the twin peaks of CM6. These models were driven with instantaneous increases of organic matter burial of 50%. This is a high figure, and whether this is a value which is plausible is beyond the scope of this work, however the size of CM6 does suggest a major shift in the carbon isotope system at the time, and so large and perhaps unique events in the reorganisation of carbon burial may not be out of the question. It should also be noted that although the fit between model and data is very good, the model itself and the driving perturbations are very simplistic, and, as discussed further below, there may not be only one mechanism at work driving the changes seen at CM6. It may be that further feedbacks and magnifying effects not dealt with in KA1 (such as methane and

temperature variations) could also be important. Nonetheless, the close fit between the data and model, unique amongst all scenarios tested here, should be seen as strong evidence that the two proxy records (CO_2 and carbonate $\delta^{13}C$) are pointing towards what has become the traditional explanation for this and many other shifts in carbon isotope records; that organic matter burial changes drive what is seen in the carbonate carbon isotope records. It should be noted, however, that it is the combination of CO_2 and carbon isotope records at CM6 which point strongly to organic matter burial, and this does not strengthen the case for suggesting that all carbon isotope excursions can be directly interpreted as organic matter burial indicators without further secondary proxy evidence.

Secondary effects which may be important when interpreting the records could include methane cycling and the effect of changing ocean temperatures. The methane models presented above suggest that although methane can have a effect on the global carbon isotope reservoir, the effect is likely to be minor. Although methane fluxes are not well known now or in the past, it is unlikely that they were large enough to have a significant effect. Although the second methane experiment was able to demonstrate that rapid changes in carbon isotopes can be driven by methane flux changes, the size of methane flux required to come close to even the background changes in carbonate $\delta^{13}C$ is unlikely to be reasonable in a real world scenario, and the size of flux required to cause the large excursions of the Monterey excursion as envisioned by Berger (2007) make methane an unlikely driver of the CM events.

Temperature change should also be considered. As shown above, a global change in ocean temperature can have a significant effect on the carbonate record. Whether the large temperature drop demonstrated by our records is reasonable (see discussion in

Chapter 5) and whether similar temperature changes happened globally (which would be required to cause the modelled change in $\delta^{13}C$) is uncertain, but the model does demonstrate that simple temperature changes need to be considered when interpreting carbonate $\delta^{13}C$ records.

The final volcanic flux experiments demonstrated that although changes in volcanism can potentially lead to perturbations in the carbon isotope system, it is unlikely that this mechanism could lead to an excursion similar in nature to CM6. Both the size and rapidity of change in both the carbon isotope and carbon dioxide proxy records are inconsistent with the variations which could be reasonably caused by variations in global volcanism.

6.2 Palaeoproductivity records across CM6

6.2.1 Introduction and Assumptions

The modelling results discussed in section 6.1.10 suggest that the most likely cause of CM6 is an increase in the burial of organic matter. One mechanism to increase the burial of organic carbon would be increasing the primary productivity of the ocean, driving increased export productivity and likely greater burial of organic matter. It is therefore necessary to look for any evidence of increased productivity over CM6.

The recently published multi-site record of Miocene productivity in the Atlantic of Diester-Haass et al. (2009) is reproduced in Figure 54 (Site 1265 is not reproduced here as it does not show a clearly defined CM6). This record, produced from benthic foraminiferal accumulation rates (BFAR) does not show a long term increase over the longer-term Monterey carbon isotope excursion, and the authors conclude that there is little evidence of increased productivity over the whole of the excursion. However closer inspection of the record does reveal some correlation between the productivity and carbon isotope records at CM6, and hints that perhaps there is increased productivity during this particular carbon maximum event.

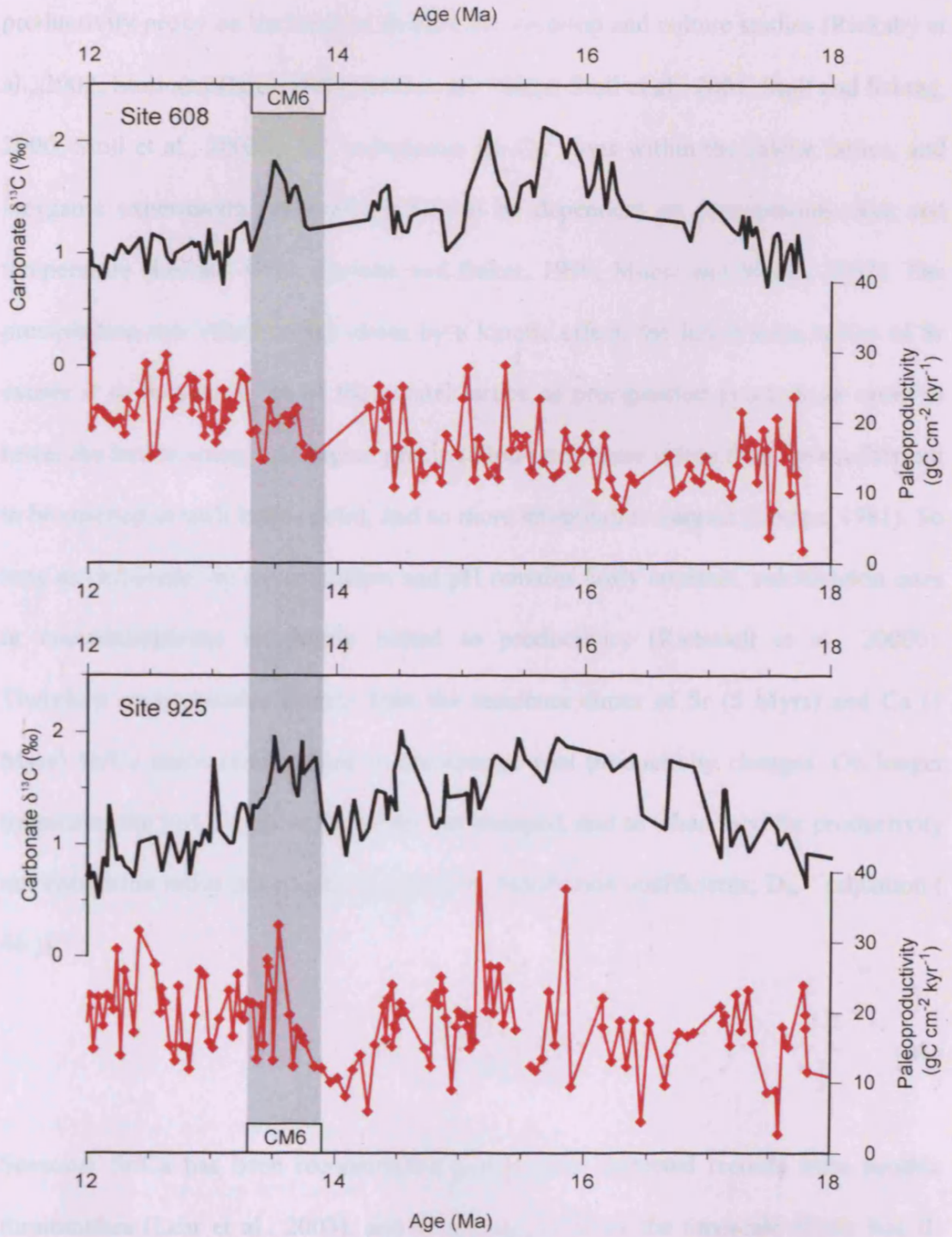

Figure 54: Benthic foraminiferal carbon isotopes and palaeoproductivity records (in gC cm^{-2} kyr^{-1}) derived from benthic foraminiferal mass accumulation rates from (Diester-Haass et al., 2009). Records are from ODP sites 608 in the North Atlantic and 925 in the equatorial pacific.

An alternative productivity proxy to the BFAR used by Diester-Haass et al. (2009) is the use of carbonate Sr/Ca ratios. Coccolith carbonate Sr/Ca has been suggested as a productivity proxy on the basis of down-core, core-top and culture studies (Rickaby et al., 2002; Stoll and Bains, 2003; Stoll et al., 2002a; Stoll et al., 2001; Stoll and Schrag, 2000; Stoll et al., 2002b). Sr^{2+} substitutes for Ca^{2+} ions within the calcite lattice, and inorganic experiments have shown this to be dependent on precipitation rates and temperature (Lorens, 1981; Malone and Baker, 1999; Mucci and Morse, 1983). The precipitation rate effect comes about by a kinetic effect, the larger ionic radius of Sr causes it to be forced out of the crystal lattice as precipitation proceeds in order to lower the lattice energy. At higher precipitation rates, there is less time for equilibrium to be reached at each lattice point, and so more strontium is trapped (Lorens, 1981). So long as carbonate ion concentration and pH remains fairly constant, calcification rates in coccolithophores is closely linked to productivity (Riebesell et al., 2000b). Therefore on timescales shorter than the residence times of Sr (5 Myrs) and Ca (1 Myrs) Sr/Ca ratios can be used to reconstruct past productivity changes. On longer timescales the Sr/Ca ratio of the ocean has changed, and so when used for productivity reconstruction ratios are usually reported as distribution coefficients; D_{Sr} (equation (46)).

$$D_{Sr} = \frac{Sr/Ca_{carbonate}}{Sr/Ca_{seawater}} \qquad (46)$$

Seawater Sr/Ca has been reconstructed using depth-corrected records from benthic foraminifera (Lear et al., 2003), and so a mean value of the timescale of the Ras Il-Pellegrin section can be estimated (Figure 55)

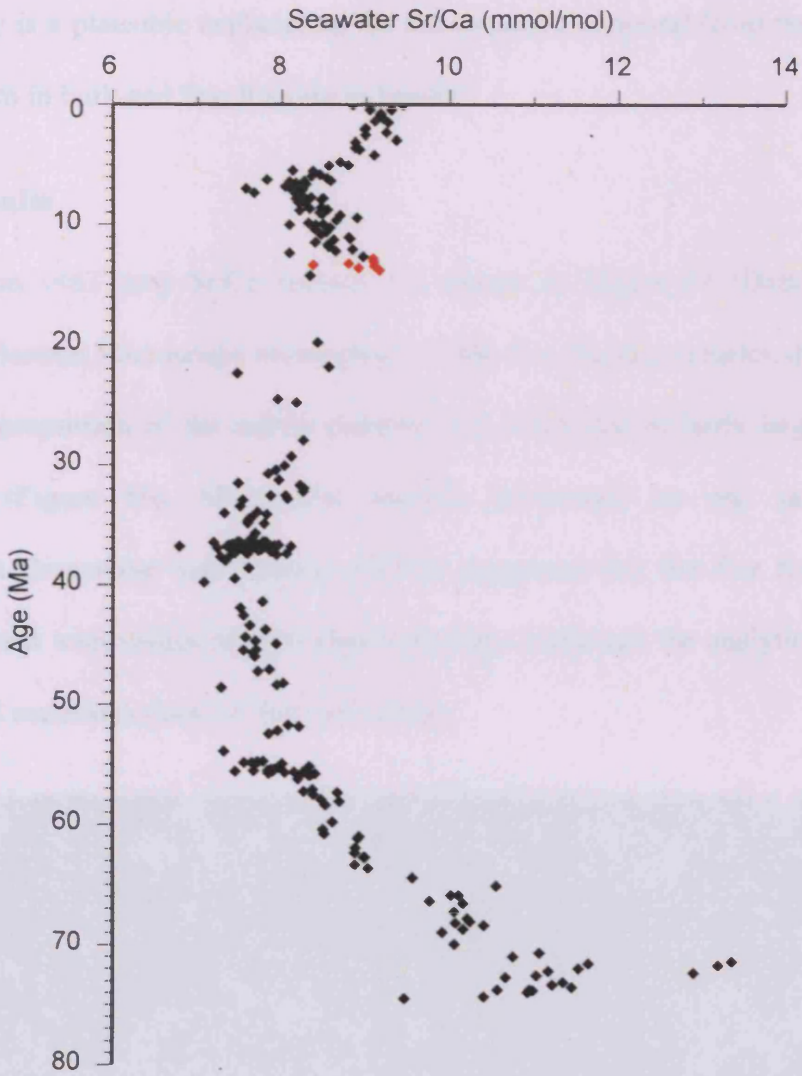

Figure 55 Cenozoic seawater Sr/Ca reconstructed from benthic foraminiferal records replotted from (Lear et al., 2003). The values corresponding to the timespan of the RIP section are highlighted in red, and give an average value of 8.9 mmol/mol over the period studied here.

The separation of a monospecific sample of coccoliths from a sediment sample is, although technically possible, a difficult and involved process (Stoll and Ziveri, 2002). Investigations into the derivation of a productivity signal from bulk and fine fraction sediment have therefore been undertaken, where the dominant source of analysed calcite is from coccoliths (Billups et al., 2004). These authors propose "that

productivity is a plausible explanation for the observed temporal [over the Cenozoic] Sr/Ca pattern in bulk and fine fraction sediment".

6.2.2 Results

Fine fraction (<63 μm) Sr/Ca records are shown in Figure 57 (Data Table 10). Scanning Electron Microscope investigation of the fine fraction samples showed that a significant proportion of the calcite material was composed of fairly large (~10 μm) coccoliths (Figure 56). Microprobe analysis performed on one sample using Wavelength Dispersive Spectrometry (WDS) suggested that the fine fraction value was consistent with values of individual coccoliths (although the analytical precision of the WDS method is poor for thin coccoliths).

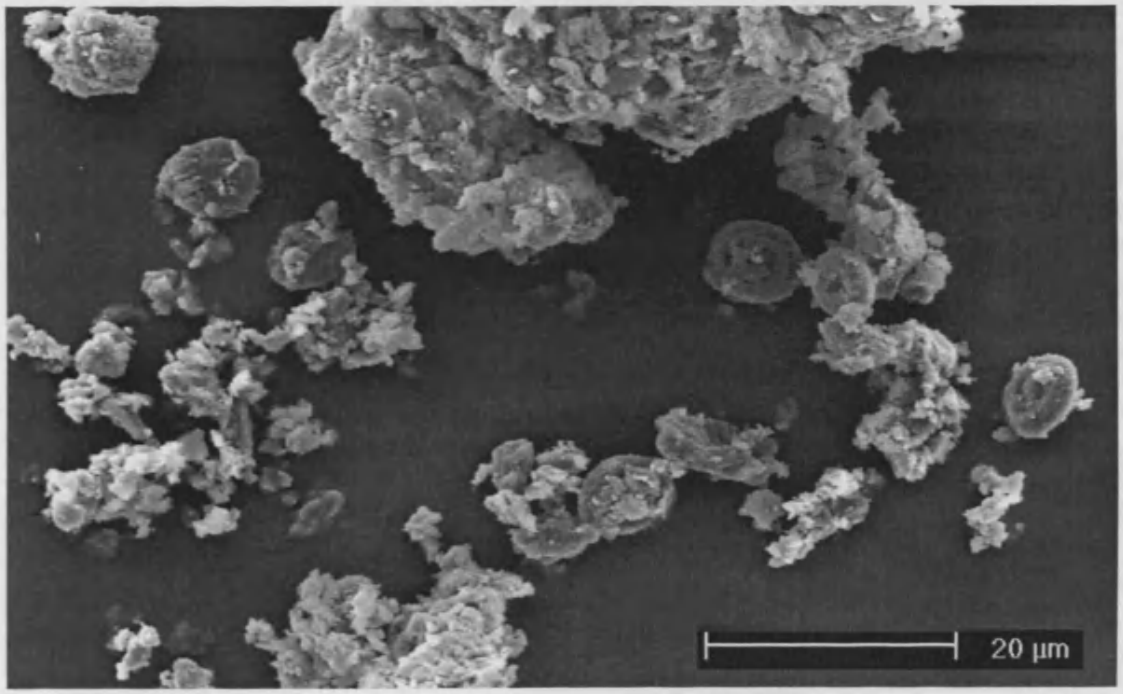

Figure 56: A typical SEM view of fine fraction (<63 μm) material (this from sample MT4) showing multiple large coccoliths. Note that the aggregate material in the top of the figure also contains multiple coccoliths.

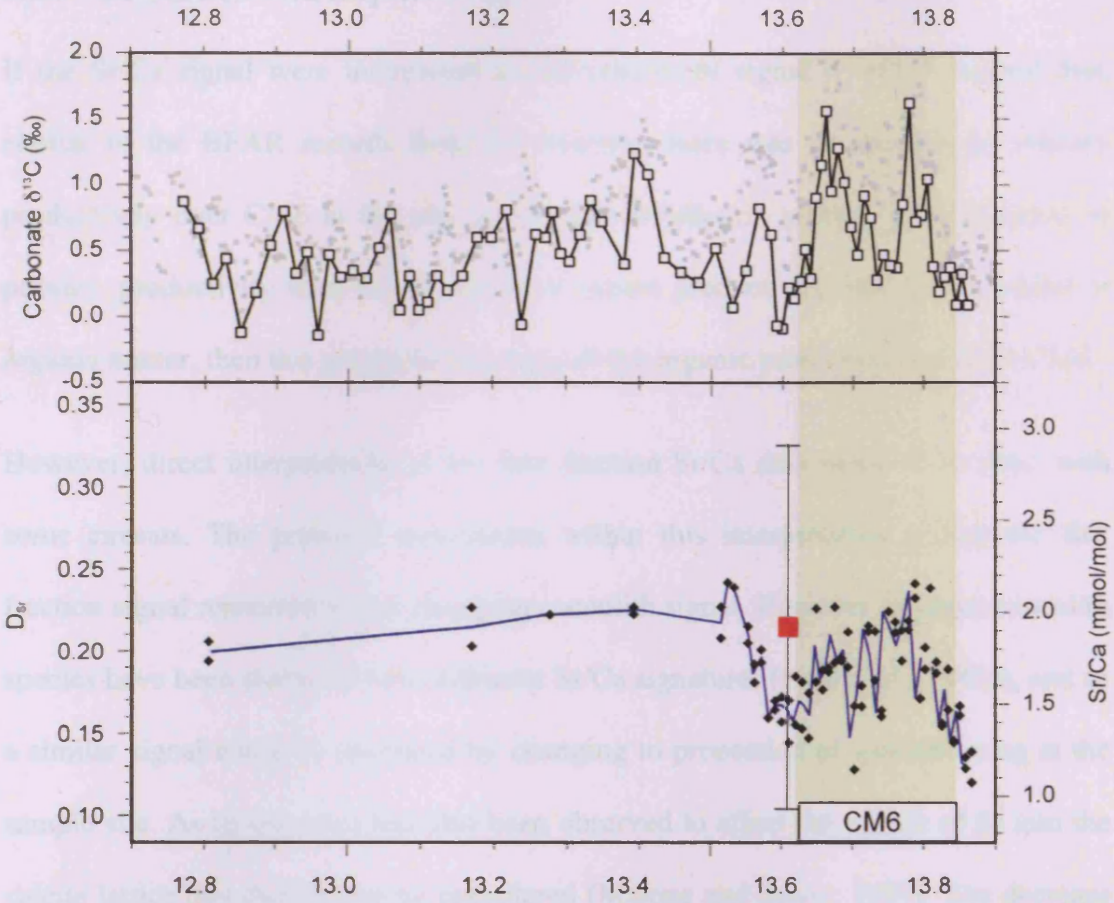

Figure 57: Carbonate carbon isotope records from RIP upper panel (black open squares and line are from this study, grey closed squares are the higher resolution work of Abels et al. (2005)) with CM6 highlighted in grey. Lower panel; fine fraction (< 63 µm) Sr/Ca records (mmol/mol, also shown as D_{Sr} using reconstructed Miocene seawater Sr/Ca (see text)), black closed diamonds with mean line in blue. Coccolith fraction as measured by analytical SEM (WDS) is shown as the red square with 2σ error bar.

Observed Sr/Ca increases from the start of the record from 1.1 mmol/mol to 2.2 mmol/mol over just 100 kyrs, reaching a peak coinciding with CM6a. The values then decrease over before and across CM6b, dropping to 1.5 mmol/mol over the next 200 kyrs, reaching a local minimum at 13.6 Ma before increasing again to 2.0 mmol/mol and stabilising.

6.2.3 Discussion and Implications

If the Sr/Ca signal were interpreted as a productivity signal it would suggest that, similar to the BFAR records from the Atlantic, there was an increase in primary productivity over CM6 at the site of the Ras Il-Pellegrin section. If an increase in primary productivity then led to increased export productivity and greater burial of organic matter, then this would further support the organic burial hypothesis for CM6.

However, direct interpretation of the fine fraction Sr/Ca data needs to be done with some caveats. The principle assumption within this interpretation is that the fine fraction signal represents a true changing coccolith signal. However different coccolith species have been shown to have different Sr/Ca signatures (Stoll et al., 2002a), and so a similar signal could be produced by changing to proportion of species living at the sample site. As temperature has also been observed to affect the uptake of Sr into the calcite lattice this should also be considered (Malone and Baker, 1999). The decrease in temperature observed across the E3 ice growth event could also produce an increase in Sr/Ca ratios, although the proportion of the signal which could be explained by this mechanism is difficult to ascertain.

Beyond the difficulties of Sr/Ca ratios in coccoliths themselves, an underlying assumption here is that the fine fraction material is predominantly coccolith and coccolith debris, and that the observed signal is representative of coccolith material. Variations in the D_{Sr} of planktonic foraminifera have been shown to result from test size, growth rate and temperature (Elderfield et al., 2000), and benthic foraminifera D_{Sr} has been shown to vary with water depth (McCorkle et al., 1995). Addition of calcitic material from these sources could have the potential to severely limit the potential of fine fraction Sr/Ca as a productivity indicator.

Nevertheless, the agreement in the positive trends of BFAR and fine fraction Sr/Ca productivity indicators over CM6 should be taken into account when considering the evidence for the various hypotheses for CM6.

6.3 The Monterey Excursion

The Monterey excursion is a long term positive carbon isotope excursion which spans from ~13.5 to ~16.9 Ma. The excursion coincides with a period of global warmth and high sea levels and the cause of the isotope excursion remains unclear (Vincent et al., 1985; Vincent and Berger, 1985; Kennett, 1986; Woodruff and Savin, 1991; Flower and Kennett, 1993, 1994; Holbourn et al., 2004, 2007). To span the entire excursion, records from the Ras il-Pellegrin and Moria sections detailed elsewhere (Chapters 3 and 4) are combined with a record from ODP Site 761B. ODP Site 761B lies on the Wombat Plateau, north west of Australia (16° 44.23' S, 115° 32.10' E; Figure 58). Samples from this site were analysed for bulk carbonate carbon and bulk organic carbon stable isotopes (Figure 59; Data Table 11 and Data Table 12; sections 2.1 and 2.2). The long term bulk organic and carbonate carbon isotope records show a long term positive excursion in both the carbonate and bulk organic carbon isotope records (Figure 59).

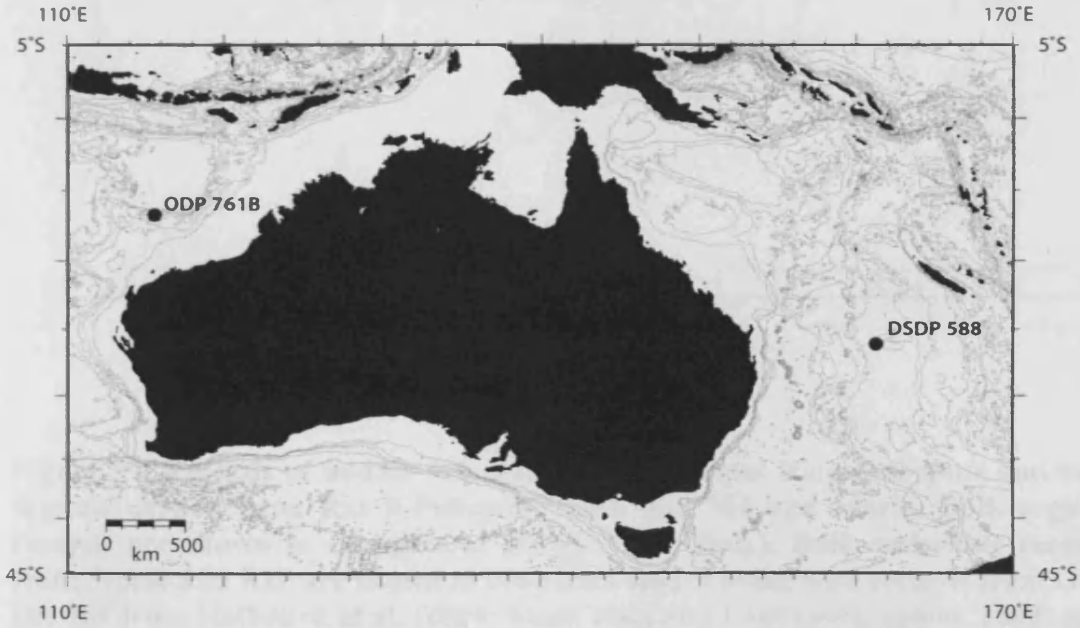

Figure 58 (previous page): ODP Site 761B lies on the Wombat Plateau, northwest of Australia (Leg 122; 16° 44.23' S, 115° 32.10' E) at a water depth of 2168 m. DSDP Site 588 lies on the Lord Howe Rise, east of Australia (Leg 90; 26° 6.7' S 161° 13.6' E).

To better visualise the relationship between carbonate and organic carbon isotope records, $\Delta\delta^{13}C$ can be defined as the difference between the two records (equation (47))

$$\Delta\delta^{13}C = \delta^{13}C_{carb} - \delta^{13}C_{org} \qquad (47)$$

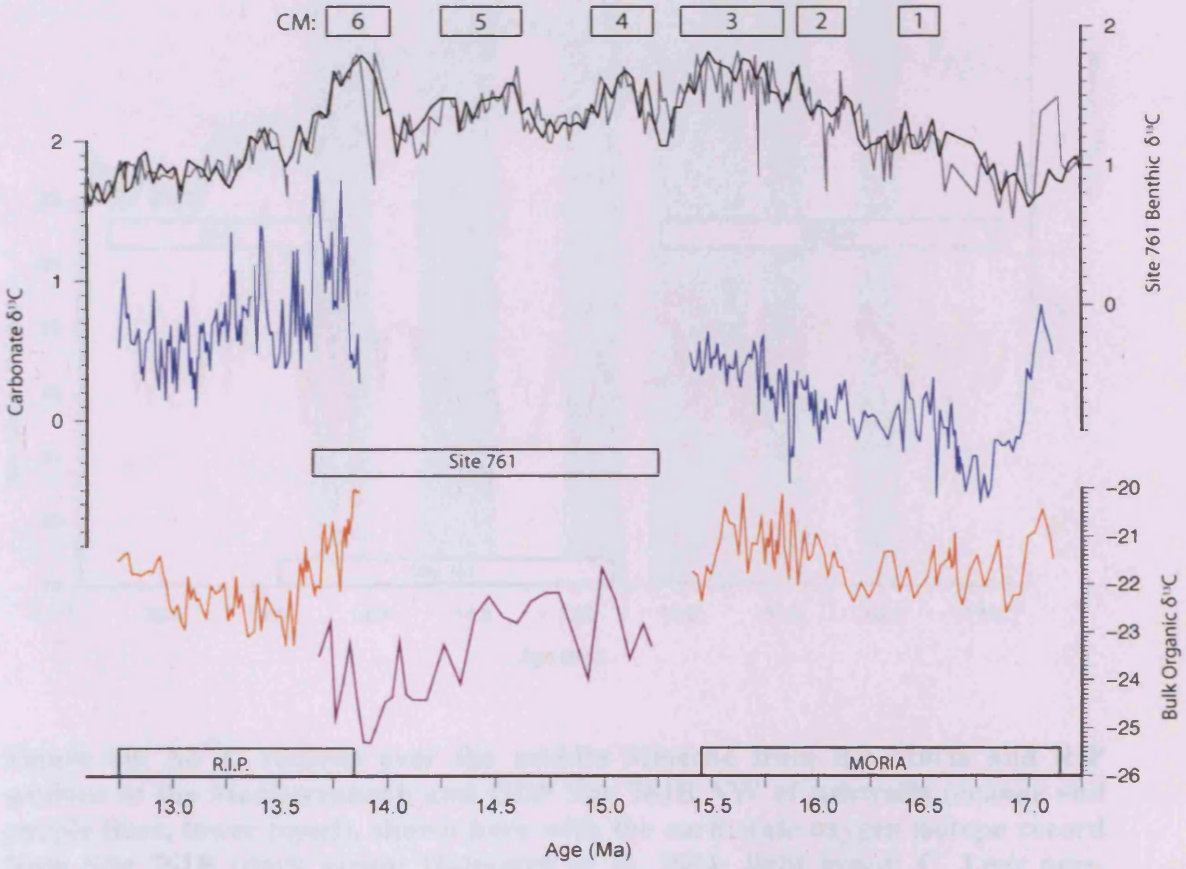

Figure 59: Records of middle Miocene carbon isotopes from carbonate and bulk organic carbon from Ras il-Pellegrin, ODP site 761 and Moria. Bulk organic records are shown in orange and purple (this study). Bulk carbonate records from Moria and RIP are shown in blue (this study) along with records from ODP site 761 from Holbourn et al. (2004; black line) and Lear (pers. comm. 2009; grey line). The position of CM events is indicated by the boxes above follow the definitions of Holbourn et al. (2004) and Woodruff and Savin (1991), see Table 13.

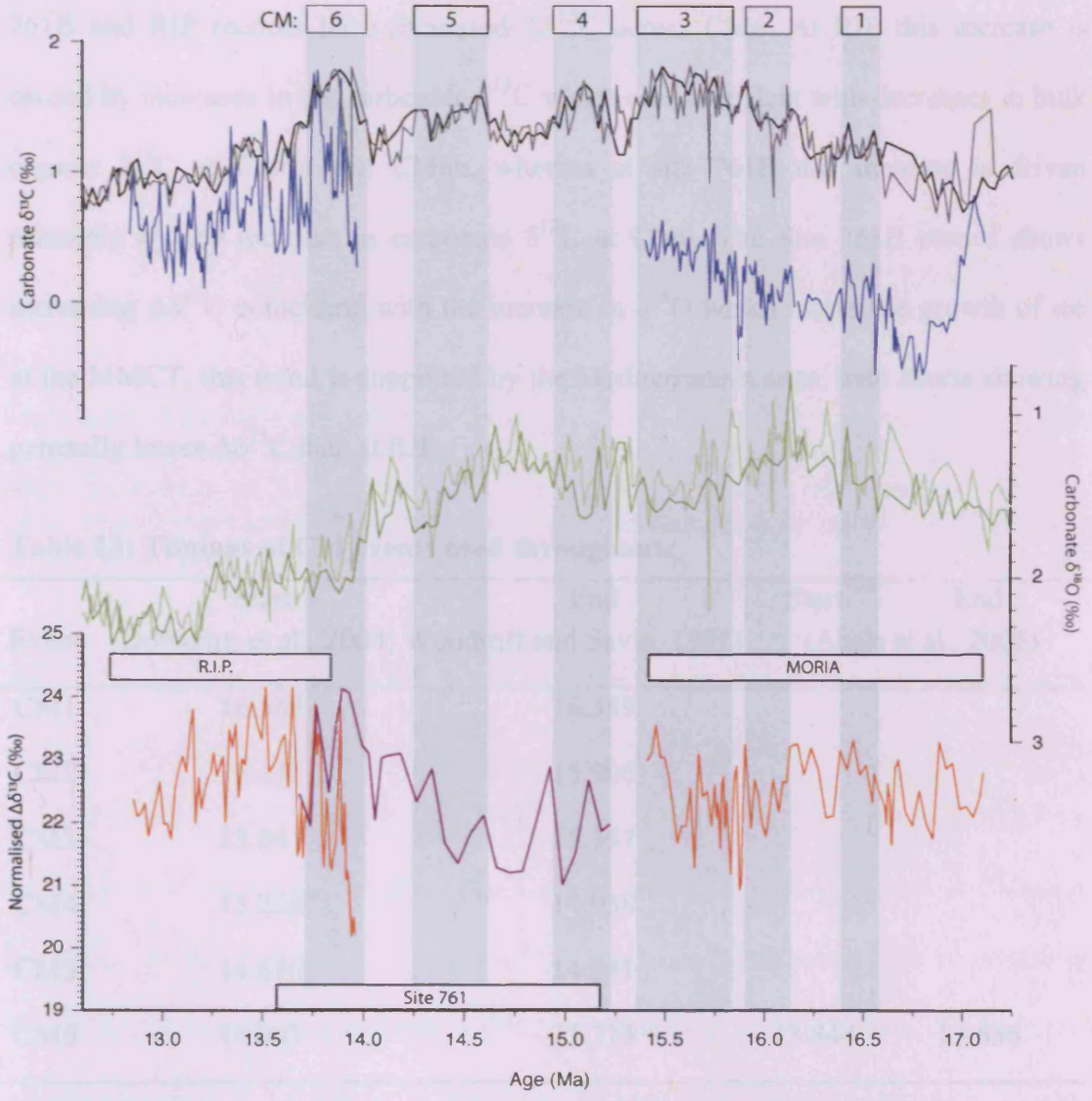

Figure 60: $\Delta\delta^{13}C$ records over the middle Miocene from the Moria and RIP sections in the Mediterranean and ODP Site 761B NW of Australia (orange and purple lines, lower panel), shown here with the carbonate oxygen isotope record from Site 761B (dark green; Holbourn et al. 2004; light green; C. Lear pers. comm., 2009) and carbonate carbon isotope records from Site 761B (black line; Holbourn et al., 2004; grey line; C. Lear pers. comm., 2009) and from RIP and Moria (blue lines). The positions of CM events are marked by shading and follow the definitions of Holbourn et al., (2004) and Woodruff and Savin (1991). Due to slight differences in the age models of RIP and Site 761B the RIP record has been shifted by 0.09Myrs based on the position of CM6 in the $\delta^{13}C$ record for each site. $\Delta\delta^{13}C$ records have been normalised to their individual means.

To construct the composite record shown in Figure 60 the $\Delta\delta^{13}C$ records for each site are normalised to their means. The $\Delta\delta^{13}C$ record (Figure 60) shows that both the site 761B and RIP records have increased $\Delta\delta^{13}C$ across CM6. At RIP this increase is caused by increases in the carbonate $\delta^{13}C$ which are coincident with decreases in bulk organic $\delta^{13}C$ at CM6a and CM6b, whereas at site 761B this increase is driven primarily by the increase in carbonate $\delta^{13}C$ at CM6. The Site 761B record shows increasing $\Delta\delta^{13}C$ coinciding with the increase in $\delta^{18}O$ which marks the growth of ice at the MMCT, this trend is supported by the Mediterranean sites, with Moria showing generally lower $\Delta\delta^{13}C$ than at RIP.

Table 13: Timings of CM events used throughout.

Event	Start (Holbourn et al., 2004; Woodruff and Savin, 1991)	End (Holbourn et al., 2004; Woodruff and Savin, 1991)	Start (Abels et al., 2005)	End (Abels et al., 2005)
CM1	16.583	16.389		
CM2	16.131	15.906		
CM3	15.841	15.357		
CM4	15.228	14.938		
CM5	14.616	14.241		
CM6	14.003	13.713	13.844	13.636

The interpretation of bulk organic carbon isotopes is complicated by uncertainty with regard to the source of the organic matter. The possible interpretations are covered in greater detail in section 3.3 but are briefly: (1) A single marine source, allowing interpretation of changes in ε_p in concert with carbonate $\delta^{13}C$, (2) changes in source organism but predominantly a marine source, (3) changes in the contribution of terrestrial OM reaching the site, (4) changes in ocean stratification.

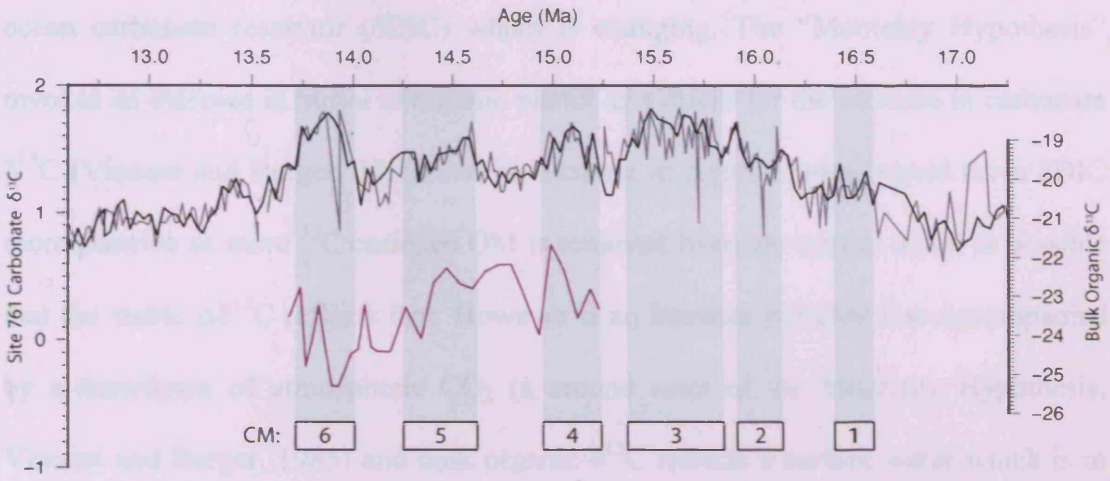

Figure 61: The bulk organic carbon isotope record (purple line; this study) and carbonate carbon isotope record (grey line; C. Lear pers. comm., 2009; black line; Holbourn et al., 2004) from ODP Site 761. The positions of Carbon Maximum events are indicated by shading and follow the definitions of Holbourn et al. (2004) and Woodruff and Savin (1991).

As (2) and (3) are variations which will be specific to a single site, the addition of a second record can go some way to determining whether these are plausible interpretations. This is possible for CM6 with the addition of a record from ODP Site 761 (Figure 61) to the records from Ras il-Pellegrin (Figure 62). Both records do show increases in $\Delta\delta^{13}C$ over CM6, however for the Site 761B record this is primarily driven by the increase in carbonate $\delta^{13}C$ and, unlike at RIP there is no statistically significant correlation (positive or negative) between carbonate and organic $\delta^{13}C$ over CM6 at 761B ($r=0.2$, $n=10$, $p>0.05$) it is therefore not possible to rule out local variations as the cause of the negative correlation between carbonate and organic $\delta^{13}C$ over CM6 at RIP.

At the start of the Monterrey Excursion, between 16.9 and 15.5 Ma, carbonate and organic $\delta^{13}C$ track each other closely, resulting in essentially flat $\Delta\delta^{13}C$ (Figure 59; Figure 60). As whatever is driving the increase in $\delta^{13}C$ is affecting both organic and carbonate $\delta^{13}C$ equally, is seems plausible that it is the $\delta^{13}C$ of the whole

ocean carbonate reservoir (δDIC) which is changing. The "Monterey Hypothesis" invokes an increase in burial of organic matter as a driver for the increase in carbonate $\delta^{13}C$ (Vincent and Berger, 1985) and an increase in organic burial would drive δDIC more positive as more ^{12}C enriched OM is removed from the system and it is possible that the stable $\Delta\delta^{13}C$ reflects that. However if an increase in burial was accompanied by a drawdown of atmospheric CO_2 (a second tenet of the Monterey Hypothesis; Vincent and Berger, 1985) and bulk organic $\delta^{13}C$ reflects a surface water which is in equilibrium with the atmosphere, then $\Delta\delta^{13}C$ would be expected to decrease as atmospheric CO_2 and therefore ε_p decreased. The evidence from RIP is that $\Delta\delta^{13}C$ is not reflecting such a reservoir, as the CO_2 reconstructions presented in Chapter 5 record stable or decreasing CO_2 as $\Delta\delta^{13}C$ increased, it is possible therefore that $\Delta\delta^{13}C$ represents a broader organic matter reservoir and not just that in equilibrium with atmospheric CO_2. It is therefore plausible that the main driver for the $\delta^{13}C$ of this reservoir at the start of the Monterey Excursion is changing δDIC driven by an increase in OM burial, and that the $\Delta\delta^{13}C$ presented here supports the Monterey Hypothesis.

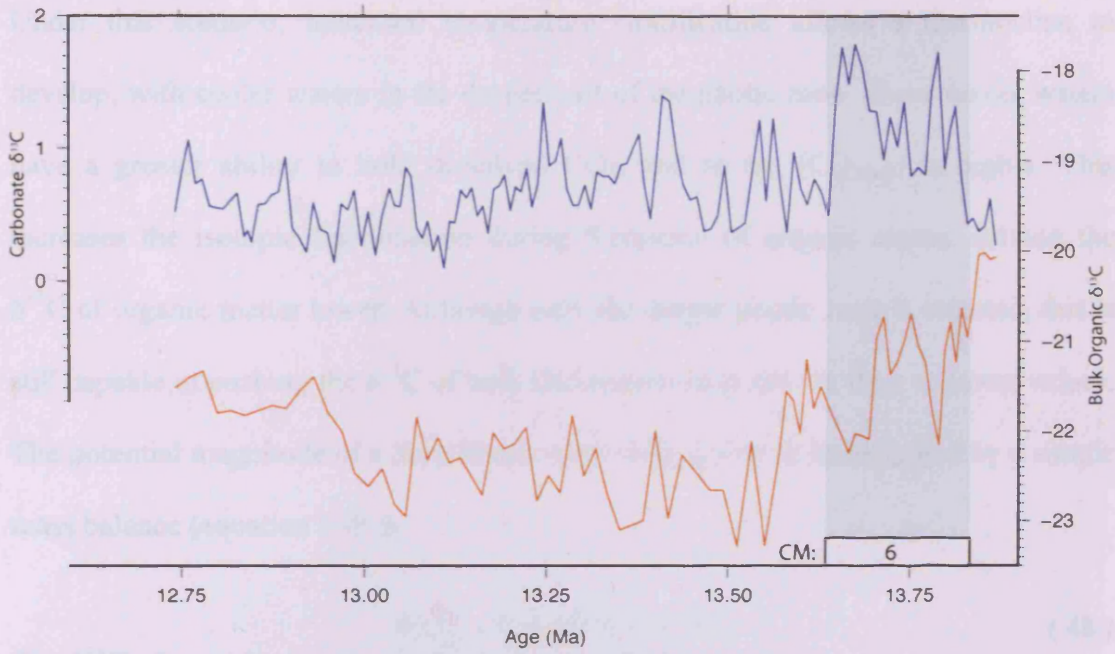

Figure 62: The bulk organic carbon isotope record (orange line) and carbonate carbon isotope record (blue line) from Ras il-Pellegrin. The position of the CM6 event is indicated by shading.

Following the period at the start of the Monterey Excursion where $\Delta\delta^{13}C$ is stable is an increase in $\Delta\delta^{13}C$ from ~15.5 to 13.5 Ma. If $\Delta\delta^{13}C$ is being driven by changes in ε_p forced by atmospheric CO_2, then the increase in $\Delta\delta^{13}C$ from ~15 to 13.5 Ma would suggest an increase in CO_2. An increase in CO_2 is supported by neither the boron nor alkenone CO_2 reconstructions presented in Chapter 5 for the period over CM6, nor is it supported by longer term, lower resolution records which show either stable or decreasing CO_2 over this period (Pagani et al., 1999; Pearson and Palmer, 2000; Kürschner et al., 2008) and so is not the preferred interpretation. As the bulk organic $\delta^{13}C$ more likely incorporates material from throughout the whole of the photic zone, rather than purely the near surface (as alkenone $\delta^{13}C$ does), it is plausible that data would seem to support the hypothesis that there were changes in ocean stratification in the Miocene record, and that it is this which leads to the increase in $\Delta\delta^{13}C$.

Under this scenario, increased temperature stratification allows a thermocline to develop, with cooler waters in the deeper part of the photic zone. These cooler waters have a greater ability to hold dissolved CO_2, and so the $[CO_{2(aq)}]$ is higher. This increases the isotopic fractionation during formation of organic matter, driving the $\delta^{13}C$ of organic matter lower. Although only the deeper photic zone is affected, this is still capable of pushing the $\delta^{13}C$ of bulk OM preserved at the sea floor to lower values. The potential magnitude of a deep photic zone cooling can be investigated by a simple mass balance (equation (48)).

$$\delta_x(F_S + F_D) = \delta_S F_S + \delta_D F_D \qquad \textbf{(48)}$$

$\delta_x = \delta^{13}C$ of organic matter exported to the sea floor.
$\delta_S = \delta^{13}C$ of organic matter exported from the shallow photic zone.
$\delta_D = \delta^{13}C$ of organic matter exported from the deep photic zone.
F_S = Proportion of exported organic matter sourced from the shallow photic zone.
F_D = Proportion of exported organic matter sourced from the deep photic zone.

The sensitivity of the $\delta^{13}C$ of organic matter exported from the deep photic zone to temperature can be calculated using equations (12) – (22) and is ~0.4‰/°C for an atmospheric CO_2 level of ~300ppm. Coupling this sensitivity with the mass balance shown in equation (48) allows estimation of the proportion of OM export from the photic zone which is affected by a decrease in temperature in order to drive a specific change in $\Delta\delta^{13}C$ (Figure 63). This model assumes that all organic matter reaching the sediment record is effected by $[CO_{2(aq)}]$ in the same way, and assumes that this sensitivity is constant, this seems unlikely, and so the F_D predicted for a given temperature and $\delta^{13}C$ are likely to be an underestimate.

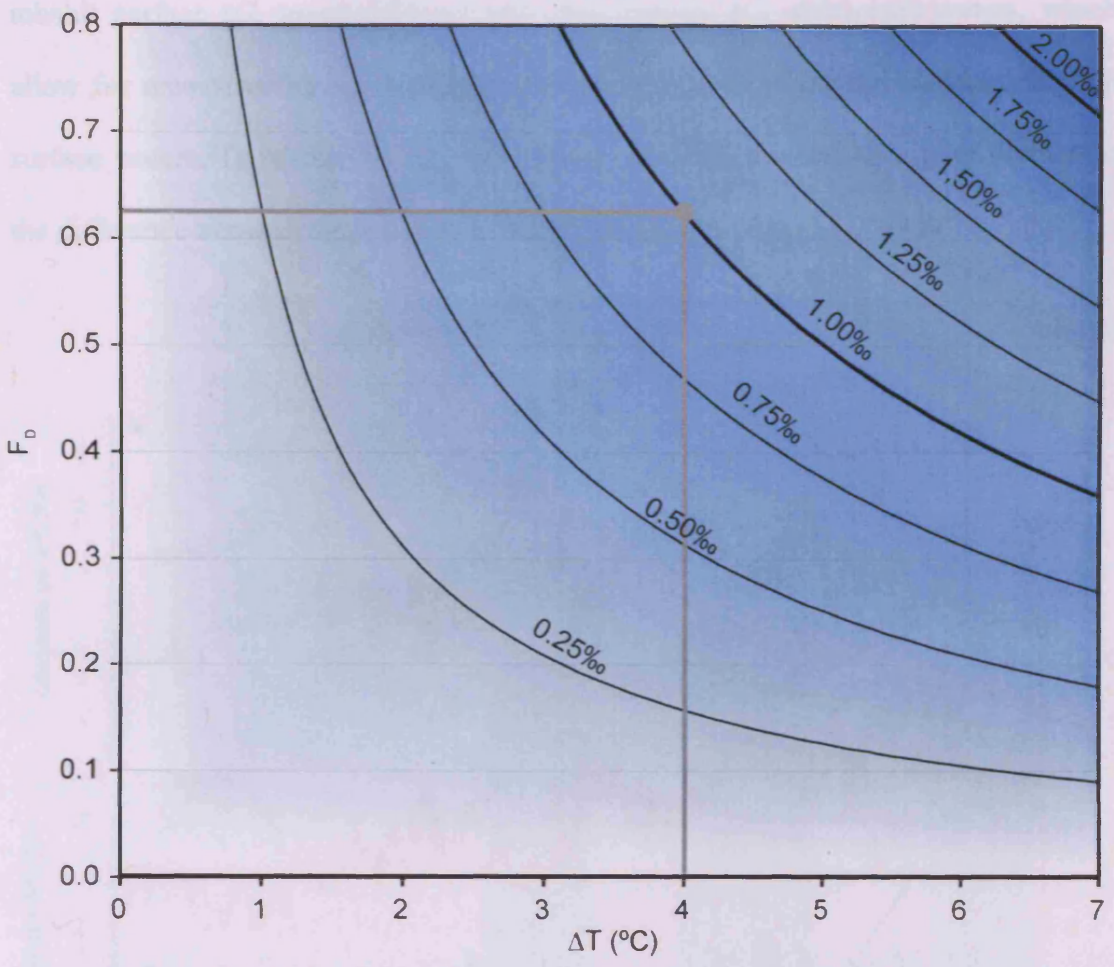

Figure 63: Relationship between changes in deep photic zone temperature (ΔT) and the proportion of the photic zone affected (F_D) in order to drive a specified change in the $\delta^{13}C$ of exported organic matter (δ_x; labelled lines). The temperature dependent sensitivity of 0.4‰/°C used to construct this plot is valid for an atmospheric CO_2 of ~300 ppm, which is the mean CO_2 estimated over CM6. For example, to drive a 1‰ reduction in δ_x driven by a 4°C drop in temperature requires 63% of the photic zone to undergo such a change in temperature (see grey lines).

If the changes in the $\Delta\delta^{13}C$ record do represent global changes in ocean stratification then it should be possible to identify these trends in other records from other sites. Flower and Kennett (1993a) generated high resolution stable isotope records from *Globoquadrina dehiscens* and *Globerigerinoides quadrilobatus* from DSDP Site 588 (S. Pacific; 26° 6.7'S, 116° 13.6'E; Figure 58). These two planktonic foraminifera

inhabit surface (*G. quadrilobatus*) and deep surface (*G. dehiscens*) waters, which allow for reconstruction of the temperature difference between the surface and deep surface waters. To identify changes in thermal stratification $\Delta\delta^{18}O$ can be defined as the difference between the records from the two species (equation **(49)**).

$$\Delta\delta^{18}O = \delta^{18}O_{G.quadrilobatus} - \delta^{18}O_{G.\ dehiscens} \qquad (49)$$

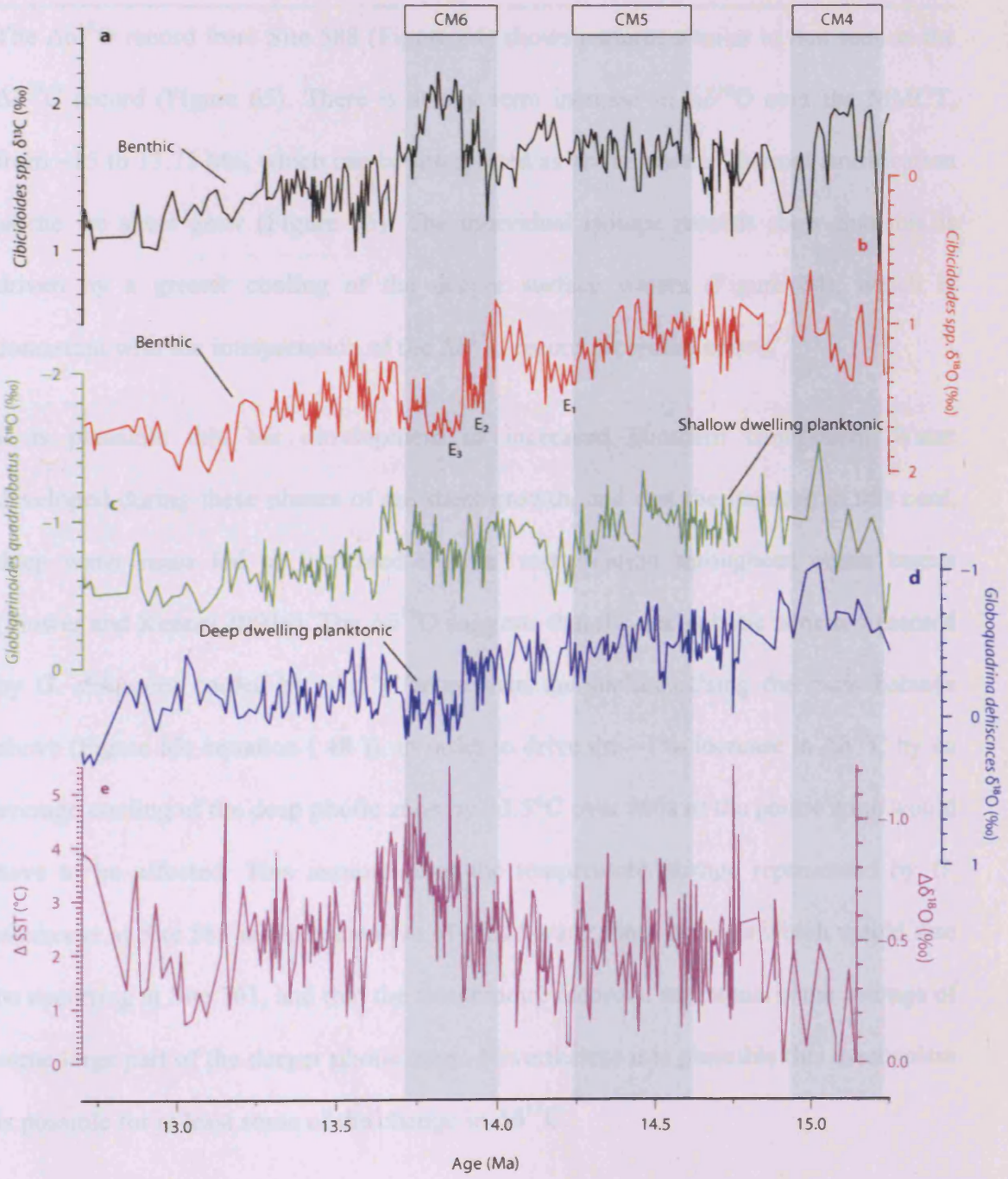

Figure 64 previous page: The carbon isotope record from benthic foraminifera (*Cibicidoides* sp.) from DSDP Site 588 shows the familiar pattern of CM events (panel a; black line), with the stepped transition of the MMCT visible in the oxygen isotope record (panel b; red line). By using shallow dwelling foraminifera *Globigerinoides quadrilobatus* (panel c; green line) and deep surface dweller *Globoquadrina dehiscens* (panel d; blue line) a record of $\Delta\delta^{18}O$ can be constructed (panel e; pink line). Also shown here is a equivalent ΔSST axis generated from the $\Delta\delta^{18}O$ using the temperature sensitivity of Erez and Luz (1983) for *Globigerinoides sacculifer*. All data are from Flower and Kennett 1993a, plotted on an age model updated by Holbourn et al. 2007.

The $\Delta\delta^{18}O$ record from Site 588 (Figure 64) shows patterns similar to that seen in the $\Delta\delta^{13}C$ record (Figure 65). There is a long term increase in $\Delta\delta^{18}O$ over the MMCT, from ~15 to 13.75 Ma, which can be interpreted as an increase in thermal stratification as the ice sheet grew (Figure 65). The individual isotope records show that this is driven by a greater cooling of the deeper surface waters (Figure 64), which is consistent with the interpretation of the $\Delta\delta^{13}C$ record presented above.

It is plausible that the development of increased Southern Component Water developed during these phases of ice sheet growth, and that the increase in this cool, deep water mass led to increased thermal stratification throughout ocean basins (Flower and Kennet 1993a). The $\Delta\delta^{18}O$ suggests that the deep photic zone represented by *G. dehiscens* cooled by ~3.5°C more than the surface. Using the mass balance above (Figure 63; equation **(48)**), in order to drive the ~1‰ increase in $\Delta\delta^{13}C$ by an average cooling of the deep photic zone by ~3.5°C over 80% of the photic zone would have to be affected. This assumes that the temperature change represented by *G. dehiscens* at Site 588 is representative of broad water mass changes which would also be occurring at Site 761, and that the temperature recorded represents some average of some large part of the deeper photic zone. Nevertheless it is plausible this mechanism is possible for at least some of the change in $\Delta\delta^{13}C$.

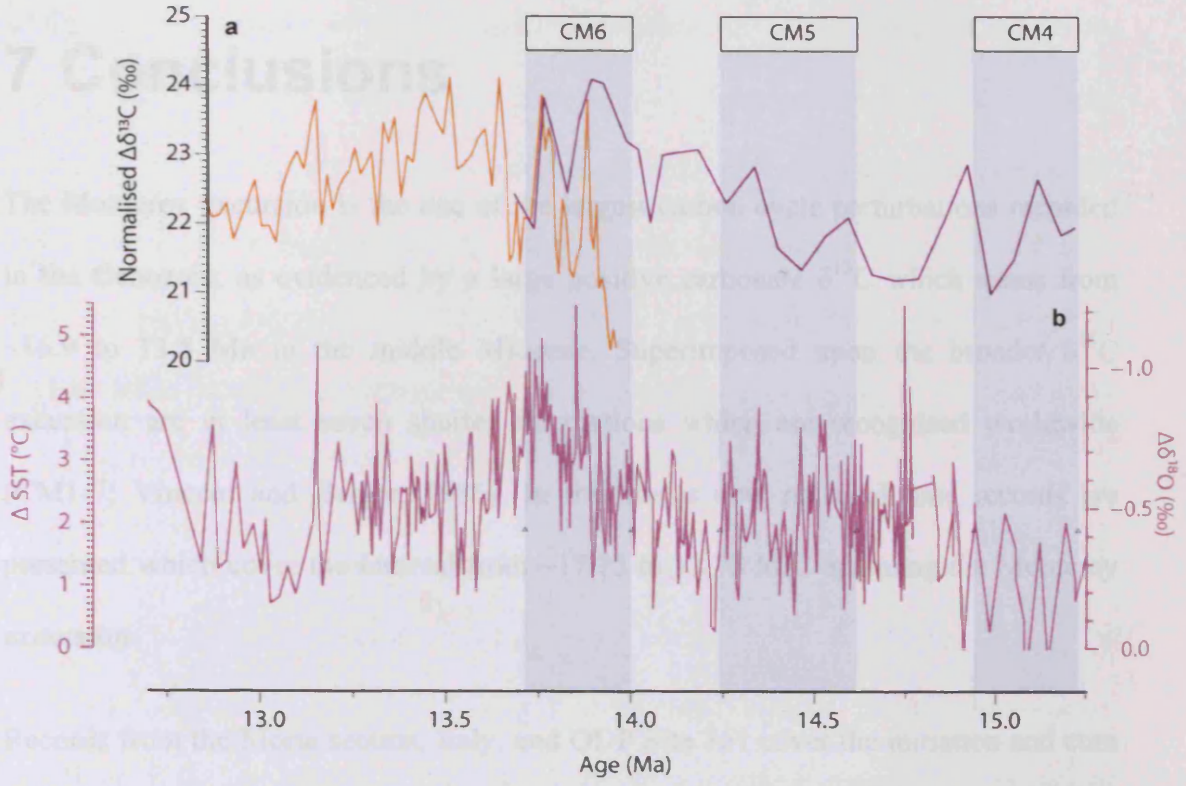

Figure 65: $\Delta\delta^{13}C$ records from Site 761B (panel a; purple line) and RIP (panel a; orange line) increase at the same time as the increase $\Delta\delta^{18}O$ seen at Site 588 (panel b; pink line; Flower and Kennett, 1993a). The timing CM events are shown as grey bars, and follow the definitions of Holbourn et al. (2004) and Woodruff and Savin (1991).

7 Conclusions

The Monterey excursion is the one of the largest carbon cycle perturbations recorded in the Cenozoic, as evidenced by a large positive carbonate $\delta^{13}C$ which spans from ~16.9 to 13.5 Ma in the middle Miocene. Superimposed upon the broader $\delta^{13}C$ excursion are at least seven shorter fluctuations which are recognised worldwide (CM1-7; Vincent and Berger, 1985). In this thesis new palaeoclimate records are presented which cover the interval from ~17.75 to 12.75 Ma, spanning the Monterey excursion.

Records from the Moria section, Italy, and ODP Site 761 cover the initiation and core of the Monterey excursion, and span the interval of growth of the East Antarctic Ice Sheet (EAIS) which is represented by the Middle Miocene Climate Transition (MMCT). Coupled records of bulk organic and carbonate carbon from these sites suggest that the central tenet of the Monterey Hypothesis, that the carbonate $\delta^{13}C$ excursion is driven by increased OM burial, is correct. Furthermore, these records show tentative evidence of enhanced oceanic temperature stratification as the MMCT progressed.

The Ras il-Pellegrin (RIP) section, Malta affords a unique opportunity to study the largest of the CM events; CM6, at a site where a simple tectonic history and high sedimentation rate have resulted in exceptional preservation of both carbonate microfossils and organic biomarkers. The multi-proxy approach followed here allowed for multiple records of pCO_2, temperature and other climate parameters to be reconstructed at an unprecedented temporal resolution over the event. Both alkenone and boron palaeobarometry records show a ~50 ppm CO_2 decrease during CM6. The

pCO_2 decrease, coupled with the magnitude of the carbon isotope excursion and results from carbon system models, are consistent with an increase in organic carbon burial, implying that the recently proposed silicate weathering hypothesis (Shevenell et al., 2008) is untenable. Mg/Ca and $U_{37}^{K'}$ based temperature reconstructions at RIP show high sea surface temperatures (SST, ~30°C) throughout the study interval, with the highest SSTs recorded immediately prior to CM6 declining rapidly at the start of the record coincident with the last phase of EAIS growth ("E3").

Atmospheric pCO_2 was near 300 ppm throughout the interval covered by RIP, somewhat higher than estimates from previous lower resolution alkenone- (Pagani et al., 1999) and boron-based (Pearson and Palmer, 2000) studies. These differences are attributed to the use of more accurate (and higher) sea surface temperatures in the case of the alkenone estimates and a combination of more accurate $\delta^{11}B$ measurements and better foraminiferal preservation at RIP in the case of the $\delta^{11}B$ estimates. Crucially, the pCO_2 estimates presented here suggest an emerging consensus for Miocene pCO_2 between these latest alkenone, boron isotope and leaf stomatal (Kürschner et al., 2008) approaches. The large SST decrease associated with CM6 is coincident with only a moderate drop in pCO_2 and the generally higher temperatures for atmospheric pCO_2 levels only slightly higher than pre-industrial values hint towards a higher than modern climate sensitivity in the middle Miocene. However, this conclusion requires further work to ascertain the true global mean average temperature of the middle Miocene. The results presented here do however, reaffirm the enigma of a warmer would with less ice than today but with comparable levels of atmospheric pCO_2.

8 Further Work

The Ras il-Pellegrin section is a superb geological archive for the 1.1 Myrs of the middle Miocene which it spans. Although there has already been significant work done on the Blue Clay Formation the full potential of the site has not yet been tapped. The exceptional preservation of foraminifera make it an ideal location for geochemical studies beyond the scope of this work. The high sedimentation rates make the site suitable for high resolution work beyond what has been studied here (the ~8 kyr resolution of this work was achieved with a 35 cm sampling interval). Fluctuations in oxygen isotopes have already demonstrated that orbitally paced climate fluctuations are present throughout the period which the site covers (Abels et al., 2005) the preservation quality of RIP would make the site ideal for multi-proxy investigation of these cycles at the glacial-interglacial timescale. The presence of alkenones at a site with such exceptional preservation would allow high resolution alkenone isotope analysis to be coupled with foraminiferal boron isotopes over a substantial period of time at high resolution at a period where these two proxies are the best method of reconstructing past atmospheric CO_2. A study of this sort would greatly increase knowledge of both proxies, as well as elucidating the interplay between CO_2 and climate on glacial-interglacial timescales deep into the Cenozoic. The preservation of alkenones also increases the likelihood of glycerol dialkyl glycerol tetraether (GDGT) preservation at the site, making possible temperature reconstruction using the TEX_{86}, alkenone unsaturation and Mg/Ca palaeothermometers.

Although the Blue Clay Formation does not cross the Langhian-Serravallian boundary, the presence of a clay rich interval within the Globigerina Limestone Formation (the "CRI" of John et al. (2003)) would allow investigation of changes in conditions across

the ice sheet growth should alkenone and foraminiferal preservation prove to be as good in that interval as in the rest of the Blue Clay.

The apparent high temperatures prevailing at RIP during the Serravallian meant that the alkenone unsaturation index was unable to fully reconstruct the pattern of temperature change at this site. Although through the use of Mg/Ca this problem was largely averted, use of the TEX_{86} palaeothermometer (Schouten et al., 2002) which is capable of reconstructing temperatures higher than the limit of the alkenone unsaturation index, would allow confirmation of the absolute temperatures and pattern for this site. As temperatures play an important role in the estimation of absolute atmospheric pCO_2 from alkenone isotopes, it would also help to confirm the relatively low levels of CO_2 at a time of high global temperatures. The excellent preservation of organic material at RIP would suggest that the glycerol dialkyl glycerol tetraethers necessary for TEX_{86} would be present at the site.

Although there can be significant confidence that the records determined from the Ras il-Pellegrin signal reflect a global signal, there is still uncertainty about variations in the contributions of terrestrial organic material to the site. One possibility to shed further light on this problem is the branched and isoprenoid tetraether index (BIT) (Kim et al., 2006) which has been shown to record changing terrestrial contributions to marine sites.

The thermal stratification suggested by the $\Delta\delta^{13}C$ records could be further investigated by the addition of further records of shallow and deep surface foraminifera in order to assess whether the variability recorded is truly global. There is potential for the use of Mg/Ca ratios in such foraminifera to directly determine the thermal gradient. This, coupled with the use of more complex ocean carbonate models with the ability to

model multiple layers of an ocean would allow for testing of whether thermal stratification is a valid explanation for the $\Delta\delta^{13}C$ records presented here.

The Moria section offers a site which is well exposed and the high sedimentation rate (which averages 35.8 $mMyr^{-1}$ over the section) allows for high resolution sampling, however the position of the section in the Apennine forehills means the section has undergone significant disturbance. This is demonstrated by the poor preservation of foraminifera, which have undergone recrystalisation. The site is therefore not suitable for detailed inorganic geochemical study. Organic matter contents are not high, but it is possible that there is preservation of biomarkers and this deserves investigation. Also, the high sedimentation rate, along with the preservation of a globally correlative isotope signal, would make this site a good candidate for astronomical tuning of the Burdigalian-Langhian boundary, and makes it a good candidate for the basal Burdigalian GSSP.

9 References

Abels, H.A., Hilgen, F.J., Krijgsman, W., Kruk, R.W., Raffi, I., Turco, E., and Zachariasse, W.J., 2005, Long-period orbital control on middle Miocene global cooling: Intergrated stratigraphy and astronomical tuning of the Blue Clay Formation on Malta: *Paleoceanography*, v. 20, doi:10.1029/2004PA001129.

Akgun, F., Kayseri, M.S., and Akkiraz, M.S., 2007, Palaeoclimatic evolution and vegetational changes during the Late Oligocene – Miocene period in Western and Central Anatolia (Turkey): *Palaeogeography, Palaeoclimatology, Palaeoecology,* v. 253, p. 56-90.

Anand, P., Elderfield, H., and Conte, M.H., 2003, Calibration of Mg/Ca thermometry in planktonic foraminifera from a sediment trap time series: *Paleoceanography*, v. 18, doi:10.1029/2002PA000846.

Andersen, N., Muller, P.J., Kirst, G., and Schneider, R.R., 1999, The d13C signal in C37:2 alkenones as a proxy for reconstructing Late Quarternary pCO_2 in surface waters from the South Altlantic, *in* Fisher, G., and Wefer, G., eds., *Proxies in paleoceanography: examples from the South Atlantic*, Springer, p. 469-488.

Anderson, G.M., 1976, Error propogation by the Monte Carlo method in geochemical calculations: *Geochimica et Cosmochimic Acta*, v. 40, p. 1533-1538.

Barker, S., and Elderfield, H., 2002, Foraminiferal calcification response to glacial-interglacial changes in atmospheric CO_2: *Science*, v. 297, p. 833-836.

Barker, S., Greaves, M., and Elderfield, H., 2003, A study of cleaning procedures used for foraminiferal Mg/Ca paleothermometry: *Geochemistry Geophysics Geosystems*, v. 4(9), 8407, doi:10.1029/2003GC000559.

Bellanca, A., Sgarrella, F., Neri, R., Russo, B., Sprovieri, M., Bonaduce, G., and Rocca, D., 2002, Evolution of the Mediterranean basin during the late Langhian early Serravallian: An integrated paleoceanographic approach: *Rivista Italiana Di Paleontologia E Stratigrafia*, v. 108, p. 223-239.

Berger, W.H., 2007, Cenozoic cooling, Antarctic nutrient pump, and the evolution of whales: *Deep-Sea Research Part II-Topical Studies in Oceanography*, v. 54, p. 2399-2421.

Berner, R.A., and Kothavala, Z., 2001, Geocarb III: A revised model of atmospheric CO_2 over phanerozoic time: *American Journal of Science*, v. 301, p. 182-204.

Berner, R.A., Lasaga, A.C., and Garrels, R.M., 1983, The carbonate-silicate geochemical cycle and its effect on atmospheric carbon dioxide over the past 100 million years: *American Journal of Science*, v. 283, p. 641-683.

Beer, C.J., Schiebel, R., and Wilson, P.A., 2010, Testing planktic foraminiferal shell weight as a surface water [CO_3^{2-}] proxy using plankton net samples: *Geology,* v. 38, p. 103-106.

Bidigare, R.R., Fluegge, A., Freeman, K.H., Hanson, K.L., Hayes, J.M., Hollander, D., Jasper, J.P., King, L.L., Laws, E.A., Milder, J., Millero, F.J., Pancost, R.D., Popp, B.N., Steinberg, P.A., and Wakeham, S.G., 1997, Consistent fractionation of ^{13}C in nature and in the laboratory: Growth-rate effects in some haptophyte algae: *Global Biogeochemical Cycles*, v. 11, p. 279-292.

Billups, K., and Schrag, D.P., 2002, Paleotemperatures and ice volume of the past 27 Myr revisited with paired Mg/Ca and $^{18}O/^{18}O$ measurements on benthic foraminifera: *Paleoceanography*, v. 17, doi:10.1029/2000PA000567.

Billups, K., and Schrag, D.P., 2003, Application of benthic foraminiferal Mg/Ca ratios to questions of Cenozoic climate change: *Earth and Planetary Science Letters*, v. 209, p. 181-195.

Billups, K., Rickaby, R.E.M., and Schrag, D.P., 2004, Cenozoic pelagic Sr/Ca records: Exploring a link to paleoproductivity: *Paleoceanography*, v. 19, doi:10.1029/2004PA001011.

Bijma, J., Spero, H., and Lea, D., 1999, Reassessing foraminiferal stable isotope geochemistry: Impact of the ocean carbonate system (experimental results), *in* Fischer, G., and Wefer, G., eds., *Uses of proxies in paleoceanography: Examples from the South Atlantic*: Berlin, Heidelberg, Springer-Verlag, p. 489–512.

Bijma, J., Hönisch, B., and Zeebe, R.E., 2002, Impact of the ocean carbonate chemistry on living foraminiferal shell weight: Comment on "Carbonate ion concentration in glacial-age deep waters of the Caribbean Sea" by W. S. Broecker and E. Clark: *Geochemistry Geophysics Geosystems*, v. 3, doi: 10.1029/2002GC000388.

Bluth, G.J.S., and Kump, L.R., 1991, Phanerozoic plaeogeology: American Journal of *Science*, v. 291, p. 248-308.

Böhme, M., 2003, The Miocene Climatic Optimum: evidence from ectothermic vertebrates of Central Europe: *Palaeogeography Palaeoclimatology Palaeoecology*, v. 195, p. 389-401.

Bonaduce, G., and Barra, D., 2002, The ostracods in the palaeoenvironmental interpretation of the late Langhian - early Serravailan section of Ras il-Pellegrin (Malta): *Rivista Italiana Di Paleontologia E Stratigrafia*, v. 108, p. 211-222.

Boyle, E.A., and Keigwin, L.D., 1985, Comparison of Atlantic and Pacific Paleochemical Records for the Last 215,000 Years - Changes in Deep Ocean Circulation and Chemical Inventories: *Earth and Planetary Science Letters*, v. 76, p. 135-150.

Brassell, S.C., 1993, Applications of biomarkers for delineating marine paleoclimatic fluctiations during the Pleistocene, *in* Engel, M.H., and Macko, S.A., eds., *Organic Geochemistry: Principles and Applications*, Plenum Press, p. 699-738.

Brassell, S.C., Eglinton, G., Marlowe, I.T., Pflaumann, U., and Sarnthein, M., 1986, Molecular stratigraphy: a new tool for climatic assessment: *Nature*, v. 320, p. 129-133.

Brassell, S.C., Dumitrescu, M., and Party, O.L.S.S., 2004, Recognition of alkenones in a lower Aptian porcellanite from the west-central Pacific: *Organic Geochemistry*, v. 35, p. 181-188.

Broecker, W. S., and Peng, T.-H., 1987, The Role of $CaCO_3$ Compensation in the Glacial to Interglacial Atmospheric CO_2 Change, *Global Biogeochem. Cycles*, v. 1, p, 15–29.

Brown, S.J., and Elderfield, H., 1996, Variations in Mg/Ca and Sr/Ca ratios of planktonic foraminifera caused by postdepositional dissolution: Evidence of shallow Mg-dependent dissolution: *Paleoceanography*, v. 11, p. 543-551.

Burkhardt, S., Riebesell, U., and Zondervan, I., 1999, Effects of growth rate, CO_2 concentration, and cell size on the shable carbon isotope fractionation in marine phytoplankton: *Geochimica et Cosmochimic Acta*, v. 63, p. 3729-3741.

Cande, S.C., and Kent, D.V., 1995, Revised calibration of the geomagnetic polarity timescale for the Late Cretaceous and Cenozoic: *Journal of Geophysical research*, v. 100, p. 6093-6095.

Cassar, N., Laws, E.A., and Popp, B.N., 2006, Carbon isotopic fractionation by the marine diatom Phaeodactylum tricornutum under nutrient- and light-limited growth conditions: *Geochimica et Cosmochimic Acta*, v. 70, p. 5323-5335.

Cerling, T.E., Harris, J., M, Macfadden, B.J., Leakey, M.G., Quade, J., Eisenmann, V., and Ehleringer, J.R., 1997, Global vegetation change through the Miocene/Pliocene boundary: *Nature*, v. 389, p. 153-158.

Chamley, H., 1989, Clay mineral sedimentation in the Ocean, *in* Paquet, H., and Clauer, N., eds., *Soils and Sediments (mineralogy and geochemistry)*: Berlin, Spring-Verlag, p. 269-302.

Chylek, P., and Lohmann, U., 2008, Aerosol radiative forcing and climate sensitivity deduced from the Last Glacial Maximum to Holocene transition: *Geophysical Research Letters,* v. 35, doi:10.1029/2007GL032759.

Coe, A.L., Cohen, A.S., Maddison, E.J., and Weedon, G.P., 2008, Mid-Miocene global cooling: Insights from new integrated data from the organic-rich Monterey Formation, California: *Eos, Transactions, American Geophysical Union*, v. 89, p. PP3D-08.

Conte, M.H., Volkman, J.K., and Eglinton, G., 1994, Lipid biomarkers of the Haptophyta, *in* Green, J.C., and Leadbeater, B.S.C., eds., *The Haptophyte Algae*, Clarendon, p. 351-377.

Conte, M.H., Sicre, M.A., Ruhlemann, C., Weber, J.C., Schulte, S., Schulz-Bull, D., and Blanz, T., 2006, Global temperature calibration of the alkenone unsaturation index ($U_{37}^{K'}$) in surface waters and comparison with surface sediments: *Geochemistry Geophysics Geosystems*, v. 7, Q02005, doi:10.1029/2005GC001054

Craig, H., 1957, Isotopic standards for carbon and oxygen & correction factors for mass spectrometric analysis: *Geochimica et Cosmochimica Acta*, v. 12, p. 133-149.

Dart, C.J., Bosence, W.J., and McClay, K.R., 1993, Stratigraphy and structure of the Maltese graben system: *Journal of the Geological Society, London*, v. 150, p. 1153-1166.

De Boer, P.L., and Wonders, A.A.H., 1984, Astronomically induced rhythmic bedding in Cretaceous pelagic sediments near Moria (Italy, Albian, Cenomanian, Umbrian Apennines): Milankovitch and climate. *Proc. NATO workshop, Palisades, 1982.* Vol. 1, p. 177-190.

DeConto, R.M., Pollard, D., Wilson, P.A., Palike, H., Lear, C.H., and Pagani, M., 2008, Thresholds for Cenozoic bipolar glaciation: *Nature*, v. 455, p. 652-655.

Deino, A., Channell, J., Coccioni, R., De Grandis, G., Depaolo, D.J., Fornaciari, E., Emmanuel, L., Laurenzi, M.A., Montanari, A., Rio, D., and Renard, M., 1997, Intergrated Stratigraphy of the Upper Burdigalian - Lower Langhian section at Moria (Marche region, Italy), *in* Montanari, A., Odin, G.S., and Coccioni, R., eds., *Miocene Stratigraphy: An Intergrated Approach*, Volume 15: Developments in Palaeontology and Stratigraphy: Amsterdam, Lausanne, New York, Oxford, Shannon, Tokyo, Elsevier, p. 316-341.

Delaney, M.L., and Linn, L.J., 1993, Interstitial water and bulk calciate chemistry, Leg 130, and calcite recrystallization, *in* Berger, W.H., Kroenke, L.W., and Mayer, L.A., eds., *Proceedings of the Ocean Drilling Program Scientific Results*, v. 130: College Station, ODP, p. 561-572.

Dickens, G.R., O'Neil, J.R., Rea, D.K., and Owen, R.M., 1995, Dissociation of oceanic methane hydrate as a cause of the carbon isotope excursion at the end of the Paleocene: *Paleoceanography*, v. 10, p. 965-971.

Diester-Haass, L., Billups, K., Grocke, D.R., Francois, L., Lefebvre, V., and Emeis, K.C., 2009, Mid-Miocene Paleoproductivity in the Atlantic Ocean and Implications for the Global Carbon Cycle: *Paleoceanography*, v. 24, PA1209, doi:10.1029/2008PA001605

Duplessy, J.-C., Labeyrie, L., Juillet-Leclerc, A., Maitre, F., Duprat, J., and Sarnthein, M., 1991, Surface salinity reconstructions of the North Atlantic Ocean during the last glacial maxiumum: *Oceanoligica Acta*, v. 14, p. 311-324.

Eglinton, G., and Hamilton, R.J., 1967, Leaf Epicuticular Waxes: *Science*, v. 156, p. 1322-1335.

Elderfield, H., Cooper, M., and Ganssen, G., 2000, Sr/Ca in multiple species of planktonic foraminifera: Implications for reconstructions of seawater Sr/Ca: *Geochemistry Geophysics Geosystems*, v. 1, doi:10.1029/1999GC000031.

Emiliani, C., 1954, Depth habitats of some species of pelagic foraminifera as indicated by oxygen isotope ratios: American Journal of Science, v. 252, p. 149-158.

Epstein, S., Buchsbaum, R., Lowenstam, H., and Urey, H.C., 1951, Carbonate-water isotopic temperature scale: *Geological Society of America Bulletin*, v. 63, p. 417-426.

Erez, J., and Boaz, L., 1983, Experimental paleotemperature equation for planktonic foraminifera: *Geochimica et Cosmochimic Acta*, v. 47, p. 1025-1031.

Farrimond, P., Eglinton, G., and Brassell, S.C., 1986, Alkenones in Cretaceous black shales, Blake-Bahama Basin, western North Atlantic, *in* Leythaeuser, D., and Rullkötter, J., eds., *Advances in Organic Geochemistry 1985*, Volume 10: Organic Geochemistry, p. 897-903.

Felix, R., 1973, *Oligo-Miocene stratigraphy of Malta and Gozo*: Utrecht, University of Utrecht.

Flower, B.P., and Kennett, J.P., 1993a, Middle Miocene ocean-climate transition: high resolution oxygen and carbon isotopic records from DSDP Site 588A, southwest Pacific: *Paleoceanography*, v. 8, p. 811-843.

Flower, B.P., and Kennett, J.P., 1993b, Relations between Monterey Formation Deposition and Middle Miocene Global Cooling - Naples-Beach Section, California: *Geology*, v. 21, p. 877-880.

Fogel, M.L. and Cifuentes, L.A., 1993, Isotope fractionation during primary production, *in* Engel, M.H. and Macko, S.A., eds., *Organic Geochemistry, Principles and Applications,* Plenum Press, New York and London, p 73-98.

Foster, G.L., 2008, Seawater pH, pCO_2 and $[CO_3^{2-}]$ variations in the Caribbean Sea over the last 130 kyr: A boron isotope and B/Ca study of planktic forminifera: *Earth and Planetary Science Letters*, v. 271, p. 254-266.

Freeman, K.H., and Hayes, J.M., 1992, Fractionation of carbon isotopes by phytoplankton and estimates of ancient CO_2 levels: *Global Biogeochemical Cycles,* v. 6, p. 185-198.

Fry, B., and Sherr, E.B., 1984, $\delta^{13}C$ measurements as indicators of carbon flow in marine and freshwater ecosystems: *Contributions in Marine Science*, v. 27, p. 13-47.

Fung, I., John, J., Lerner, J., Matthews, E., Prather, M., Steele, L.P., and Fraser, P.J., 1991, Three-Dimensional Model Synthesis of the Global Methane Cycle: *Journal of Geophysical Research*, v. 96(D7), p. 13,033–13,065.

Garcia, H.E., Locarnini, R.A., Boyer, T.P., and Antonov, J.I., 2006, *World Ocean Atlas 2005, Volume 4: Nutrients (phosphate, nitrate, silicate)*: Washington, U.S. Government Printing Office, pp. 396

Goericke, R., Montoya, J.P., and Fry, B., 1994, Physiology of isotopic fractionation in algae and cyanobacteria: *Stable Isotopes in Ecology and Environmental Science,* p. 187-221.

Grasso, M., and Reuther, C.D., 1988, The western margin of the Hyblean plateau: a neotectonic transform system on the SE Sicilian foreland: *Annales Tectonicae*, v. 2, p. 107-120.

Hatch, M.D., 1987, C_4 photosynthesis: a unique blend of modified biochemistry, anatomy and ultrastructure: *Biochimica et Biophysica Acta*, v. 895, p. 81-106.

Hayes, J.M., Strauss, H., and Kaufman, A.J., 1999, The abundance of ^{13}C in marine organic matter and isotopic fraactionation in the global biogeochemical cycle of carbon during the past 800 Ma: *Chemical Geology*, v. 161, p. 103-125.

Hedges, J.I., Clark, A., Quay, P.D., Richey, J.E., Devol, A.H., and de M. Santos, U., 1986, Compositions and fluxes of particulate organic material in the Amazon River: *Limnology & Oceanography*, v. 31, p. 717-738.

Hedges, J.I., Keil, R.G., and Benner, R., 1997, What happens to terrestrial organic matter in the ocean?: *Organic Geochemistry*, v. 27, p. 195-212.

Hemleben, C., Spindler, M., and Anderson, O.R., 1989, *Modern planktonic foraminifera*: New York, Springer-Verlag.

Hemming, N.G., and Hanson, G.N., 1992, Boron isotopic composition and concentration in modern marine carbonates: *Geochimica et Cosmochimica Acta*, v. 56, p. 537-543.

Henderiks, J., and Pagani, M., 2007, Refining ancient carbon dioxide estimates: Significance of coccolithophore cell size for alkenone-based pCO_2 records: *Paleoceanography*, v. 22, PA3202, doi:10.1029/2006PA001399.

Henderiks, J., and Pagani, M., 2008, Coccolithophore cell size and the Paleogene decline in atmospheric CO_2: *Earth and Planetary Science Letters*, v. 269, p. 576-584.

Hilgen, F.J., Abels, H.A., Iaccarino, S., Krijgsman, W., Raffi, I., Sprovieri, R., Turco, E. and Zachariasse, W,J., 2009 The global stratotype section and point (GSSP) of the Serravallian stage (middle Miocene): *Episodes,* v. 32, p. 152-166.

Holbourn, A., Kaandorp, R.J.G., Schulz, M., and Erlenkeuser, H., 2005, Impacts of orbital forcing and atmospheric carbon dioxide on Miocene ice-sheet expansion: *Nature*, v. 438, doi:10.1038/nature04123.

Hollander, D.J., and McKenzie, J.A., 1991, CO_2 control on carbon-isotope fractionation during aqueous photosynthesis: A paleo-CO_2 barometer: *Geology*, v. 19.

Iaccarino, S., 1985, Mediterranean Miocene and Pliocene planktic foraminifera, *in* Bolli, H.M., Saunders, J.B., and Perch-Nielsen, K., eds., *Plankton Stratigraphy*: Cambridge, Cambridge University Press, p. 283-314.

Ivanov, D., Ashraf, A.R., Mosbrugger, V. and Palamarev, E., 2002, Palynological evidence for Micoene climate change in the Forecarpathian basin (Central Paratethys, NW Bulgaria): *Palaeogeography, Palaeoclimatology, Palaeoecology,* v. 178, p. 19-37.

Jacobs, E., Weissert, H., Shields, G., and Stille, P., 1996, The Monterey event in the Mediterranean: A record from shelf sediments of Malta: *Paleoceanography*, v. 11, p. 717-728.

Jasper, J.P., and Hayes, J.M., 1990, A carbon isotope record of CO_2 levels during the late Quaternary: *Nature*, v. 347, p. 462-464.

Jasper, J.P., Hayes, J.M., Mix, A.C., and Prahl, F.G., 1994, Photosynthetic fractionation of ^{13}C and concentrations of dissolved CO_2 in the central equatorial Pacific during the last 255,000 years: *Paleoceanography*, v. 9, p. 781-798.

John, C.M., Mutti, M., and Thierry, A., 2003, Mixed carbonate-siliciclastic record on the North African margin (Malta) - coupling of weathering processes and mid Miocene climate: *Bulletin of the Geological Society of America*, v. 115, p. 217-229.

Jongsma, D., van Hinte, J.E., and Woodside, J.M., 1985, Geological structure and neotectonics of the north African continental margin south of Sicily: *Marine and Petroleum Geology*, v. 2, p. 156-177.

Kakihana, H., Kotake, M., Satoh, S., Nomura, M., and Okamoto, M., 1977, Fundamental studies on the ion-exchange sepatation of boron isotopes: *Bulletin of the Chemical Society of Japan*, v. 50, p. 158-163.

Katz, A., 1973, The interaction of magnesium with calcite during crystal growth at 25-90°C and at one atmosphere: *Geochimica et Cosmochimica Acta*, v. 37, p. 1563-1586.

Kawamura, K., and Gagosian, R.B., 1987, Identification of Moega-Oxocarboxylic acids as Acetal Esters in Aerosols using capillary gas-chromatography mass-spectrometry: *Journal of Chromotography*, v. 390, p. 371-377.

Kim, J.-H., Schouten, S., Buscail, R., Ludwig, W., Bonnin, J., Sinninghe Damsté, J.S., and Bourrin, F., 2006, Origin and distribution of terrestrial organic matter in the NW Mediterranean (Gulf of Lions): Exploring the newly developed BIT index: *Geochemistry Geophysics Geosystems*, v. 7, doi:10.1029/2006GC001306.

Klinkhammer, G.P., Mix, A.C., and Haley, B.A., 2009, Increased dissolved terrestrial input to the coastal ocean during the last deglaciation: *Geochemistry Geophysics Geosystems,* v. 10, doi:10.1029/2008GC002219.

Klochko, K., Kaufman, A.J., Yoa, W., Byrne, R.H., and Tossell, J.A., 2006, Experimental measurement of boron isotope fractionation in seawater: *Earth and Planetary Science Letters*, v. 248, p. 261-270.

Kump, L.R., and Arthur, M.A., 1999, Interpreting carbon-isotope excursions: carbonates and organic matter: *Chemical Geology*, v. 161, p. 181-198.

Kump, L.R., Arthur, M.A., Patzkowsky, M.E., Gibbs, M.T., Pinkus, D.S., and Sheehan, P.M., 1999, A weathering hypothesis for glaciation at high atmospheric pCO_2 during the Late Ordovician: *Palaeogeography, Palaeoclimatology, Palaeoecology*, v. 152, p. 173-187.

Kürschner, W.M., Kvacek, Z., and Dilcher, D.L., 2008, The impact of Miocene atmospheric carbon dioxide fluctuations on climate and the evolution of terrestrial ecosystems: *Proceedings of the National Academy of Sciences of the United States of America*, v. 105, p. 449-453.

Kuypers, M.M.M., Pancost, R.D., and Sinninghe Damsté, J.S., 1999, A large and abrupt fall in atmospheric CO_2 during Cretaceous times: *Nature*, v. 399, p. 342-345.

Laskar, J., Joutel, F., and Boudin, F., 1993, Orbital precession and insolation quantities for the Earth from -20Myr to +10Myr: *Astronomy and Astrophysics*, v. 270, p. 522-533.

Laws, E.A., Popp, B.N., Bidigare, R.R., Kennicutt, M.C., and Macko, S.A., 1995, Dependence of phytoplankton carbon isotopic composition on growth rate and [CO_2]aq: Theoretical considerations and experimental results: *Geochimica et Cosmochimic Acta*, v. 59, p. 1131-1138.

Laws, E.A., Bidigare, R.R., and Popp, B.N., 1997, Effect of growth rate and CO_2 concentration on carbon isotopic fractionation by the marine diatom Phaeodactylum tricornutum: *Limnology and Oceanography*, v. 42, p. 1552-1560.

Lazerte, B.D., 1983, Stable carbon isotope ratios: implications for the source of sediment carbon and for phytoplankton carbon assimilation in Lake Memphremagog, Quebec: *Canadian Journal of Fisheries and Aquatic Sciences*, v. 40, p. 1658-1666.

Lea, D.W., Pak, D.K., and Spero, H.J., 2000, Climate impact of late Quarternary equatorial sea surface temperature variations: *Science*, v. 289, p. 1719-1724.

Lear, C.H., Elderfield, H., and Wilson, P.A., 2000, Cenozoic deep-sea temperatures and global ice volumes from Mg/Ca in benthic foraminiferal calcite: *Science*, v. 287, p. 269-272.

Lear, C.H., Elderfield, H., and Wilson, P.A., 2003, A Cenozoic seawater Sr/Ca record from benthic foraminiferal calcite and its application in determining global weathering fluxes: *Earth and Planetary Science Letters*, v. 2008, p. 69-84.

Lear, C.H., Rosenthal, Y., Coxall, H.K., and Wilson, P.A., 2004, Late Eocene to early Miocene ice sheet dynamics and the global carbon cycle: *Paleoceanography*, v. 19. PA4015, doi:10.1029/2004PA001039

Lelieveld, J., Crutzen, P.J., and Dentener, F., 1998, Changing concentration, lifetime and climate forcing of atmospheric methane: *Tellus B*, v. 50, p. 128-150.

Lemarchand, D., Gaillardet, J., Lewin, E., and Allegre, C.J., 2000, The influence of rivers on marine boron isotopes and implications for reconstructing past ocean pH: *Nature*, v. 408, p. 951-954.

Lemarchand, D., Gaillardet, J., Lewin, E., and Allegre, C.J., 2002, Boron isotope systematics in large rivers: Implications for the marine boron budget and paleo-pH reconstruction over the Cenozoic: *Chemical Geology*, v. 190, p. 123-140.

Leopold, E.B., and Liu, G., 1994, A long pollen sequence of Neogene age, Alaska Range: *Quaternary International*, v. 22/23, p. 103-140.

Locarnini, R.A., Mishonov, J.I., Antonov, J.I., Boyer, T.P., and Garcia, H.E., 2006, *World Ocean Atlas 2005, Volume 1: Temperature*: Washington, D.C., U.S. Government Printing Office.

Lorens, R.B., 1981, Sr, Cd, Mn and Co distribution coefficients in calcite as a function of calcite precipitation rate: *Geochimica et Cosmochimica Acta*, v. 45, p. 553-561.

Lourens, L.J., Hilgen, J., Laskar, J., Shackleton, N.J., and Wilson, P.A., 2004, The Neogene Period, *in* Gradstein, F., Ogg, J., and Smith, A., eds., *Geologic Time Scale 2004*: New York, Cambridge University Press.

Lowenstein, T.K., and Demicco, R.V., 2006, Elevated Eocene atmospheric CO_2 and its subsequent decline: *Science*, v. 313, p. 1928.

Luthi, D., Le Floch, M., Bereiter, B., Blunier, T., Barnola, J.-M., Siegenthaler, U., Raynaud, D., Jouzel, J., Fischer, H., Kawamura, K., and Stocker, T.F., 2008, High-resolution carbon dioxide concentration record 650,000-800,000 years before present: *Nature*, v. 453, p. 379-382.

Lyle, M., Barron, J., Bralower, T.J., Huber, M., Lyle, A.O., Ravelo, A.C., Rea, D.K., and Wilson, P.A., 2008, Pacific ocean and Cenozoic evolution of climate: *Reviews of Geophysics*, v. 46, RG2002, doi:10.1029/2005RG000190.

Malone, M.J., and Baker, P.A., 1999, Temperature dependence of the strontium distribution coefficient in calcite: An experimental study from 40 degrees to 200 °C and application to natural diagenetic calcites: *Journal of Sediment Research*, v. 69, p. 216-223.

Marlowe, I.T., 1984, *Lipids as paleoclimatic indicators*: Bristol, University of Bristol.

Marlowe, I.T., Brassell, S.C., Eglinton, G., and Green, J.C., 1984, Long chain unsaturated ketones and sters in living algae and marine sediments: *Organic Geochemistry*, v. 6, p. 135-141.

Marlowe, I.T., Brassell, S.C., Eglinton, G., and Green, J.C., 1990, Long-chain alkenones and alkyl alkenoates and the fossil coccolith record of marine sediments: *Chemical Geology*, v. 88, p. 349-375.

Maslin, M.a., Shackleton, N.J., and Pflaumann, U., 1995, Surface-water temperature, salinity, and density changes in the northeast Atlantic during the last 45,000 Years - Heinrich events, deep-water formation, and climatic rebounds: *Paleoceanography*, v. 10, p. 527-544.

Matson, E.A., and Brinson, M.M., 1990, Stable carbon isotopes and the C:N ratio in the estuaries of the Pamlico and Neuse Rivers, North Carolina: *Limnology & Oceanography*, v. 35, p. 1290-1300.

McCorkle, D.C., Martin, P.A., Lea, D.W., and Klinkhammer, G.P., 1995, Evidence of a dissolution effect on benthic foraminiferal shell chemistry: $\delta^{13}C$, Cd/Ca, Ba/Ca and Sr/Ca, results from the Ontong Java Plateau: *Paleoceanography*, v. 10, p. 699-714.

Miller, K.G., and Katz, M.E., 1987, Oligocene to Miocene benthic foraminiferal and abyssal circulation changes in the North Atlantic: *Micropaleontology*, v. 33, p. 97-149.

Miller, K.G., Wright, J.D., and Fairbanks, R.G., 1991, Unlocking the ice house: Oligocene-Miocene oxygen isotopes, eustacy and margin erosion: *Journal of Geophysical research*, v. 96 (B4), p. 6829-6848.

Mook, W.G., Bommerson, J.C., and Staverman, W.H., 1974, Carbon isotope fractionation between dissolved bicarbonate and gaseous carbon dioxide: *Earth and Planetary Science Letters*, v. 22, p. 169-176.

Mucci, A., and Morse, J.W., 1983, The incorporation of Mg^{2+} and Sr^{2+} into calcite overgrowths - influences of growth-rate and solution composition: *Geochimica et Cosmochimica Acta*, v. 47, p. 217-233.

Müller, P.J., Kirst, G., Ruhland, G., von Storch, I., and Rosell-Melé, A., 1998, Calibration of the alkenone paleotemperature index $U^{K'}_{37}$ base on core tops from the eastern South Atlantic and global ocean (60°N-60°S): *Geochimica et Cosmochimic Acta*, v. 62, p. 1757-1772.

Myhre, G., Highwood, E.J., Shine, K.P., and Stordal, F., 1998, New estimates of radiative forcing due to well mixed greenhouse gases: *Geophysical Research Letters,* v. 25, p. 2715-2718.

Ni, Y., Foster, G.L., Bailey, T., Elliott, T., Schmidt, D.N., Pearson, P., Haley, B., and Coath, C., 2007, A core top assessment of proxies for the ocean carbonate system in surface-dwelling foraminifers: *Paleoceanography*, v. 22. PA3212, doi:10.1029/2006PA001337

Nürnberg, D., Bijma, J., and Hemleben, C., 1996, Assessing the reliability of magnesium in foraminiferal calcite as a proxy for water mass temperatures: *Geochimica et Cosmochimica Acta*, v. 60, p. 803-814.

Pagani, M., 2002, The alkenone-CO_2 proxy and ancient atmospheric carbon dioxide: *Philosophical Transactions of the Royal Society of London Series A-Mathematical Physical and Engineering Sciences*, v. 360, p. 609-632.

Pagani, M., Arthur, M.A., and Freeman, K.H., 1999a, Miocene evolution of atmospheric carbon dioxide: *Paleoceanography*, v. 14, p. 273-292.

Pagani, M., Freeman, K.H., and Arthur, M.A., 1999b, Late Miocene atmospheric CO_2 Concentrations and the Expansion of C_4 grasses: *Science*, v. 285, p. 876-879.

Pagani, M., Freeman, K.H., Ohkouchi, N., and Caldeira, K., 2002, Comparison of water column [CO_2aq] with sedimentary alkenone-based estimates: A test of the alkenone-CO_2 proxy: *Paleoceanography*, v. 17, doi:10.1029/2002PA000756.

Pagani, M., Zachos, J.C., Freeman, K.H., Tipple, B., and Boharty, S., 2005a, Marked decline in atmospheric carbon dioxide concentrations during the Paleogene: *Science*, v. 309, p. 600-603.

Pagani, M., Lemarchand, D., Spivack, A., Gaillardet, J., 2005b, A critical evaluation of the boron isotope-pH proxy: The accuracy of ancient ocean pH estimates: *Geochimica et Cosmochimica Acta*, v. 69, p. 953-961.

Pagani, M., Liu, Z., LaRiviere, J., and Ravelo, A.C., 2010, High Earth-system climate sensitivity determined from Pliocene carbon dioxide concentrations: *Nature Geoscience,* v. 3, p. 27-30.

Paillard, D., Labeyrie, L., and Yoiu, P., 1996, Macintosh program performs time-series analysis: *Eos, Transactions, American Geophysical Union*, v. 77, p. 379.

Palmer, M.R., Pearson, P.N., and Cobb, S.J., 1998, Reconstructing past ocean pH-depth profiles: *Science*, v. 282, p. 1468-1471.

Paul, H.A., Zachos, J.C., Flower, B.P., and Tripati, A., 2000, Orbitally induced climate and geochemical variability across the Oligocene/Miocene boundary: *Paleoceanography*, v. 15, p. 471-485.

Pearcy, R.W. and Ehleringer, J., 1983, Comparative ecophysiology of C_3 and C_4 plants: *Plant, Cell and Environment*, v. 7, p. 1-13.

Pearson, P.N. and Palmer, M.R., 1999, Middle Eocene Seawater pH and Atmospheric Carbon Dioxide Concentrations: *Science*, v. 284, p. 1824-1826.

Pearson, P.N. and Palmer, M.R., 2000, Atmospheric carbon dioxide concentrations over the past 60 million years: *Nature*, v. 406, p. 695-699.

Pearson, P.N. and Shackleton, N.J., 1995, Neogene multispecies planktonic foraminifer stable isotope record, site 871, Limalok Guyot, *in* Haggerty, J.A., Premoli Silva, I., Rack, F., and McNutt, M.K., eds., *Proceedings of the Ocean Drilling Program, Scientific Results*, Volume 144, p. 401-410.

Pearson, P.N., Ditchfield, P.W., Singano, J., Harcourt-Brown, K.G., Nicholas, C.J., Olsson, R.K., Shackleton, N.J., and Hall, M.A., 2001, Warm tropical sea surface temperatures in the Late Cretaceous and Eocene epochs: *Nature*, v. 413, p. 481-487.

Pedley, H.M., 1975, *The Oligo-Miocene sediments of the Maltese islands*: Hull, University of Hull.

Pedley, H.M., House, M.R., and B., W., 1976, The geology of Malta and Gozo: *Proceedings of the Geologists' Association*, v. 87, p. 325-341.

Petit, J.R., Jouzel, J., Raynaud, D., Barkov, N.I., Barnola, J.M., Basile, I., Bender, M., Chappellaz, J., Davis, M., Delaygue, G., Delmotte, M., Kotlyakov, V.M.,

Legrand, M., Lipenkov, V.Y., Lorius, C., Pepin, L., Ritz, C., Saltzman, E., and Stievenard, M., 1999, Climate and atmospheric history of the past 420,000 years from the Vostok ice core, Antarctica: *Nature*, v. 399, p. 429-436.

Pialli, G., and Alvarez, W., 1997, Tectonic Setting of the Miocene Northern Apennines: The problem of contemporaneous compression and extension, *in* Montanari, A., Odin, G.S., and Coccioni, R., eds., *Miocene Stratigraphy: An Intergrated Approach*, Volume 15: Developments in Paleontology and Stratigraphy: Amsterdam, Elsevier, p. 157-185.

Popp, B.N., Laws, E.A., Bidigare, R.R., Dore, J.E., Hanson, K.L., and Wakeham, S.G., 1998, Effect of phytoplankton cell geometry on carbon isotopic fractionation: *Geochimica et Cosmochimic Acta*, v. 62, p. 69-77.

Prahl, F.G., and Wakeham, S.G., 1987, Calibration on unsaturation patterns in long-chain ketone compositions for paleotemperature assessment: *Nature*, v. 330. 367-369

Prahl, F.G., Ertel, J.R., Goni, M.A., Sparrow, M.A., and Eversmeyer, B., 1994, Terrestrial organic carbon contributions to sediments on the Washington margin: *Geochimica et Cosmochimica Acta*, v. 58, p. 3035-3048.

Ravizza, G., Dalai, T., Paquay, F., Lear, C.H. and Badger, M.P.S., *in prep.,* Mid-Miocene weathering as constrained by the marine Os record: Evidence of weak climate-weathering feedback.

Rau, G.H., Takahashi, T., and Des Marais, D.J., 1989, Latitudinal variations in plankton $\delta^{13}C$: implications for CO_2 and productivity in past oceans: *Nature*, v. 341, p. 519-518.

Raymo, M.E., and Ruddiman, W.F., 1992, Tectonic forcing of late Cenozoic climate: *Nature*, v. 359, p. 117-122.

Rea, D.K., and Leinen, M., 1984, Crustal Subsidence and calcite deposition in the south Pacific ocean, *in* Bailey, M., ed., *Initial reports of the Deep Sea Drilling Project,* v. 92: Washington (U.S. Govt. Printing Office), p. 299-303.

Reagan, M.T., and Moridis, G.J., 2008, Dynamic response of oceanic hydrate deposits to ocean temperature change: *Journal of Geophysical Research*, v. 113, C12023, doi:10.1029/2008JC004938.

Rickaby, R.E.M., Schrag, D.P., Zondervan, I., and Riebesell, U., 2002, Growth rate dependence of Sr incorporation during calcification of Emiliania huxleyi: *Global Biogeochemical Cycles*, v. 16, 1006, doi:10.1029/2001GB001408.

Riebesell, U., Revill, A.T., Holdsworth, D.G., and Volkman, J.K., 2000a, The effects of varying CO_2 concentration on lipid composition and carbon isotope fractionation in Emiliania huxleyi: *Geochimica et Cosmochimic Acta*, v. 64, p. 4179-4192.

Riebesell, U., Zondervan, I., Rost, P.D., Tortell, R.E., Zeebe, R.E., and Morel, F.M.M., 2000b, Reduced clacification of marine plankton in response to increase atmospheric CO_2: *Nature*, v. 407. p. 364-367

Rio, D., Cita, M.B., Iaccarino, S., Gelati, R., and Gnaccolini, M., 1997, Langhian, Serravallian and Tortonian Historical Stratotypes, *in* Montanari, A., Odin, G.S., and Coccioni, R., eds., *Miocene Stratigraphy: An Intergrated Approach*, Volume 15: Developments in Palaeontology and Stratigraphy: Amsterdam, Elsevier, p. 57-87.

Robert, C., and Chamley, H., 1991, Development of early Eocene warm climates, as inferred from clay mineral variations in oceanic sediments: *Global and Planetary Change*, v. 89, p. 315-332.

Rohling, E. J., and Bigg, G.R., 1998, Paleosalinity and $\delta^{18}O$: A critical assessment: *Journal of Geophysical Research,* v. 103, p. 1307-1318.

Romanek, C.S., Grossman, E.L., and Morse, J.W., 1992, Carbon isotopic fractionation in synthetic aragonite and calcite: Effects of temperature and precipitation rate: *Geochimica et Cosmochimica Acta*, v. 56, p. 419-430.

Rosenthal, Y., and Lohmann, G.P., 2002, Acurrate estimation of sea surface temperatures using dissolution-corrected calibrations for Mg/Ca paleothermometry: *Paleoceanography*, v. 17, 1044, doi:10.1029/2001PA000749.

Rosenthal, Y., Boyle, E.A., and Slowey, N., 1997, Temperature control on the incorporation of magnesium, strontium, fluorine, and cadmium into benthic foraminiferal shells from Little Bahama Bank: Prospects for thermocline paleoceanography: *Geochimica et Cosmochimica Acta*, v. 61, p. 3633-3643.

Rosenthal, Y., Lohmann, G.P., Lohmann, K.C., and Sherrell, R.M., 2000, Incorporation and preservation of Mg in *Globigerinoides sacculifer*: Implications for reconstructing the temperature and $^{18}O/^{16}O$ of seawater: *Paleoceanography*, v. 15, p. 135-145.

Rost, B., Zondervan, I., and Riebesell, U., 2002, Light-dependent carbon isotope fractionation in the coccolithophorid Emiliania huxleyi: *Limnology and Oceanography*, v. 47, p. 120-128.

Royer, D.L., Berner, R.A., Montanez, I.P., Tabor, N.J., and Beerling, D.J., 2004, CO_2 as a primary driver of Phanerozoic climate: *GSA Today*, v. 14, p. 4-10.

Sanyal, A., Hemming, N.G., Hanson, G.N., and Broecker, W.S., 1995, Evidence for a higer pH in the glacial ocean from boron isotopes in foraminifera: *Nature*, v. 373, p. 234-236.

Sanyal, A., Hemming, N.G., Broecker, W.S., and Hanson, G.N., 1997, Changes in pH in the eastern equatorial Pacific across stage 5-6 boundary based on boron isotopes in foraminifera: *Global Biogeochemical Cycles*, v. 11, p. 125-133.

Savin, S.M., Douglas, R.G., and Stehli, F.G., 1975, Tertiary marine paleotemperatures: *Geological Society of America Bulletin*, v. 86, p. 1499-1510.

Scalan, R.S., and Smith, J.E., 1970, An Improved Measure of Odd-Even Predominance in Normal Alkanes of Sediment Extracts and Petroleum: *Geochimica et Cosmochimica Acta*, v. 34, p. 611-620.

Schmidt, G. A., 1999, Error analysis of paleosalinity calculations: *Paleoceanography*, v .14, p. 422-429.

Schoell, M., Schouten, S., Sinninghe Damsté, J.S., de Leeuw, J.W., and Summons, R.E., 1994, A Molecular Organic Carbon Isotope Record of Miocene Climate Changes: *Science*, v. 263, p. 1122-1125.

Schouten, S., Hopmans, E.C., Schefuβ, E., and Sinninghe Damsté, J.S., 2002, Distributional variations in marine crenachaeotal membrane lipids: a new organic proxy for reconstructing ancient sea water temperatures?: *Earth and Planetary Science Letters*, v. 204, p. 265-274.

Schubert, C.J., and Calvert, S.E., 2001, Nitrogen and carbon isotopic composition of marine and terrestrial organic matter in Arctic Ocean sediments: Implications for nutrient utilization and organic matter composition: *Deep-Sea Research Part I: Oceanographic Research Papers*, v. 48, p. 789-810.

Shackleton, N.J., and Kennett, J.P., 1975, Paleotemperature history of the Cenozoic and the initiation of antarctic glaciation: Oxygen and Carbon isotope analyses

in DSDP sites 277, 279 and 281, *in* White, S.M. ed., *Initial reports of the Deep Sea Drilling Project*, v. 29, p. 743-755.

Shackelton, N.J., Crowhurst, S.J., Weedon, G.P., and Laskar, J., (1999), Astronomical calibration of Oligocene-Miocene time: *Philosophical Transactions of the Royal Society, London A,* v. 357, p. 1907-1929.

Sharma, T., and Clayton, R.N., 1965, Measurement of O^{18}/O^{16} Ratios of Total Oxygen of Carbonates: *Geochimica et Cosmochimic Acta*, v. 29, p. 1347-1353

Shevenell, A.E., Kennett, J.P., and Lea, D.W., 2004, Middle Miocene Southern Ocean cooling and antarctic cryosphere expansion: *Science*, v. 305, p. 1766-1770.

Shevenell, A.E., Kennett, J.P., and Lea, D.W., 2008, Middle Miocene ice sheet dynamics, deep-sea temperatures, and carbon cycling: A Southern Ocean perspective: *Geochemistry Geophysics Geosystems*, v. 9, Q02006, doi:10.1029/2007GC001736

Simon, L., Lecuyer, C., Marechal, C., and Coltice, N., 2006, Modelling the geochemical cycle of boron: Implications for the long-term $\delta^{11}B$ evolution of seawater and oceanic crust: *Chemical Geology*, v. 225, p. 61-76.

Solomon, S., D. Qin, M. Manning, Z. Chen, M. Marquis, K.B. Averyt, M. Tignor and H.L. Miller (eds.), 2007, Contribution of working group I to the fourth assessment report of the Intergovernmental panel on climate change, Cambridge University Press, Cambridge.

Spivack, A.J., and Edmond, J.M., 1987, Boron Isotope exchange between seawater and the oceanic crust: *Geochimica et Cosmochimica Acta*, v. 51, p. 1033-1043.

Stanley, S.M. and Hardie, L.A., 1998, Secular oscillations in the carbonate mineralogy of reef-building and sediment producing organisms driven by tectonically forced shifts in seawter chemistry: *Palaeogeography, Palaeoclimatology, Palaeoecology,* v. 155, p. 3-19.

Stoll, H.M., and Bains, S., 2003, Coccolith Sr/Ca records of productivity during the Paleocene-Eocene thermal maximum from the Weddell Sea: *Paleoceanography*, v. 18, doi:1029/2002PA000875.

Stoll, H.M., and Schrag, D.P., 2000, Coccolith Sr/Ca as a new indicator of coccolithophorid calcification and growth rate: *Geochemistry, Geophysics, Geosystems*, v. 1, 1006, doi:10.1029/1999GC000015.

Stoll, H.M., and Ziveri, P., 2002, Separation of monospecific and restricted coccolith assembalges from sediments using differential settling velocity: *Marine Micropaleontology*, v. 46, p. 209-221.

Stoll, H.M., Rosenthal, Y., and Falkowski, P.G., 2001, Climate proxies from Sr/Ca of coccolith calcite: Calibrations from continuous culture of Emiliania huxleyi.: *Geochimica et Cosmochimica* Acta, v. 66, p. 927-936.

Stoll, H.M., Class, M.K., Probert, I., Encinar, J.R., and Ignacio Garcia Alonso, A., 2002a, Calcification rate and temperature effects on Sr partitioning in coccoliths of multiple species of coccolithophorids in culture.: *Global and Planetary Change*, v. 34, p. 153-171.

Stoll, H.M., Ziveri, P., Geisen, M., Probert, I., and Young, J.R., 2002b, Potential and limitations of Sr/Ca ratios in coccolith carbonate: new perspectives from cultures and monospecific samples from sediments: *Philisophical Transactions of the Royal Society, London A*, v. 360, p. 719-747.

Subcommision for Stratigraphic Information, 2009, GSSP Table - Cenozoic Era, accessed 4th July 2009 http://stratigraphy.science.purdue.edu/gssp/.

Syabryaj, S., Utescher, T., Molchanoff, S., and Bruch, A.A., 2007, Vegetation and palaeoclimate in the Miocene of Ukraine: *Palaeogeography, Palaeoclimatolgy and Palaeoecology*, v. 253, p. 153-168.

Tan, F.C., and Strain, P.M., 1979, Organic carbon isotope ratios in recent sediments in the St Lawrence Estuary and the Gulf of St Lawrence: *Estuarine and Coastal Marine Science*, v. 8, p. 213-225.

Taylor, S.R., and McLennan, S.M., 1985, *The Contintental Crust: Its Compositions and Evolution*: Oxford, Blackwell Scientific.

Urey, H.C., 1947, The thermodynamic properties of isotopic substances: *Journal of the Chemical Society*, p. 562-581.

Vincent, E., and Berger, W.H., 1985, Carbon dioxide and polar cooling in the Miocene: The Monterey Hypothesis, *in* Sundquist, E.T., and Broecker, W.S., eds., *The Carbon Cycle and Atmospheric CO_2: Natural Variations Archean to Present*, Volume 32: Geophysical Monograph Serials: Washington, AGU, p. 455-468.

Visser, J.P., 1991, Clay mineral stratigraphy of the Miocene to Holocene marine sediments in the central Mediterranean: *Geologica Ultraiectina*, v. 75, p. 243.

Volkman, J.K., 2000, Ecological and environmental factors affecting alkenone distributions in seawater and sediments: *Geochemistry Geophysics Geosystems*, v. 1, 1036, doi:10.1029/2000GC000061.

Vrielynck, B., Odin, G.S. and Dercourt, J., Miocene palaeogeography of the Tethys ocean; potential global correlations in the Mediterranean *in* Montanari, A., Odin, G.S., and Coccioni, R., eds., *Miocene Stratigraphy: An Intergrated Approach*, Volume 15: Developments in Palaeontology and Stratigraphy: Amsterdam, Lausanne, New York, Oxford, Shannon, Tokyo, Elsevier, p. 157 – 165.

Weigers, J.W.H., Schouten, S., Schefuß, E., Schneider, R.R., and J.S., S.D., 2009, Disentangline marine, soil and plant organic carbon contributions to continental margin sediments: A multi-proxy approach in a 20,000 year sediment record from the Congo deep-sea fan: *Geochimica et Cosmochimica Acta*, v. 73, p. 119-132.

Weiss, R.F., 1970, The solubility of nitrogen, oxygen and argon in water and seawater: *Deep-Sea Research*, v. 17, p. 721-735.

Weiss, R.F., 1974, Carbon dioxide in water and seawater: The solubility of a non-ideal gas: *Marine Chemistry*, v. 2, p. 203-215.

Wilkinson, B.H., and Algeo, T.J., 1989, Sedimentary carbonate record of calcium-magnesium cycling: *American Journal of Science*, v. 289, p. 1158-1194.

Woodruff, F., and Savin, S., 1991, Mid-Miocene isotope stratigraphy in the deep sea: high resolution correlations, paleoclimatic cycles, and sediment preservation: *Paleoceanography*, v. 6, p. 755-806.

Yapp, C.J., 2004, $Fe(CO_3)OH$ in goethite from a mid-latitude North American Oxisol: Estimate of atmospheric CO_2 concentration in the Early Eocene "climatic optimum": *Geochimica et Cosmochimica Acta*, v. 68, p. 935-947.

Yu, J., Elderfield, H., and Honisch, B., 2007, B/Ca in planktonic foraminifera as a proxy for surface seawater pH: *Paleoceanography*, v. 22, doi:10.1029/2006PA001347.

Zachos, J., Pagani, M., Sloan, L., Thomas, E., and Billups, K., 2001, Trends, rhythms, and aberrations in global climate 65 Ma to present: *Science*, v. 292, p. 686-693.

Zachos, J.C., Dickens, G.R., and Zeebe, R.E., 2008, An early Cenozoic perspective on greenhouse warming and carbon-cycle dynamics: *Nature*, v. 451, p. 279-283.

Zeebe, R.E., and Wolf-Gladrow, D.A., 2001, *CO_2 in Seawater: Equilibrium, Kinetics, Isotopes*: Amsterdam, Elsevier.

10 Appendix I: Data Tables

Data Table 1: Coarse Percent, RIP section

Height in section (m)	Age (Ma)	Coarse %
0.00	13.867	35.1
0.35	13.860	27.0
0.70	13.852	23.3
1.05	13.844	15.3
1.40	13.836	20.0
1.75	13.829	35.9
2.10	13.821	19.0
2.45	13.813	3.6
2.80	13.805	7.4
3.15	13.798	8.7
3.50	13.790	1.7
3.85	13.780	2.1
4.20	13.771	1.7
4.55	13.761	3.8
4.90	13.751	1.7
5.25	13.742	5.1
5.60	13.732	6.6
5.95	13.722	3.7
6.30	13.713	4.8
6.65	13.703	24.1
7.00	13.694	4.2
7.35	13.684	1.8
7.70	13.674	2.7
8.05	13.665	6.6
8.40	13.655	2.0
8.75	13.646	1.7
9.10	13.636	12.0
9.45	13.627	12.8
9.80	13.617	2.0
10.15	13.608	1.8
10.50	13.598	7.5
10.85	13.589	2.0
11.20	13.579	2.1
11.55	13.570	3.7
11.90	13.560	5.0
12.25	13.551	6.4
12.60	13.541	3.6
12.95	13.532	4.9
13.30	13.522	2.2
13.65	13.513	3.2
14.00	13.503	2.3

Height in section (m)	Age (Ma)	Coarse %
14.35	13.494	3.1
14.70	13.484	5.1
15.05	13.475	10.9
15.40	13.465	6.6
15.75	13.456	8.6
16.10	13.446	8.7
16.45	13.437	7.0
16.80	13.427	3.8
17.15	13.418	5.8
17.50	13.408	7.4
17.85	13.400	5.3
18.20	13.392	1.7
18.55	13.384	6.8
18.90	13.375	4.8
19.60	13.359	4.0
19.95	13.351	2.5
20.30	13.343	3.9
20.65	13.335	5.2
21.00	13.326	5.0
21.35	13.318	5.5
21.70	13.310	5.7
22.05	13.302	6.4
22.40	13.294	3.7
22.75	13.286	9.4
23.10	13.277	7.4
23.45	13.269	4.8
23.80	13.261	3.4
24.15	13.253	3.4
24.50	13.245	2.1
24.85	13.237	6.1
25.20	13.230	2.3
25.55	13.222	1.5
25.90	13.215	3.3
26.25	13.207	2.6
26.60	13.199	4.3
26.95	13.192	2.4
27.30	13.184	5.5
27.65	13.177	2.9
28.00	13.169	10.2
28.35	13.162	6.8
28.70	13.154	3.4
29.05	13.147	3.5
29.40	13.139	4.1
29.75	13.132	2.2
30.10	13.124	4.0
30.45	13.117	3.0
30.80	13.109	2.2
31.15	13.101	2.1

Height in section (m)	Age (Ma)	Coarse %
31.50	13.094	1.9
31.85	13.086	4.4
32.20	13.079	7.2
32.55	13.071	3.1
32.90	13.064	3.8
33.25	13.056	3.9
33.60	13.049	4.7
33.95	13.041	4.1
34.30	13.034	6.2
34.65	13.024	5.5
35.00	13.015	2.0
35.35	13.006	2.9
35.70	12.996	3.6
36.05	12.987	4.9
36.40	12.977	1.7
36.75	12.968	2.7
37.10	12.959	2.2
37.45	12.949	6.4
37.80	12.940	2.7
38.15	12.931	2.7
38.50	12.921	6.6
38.85	12.912	4.2
39.20	12.903	6.1
39.55	12.893	2.3
39.90	12.884	3.1
40.25	12.875	4.8
40.60	12.865	4.4
40.95	12.856	2.9
41.30	12.846	1.8
41.30	12.846	7.3
41.65	12.837	4.4
42.00	12.828	19.9
42.35	12.818	7.1
42.70	12.809	3.4
43.05	12.800	3.4
43.40	12.790	7.7
43.75	12.781	7.8
44.10	12.772	2.8
44.45	12.762	6.6
44.80	12.753	4.6
45.15	12.744	7.6

Data Table 2: Total Organic Carbon percent for RIP

Height in Section (m)	Age (Ma)	Total Organic Carbon (%)
0.00	13.867	0.13
0.35	13.860	0.26
0.70	13.852	0.30
1.05	13.844	0.36
1.40	13.836	0.25
1.75	13.829	0.26
2.10	13.821	0.38
2.45	13.813	0.23
2.80	13.805	0.35
3.15	13.798	0.38
3.50	13.790	0.18
3.85	13.780	0.17
4.20	13.771	0.17
4.55	13.761	0.20
4.90	13.751	0.20
5.25	13.742	0.21
5.60	13.732	0.13
5.95	13.722	0.19
6.30	13.713	0.24
6.65	13.703	0.15
7.00	13.694	0.15
7.35	13.684	0.17
7.70	13.674	0.16
8.05	13.665	0.16
8.40	13.655	0.13
8.75	13.646	0.11
9.10	13.636	0.15
9.45	13.627	0.17
9.80	13.617	0.18
10.15	13.608	0.24
10.85	13.589	0.25
11.55	13.570	0.19
12.25	13.551	0.22
12.95	13.532	0.20
13.65	13.513	0.29
14.35	13.494	0.26
15.05	13.475	0.22
15.75	13.456	0.14
16.45	13.437	0.22
17.15	13.418	0.21
17.85	13.400	0.45
18.55	13.384	0.23
19.95	13.351	0.20
20.65	13.335	0.21

Height in Section (m)	Age (Ma)	Total Organic Carbon (%)
21.35	13.318	0.24
22.05	13.302	0.26
22.75	13.286	0.20
23.45	13.269	0.20
24.15	13.253	0.25
24.85	13.237	0.26
25.55	13.222	0.35
26.25	13.207	0.46
26.95	13.192	0.28
27.65	13.177	0.23
28.35	13.162	0.20
29.05	13.147	0.35
29.75	13.132	0.30
30.45	13.117	0.27
31.15	13.101	0.46
31.85	13.086	0.41
32.55	13.071	0.46
33.25	13.056	0.27
33.95	13.041	0.28
34.65	13.024	0.57
35.35	13.006	0.32
36.05	12.987	0.28
36.75	12.968	0.32
37.45	12.949	0.38
38.15	12.931	0.38
38.85	12.912	0.39
39.55	12.893	0.33
40.25	12.875	0.17
40.95	12.856	0.15
41.65	12.837	0.25
42.35	12.818	0.17
43.05	12.800	0.19
43.75	12.781	0.16
44.45	12.762	0.15
45.15	12.744	0.18

Data Table 3: Organic C/N ratio from RIP.

Height in Section (m)	Age (Ma)	Organic C/N
0.00	13.867	4.7
0.35	13.860	6.4
0.70	13.852	6.9
1.05	13.844	6.8
1.40	13.836	6.1
1.75	13.829	5.4
2.10	13.821	5.3
2.45	13.813	3.9
2.80	13.805	5.0
3.15	13.798	5.1
3.50	13.790	2.5
3.85	13.780	2.8
4.20	13.771	2.8
4.55	13.761	3.3
4.90	13.751	4.2
5.25	13.742	3.7
5.60	13.732	3.0
5.95	13.722	3.5
6.30	13.713	5.0
6.65	13.703	3.3
7.00	13.694	2.8
7.35	13.684	2.6
7.70	13.674	2.4
8.05	13.665	2.6
8.40	13.655	2.0
8.75	13.646	1.7
9.10	13.636	3.2
9.45	13.627	3.4
9.80	13.617	2.7
10.15	13.608	4.1
10.50	13.598	2.2
10.85	13.589	4.0
11.20	13.579	2.5
11.55	13.570	3.1
12.25	13.551	4.0
12.95	13.532	3.3
13.65	13.513	4.6
14.35	13.494	4.3
15.05	13.475	4.6
15.75	13.456	4.1
16.45	13.437	4.6
17.15	13.418	4.3
17.85	13.400	6.3
18.55	13.384	4.4
19.95	13.351	4.2

Height in Section (m)	Age (Ma)	Organic C/N
20.65	13.335	4.5
21.35	13.318	5.0
22.05	13.302	5.2
22.75	13.286	4.7
23.45	13.269	4.1
24.15	13.253	4.4
24.85	13.237	4.9
25.55	13.222	5.2
26.25	13.207	7.0
26.95	13.192	5.5
27.65	13.177	4.8
28.35	13.162	4.6
29.05	13.147	5.8
29.75	13.132	5.1
30.45	13.117	4.7
31.15	13.101	6.0
31.85	13.086	6.1
32.55	13.071	6.1
33.25	13.056	4.8
33.95	13.041	5.5
34.65	13.024	7.8
35.35	13.006	5.4
36.05	12.987	5.4
36.75	12.968	5.3
37.45	12.949	5.8
38.15	12.931	5.5
38.85	12.912	6.1
39.55	12.893	5.1
40.25	12.875	3.6
40.95	12.856	2.8
41.65	12.837	3.8
42.35	12.818	3.7
43.05	12.800	4.2
43.75	12.781	4.0
44.45	12.762	3.7
45.15	12.744	3.6

Data Table 4: Bulk organic and carbonate fine fraction carbon isotopes from RIP

Height in Section (m)	Age (Ma)	Bulk Organic $\delta^{13}C$ (‰)	Fine Fraction (<63 μm) $\delta^{13}C$ (‰)
0.00	13.867	-20.07	0.09
0.35	13.860	-20.09	0.32
0.70	13.852	-20.02	0.09
1.05	13.844	-20.04	0.37
1.40	13.836	-20.62	0.30
1.75	13.829	-20.96	0.19
2.10	13.821	-20.62	0.38
2.45	13.813	-21.24	0.98
2.80	13.805	-20.79	0.77
3.15	13.798	-21.10	0.72
3.50	13.790	-22.16	1.59
3.85	13.780	-21.78	0.85
4.20	13.771	-21.24	0.37
4.55	13.761	-21.05	0.39
4.90	13.751	-20.69	0.47
5.25	13.742	-20.99	0.28
5.60	13.732	-21.23	0.75
5.95	13.722	-21.38	0.92
6.30	13.713	-20.73	0.47
6.65	13.703	-20.96	0.68
7.00	13.694	-22.09	1.01
7.35	13.684	-22.05	1.28
7.70	13.674	-22.03	0.95
8.05	13.665	-22.25	1.56
9.10	13.636	-21.70	0.29
9.45	13.627	-21.50	0.51
9.80	13.617	-21.75	0.27
10.15	13.608	-21.20	0.14
10.50	13.598	-22.03	0.22
10.85	13.589	-21.66	-0.16
11.20	13.579	-21.56	-0.17
11.55	13.570	-22.24	0.62
12.25	13.551	-23.28	0.77
12.95	13.532	-22.12	0.35
13.65	13.513	-23.28	0.02
14.35	13.494	-22.66	0.52
15.05	13.475	-22.66	0.26
15.75	13.456	-22.46	0.34
16.45	13.437	-22.26	0.45
17.15	13.418	-22.97	1.08
17.85	13.400	-21.99	1.24
18.55	13.384	-23.00	0.40
19.95	13.351	-23.10	0.72
20.65	13.335	-22.70	0.88

Height in Section (m)	Age (Ma)	Bulk Organic $\delta^{13}C$ (‰)	Fine Fraction (<63 μm) $\delta^{13}C$ (‰)
21.35	13.318	-22.19	0.62
22.05	13.302	-22.50	0.42
22.75	13.286	-21.83	0.48
23.45	13.269	-22.69	0.79
24.15	13.253	-22.49	0.60
24.85	13.237	-22.77	0.62
25.55	13.222	-21.96	-0.06
26.25	13.207	-22.14	0.82
26.95	13.192	-22.20	0.60
27.65	13.177	-22.02	0.62
28.35	13.162	-22.71	0.31
29.05	13.147	-22.50	0.20
29.75	13.132	-22.29	0.31
30.45	13.117	-22.35	0.07
31.15	13.101	-22.07	0.05
31.85	13.086	-22.32	0.31
32.55	13.071	-21.84	0.05
33.25	13.056	-22.95	0.76
33.95	13.041	-22.81	0.52
34.65	13.024	-22.42	0.29
35.35	13.006	-22.62	0.35
36.05	12.987	-22.47	0.30
36.75	12.968	-22.00	0.47
37.45	12.949	-21.79	-0.14
38.15	12.931	-21.40	0.49
38.85	12.912	-21.55	0.33
39.55	12.893	-21.75	0.80
40.25	12.875	-21.71	0.54
41.65	12.837	-21.82	-0.12
42.35	12.818	-21.77	0.44
43.05	12.800	-21.80	0.25
43.75	12.781	-21.33	0.67
44.45	12.762	-21.40	0.87
45.15	12.744	-21.51	

Data Table 5: *n*-alkane odd over even predominance (OEP) for samples from RIP

Height in section (m)	Age (Ma)	OEP ratio
0.00	13.867	4.7
0.70	13.852	3.6
1.05	13.844	5.0
1.40	13.836	7.1
1.75	13.829	2.8
2.10	13.821	6.3
2.45	13.813	2.2
3.15	13.798	4.5
3.50	13.790	4.6
3.85	13.780	6.8
4.20	13.771	6.8
4.90	13.751	4.7
5.25	13.742	6.8
5.60	13.732	5.8
5.95	13.722	6.0
6.30	13.713	7.0
6.65	13.703	6.9
7.00	13.694	4.4
7.35	13.684	5.5
7.70	13.674	4.6
8.05	13.665	3.6
8.40	13.655	4.2
8.75	13.646	5.2
9.10	13.636	5.9
9.45	13.627	7.7
9.80	13.617	4.5
10.15	13.608	4.4
18.20	13.392	4.8
22.75	13.286	5.2
33.95	13.041	5.0
43.05	12.800	4.3

Data Table 6: Carbonate stable isotopes from the Moria section

Height in Section (m)	Age (Ma)	Carbonate $\delta^{13}C$ (‰)	Carbonate $\delta^{18}O$ (‰)
20.00	17.111	0.48	-1.46
20.40	17.105	0.55	-2.49
21.00	17.094	0.59	-1.57
22.00	17.077	0.68	-1.63
23.00	17.060	0.83	-1.62
24.00	17.043	0.66	-1.48
25.00	17.026	0.52	-1.63
26.00	17.009	0.29	-2.20
27.00	16.992	0.37	-1.90
28.00	16.975	0.01	-2.21
29.00	16.957	-0.14	-2.50
30.00	16.940	-0.12	-2.16
31.00	16.923	-0.23	-2.22
32.00	16.906	-0.14	-1.94
33.00	16.889	-0.18	-2.18
34.00	16.871	-0.18	-1.75
35.00	16.855	-0.14	-2.24
36.00	16.838	-0.14	-2.16
37.00	16.820	-0.48	-2.32
38.00	16.803	-0.56	-2.39
39.00	16.786	-0.39	-2.34
40.00	16.769	-0.59	-2.42
41.00	16.752	-0.26	-2.11
42.00	16.735	-0.26	-2.10
43.00	16.717	-0.38	-2.55
44.00	16.700	-0.51	-2.30
45.00	16.684	-0.31	-2.89
45.25	16.679	-0.33	-2.41
45.50	16.675	-0.26	-2.26
45.75	16.671	-0.39	-1.87
46.00	16.666	-0.18	-2.66
46.25	16.662	-0.25	-2.35
46.50	16.658	-0.37	-2.17
46.75	16.654	-0.07	-1.84
47.00	16.649	-0.10	-2.08
47.25	16.645	-0.11	-2.21
47.50	16.641	-0.03	-2.08
47.75	16.636	0.12	-1.84
48.00	16.632	0.11	-1.90
48.25	16.628	0.03	-1.38
48.50	16.624	-0.08	-1.86
48.75	16.619	-0.21	-1.94
49.00	16.615	-0.06	-2.04
50.00	16.598	-0.05	-2.53

Height in Section (m)	Age (Ma)	Carbonate $\delta^{13}C$ (‰)	Carbonate $\delta^{18}O$ (‰)
51.00	16.581	0.08	-2.34
52.00	16.563	-0.56	-1.11
52.25	16.559	-0.09	-2.07
52.50	16.555	-0.05	-2.34
52.75	16.551	0.31	-2.40
53.00	16.534	0.04	-2.59
53.25	16.518	0.21	-2.46
53.50	16.502	0.15	-2.39
53.75	16.486	-0.16	-2.17
54.00	16.470	-0.10	-2.16
54.25	16.454	0.15	-2.90
54.50	16.438	0.16	-2.61
54.75	16.422	0.34	-2.18
55.00	16.406	-0.23	-0.95
55.25	16.388	0.12	-2.40
55.50	16.369	0.07	-2.18
55.75	16.351	-0.03	-2.22
56.00	16.333	-0.14	-2.81
56.25	16.314	-0.08	-1.95
56.50	16.296	-0.04	-1.67
56.75	16.278	0.02	-2.31
57.00	16.259	0.04	-2.42
57.25	16.241	0.02	-2.34
57.50	16.223	0.07	-1.87
57.75	16.204	-0.06	-2.44
58.00	16.186	-0.14	-1.86
58.25	16.168	0.01	-2.17
58.50	16.150	-0.03	-2.22
58.75	16.131	0.29	-1.85
59.00	16.122	0.24	-1.93
59.25	16.112	0.15	-2.35
59.50	16.103	0.26	-1.98
59.75	16.094	0.16	-2.26
60.00	16.084	0.01	-2.35
60.25	16.075	0.02	-2.46
60.50	16.065	0.10	-1.76
61.00	16.047	-0.02	-2.48
61.25	16.037	0.16	-2.44
61.50	16.028	0.00	-2.37
61.75	16.018	0.07	-2.87
62.00	16.009	-0.17	-2.08
62.25	16.000	-0.03	-2.29
62.50	15.990	0.22	-2.08
62.75	15.981	-0.04	-2.02
63.00	15.971	0.20	-2.46
63.25	15.962	0.06	-1.65
63.50	15.953	0.33	-2.15

Height in Section (m)	Age (Ma)	Carbonate $\delta^{13}C$ (‰)	Carbonate $\delta^{18}O$ (‰)
63.75	15.943	0.22	-2.15
64.00	15.934	0.22	-2.32
64.25	15.924	0.29	-2.22
64.75	15.906	0.35	-2.31
65.00	15.901	0.15	-2.97
65.25	15.896	0.24	-2.33
65.50	15.891	0.29	-1.88
65.75	15.887	-0.26	-2.65
66.00	15.882	-0.18	-2.20
66.25	15.877	-0.26	-2.26
66.75	15.867	-0.45	-2.40
67.00	15.862	0.13	-1.74
67.25	15.857	0.30	-2.42
67.50	15.852	0.41	-2.22
67.75	15.847	0.31	-2.56
68.00	15.842	0.05	-2.11
68.25	15.837	0.13	-2.32
68.50	15.833	0.27	-2.05
68.75	15.828	0.33	-2.16
69.00	15.823	0.37	-2.23
69.25	15.818	0.35	-2.43
69.50	15.813	0.11	-1.92
69.75	15.808	-0.01	-2.24
70.00	15.803	0.02	-2.23
70.20	15.799	0.11	-2.02
70.40	15.795	0.19	-1.88
70.60	15.791	0.16	-2.11
70.80	15.788	0.23	-1.82
71.00	15.784	0.25	-2.27
71.25	15.779	0.14	-2.40
71.50	15.774	0.23	-2.09
71.75	15.769	0.25	-1.78
72.00	15.764	0.35	-2.09
72.25	15.759	0.23	-2.14
72.50	15.754	0.33	-2.22
72.75	15.749	0.16	-2.66
73.00	15.744	0.61	-2.11
73.25	15.733	0.55	-2.30
73.50	15.723	0.03	-2.30
73.75	15.712	0.48	-2.76
74.00	15.701	0.57	-2.19
74.25	15.690	0.44	-2.14
74.50	15.679	0.48	-1.88
74.75	15.669	0.45	-2.37
75.00	15.659	0.40	-2.13
75.25	15.648	0.39	-2.10
75.50	15.638	0.24	-2.27

Height in Section (m)	Age (Ma)	Carbonate $\delta^{13}C$ (‰)	Carbonate $\delta^{18}O$ (‰)
75.75	15.627	0.30	-2.50
76.00	15.616	0.51	-1.90
76.25	15.605	0.37	-2.23
76.50	15.594	0.37	-3.24
76.75	15.584	0.41	-2.18
77.00	15.573	0.24	-2.37
77.25	15.562	0.48	-2.17
77.50	15.551	0.45	-2.27
77.75	15.540	0.36	-2.12
78.00	15.530	0.56	-1.94
78.25	15.519	0.44	-2.33
78.50	15.508	0.46	-2.28
78.75	15.497	0.37	-2.28
79.00	15.486	0.64	-1.73
79.25	15.475	0.55	-1.83
79.50	15.465	0.36	-2.22
79.75	15.454	0.32	-2.05
80.00	15.443	0.57	-1.84
80.25	15.432	0.42	-0.87
80.50	15.421	0.35	-1.29
80.75	15.411	0.39	-1.03
81.00	15.400	0.48	-1.81

Data Table 7: Seawater oxygen isotopes calculated from G. trilobus oxygen isotopes and Mg/Ca SST from RIP using the temperature sensitivity of Erez and Luz (1983).

Height in Section (m)	Age (Ma)	Seawater $\delta^{18}O$ (‰)
0.00	13.867	2.17
0.35	13.860	1.38
0.70	13.852	1.27
1.05	13.844	1.51
1.75	13.829	2.00
2.45	13.813	1.09
2.80	13.805	0.86
3.15	13.798	1.05
3.50	13.790	0.76
3.85	13.780	2.11
4.20	13.771	1.84
4.90	13.751	1.35
5.25	13.742	1.82
5.60	13.732	1.22
5.95	13.722	1.31
6.30	13.713	1.22
6.65	13.703	0.63
7.35	13.684	0.82
7.70	13.674	0.92
8.05	13.665	0.82
8.40	13.655	1.45
8.75	13.646	1.80
9.10	13.636	0.84
9.45	13.627	1.12
10.50	13.598	1.02
22.75	13.286	1.18
33.95	13.041	0.91

Data Table 8: Alkenone carbon isotopes, isotopic fractionation and calculated atmospheric CO_2 based on samples from the RIP section.

Height in section (m)	Age (Ma)	$\delta^{13}C_{37:2}$ (‰)	ε_p (‰)	2σ	CO_2 (ppm)	2σ
0.00	13.867	-21.39	10.54	0.50	328.1	46.8
0.35	13.860	-21.14	10.36	1.63	315.1	56.5
0.70	13.852	-21.03	9.85	0.78	294.6	44.2
1.05	13.844	-21.47	10.68	1.26	318.3	52.8
1.40	13.836	-21.45	10.57	0.58	313.9	45.9
1.75	13.829	-22.58	11.61	0.94	337.4	53.9
2.10	13.821	-20.91	9.93	0.56	291.5	43.0
2.45	13.813	-21.49	11.04	1.18	306.6	51.9
2.80	13.805	-21.01	10.50	0.54	310.2	45.6
4.55	13.761	-20.79	9.93	0.61	298.4	43.5
4.90	13.751	-20.64	9.89	1.57	300.4	52.6
5.25	13.742	-20.31	9.15	1.33	275.2	45.5
5.95	13.722	-20.87	10.38	0.64	297.5	44.8
6.65	13.703	-20.27	9.27	0.93	264.0	41.6
7.00	13.694	-21.04	10.52	0.68	293.0	44.6
7.35	13.684	-21.27	11.14	0.50	313.0	46.6
7.70	13.674	-21.37	10.94	0.51	310.7	46.1
8.05	13.665	-20.85	10.96	0.74	308.2	47.6
8.40	13.655	-21.12	10.83	0.59	305.6	46.1
9.45	13.627	-24.09	13.18	4.35	375.5	207.9
10.15	13.608	-20.47	9.17	0.86	274.7	42.0
43.05	12.800	-21.68	10.39	0.70	289.4	44.5

Data Table 9: G. trilobus boron isotopic composition, B/Ca ratio and calculated pH and atmospheric pCO_2

Height in section (m)	Age (Ma)	$\delta^{11}B$ (‰)	B/Ca (mmol/mol)	pH	pCO2 (ppm)
0.00	13.867	15.83	79.46	8.103	328.0
0.70	13.852	15.85	88.18	8.136	301.7
1.75	13.829	15.75	83.46	8.122	313.6
3.15	13.798	16.53	93.82	8.184	260.3
3.50	13.790	15.98	96.50	8.158	283.5
5.60	13.732	16.17	88.20	8.162	278.7

Data Table 10: Fine fraction carbonate Sr/Ca and D_{Sr} from RIP

Height in Section (m)	Age (Ma)	Sr/Ca (mmol/mol)	D_{Sr}
0.00	13.867	1.16	0.13
0.35	13.860	1.18	0.13
0.70	13.852	1.46	0.16
1.05	13.844	1.30	0.15
1.40	13.836	1.58	0.18
1.75	13.829	1.39	0.16
2.10	13.821	1.70	0.19
2.80	13.805	1.75	0.20
3.15	13.798	1.53	0.17
3.50	13.790	2.12	0.24
3.85	13.780	1.93	0.22
4.20	13.771	1.82	0.20
4.55	13.761	1.92	0.21
4.90	13.751	2.01	0.22
5.25	13.742	1.45	0.16
5.60	13.732	1.76	0.20
5.95	13.722	1.91	0.21
6.30	13.713	1.54	0.17
6.65	13.703	1.32	0.15
7.00	13.694	1.80	0.20
7.35	13.684	1.74	0.20
7.70	13.674	1.88	0.21
8.05	13.665	1.69	0.19
8.40	13.655	1.63	0.18
8.75	13.646	1.82	0.20
9.10	13.636	1.44	0.16
9.45	13.627	1.49	0.17
9.80	13.617	1.52	0.17
10.15	13.608	1.41	0.16
10.50	13.598	1.47	0.16
10.85	13.589	1.49	0.17
11.20	13.579	1.42	0.16
11.55	13.570	1.76	0.20
11.90	13.560	1.67	0.19
12.25	13.551	1.88	0.21
13.65	13.513	1.94	0.22
18.20	13.392	2.01	0.22
33.95	13.041	1.92	0.21
43.05	12.800	1.78	0.20

Data Table 11: Bulk organic carbon isotopes from the Moria section

Height in Section (m)	Age (Ma)	Bulk Organic $\delta^{13}C$ (‰)
20.00	17.111	-21.47
21.00	17.094	-21.00
23.00	17.060	-20.43
25.00	17.026	-20.92
27.00	16.992	-21.02
29.00	16.957	-22.23
31.00	16.923	-22.24
33.00	16.889	-22.60
35.00	16.855	-21.08
37.00	16.820	-21.66
39.00	16.786	-22.06
41.00	16.752	-21.40
43.00	16.717	-21.73
45.00	16.684	-22.45
45.50	16.675	-22.33
46.00	16.666	-22.22
46.50	16.658	-21.87
47.00	16.649	-20.93
47.50	16.641	-21.59
48.00	16.632	-21.68
48.50	16.624	-21.23
49.00	16.615	-21.48
51.00	16.581	-21.62
52.25	16.559	-22.02
52.75	16.551	-21.18
53.25	16.518	-21.86
53.75	16.486	-22.06
54.25	16.454	-22.31
54.75	16.422	-21.64
55.25	16.388	-22.17
55.75	16.351	-21.32
56.25	16.314	-21.34
56.75	16.278	-21.96
57.25	16.241	-22.31
57.75	16.204	-21.97
58.25	16.168	-22.38
58.75	16.131	-22.05
59.25	16.112	-21.65
59.75	16.094	-21.65
60.25	16.075	-21.32
61.00	16.047	-21.86
61.50	16.028	-21.37
62.00	16.009	-21.15

Height in Section (m)	Age (Ma)	Bulk Organic $\delta^{13}C$ (‰)
62.50	15.990	-20.94
63.00	15.971	-21.40
63.50	15.953	-21.52
64.00	15.934	-20.88
64.75	15.906	-22.04
65.25	15.896	-21.28
65.75	15.887	-20.53
66.25	15.877	-20.42
67.00	15.862	-21.92
67.50	15.852	-21.49
68.00	15.842	-21.26
68.50	15.833	-20.11
69.00	15.823	-20.46
69.50	15.813	-21.40
70.00	15.803	-21.07
70.40	15.795	-21.70
70.80	15.788	-21.49
71.25	15.779	-20.64
71.75	15.769	-21.24
72.25	15.759	-21.03
72.75	15.749	-21.60
73.25	15.733	-20.58
73.75	15.712	-21.18
74.25	15.690	-21.14
74.75	15.669	-21.79
75.25	15.648	-20.10
75.75	15.627	-21.41
76.25	15.605	-20.76
76.75	15.584	-20.73
77.25	15.562	-20.39
77.75	15.540	-21.04
78.25	15.519	-21.45
78.75	15.497	-21.81
79.25	15.475	-21.63
79.75	15.454	-22.36
80.25	15.432	-21.83
80.75	15.411	-21.74

Data Table 12: Bulk organic carbon isotopes from ODP site 761b

Depth (Mbsf)	Age (Ma)	Bulk organic $\delta^{13}C$ (‰)
40.580	13.656	-23.52
40.740	13.726	-22.78
40.820	13.760	-24.81
40.920	13.803	-24.12
41.020	13.846	-23.23
41.120	13.889	-24.35
41.220	14.010	-25.30
41.320	14.040	-25.31
41.520	14.100	-24.46
41.620	14.130	-24.36
41.720	14.160	-23.21
41.820	14.190	-24.31
41.920	14.220	-24.41
42.120	14.279	-24.42
42.360	14.351	-23.27
42.200	14.423	-24.09
42.400	14.483	-22.66
42.600	14.543	-22.26
42.800	14.603	-22.69
43.000	14.663	-22.82
43.200	14.723	-22.36
43.400	14.783	-22.19
43.600	14.843	-22.18
43.820	14.909	-23.11
44.020	14.969	-23.99
44.220	15.028	-21.67
44.420	15.088	-22.34
44.620	15.148	-23.57
44.820	15.208	-22.83
44.940	15.244	-23.32